NASA Contractor Report 182271

An Experimental Study of Swirling Flows as Applied to Annular Combustors

Michael Damian Seal II
Purdue University
West Lafayette, Indiana

April 1997

Prepared for
Lewis Research Center
Under Contract NAS3–24350

National Aeronautics and
Space Administration

AN EXPERIMENTAL STUDY OF SWIRLING FLOWS AS APPLIED TO ANNULAR COMBUSTORS

A Thesis

Submitted to the Faculty

of

Purdue University

by

Michael Damian Seal II

In Partial Fulfillment of the

Requirements for the Degree

of

Master of Science in Aeronautics and Astronautics

May 1988

ACKNOWLEDGEMENTS

The author wishes to express gratitude to Dr. John P. Sullivan for his efforts as major professor. His criticism, guidance and insight during the course of this research is appreciated.

The author would like to thank Dr. S. N. B. Murthy and Dr. C. P. Kentzer for their participation on the author's advisory committee.

Special thanks are in order for the technical staff at the Purdue University Aerospace Sciences Lab. Members of this staff include Scott Kepner, Bob Sanders, Dave Reagan, Bill Bader and Jack Davis.

The author would like to thank NASA Lewis Research Center and Allison-Gas Turbine Division for the financial support of this research.

TABLE OF CONTENTS

LIST OF FIGURES

Figure Page

Figure Page

Figure Page

Figure Page

Figure Page

Figure Page

Figure Page

ABSTRACT

Seal, Michael II, Damian, M.S.A.A., Purdue University, May, 1988. An Experimental Study of Swirling Flows as Applied to Annular Combustors. Major Professor: John P. Sullivan.

This thesis presents an experimental study of swirling flows with direct applications to gas turbine combustors. Two separate flowfields were investigated: a round, swirling jet and a non-combusting annular combustor model. These studies were intended to allow both a further understanding of the behavior of general swirling flow characteristics, such as the recirculation zone, as well as to provide a base for comparison for the development of computational models.

In order to determine the characteristics of swirling flows the concentration fields of a round, swirling jet were analyzed for varying amounts of swirl. The experimental method used was a light scattering concentration measurement technique known as marker nephelometry. Results indicated the formation of a zone of recirculating fluid for swirl ratios (rotational speed X jet radius over mass average axial velocity) above a certain critical value. The size of this recirculation

zone, as well as the spread angle of the jet, was found to increase with increase in the amount of applied swirl.

The annular combustor model flowfield simulated the cold-flow characteristics of typical current annular combustors: swirl, recirculation, primary air cross jets and high levels of turbulence. The measurements in the combustor model, made by the Laser Doppler Velocimetry technique, allowed the evaluation of the mean and rms velocities in the three coordinate directions, one Reynold's shear stress component and the turbulence kinetic energy. The primary cross jets were found to have a very strong effect on both the mean and turbulence flowfields. These cross jets, along with a large step change in area and wall jet inlet flow pattern, reduced the overall swirl in the test section to negligible levels. The formation of the strong recirculation zone is due mainly to the cross jets and the large step change in area. The cross jets were also found to drive a four-celled vortex-type motion (parallel to the combustor longitudinal axis) near the cross jet injection plane.

INTRODUCTION

In an economically driven society air travel is a necessary part of business. As corporations, companies, and individuals strive for success in national and international markets, lowering these travel costs is a necessity. One way to reduce these costs is through the improvement of the gas turbine engine and its various components.

Improvements in gas turbine engines come in many forms: increased efficiencies, longer life expectancies and reduced maintenance costs are three of the many possible forms. Increased efficiency means that an aircraft can fly farther for a given amount of fuel. Longer life means that the replacement of the various components need not occur as often. Reduced maintenance costs, partially due to the increase in life expectancy in combustor components, can lead to fewer personnel required to maintain the engines, reducing labor costs. All of these improvements can reduce the expense of travel.

In order to develop these improvements a major research program was initiated: HOST (turbine engine HOt Section Technology). Sponsored and directed by NASA Lewis

Research Center, this program was designed to significantly upgrade the existing technology and understanding of operating conditions in the gas turbine engine hot section. This thesis describes and discusses experimental work performed at Purdue University for the HOST Aerothermal Modelling Program.

Previously, nearly all gas turbine engine combustion chamber developments have been empirically based. Today, the drive is towards design procedures maximizing prediction methods and minimizing experimental methods. In order to reduce the amount of required experimental work accurate modelling methods must be developed and utilized with confidence. Benchmark quality experimental data is needed to be used as control values in the assessment of these advanced turbulence and scalar transport models.

Thus, the main objective of this research project was to perform a series of experimental measurements on a flowfield of geometric interest relative to current combustors which would provide a good base for comparison with various analytical codes and models. The flowfield chosen for these measurements was a model annular combustor, a model which simulates the cold flow characteristics of typical current annular combustors: swirl, recirculation, primary jet cross flow, and very high levels of turbulence.

The swirl is imparted to inlet annular jet flow through the use of vane-type swirlers. The recirculation

zone generated by the applied swirl and the large step change in area is very strong with a large amount of recirculated mass flow. The cross jets are designed to reduce the length of the recirculation zone in order to reduce the overall combustor length, as well as provide dilution air for the combustion process. The mass flow through both the inlet annular jets can be controlled to allow variability of flowfield conditions. The five inlet annular and ten primary cross jets all have very large average velocities compared to the bulk average and are the main contributors to the high levels of turbulence.

The measurements in the combustor model, acquired with a single-component Laser Doppler Velocimeter system, represent the three-dimensional nature of the flowfield. Mean velocities in the three coordinate directions (X,Y,Z) were made, as well as the root-mean-square (rms) values which also allowed the calculation of the turbulence kinetic energy. At the onset of this research the complete Reynold's stress tensor was desired, but in the end only one of the three cross terms was determined.

The recirculation zone is the most important characteristic in the combustor flowfield as it has a direct effect on the combustion stability and, hence, the combustor performance. In order to obtain a more complete understanding of the recirculation zone and it's formation, as well as associated flowfield characteristics, a second study was undertaken, a study of

two-dimensional seed particle concentration fields of a swirling, round, turbulent jet.

These concentration fields, color enhanced images in the form of flow visualization, were acquired through the use of marker nephelometry, a light scattering method for particle concentration measurement. These planar images (planes parallel to the jet axis) illustrate the various concentration patterns of the seed particles, added to and well-mixed with the jet inlet fluid, which follow the trajectories of the fluid issuing from the jet exit. The images allow analysis of the changes in the flowfield structure with changes in applied swirl.

From these studies a much better understanding of swirling flows and their application to annular combustors is realized. The measured characteristics can be used to analyze computational codes and models, allowing the improvement of the design of future combustors.

The main body of this thesis consists of five chapters. Chapter 1 includes a general overview of swirling flows, describing the characteristics associated with swirling fluid motion, and a literature review. The literature review outlines previously published works related to swirling flows and combustor flows as well as a short review of HOST-related research performed by a previous student at Purdue University, Dean Barron. Chapters 2 and 3 cover the experimental swirling jet and combustor model studies, respectively, with thorough

desriptions of the experimental configurations and presentations and discussions of the results. Chapter 4 includes a summary of this research and the conclusions.

CHAPTER 1: BACKGROUND

This chapter gives the reader background information on the subject matter considered in the research presented in this thesis. A general overview of swirling flows discusses the characteristics associated with swirling flows while a literature review discusses previous published work pertinent to the research results presented.

1.1 General Overview of Swirling Flows

For many years the effects of swirl in reacting or combusting flows has been utilized. Swirl flows are a result of the application of a spiraling motion to mean flows such as jets. This spiraling motion can be applied by various means (swirl vanes, axial-plus-tangential entry, solid-body rotation, etc.) and results in the production of a tangential, or swirl, velocity component.

Studies have shown that the application of swirl has several large scale effects on non-reacting flowfields: increased jet growth, entrainment, and decay. For reacting flows flame size, stability, and combustion intensity are similarly affected by the presence of swirl.

Swirl flows can be characterized by the swirl number, S, a non-dimensional number representing the ratio of axial flux of tangential momentum to the axial flux of axial momentum times the effective nozzle radius,

$$S = \frac{M_\theta}{M_x R} \tag{1.1}$$

where

$$M_\theta = \int_0^\infty (\rho \bar{U}\bar{W} + \rho\overline{U'W'}) R^2 dr \tag{1.2}$$

$$M_x = \int_0^\infty (\rho \bar{U}^2 + \rho\overline{U'^2} + (p-p_\infty)) r dr \tag{1.3}$$

u,v,w= components of velocity in (x,r,θ) cylindrical coordinate system.

Due to the obvious difficulty in obtaining accurate values for the swirl number caused by the evaluation of the respective integrals (1.2) and (1.3), approximations are made to (1.1) or other non-dimensional numbers are used to characterize the flows. Since this research was concerned with swirling flows generated by solid-body rotation and vane-type swirlers, a method of characterizing the corresponding amount of swirl is necessary. For swirl flows generated by solid-body rotation the amount of swirl is usually characterized by the swirl ratio, N, a non-dimensional number defined as

$$N = \frac{\omega R}{U_{ave}} \tag{1.4}$$

where

R= jet radius

ω= rotational frequency

U_{ave}= mass averaged velocity.

For swirl flows generated by vane-type swirlers the amount of swirl is usually characterized by an approximation to the swirl number, S,

$$S \equiv \frac{2}{3}\left[\frac{1 - (\frac{d_i}{d_o})^3}{1 - (\frac{d_i}{d_o})^2}\right]\tan\phi \tag{1.5}$$

where

ϕ = swirl inlet angle,

d_i = inner diameter,

d_o = outer diameter.

For general swirling flows, as the amount of inlet swirl is increased beyond zero very noticeable changes in the flowfield can be observed. For low amounts of swirl (S<0.5,N<0.8) increased jet growth or spread, increased mixing with the co-flowing fluid, and increased decay are found. As the amount of swirl is further increased a critical condition is reached. At this critical swirl number (S=0.6,N=1.0) the flow along the jet axis is found to oscillate between forward flow and backflow.

When the amount of swirl is increased beyond this critical value a definite region of backflow can be identified. The physical characteristics of this region being a function of the amount of swirl applied. The formation of this reverse flow region, known as the central toroidal recirculation zone (CTRZ), is due to the progressive development of a positive axial pressure gradient with increasing swirl. The axial pressure gradient is formed through the downstream decay of tangential velocity. Near the jet exit the swirl is at a maximum, with a large centrifugal acceleration creating a positive radial pressure gradient. Downstream, with the decay in the tangential velocity, the centrifugal acceleration is reduced allowing a higher pressure than at the jet exit. The axial pressure gradient is thus produced by the decay in tangential velocity and increases with increasing swirl.

One major difference between a freely swirling flow and swirling flow in, say, a gas turbine combustor is the effect on the flowfield by the confinement. The high entrainment rates associated with a large amount of swirl ($S>0.6, N>1.0$) may cause the swirling jet to attach to the wall, mainly due to the initial part of the jet entraining and causing backflow. In general confinement causes an increase in the recirculated mass flow, resulting in the lengthening of the CTRZ.

Designers of gas turbine combustors take full advantage of the CTRZ for several reasons. THe recirculation zone has a large and important role in flame stabilization since, in reacting flows, the CTRZ consists of a region of well mixed combustion products that act as a storage of heat. The CTRZ eliminates the need for bluff body surfaces such as stabilizer disks thereby eliminating the problem of the solid surface deterioration due to corrosion and pitting. One necessity for a stable flame is the matching of flame speed and flow velocity; this requirement is easily satisfied since the velocity of the fluid goes to zero at the CTRZ boundary. The downstream distance at which the flame becomes stabilized is much shorter, resulting in a more compact combustor.

Turbulence intensity has been seen to reach high values in recirculation bubbles. Measurements have shown large variations of absolute turbulent kinetic energy levels as well as general non-isotropy of the flowfield. The applied swirl creates a faster decay of the velocity and nozzle fluid concentration from the jet exit through the increased levels of turbulence.

1.2 Literature Review

1.2.1 Swirling Jet Literature

In recent years the structure of swirling jets has been investigated by many researchers. Most of these studies have involved the measurement of mean velocities and turbulence characteristics, usually intended for the analysis of the behavior of decay, ambient fluid entrainment, or mass flux with varying swirl.

Gore and Ranz [25] investigated the formation and characteristics of recirculation zones in swirling flows with a test apparatus which allowed variability of geometric conditions. With the application of a weak amount of swirl the general jet cross section was found to be expanded. No backflow was evident but velocities on the jet centerline were reduced from the zero swirl case, indicating the existence of an axial pressure gradient. As the amount of applied swirl was gradually increased the flow near the axis was found to oscillate between forward and backflow; this critical swirl condition depended on geometric conditions. Beyond this critical swirl the backflow region was clearly evident, with both the forward and rear stagnation points well defined.

In general, Gore and Ranz found the jet spread angle (the radial spread of the half-velocity radius with downstream distance) to be a function of the applied

swirl. One very interesting case was that of swirl generation (by a rotating swirl plate) at the jet exit. For very large amounts of applied swirl the jet expanded at right angles (spread angle of 180 degrees) with the entire region in front of the jet in backflow. When the swirl plate was recessed into the jet the jet spread angle only reached a limiting value of around 40 degrees.

Chigier and Chervinsky [12] also found the jet spread angle to be a function of the applied swirl, with their experimental results indicating that the spread angle increase continuously but approached some asymptotic value. Kerr and Fraser [30] were able to obtain higher levels of applied swirl than Chigier and Chervinsky by using a different method of swirl generation, with their results indicating a linear relation between the spread angle and swirl number, up to a swirl number of 1.2.

Pratte and Keffer [40] found that a free jet with a moderate amount of swirl issuing from a planar surface will spread in an almost linear manner, but at an angle nearly twice that of the non-swirling jet. Also discussed is the fact that the region immediately downstream of the jet exit is the region most affected by the method of swirl generation.

Several investigators have utilized the concentration field measurement technique of marker nephelometry to study the structure of jets, but only of the non-swirling

variety. Rosenweig, Hottel and Williams [47] were the first group to apply the method with their chosen flowfield being the turbulent jet.

Long, Webber and Chang [36] performed instantaneous two-dimensional concentration measurements utilizing a laser illuminated sheet and a high speed video camera. In a very similar experiment Long, Chu and Chang [35] also performed two-dimensional concentration measurements of a turbulent jet, obtaining temporal as well as spatial flowfield information by alteration of their data acquisition system. Their results, in the form of concentration contours as a function of either two position variables, C(X,Y), or one position variable and time, C(X,t), show the behavior of the large scale structures. From the C(X,Y) contours the existence of large scale coherent structures can be seen, while the C(X,t) contours give the relative convective speeds of these structures as they dissipate and coalesce.

Dahm and Dimotakis [14] investigated entrainment and mixing in the self-similar region of a turbulent jet. Instantaneous radial concentration profiles were found to not resemble the averaged profiles, indicating that the large scale structures could possibly play a more important role than previously thought.

Vranos and Liscinsky [54] performed both two-dimensional imaging and gas sampling for the concentration

measurements in the self-similar region of a turbulent jet. The agreement between the two methods was found to be very good, thus allowing confidence in the use of the marker nephelometry technique.

1.2.2 Combustor Model Studies

In recent years, several researchers have reported experiments related to swirling combustor flowfields. These experiments have utilized many various geometries, methods of swirl generation, and measurement techniques. Most of the published results for experimental work pertaining to combustor flowfields are for axisymmetric geometries. This differs from the work presented in this thesis, which pertains to a model combustor of three-dimensional, rectangular geometry. This presents no real problem since the overall features of the flowfields will be roughly independent of the geometry, whether it be axisymmetric (cylindrical) or rectangular (cartesian).

In a very recent work, Brum and Samuelson [9] reported simultaneous two-component LDV measurements in an axisymmetric combustor model with coaxial swirling jets. Of particular interest is that the often-implemented assumption of isotropy is shown to be reasonable, except in regions of high one-dimensional shear. Also of interest is that the Reynold's stress was measured directly, whereas in most other published works the Reynold's stress

is found algebraically, using time averaged quantities. These Reynold's stress results do not agree well with most of the previous works, though, possibly due to dissimilar geometries.

Vu and Gouldin [53] also reported results, from hot-wire measurements, in an axisymmetric model combustor with coaxial swirling jets, although with different geometry than Brum and Samuelson. Measured tangential velocities inside the recirculation zone were found to be very small, while the levels of turbulence and the dissipation rate were very high. Ramos and Somer [43] performed two-component LDV measurements on a test apparatus similar to that of Vu and Gouldin. Comparison to previous experimental data, particularly that of Vu and Gouldin, shows agreement of hot-wire and LDV techniques for most statistics.

Rhode, Lilley, and McLaughlin [44] reported recirculation zone studies for a swirling combustor geometry flow by flow visualization (tufts, smoke, soap bubbles) and five-hole pitot probe mean velocity measurements. Parametric studies included the effect of the swirler vane angle and the side wall expansion angle. The length and width of the recirculation zone was found to increase with increasing swirler vane angle until a critical angle is reached, where any further increase in swirl cause shortening of length but further increase in

width. The major effect of the side wall expansion angle is to shorten the corner recirculation region, with no major effect on the central recirculation region.

Ferrell, Abujelala, Busnaina, and Lilley [22] also performed flow visualization and five-hole pitot probe velocity measurements experiments on the same apparatus as [44] but with the addition of single lateral jet at some distance downstream of the swirler inlet plane. This work was the first in a series intended to characterize the mean and turbulence fields in order to allow advances to be made in computational methods.

Yoon and Lilley [55], also using the same apparatus as [44], performed further research on confined swirling flows by studying the effect of nozzle contraction ratio. The effect of a weak contraction ratio was found to be the largest for the intermediate swirl case since the contraction effect is strong enough to overwhelm the recirculation region, whereas for the weak swirl and the strong swirl the effect of the contraction is overcome by the forward flow and the centrifugal forces, respectively. The effect of strong contraction ratio is noticeable for all levels of swirl, as the recirculation zone is shortened considerably and the centerline axial velocity becomes positive.

Ferrell and Lilley [23] discuss studies of a single lateral jet injecting into swirling adn non-swirling

crossflow for various jet-to-crossflow velocity ratios. Velocity measurements were made with a six-orientation hot-wire technique for a non-swirling crossflow case while flow visualization (bubbles, sparks) was performed for various swirling crossflow cases. Ferrell, Aoki and Lilley [21] discuss additional flow visualization (helium bubbles, multi-spark) of single lateral jet injection which illustrates an organized eddy structure for low values of the jet-to-crossflow velocity ratio. These techniques, in general, demonstrated the effects of a range of velocity ratios and swirl strengths. In a follow-up experiment to these experiments Ong and Lilley [39] performed six-orientation hot-wire velocity measurements for various crossflow cases at one velocity ratio for the single lateral jet.

1.2.3 Dean Barron's Work

Dean Barron [2], a previous researcher also involved with the HOST program, performed measurements very similar to the work presented in this thesis. His results included two-component LDV measurements made in a test apparatus of square cross-section with a single vane-type swirler. This apparatus was originally constructed to allow the measurement of the flow conditions at the swirler exit plane since these measurements would have been very difficult to impossible in the five swirler apparatus.

The test apparatus, which can be seen in figures (1.1) and (1.2), was a 3.0 in.x 3.0 in. cross section duct with a length of 10 duct heights, or 30.0 in.. Since conditions at the swirler exit were desired the same annular jet and swirler unit used in the model combustor studies were utilized in this simpler apparatus; no primary cross jets were employed. The swirler exit measurements were actually made at a downstream distance of 0.05 in., as close to the swirler exit plane as possible.

Due to limitations in fan power (a small centrifugal fan drives the flow in a suck-through fashion) the operating condition of the annular jet, the pressure drop across its length, was lower than that of the annular jets in the model combustor. This was decided to be of no real consequence as the distributions and behavior of the flow characteristics were desired, not the absolute magnitudes. Along with the measurements at the swirler exit plane, measurements of the velocity profiles at several downstream locations were made, illustrating the behavior of the swirl and recirculation.

Figures (1.3(a-c)) shows a cascade plot of the $\overline{U}$ (axial), $\overline{V}$ and $\overline{W}$ velocity components at the swirler exit plane. The axial flux is greater at the outer portion of the swirler than for the inner portion with a peak axial velocity of nearly 100 ft./sec.; the minimum is near zero.

From the orientation of the swirler vanes and the direction from which the fluid exits these vanes (see figure (1.4)) one would expect $\overline{V}$ to be large and positive for the higher Z and large and negative for lower Z. From the $\overline{U}$ distribution one saw the radial shift of the axial flux, which results in a shift in the expected $\overline{V}$ and $\overline{W}$ velocities. The shift in the $\overline{V}$ distribution can be seen in figure (1.3(b)), as $\overline{V}$ is positive over almost the entire range.

The combination of the $\overline{V}$ and $\overline{W}$ data can be seen in vector form in figure (1.5) which also shows the radial component of velocity. One can see that the velocities are very low in the region near the hub of the swirler, the larger velocities occupying the region near the outer radius.

The data for $\overline{U}$, $\overline{V}$ and $\overline{W}$ for the X=1.50 in. downstream location can be seen in figures (1.6(a-c)). The main feature to be seen in this figure is the concentration of large, positive axial velocities in the corners and near the walls. In the center of the duct there is a considerable amount of backflow, a maximum backflow velocity of -25 ft./sec. occurring in the center of the duct, with nearly all the positive axial flux located in a region roughly 0.5 in. from the walls. The velocity peak, on the order of 45 ft./sec., occurs very near the wall and was not detected exactly in these measurements.

The swirling flow pattern can be seen rather clearly in figure (1.6(a-c)). This figure, in particular, shows the magnitude of the swirl velocity, with $\overline{W}$ increasing from a relatively low level, near 5 ft./sec., in the lower Z range and gradually building up to very high values, on the order of 40 ft./sec., for Z=1.50 in.. The combination of the $\overline{V}$ and $\overline{W}$ velocities can be seen in vector form in figure (1.7), where the overall swirling motion is seen clearly and distinctly.

For the X=3.0 in. downstream case (figures (1.8(a-c))), one can see that the peaks in the positive axial flux have decayed and the recirculation zone has become slightly smaller. At the Z=3.00 in. location, the maximum axial velocity has been reduced to 30 ft./sec.. The reduction in the strength of the recirculation can be seen in the maximum recirculating velocity of nearly -20 ft./sec.. This reduction in recirculating mass flow must occur with a reduction in the positive axial flux along the walls.

The YZ-plane vector plot, seen in figure (1.9), shows much similarity to that at X=1.50 in.. The vector plot for X=4.50 in., found in figure (1.10), and that for X=6.00 in., found in figure (1.11), show the decay in the swirl with downstream distance. One can see from these diagrams that the swirl structure remains the same with downstream distance; only the magnitudes change.

Figure (1.12) shows a vector plot in the XY-plane for the Z=1.50 in. location. One can see the strong flux out of the swirler as well as the positive axial flux along the walls and the recirculation along the center of the duct. One can also see that the results for the downstream stations at X=4.50 in. and X=6.00 in. are very similar to that at X=3.00 in.. From some flow visualization experiments the recirculation zone was seen to extend the entire length of the duct, and it can be assumed that all stations downstream of X=3.00 in. are very similar in nature.

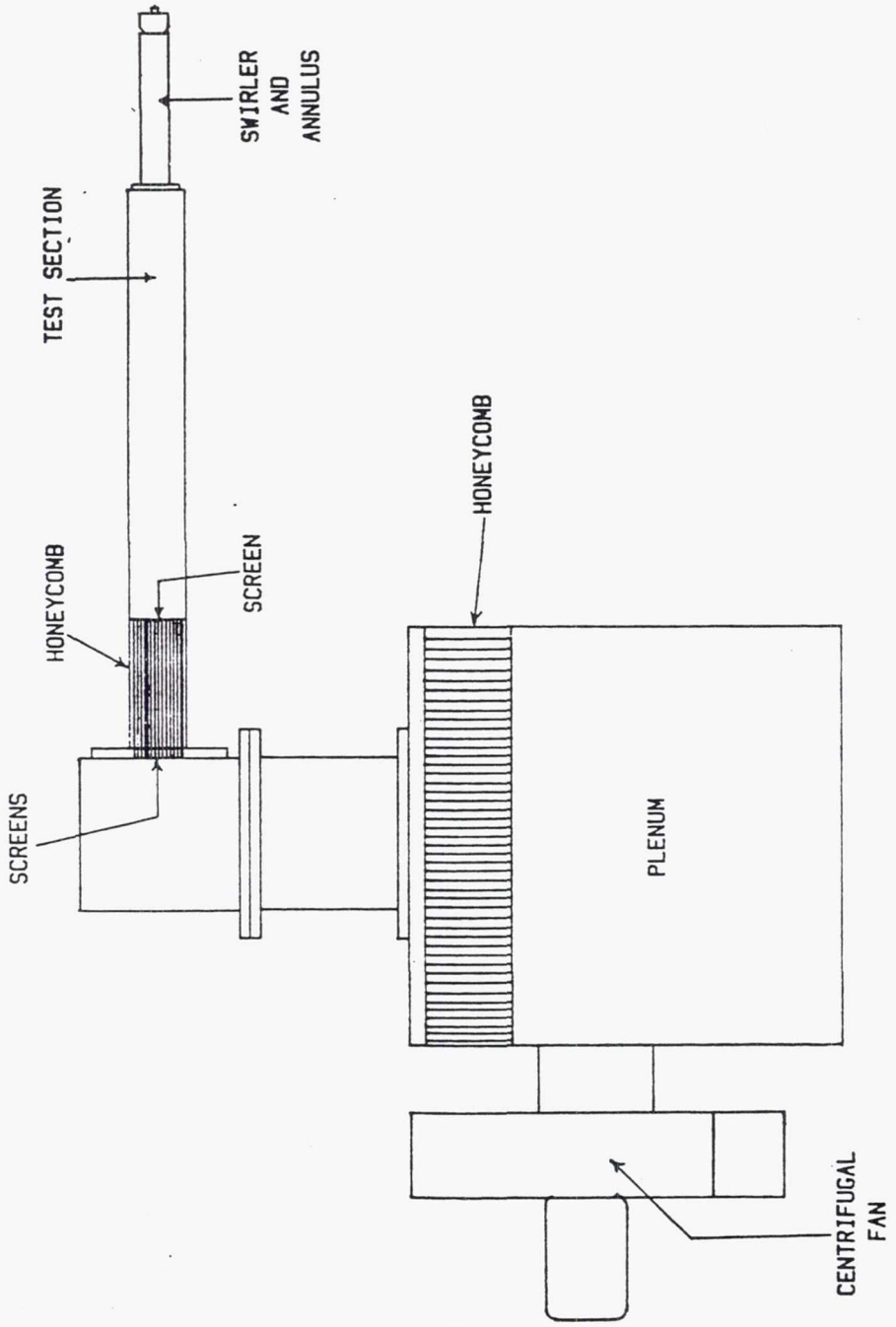

Figure 1.1 Single Swirler Apparatus

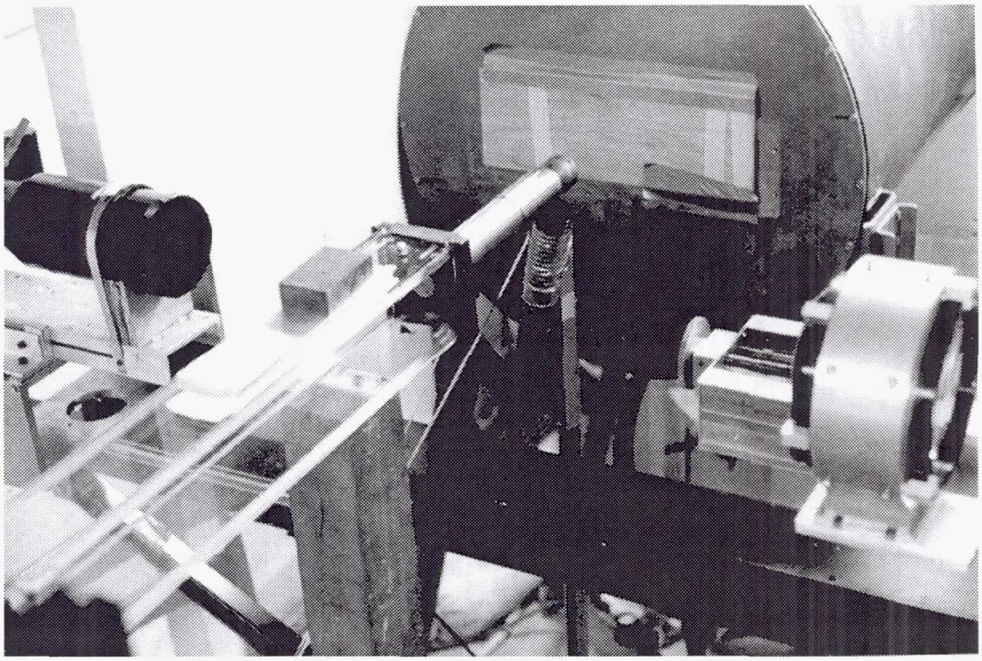

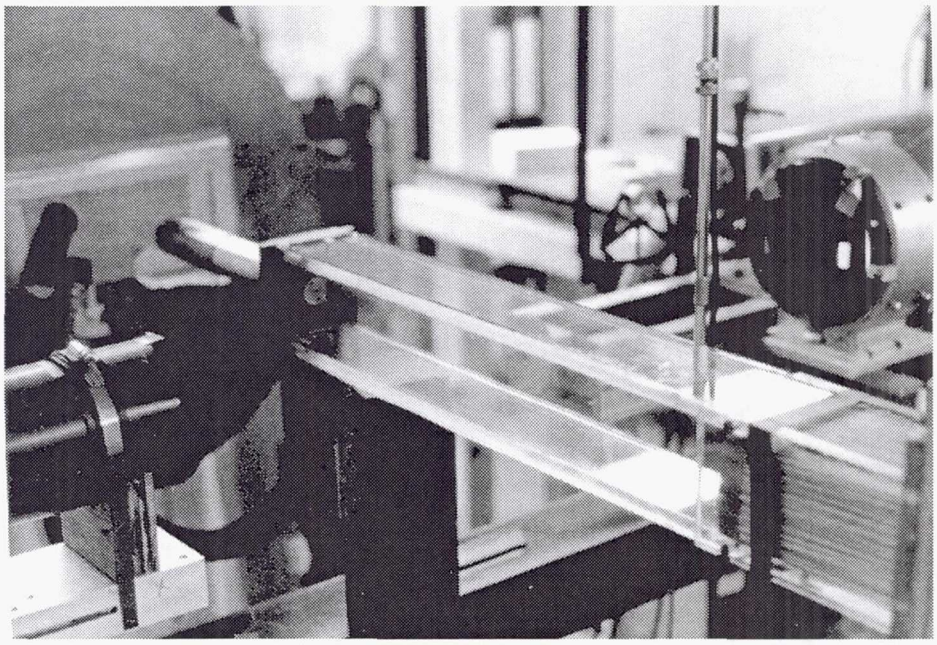

Figure 1.2 Photographs of Single Swirler Apparatus

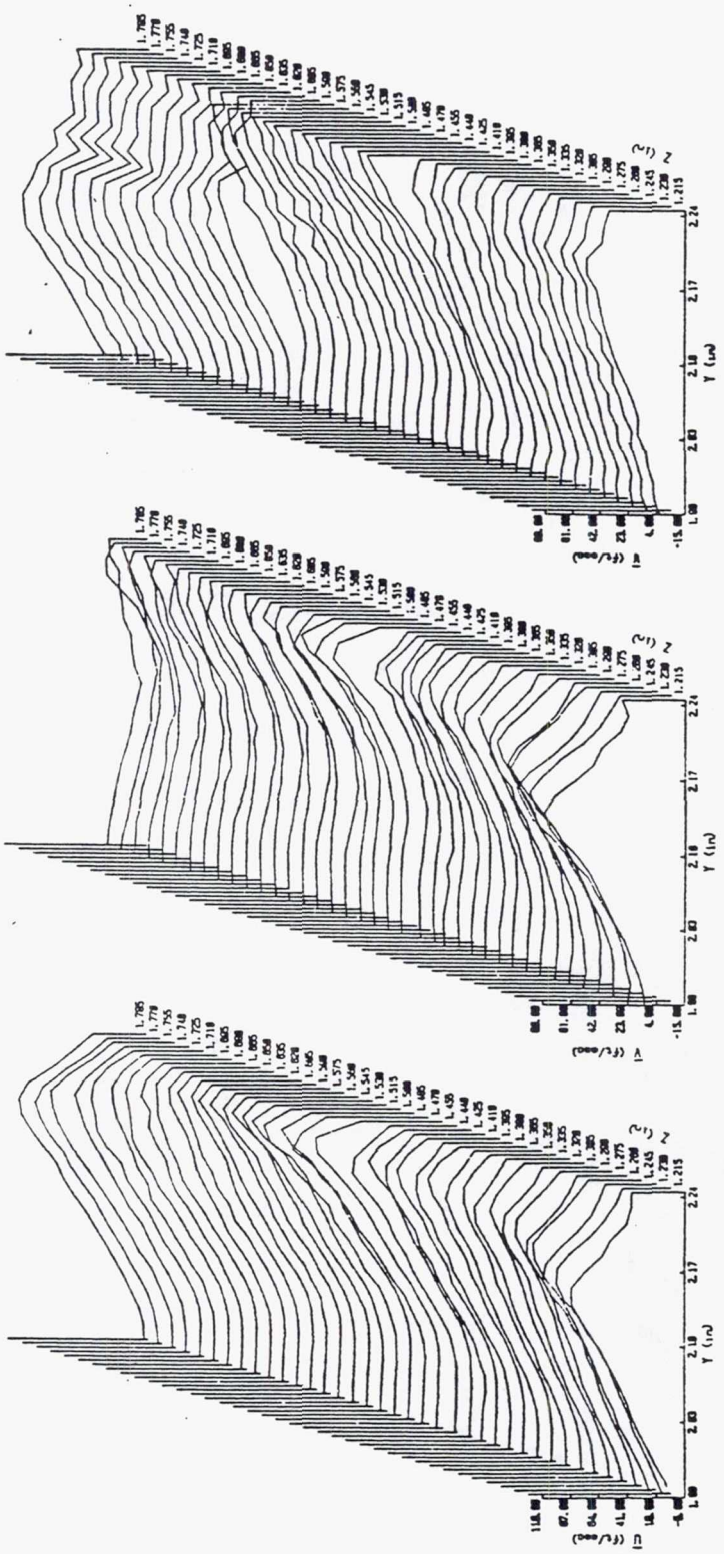

Figure 1.3 Mean Velocity $(\bar{U},\bar{V},\bar{W})$ Contours at Swirler Exit

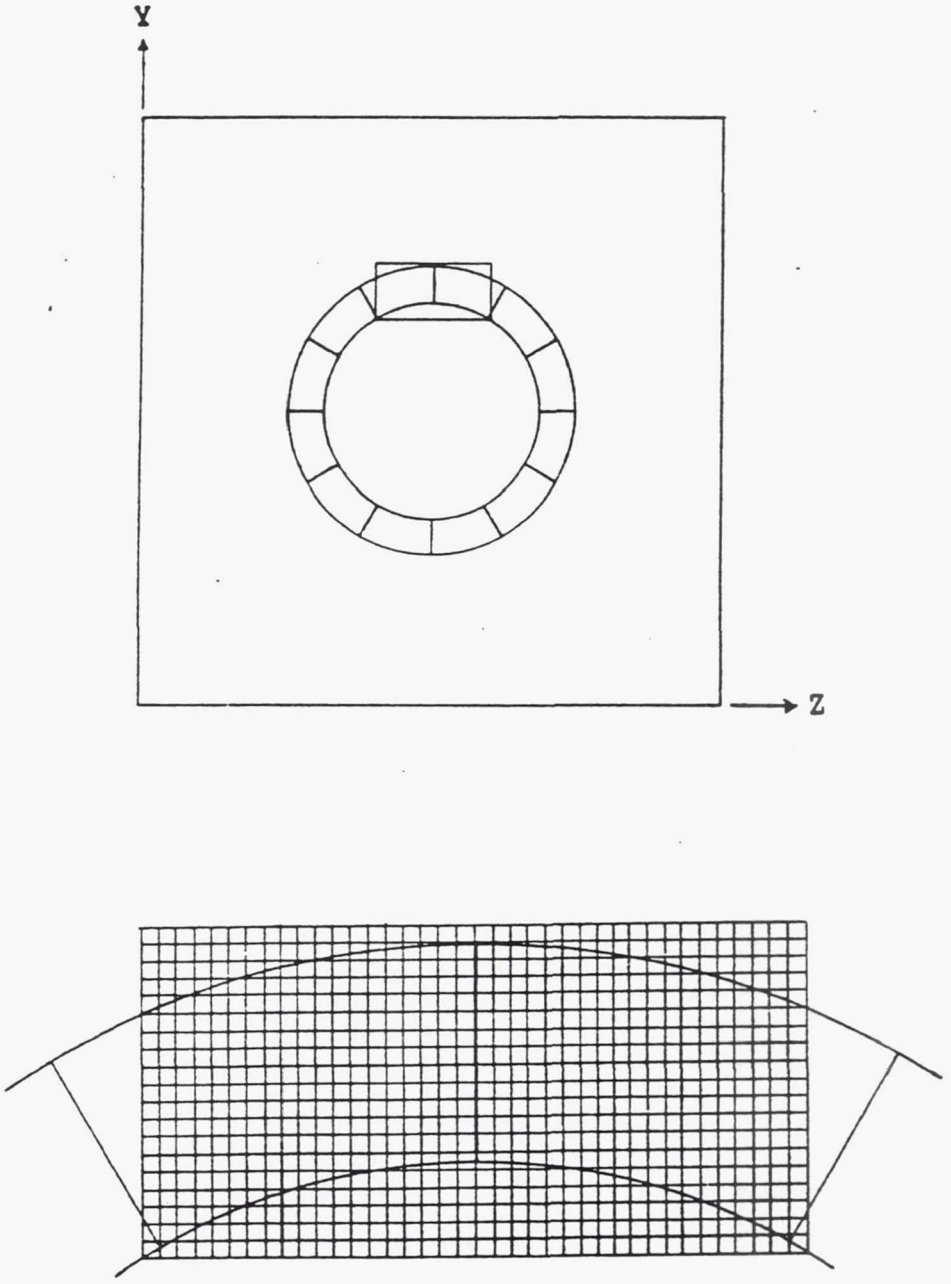

Figure 1.4 Swirler Inlet Data Grid

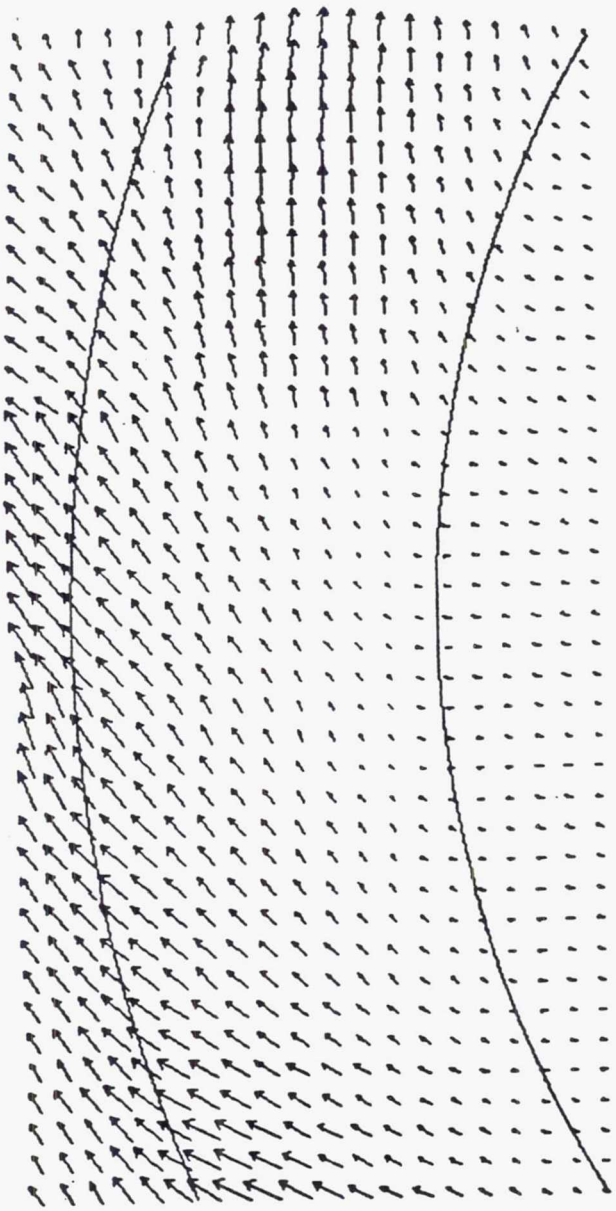

Figure 1.5 YZ-Plane Vector Plot at Swirler Exit

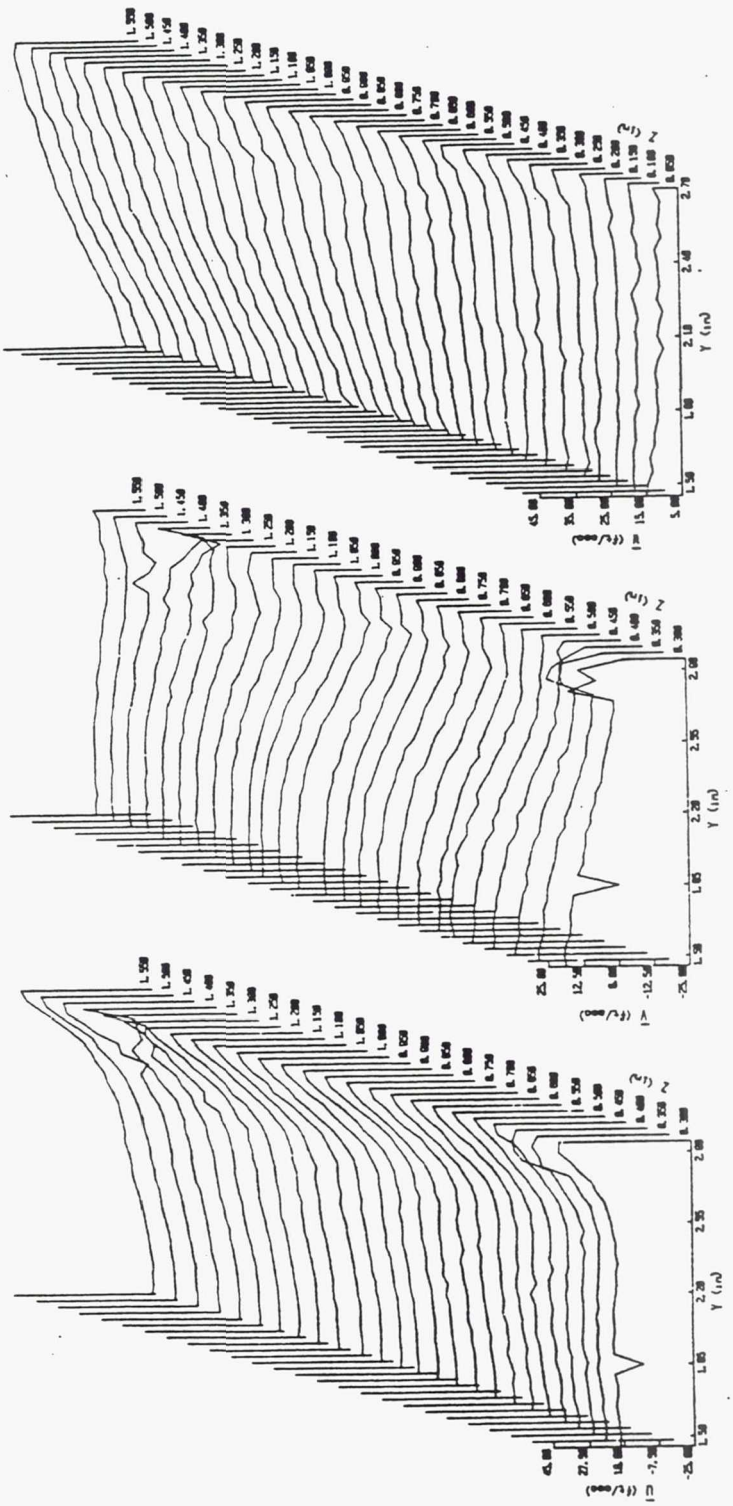

Figure 1.6 Mean Velocity $(\overline{U},\overline{V},\overline{W})$ Contours at X=1.50 in.

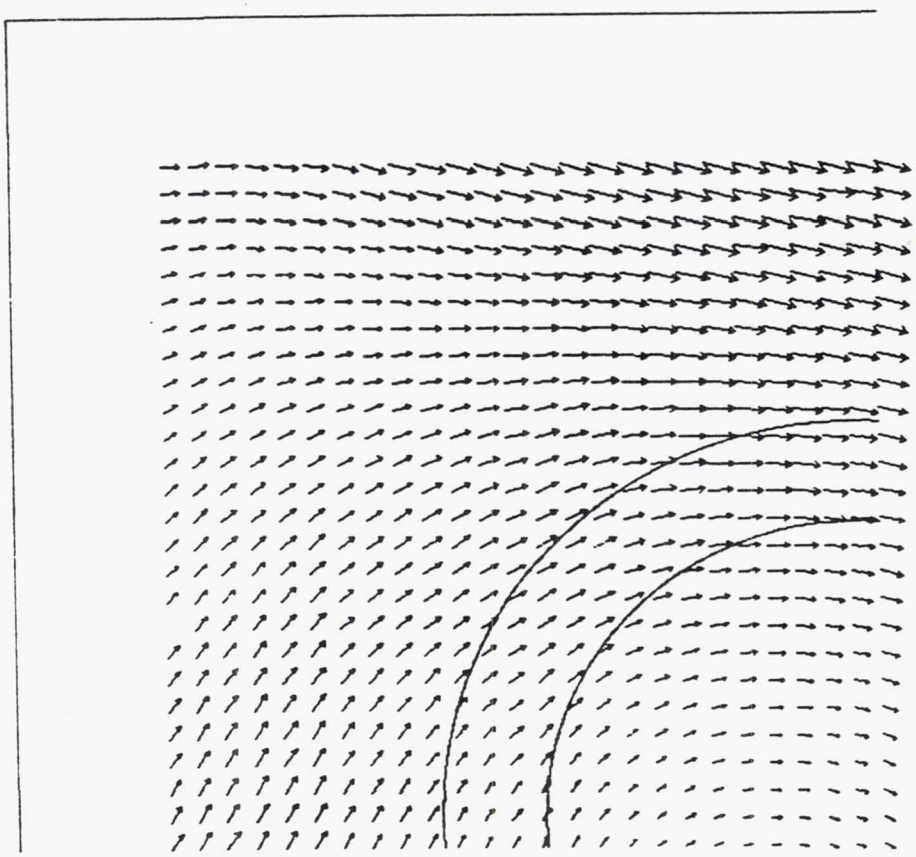

Figure 1.7 YZ-Plane Vector Plot at X=1.50 in.

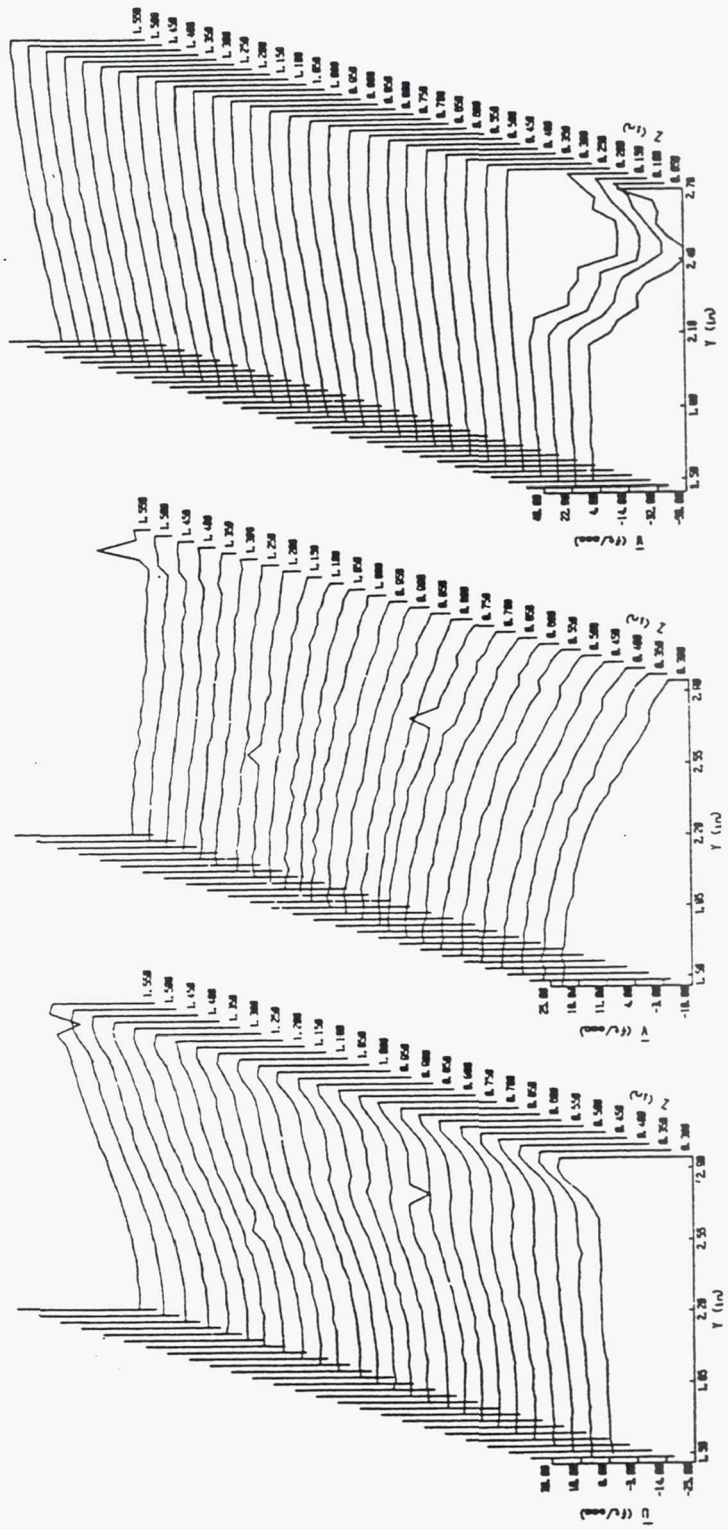

Figure 1.8 Mean Velocity ($\bar{U}$,$\bar{V}$,$\bar{W}$) Contours at X=3.00 in.

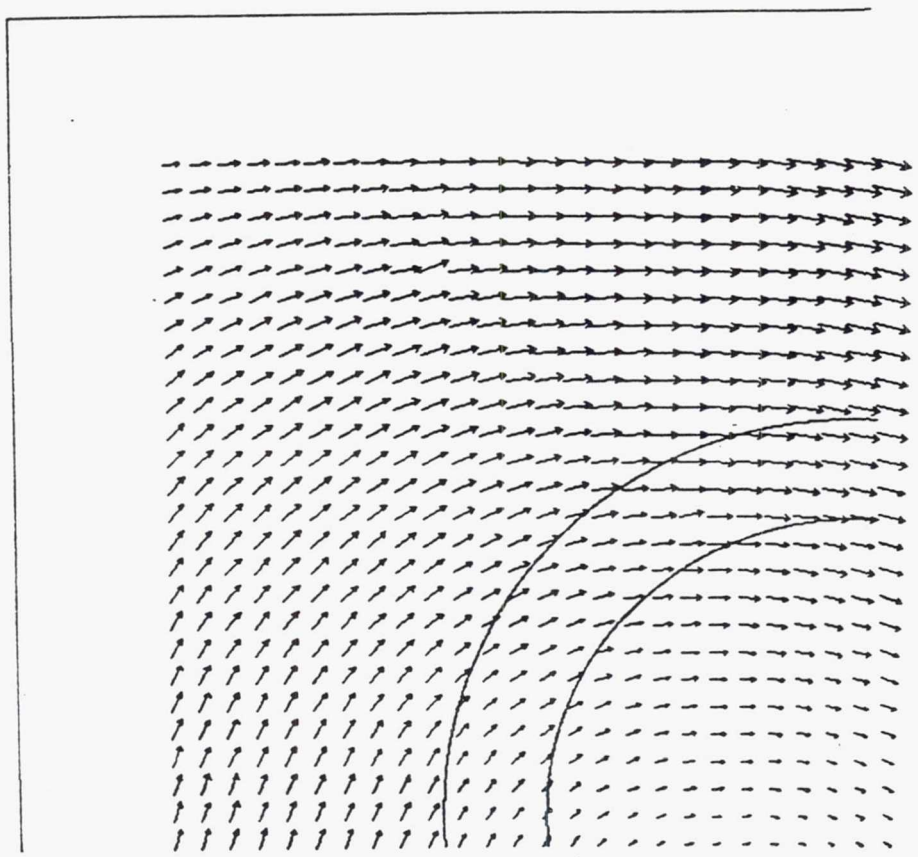

Figure 1.9 YZ-Plane Vector Plot at X=3.00 in.

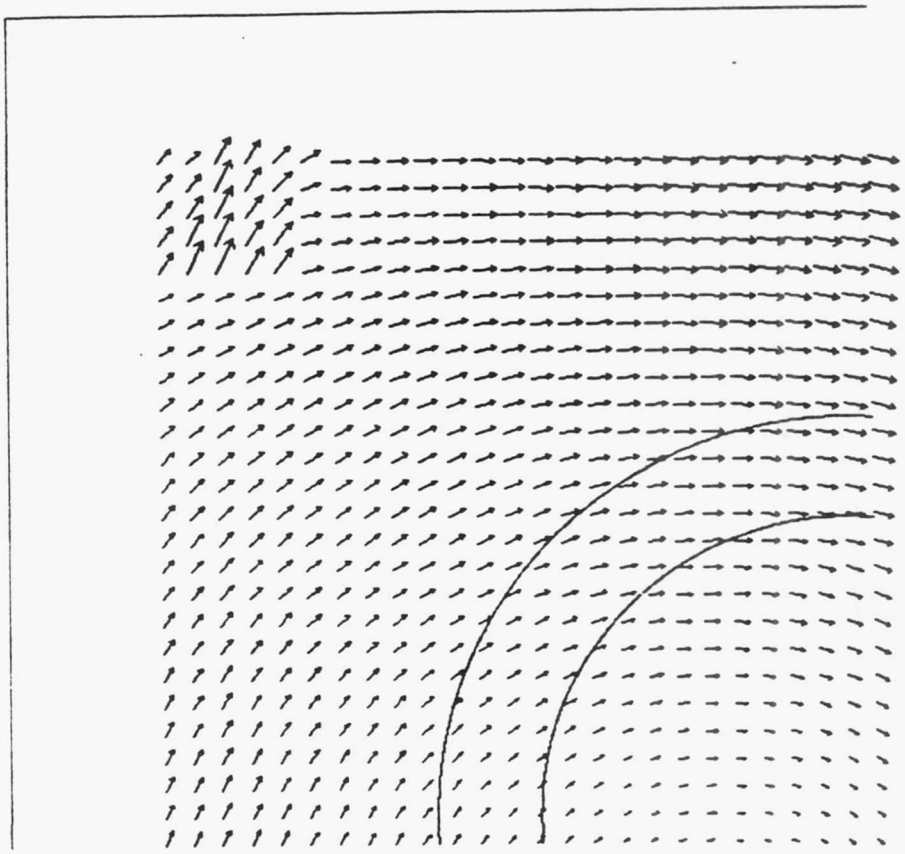

Figure 1.10 YZ-Plane Vector Plot at X=4.50 in.

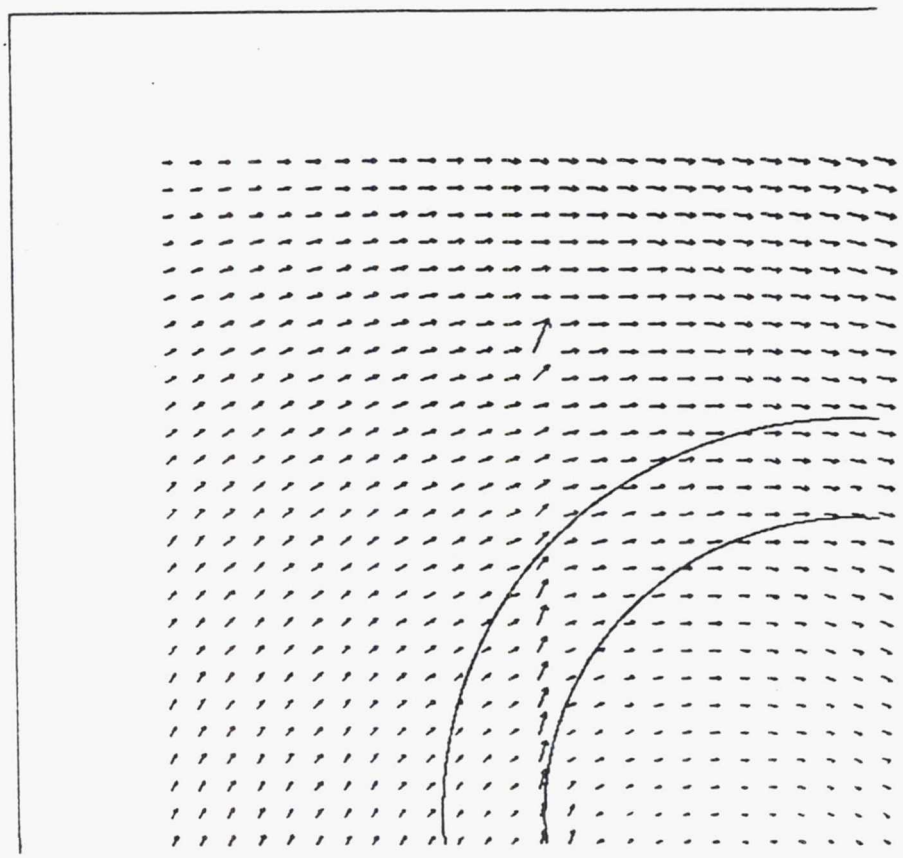

Figure 1.11 YZ-Plane Vector Plot at X=6.00 in.

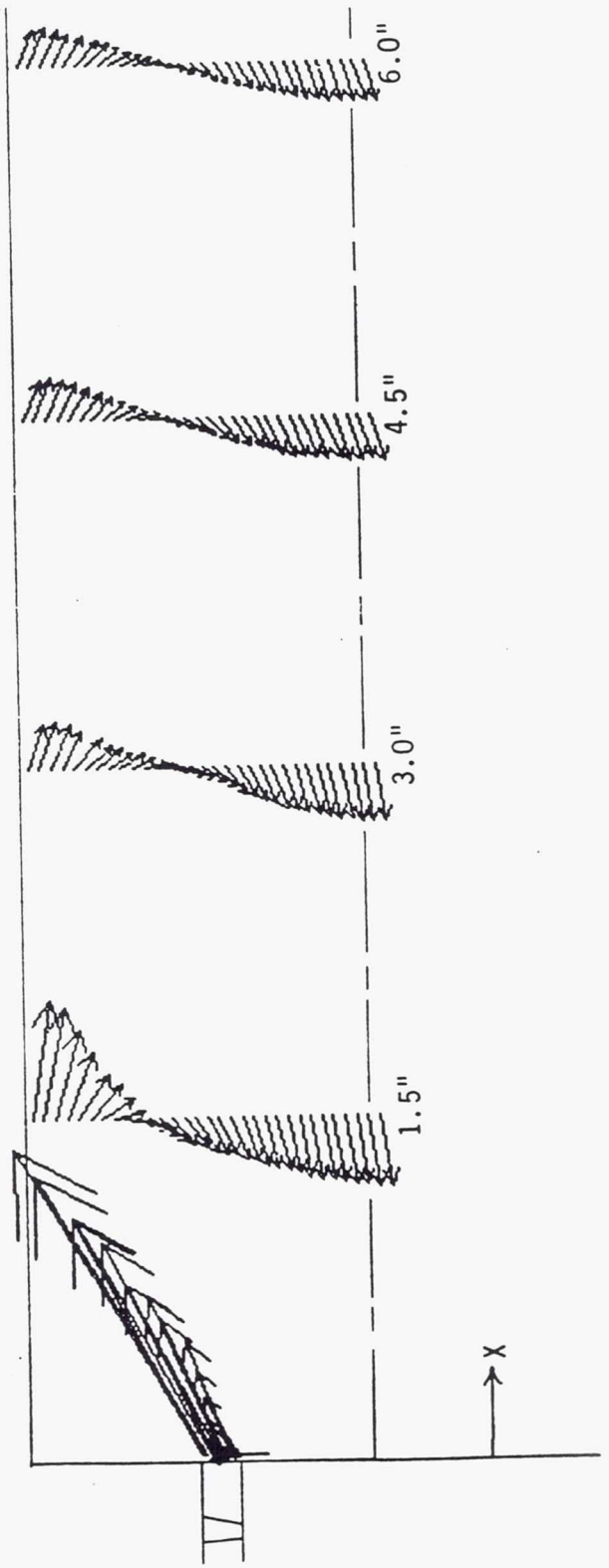

Figure 1.12 XY-Plane Vector Plot at Center of Duct

CHAPTER 2: SWIRLING JET STUDY

Of all the characteristics of swirling flows the recirculation zone is of the most interest. The recirculation zone is critical in the stability of the combustion process and, hence, must be fully understood in order to allow the improved design of combustion chambers. Although the size, shape and strength of the recirculation zones depend on the method of swirl application or generation the general characteristics remain the same.

This segment of the research described in this thesis involved the study of seed particle concentration fields of a swirling, turbulent jet. Using a light scattering concentration measurement technique known as marker nephelometry color enhanced video images of these fields were produced. These images allowed the analysis of the formation of the recirculation zone and associated characteristics of the swirling jet. Discussions of the experimental apparatus, measurement technique, and data acquisition systems are included in this section along with the presentation and discussion of the results.

2.1 Experimental Apparatus

The experimental jet apparatus for the swirling jet concentration studies is shown in figure (2.1). Ambient laboratory air is drawn into the mixing section by an electric fan, with the injection of the seed particles occurring immediately downstream. The seed particles are created by atomization of a combination of ethyl alcohol and fog juice (Deod. Apco 467) with a TSI Atomizer and enter the mixing section of the jet apparatus with an approximate particle diameter of 1 um. This type of seed particle is favored over other possible seed particles due to very good light scattering properties as well as the ability of the particles to follow the actual fluid motion. The mixing section contains several banks of screen and straws in order to reduce the level of turbulence (the straws and screens reduce the turbulence scales and thus increase dissipation). A contraction section (contraction ratio= 36.0) is mounted to the exit of the mixing section to increase the axial velocity and further decrease the turbulence.

Upon exit from the contraction section the flow enters the rotating section, a three-dimensional view of which can be seen in figure (2.2). The rotating section consists of a straight tube with an inside diameter of 2.00 in., the entire length of which is filled with straws. These straws, 3.00 mm in diameter, drive the solid

body rotation of the flow. The rotation in this section is produced by a hydraulic motor via gear and chain drive, allowing infinite adjustability of the rotational speed. The axial average could be controlled also, allowing nearly any combination of axial speed, rotational speed and swirl ratio. The mass-averaged speed through the jet chosen for this experiment was 8.40 ft./sec., giving a Reynold's number based on jet diameter of 8900.

2.2 General Theory of Marker Nephelometry

Marker Nephelometry is a technique by which concentration fields can be studied by seeding the feeding fluid stream with passive marker particles and detecting the marker particle concentration by a light scattering, optical method. Rosenweig [46] first developed the theory and basic method and, along with Hottel and Williams [47], was the first to apply the technique. Becker [3] gives a very thorough and complete analysis of the technique.

The measured concentration field is relative in nature, not absolute: the actual concentration at a point in the flowfield cannot be directly measured, only the concentration at that point relative to the concentration at another point in the flowfield. This method requires the use of some type of light source (laser, lamp, etc.) to illuminate the flowfield on interest, particles to scatter the incident light and a detection device

(photomultiplier tube, SIT, etc.) to collect the scattered light. In some flowfields naturally occurring particles scatter adequate light for the method to be successful but in most cases some type of light scattering seed particle must be added to the flow. Seeding of the fluid issuing from the jet exit was necessary for this experiment since no light scattering particles existed in the ambient air.

Ideally the light scattered by marker particles is a linear function of the number of marker particles residing in the measurement volume. This linear behavior depends on two criteria: independent scattering and mono-disperse marker particles. The first condition is rather easily satisfied as, from Becker [3], independent scattering occurs for marker particle density sufficiently small such that the center-to-center distance between particles is greater than 3 radii. This correspond to a marker particle volume fraction of 30%. For this experiment, this condition is easily satisfied.

The second condition, the need for mono-disperse particles, is not as easily met. Mono-disperse particles are all of the same size. Since nearly all particle generators create poly-disperse particles the intensity of the scattered light will not be linearly related to the number of particles in the measurement volume but will be a weighted function of the various particle sizes existing there.

From Schaughnessy and Morton [48] the logical assumption to be made is that the statistical distribution of particle sizes is the same at every point in the flowfield. This assumption will fail when the sample of marker particles is so small (very low concentration) as to not characterize the correct distribution of sizes. This does not create a problem in this experiment since the essential characteristics observed are dictated by the higher levels of concentration.

2.3 Optical Configuration

The optical configuration utilized in the early marker nephelometry studies consisted of a conventional light source (focussed to a point in the flowfield) and a photomultiplier tube. The measuring resolution of this setup was limited by the electronic noise inherent in the detector; for low concentration levels the signal from the measuring volume was of the same order of magnitude as the noise. Since the electronic noise is a fixed value a more powerful light source would improve the resolution.

The solution was to use a laser as the light source along with a photomultiplier tube. In order to measure concentration levels in an entire two-dimensional field, though, the measurement volume would have to translate across the entire flowfield of interest. To facilitate these concentration field measurements a system was

devised which allowed the simultaneous concentration measurement at all points in the flowfield: the laser beam was expanded into a two-dimensional sheet with a video camera imaging the field of interest. This latter configuration was used in this experiment.

The source of illumination for light scattering is a Spectra-Physics 5-watt Argon-Ion laser. The illumination, in the form of a sheet of laser light (0.04 in. thickness), is produced by focussing the principle wavelengths (blue, 488.0 nm and green, 514.5 nm) of the laser output by means of a pair of lenses and diverging the focussed beam with a cylindrical lens, the resultant laser sheet being formed along the longitudinal axis of the jet. An overall view can be seen in figure (2.3).

Non-uniformity in the laser light sheet exists for two reasons: the gaussian light intensity profile of the laser beam and imperfections in the cylindrical lens. For this experiment a small diameter glass lens was chosen so that the portion of the laser sheet illuminating the flowfield was the center of the gaussian distribution, resulting in a low level of non-uniformity due to the gaussian light distribution of the laser beam. The chosen lens also had very few imperfections resulting in a low level of distortion.

2.4 Data Acquisition

The Mie scattered light from the marker particles is collected by a Panasonic video camera, operating at a frequency of 60 Hz. The digital images are then stored on video tape, allowing retrieval and analysis via a IBM PC/AT system. Through image processing software each video image is divided into a 512x512 pixel matrix (262,144 pixels). Single frame images or multiple frame averages can then be created. Mathematical operations, such as averaging and other statistics, can then be performed on the individual pixels.

The process of converting the information in a video image of scattered light to concentration levels is known as pseudo-color, or color enhanced, imaging. This process digitizes the scattered light intensity, which the computer stores as voltage levels, into 256 discrete color levels. Each color level corresponds to some range of light intensity, or the corresponding particle concentration, allowing the clear visualization of the concentration level contours.

2.5 Results and Discussion

Two-dimensional concentration fields/flow visualization images of the initial region (X/D<7) of a swirling turbulent jet are given for seven different swirl

ratios: 0.00, 0.33, 0.66, 1.00, 1.33, 1.66 and 2.00. For each of these swirl ratios color enhanced video images corresponding to single frames and 127 averaged frames are shown. These images can be seen in figures (2.4-2.10).

The imaged region of the flowfield extended roughly 7 jet diameters in both the downstream direction and direction perpendicular to the jet axis. With a jet diameter of 2.0 in., the imaged area was 252 in. For this set of images the laser sheet thickness was 0.04 in., resulting in a measurement volume size of 0.03 in. x 0.03 in. x 0.04 in., small enough to resolve all but the smallest scales found in the flowfield, such as those corresponding to the Kolmogoroff universal length scale. Using an estimate of the turbulent dissipation from Tennekes and Lumley [52], the Kolmogoroff universal length and time scales,

$$\eta = \left(\frac{\nu^3}{\varepsilon}\right)^{\frac{1}{4}} \tag{2.1}$$

$$\tau = \left(\frac{\nu}{\varepsilon}\right)^{\frac{1}{2}} \tag{2.2}$$

are found to be on the order of 0.01 in. and 0.005 sec. Since the camera operated at a 60 Hz rate, resulting in a time resolution of 0.0167 sec., the single frame images

are not instantaneous but averaged over a small time interval.

When these images were acquired great care was taken to ensure that the laser intensity was the same for all the cases; this allows the direct comparison between images. Before a new case was to be imaged the test facility was flushed with fresh ambient air to ensure a near zero background marker particle concentration level. This was required since the during the operation of the swirling jet apparatus the room became rather quickly saturated with the marker particles. The saturation occurred very slowly, though, compared with the time required for a complete sequence of images at one swirl ratio, allowing characteristics such as the time-averaged spread angle to remain constant in time.

One can immediately see the variations in the flowfield as the swirl ratio is increased as well as the differences between the single frames and multiple frame averages. In general, several phenomena occur with an increase in swirl:

(1) an increase in the spread angle of the jet,

(2) the formation of a recirculation zone when a critical swirl ratio is reached,

(3) the growth of this recirculation region with an increase in swirl.

The zero swirl case can be seen in figures (2.4(a-b)). Jet flows with zero swirl are characterized by a very small jet spread angle which, for the 127 frame average image, is measured to be 24 degrees. One can see from figure (2.4(b)) some apparently wavy behavior of the jet boundary. This behavior can be attributed to the use of straws in the rotating section: some of the straws were not exactly aligned parallel to the jet axis and interacted with neighboring straws to develop undesirable secondary flows and jet growth. This effect does cause some small errors in the spread angle measurement for the N=0.00 and N=0.33 cases, but not for the larger levels of swirl.

The spread angles given for these images represent the spread of the visible radial extent of marker particles with downstream distance; most jet studies, usually involving the measurement of velocity profiles, define the spread angle as the spread of the velocity half radius with downstream distance. A comparison of the single and multiple frame averaged images reveals the dissimilar nature of the single frame and averaged profiles. The single frame image can be seen to show very large scale fluctuations for x/D>2, with a corresponding large amount of intermittency near the jet boundary, while the averaged image shows very smooth contours. Dahm and

Dimotakis [14] discovered the same behavior in their jet studies.

One can see from figures (2.4(a-b)) a discrepancy in the background intensity level, seen above and below the jet, and an apparent distortion of the corners of the images. The distortion effect is due to non-linear camera response while the variation in the background intensity level is due to some type of reflection causing undesired illumination. These two effects are present in all the processed images but do not hinder the study of the flow structure.

Figures (2.5(a-b)) show single and averaged images corresponding to the first case of applied swirl, N=0.33. The measured spread angle, 22 degrees, is smaller than that reported for the zero swirl case but, as stated before, the results of these two cases are in slight error. As with the zero swirl case very large scale fluctuations can be seen from the single frame image, resulting in profiles that do not resemble the mean.

The images for the N=0.66 case can be found in figure (2.6(a-b)). Immediately visible in the averaged image is the reduced downstream extension of the various intensity levels compared to the N=0.33 and N=0.00 cases. This is due to the reduction in the rate of the downstream convection which, in turn, is due to the development of a small, axial pressure gradient with increase in swirl.

This pressure gradient also existed at the N=0.33 case but was so small as to be almost negligible. Unlike the N=0.00 and N=0.33 cases, which show a nearly constant rate of jet spread with downstream distance, the spread for N=0.66 displays two distinct spread angles: 30 degrees for x/D<2.5 and 12 degrees for x/D>2.5.

The first sign of recirculating flow can be seen in the single frame image for N=1.00 (figures (2.7(a-b))), where large scale fluctuations can be seen to occur much closer to the jet exit than for the previous cases. The regions of higher concentration appear to diverge at a downstream distance of x/D=1.5, indicating a backflow of fluid with lower marker particle concentration; this fluid must recirculate from stations located further downstream. The averaged image shows no direct signs of recirculation, only a further reduction in the downstream extension of the various concentration levels. The averaged image also shows the change in the spread angle at the downstream location x/D=2, similar to that at N=0.66. The spread angle measured in the initial region of the flowfield is 45 degrees.

The next level of swirl, N=1.33, shows signs of the recirculation zone in both the single frame and the multiple frame average images (figures (2.8(a.b)). The fluid exiting the jet, with very high levels of marker particle concentration, can be seen to move radially

around a region of marker particle deficit, which is due to backflow from downstream stations. The formation of the forward stagnation point can be clearly seen but not for the rear (downstream) stagnation point. As with the previous cases large scale fluctuations are prevalent in most of the flowfield. An increase in the size of the region of intermittency also occurs as small volumes of ambient fluid are transported across most of the radial extent of the flowfield. Similar to the previous cases the spread angle can be seen to have an increased value, 80 degrees, in the initial portion of the flowfield ($x/D<1$), with the subsequent motion of the highly concentrated fluid around the recirculation zone.

The single frame and multiple frame averaged images for the N=1.66 case can be seen in figures (2.9(a-b)). The recirculation zone formed at this level of swirl is larger than for the N=1.33 case with a corresponding increase in the spread angle (to 140 degrees) in the initial mixing region. The single frame image shows fluid of very low concentration fluid recirculating; small regions of unmixed, ambient fluid can be seen to exist in the recirculation zone, but at a very low rate of occurrence. As with the N=1.33 case the location of the forward stagnation point can be clearly seen while the rear (downstream) stagnation point cannot be discerned.

Figures (2.10(a-b)) illustrate the concentration field for the N=2.00 case. From these figures the fluid motion appears to be completely upstream, as the highly concentrated fluid can be seen to issue from the jet exit and flow around the lip of the jet; in actuality, the recirculation zone is so large that the imaged area is only a small portion of the total recirculation zone size. This same type of behavior was observed by Gore and Ranz [25], who applied enough swirl to a jet flow to cause it to diverge at right angles to the jet axis at the jet exit. These figures show that most of the fluid existing in the recirculation zone is ambient, or of very low concentration levels. This indicates the large amount of diffusion that has occurred during the fluid motion around the recirculation zone, another indication of the large scale of the recirculation zone.

The final figure, figure (2.11), shows the variation in the spread angle as a function of the swirl ratio. One can see the very smooth resulting curve, which increases past 180 degrees for the higher swirl ratios. This set of data can be curve fit to be represented by the relation

$$\theta = 12.49e^{1.41N} \qquad (2.3)$$

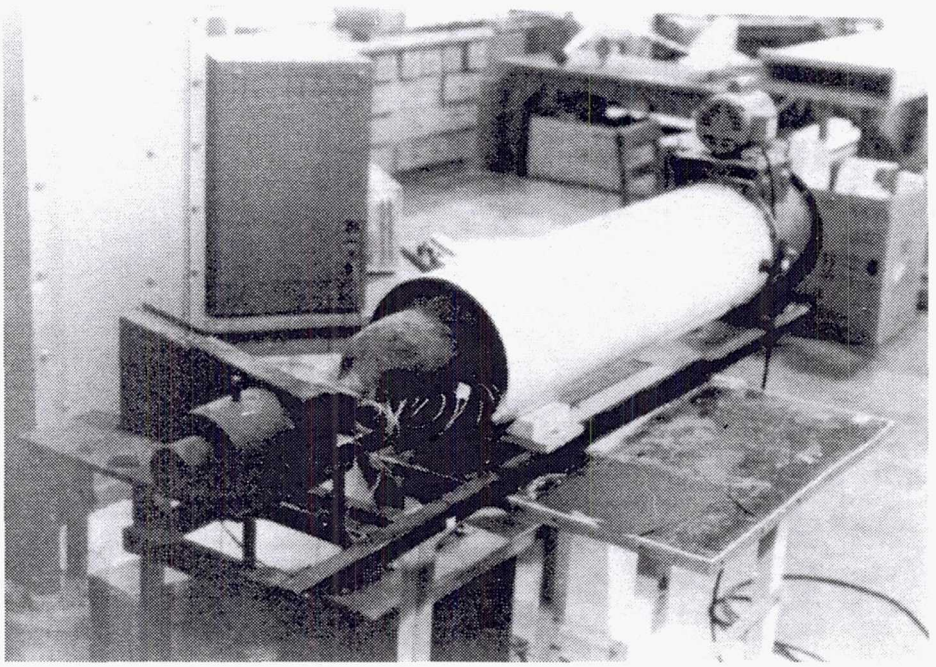

Figure 2.1 Photograph of Swirling Jet Apparatus

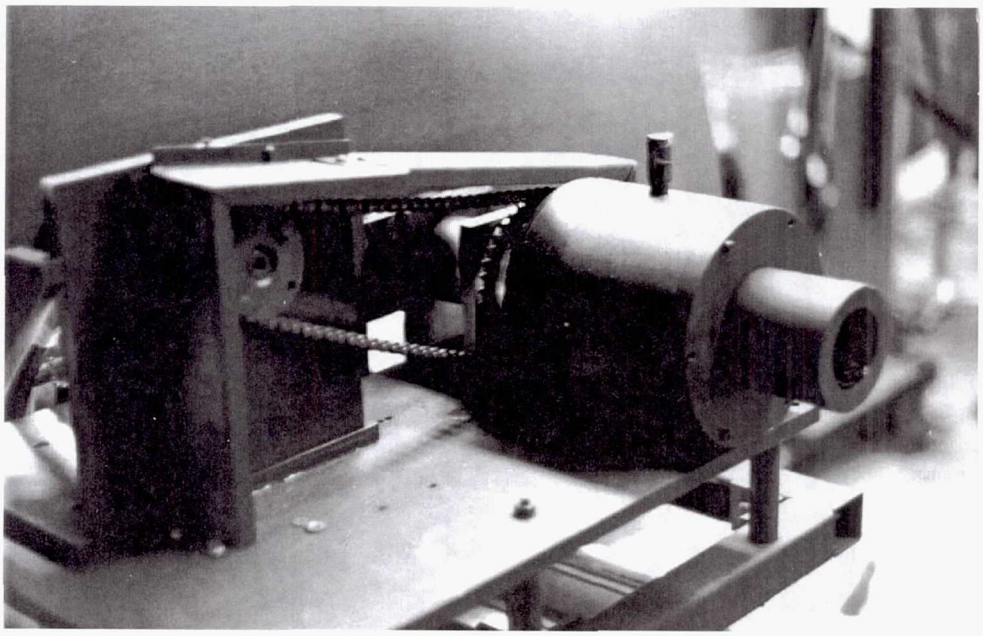

Figure 2.2 Photograph of Rotating Section of Swirling Jet

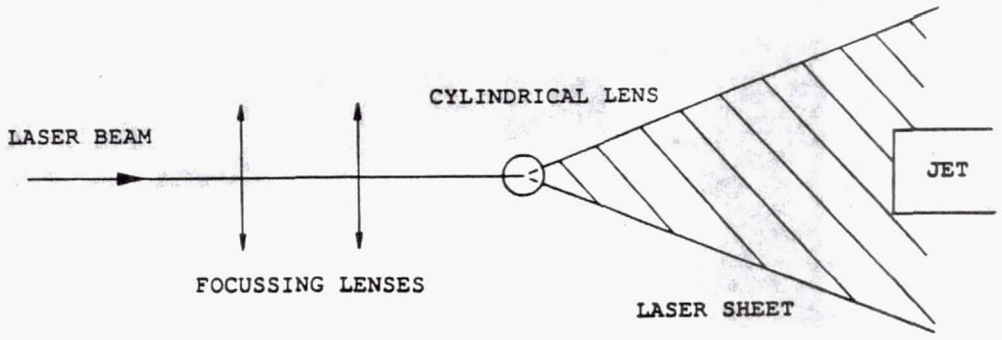

Figure 2.3 Optical Configuration for Concentration Measurement

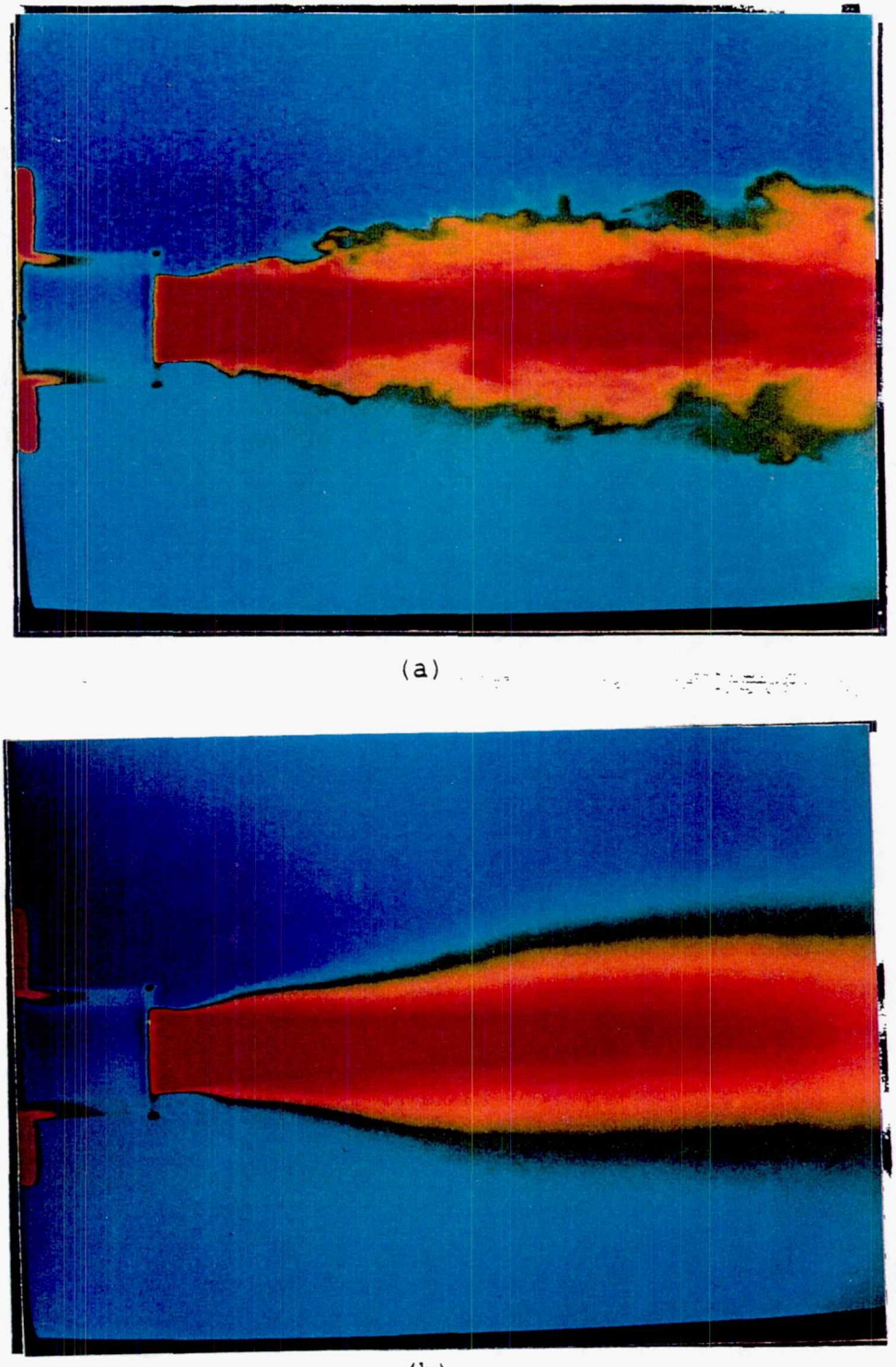

Figure 2.4 Concentration Fields for N=0.00: (a) 1 Frame; (b) 127 Frames

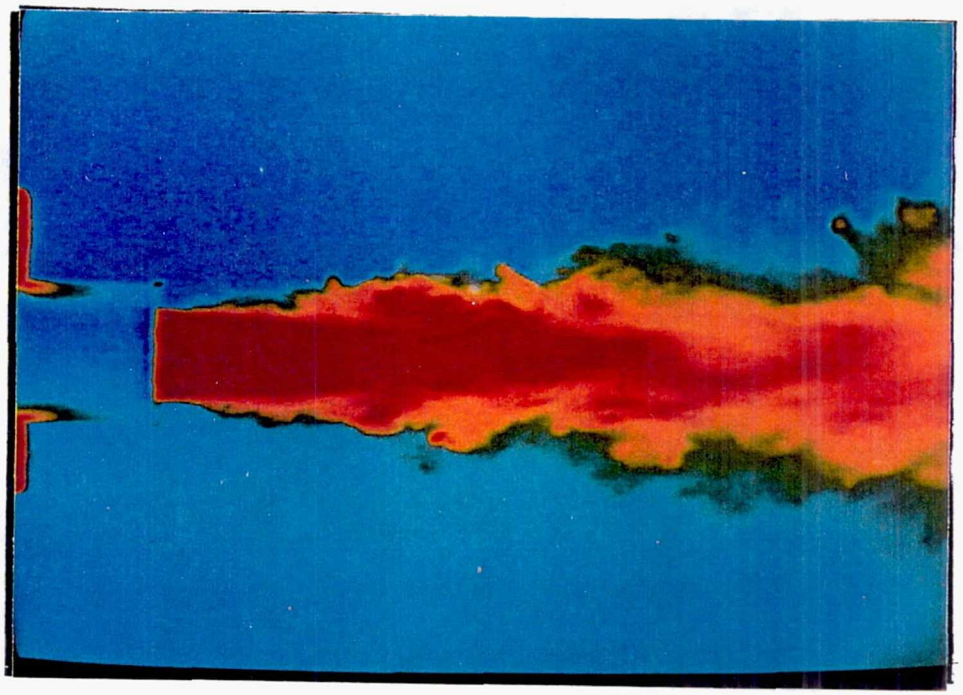

(a)

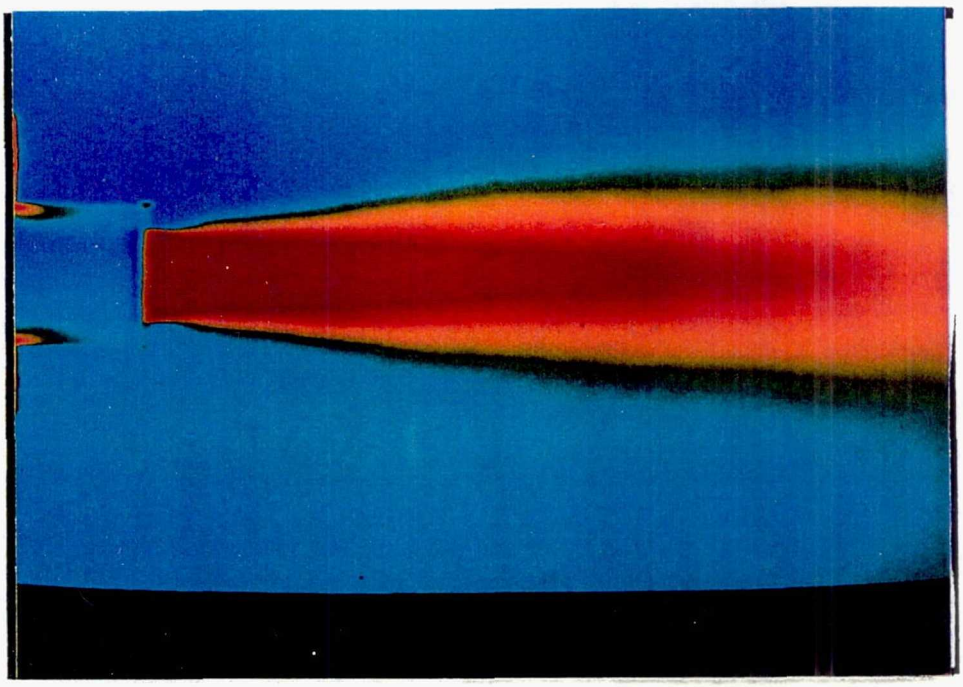

(b)

TE92-2406

Figure 2.5 Concentration Fields for N=0.33: (a) 1 Frame; (b) 127 Frames

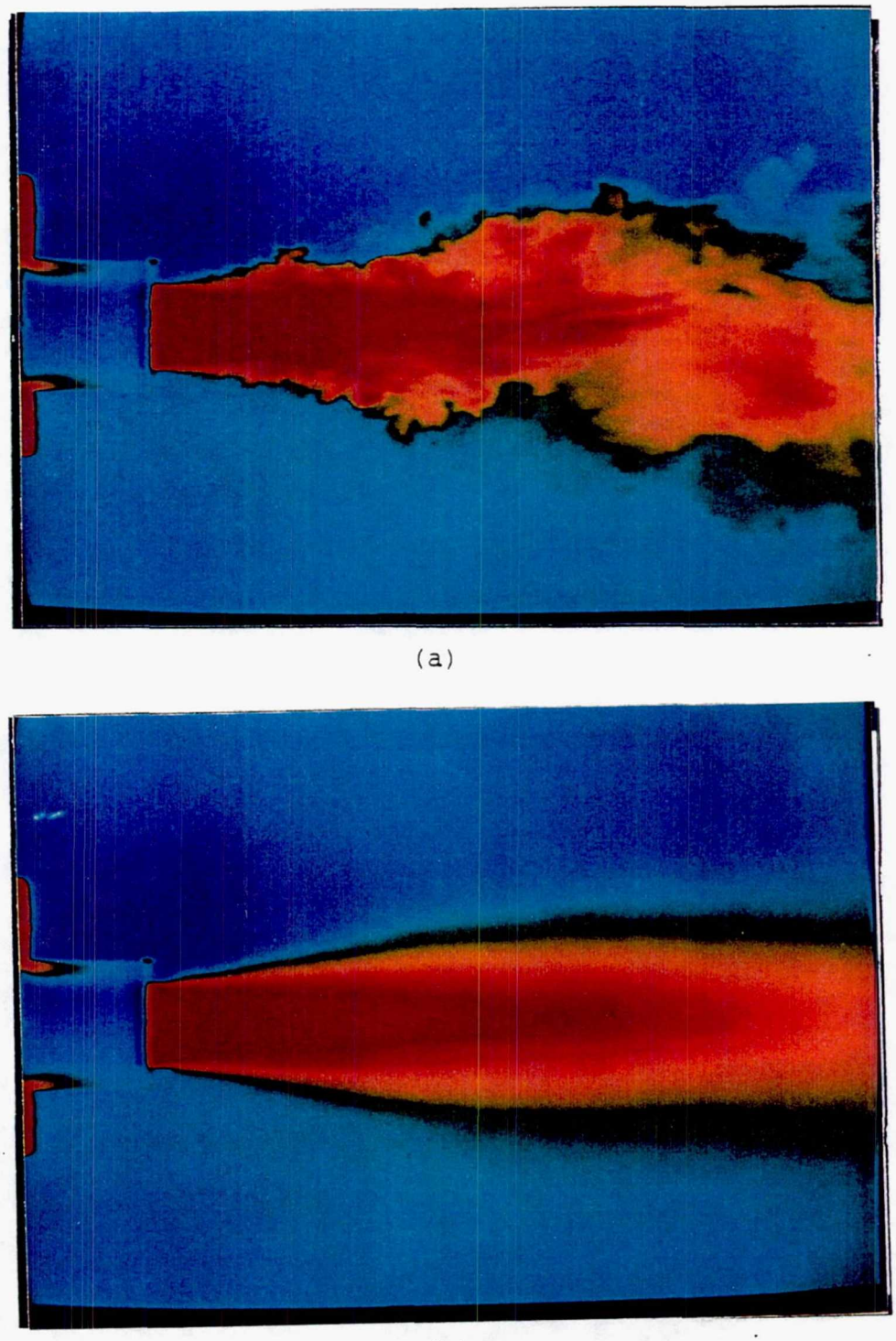

Figure 2.6 Concentration Fields for N=0.66: (a) 1 Frame; (b) 127 Frames

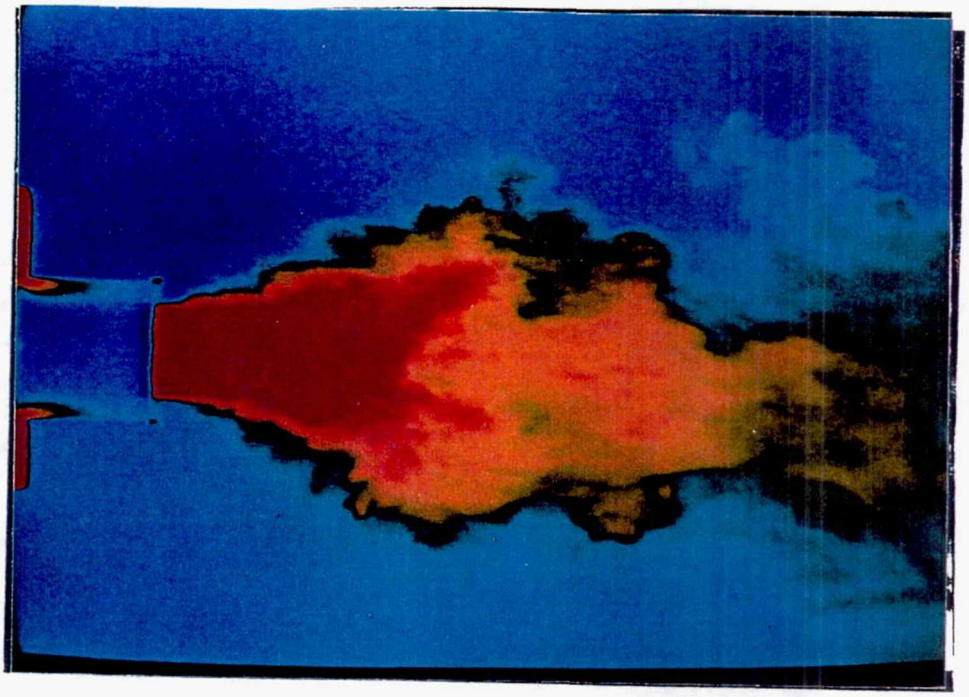

(a)

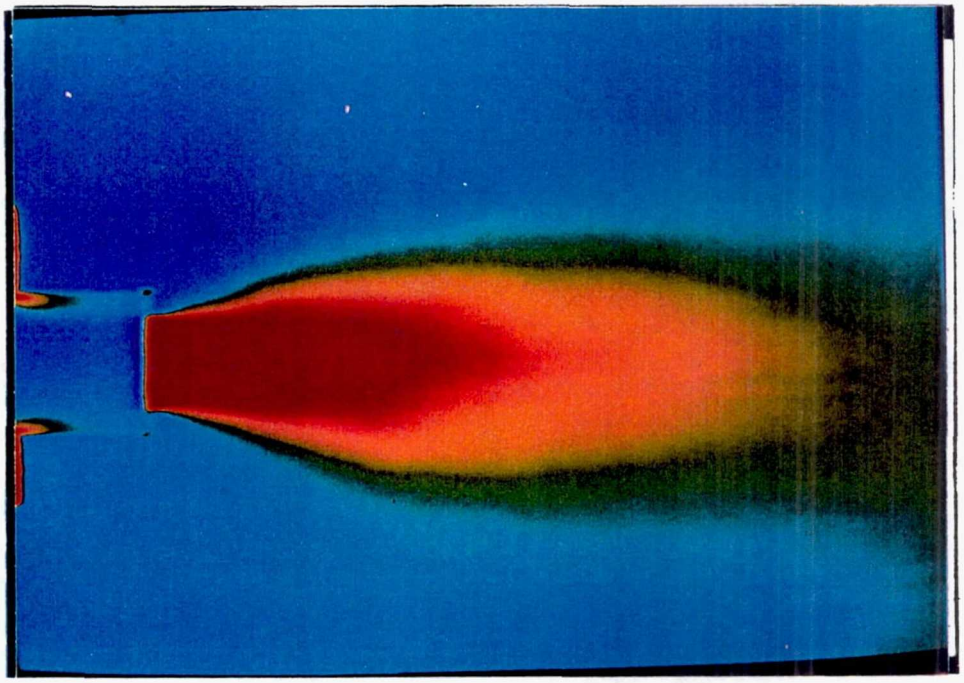

(b)

TE92-2408

Figure 2.7 Concentration Fields for N=1.00: (a) 1 Frame; (b) 127 Frames

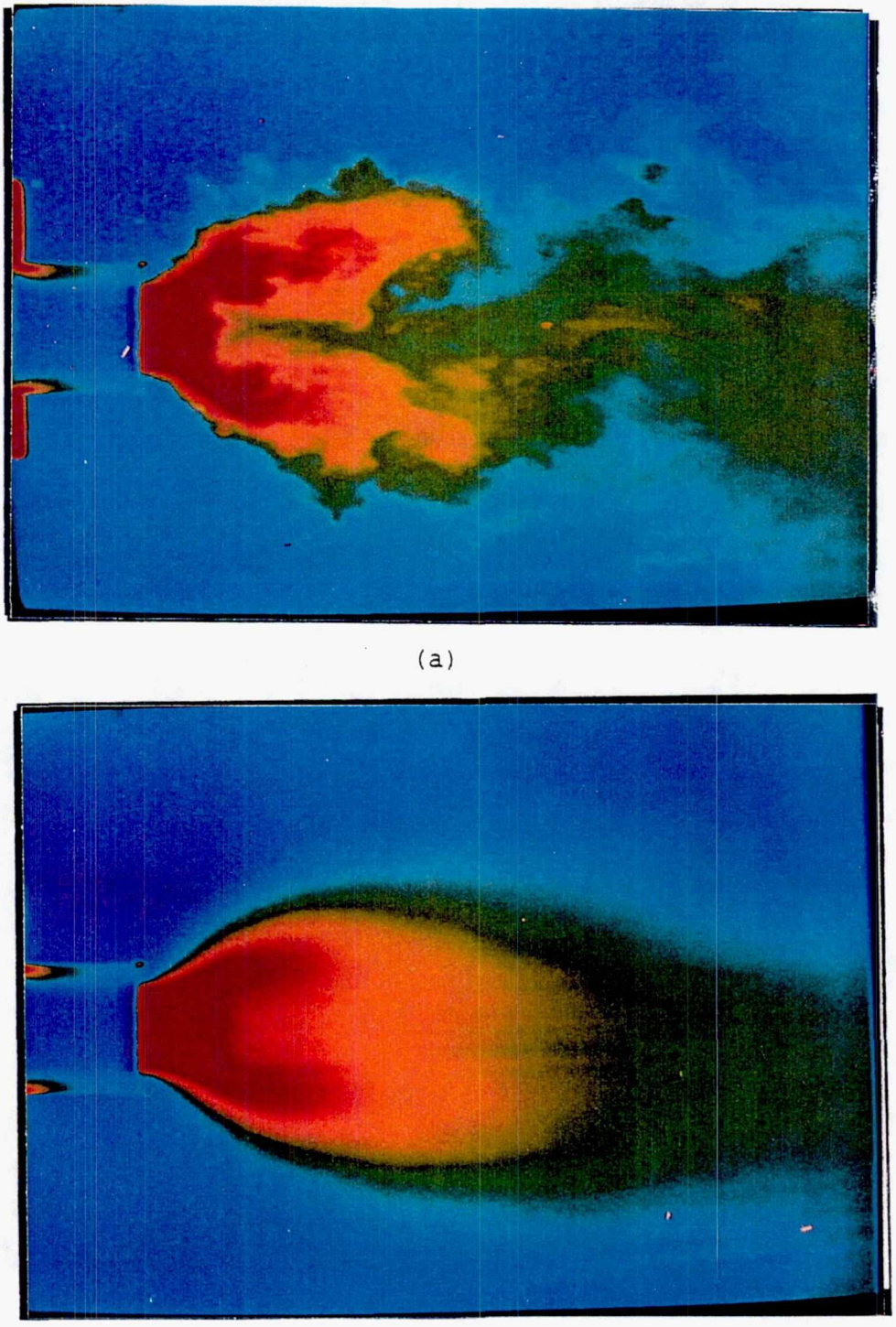

Figure 2.8 Concentration Fields for N=1.33: (a) 1 Frame; (b) 127 Frames

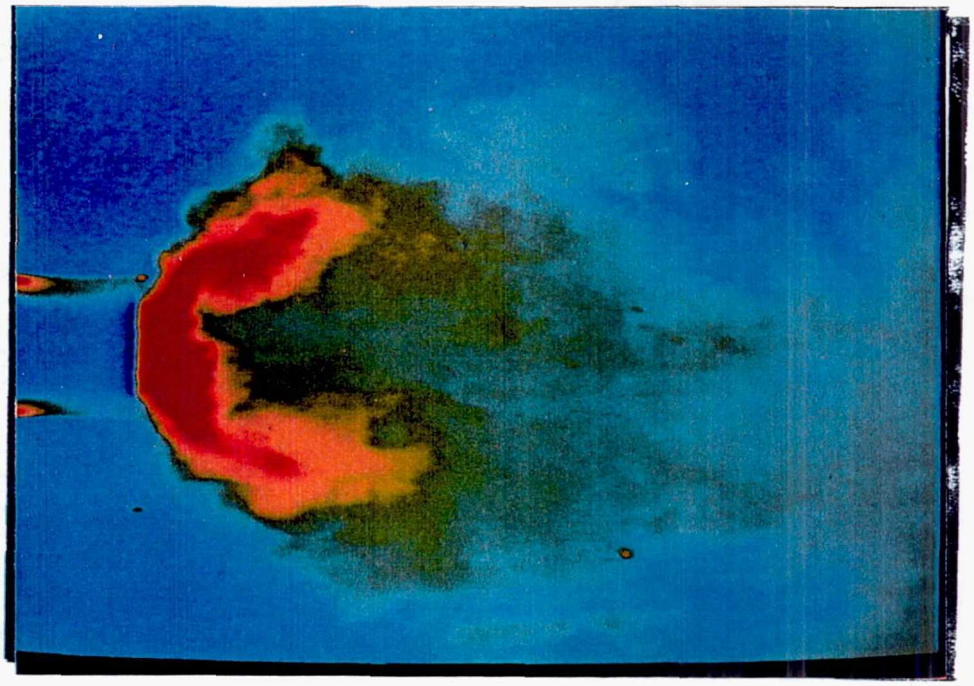

(a)

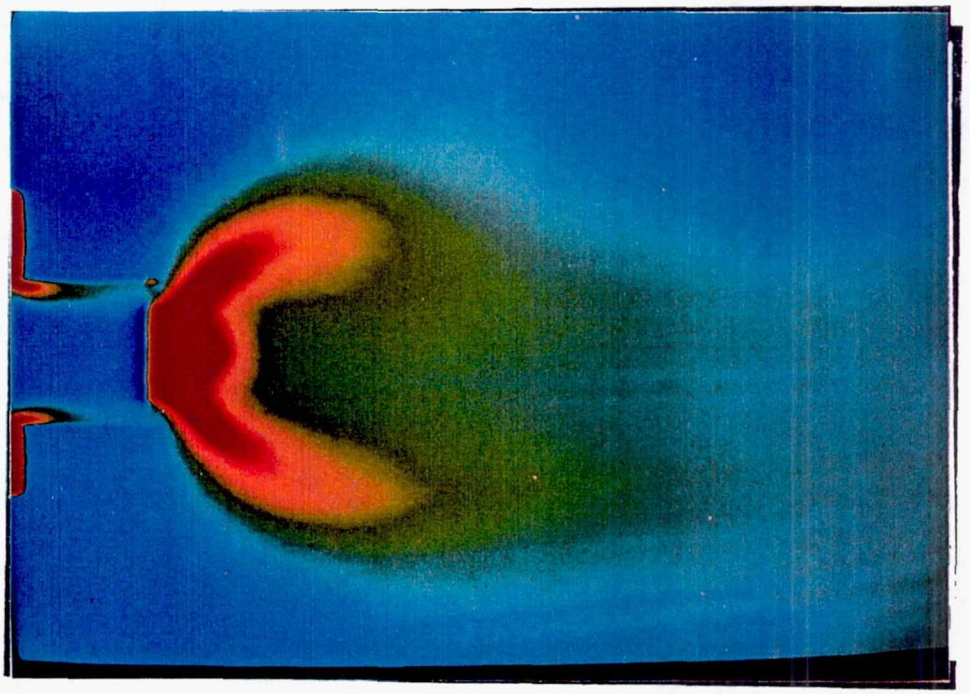

(b)

TE92-2410

Figure 2.9 Concentration Fields for N=1.66: (a) 1 Frame; (b) 127 Frames

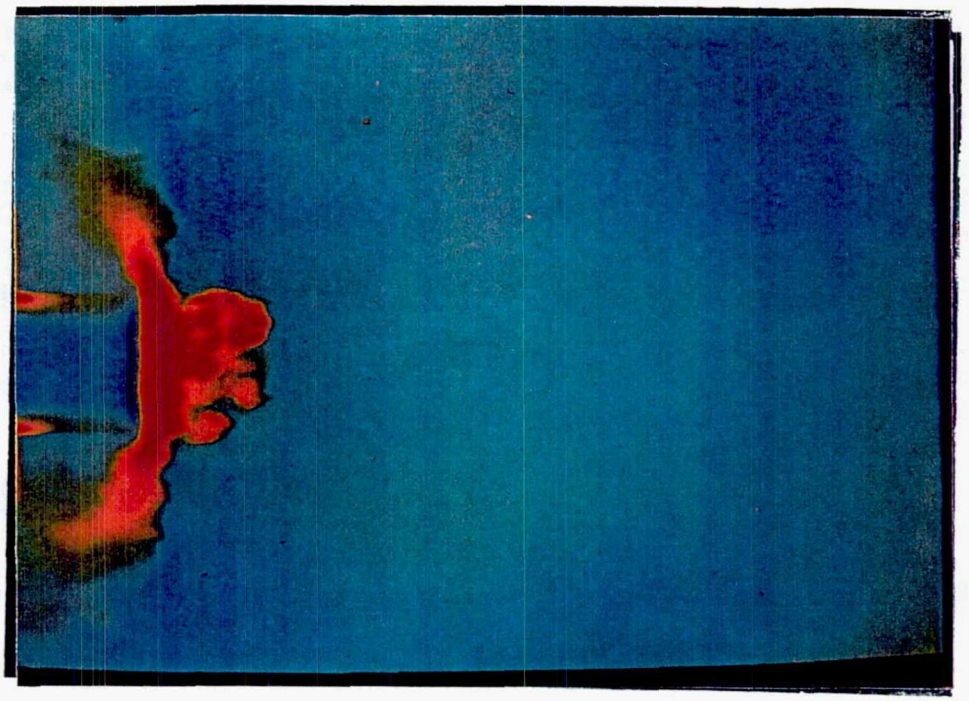

(a)

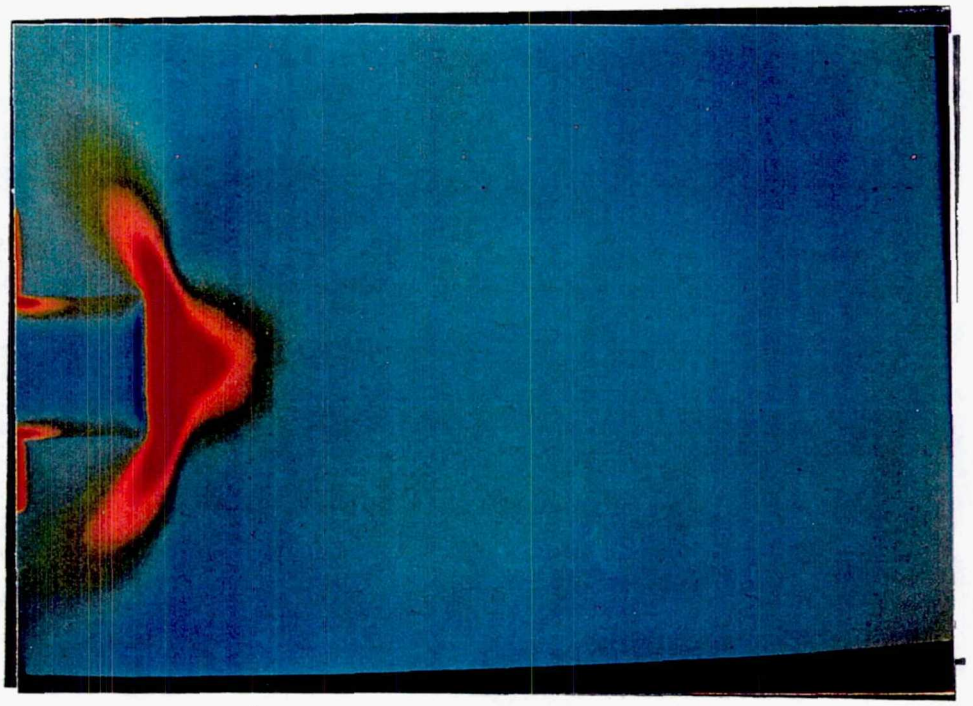

(b)

TE92-2411

Figure 2.10 Concentration Fields for N=2.00: (a) 1 Frame; (b) 127 Frames

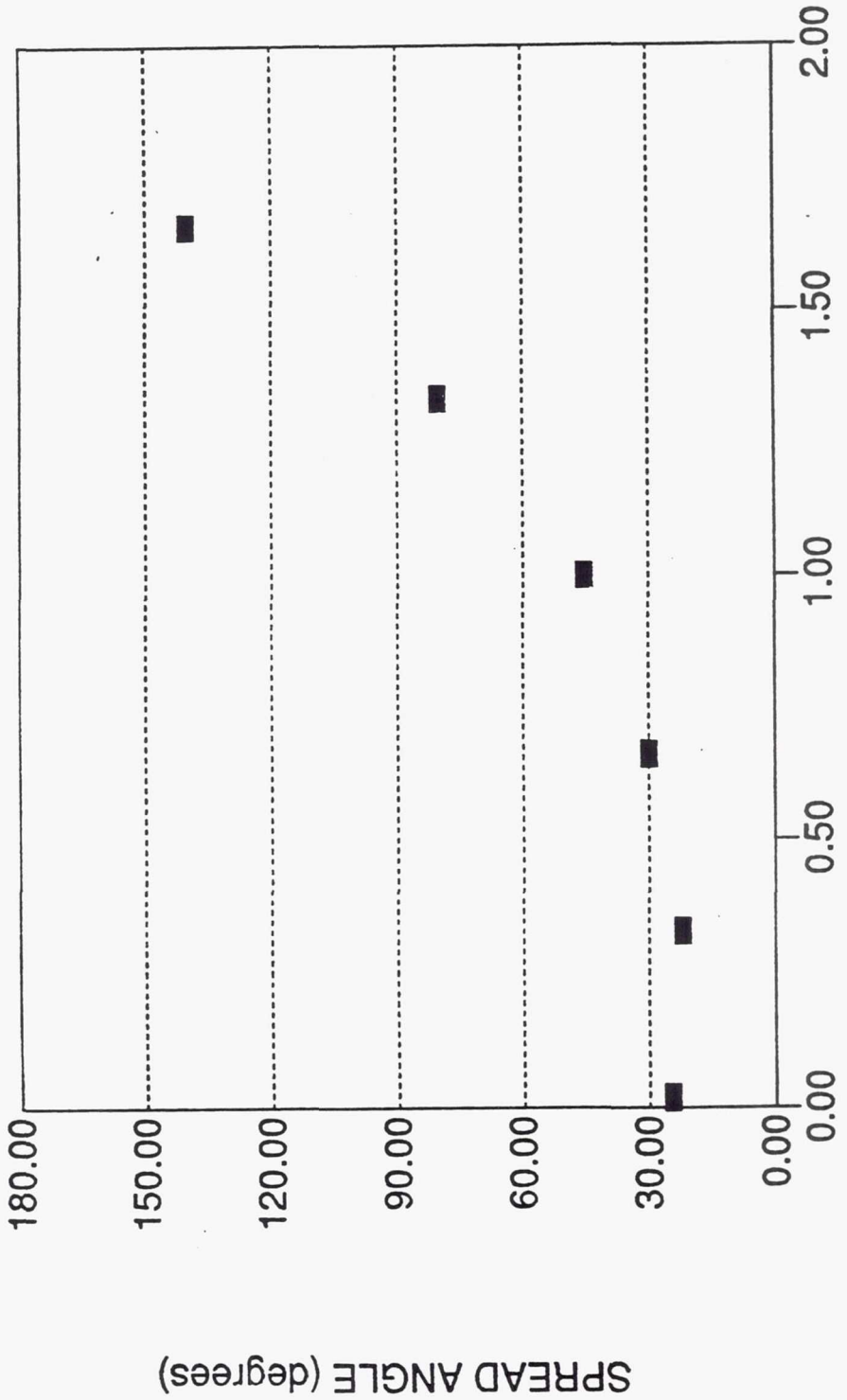

Figure 2.11 Relation Between Spread Angle and Swirl Ratio

CHAPTER 3: ANNULAR COMBUSTOR MODEL STUDY

The annular combustor model was designed to allow measurements in a flowfield similar to that existing in current annular combustors. These measurements are to be used as a database in the development and analysis of computational methods for the design of future gas turbine combustors. The flow characteristics determined include the mean and rms velocities in the three coordinate directions, the turbulence kinetic energy and one Reynold's stress component.

Measurements were made by Laser Doppler Velocimetry, an optical technique which does not intrude into or disturb the flow field of interest. Discussions of the general theory of LDV, experimental apparatus, measurement technique and data acquisition system are included in this section followed by the presentation and discussion of the results. An account of related errors and uncertainties can be found in Appendix B.

3.1 Experimental Apparatus

The annular combustion chamber model, several views of which can be seen in figures (3.1) and (3.2), was

designed to simulate the cold (non-reacting) flow characteristics of a current gas turbine combustor: swirl, recirculation, primary cross jets, and high levels of turbulence. The recirculation zone, typical of mixing zones in current combustors, is generated by the swirl imparted to the inlet annular jet flow by a set of swirl vanes. The length of this recirculation zone is determined by the location and strength of the primary cross jets. In order to allow the best possible modelling of actual combustor conditions the annular and primary cross jets were fully developed prior to entry into the test section.

In an ideal annular combustion chamber geometric similarity exists for each swirler. This geometric similarity is in the form of a volume or cell, of the flowfield extending downstream of the swirler inlet plane. The flow patterns and characteristics in each of these cells will be the same, along with the boundary conditions. The arrangement of these cells can be seen in figure (3.3). Therefore, in order to understand the characteristics of the flowfield one need only consider the region or cell corresponding to one swirler.

The same principle is utilized in the experimental apparatus. Due to the possibility of cell-to-cell mass transfer resulting from secondary flow patterns, as occurs in actual combustors, the decision was made to use multiple cells in the experimental apparatus. By allowing

the adjacent cells to interact the development of these secondary flows was possible. The choice of five cells over three cells was made on the basis of the two extra cells adding more interaction between cells and, hence, more realism.

In an actual combustor a cell would be slightly curved, as can be seen in figure (3.4). Comparing this to the combustor model cell one can assume the effect of the curvature to be slight or negligible, thus allowing the duct and the swirler cell to be constructed with a simple rectangular cross-section.

The duct rectangle cross section has a aspect ratio of 5, with a duct height of 3.00 in. and a width of 15.00 in. and a cross section corresponding to each swirler cell of 3.00 in. by 3.00 in.. The duct has a downstream extension from the swirler head plate of 10 duct heights, or 30.00 in.. For this experiment the configuration consisted of two opposing primary cross jets mounted along the cell centerlines. The centerlines of the jets were located one duct height, 3.00 in., downstream of the test section inlet plane.

The duct was originally constructed from 0.500 in. thick plexiglass plates throughout. This choice of materials proved unsuitable for some of the LDV measurements due to factors such as:

1) loss of beam cross-over at the probe volume,

2) loss of pinhole alignment,

3) change in effective focal distance to the receiving lens.

All three of these factors can attributed to the slight variations in the thickness of the plexiglass sheets. The first factor can also be attributed to scratches in the surfaces of these sheets. Scratches are a problem with plexiglass applications such as this one due to the necessary continual cleaning of the surfaces.

The measurements that were the most dramatically affected by the use of plexiglass were those made in the XY-plane. These measurements were affected more than those in the XZ-or YZ-planes due to the fact that the beams passed through the duct side walls at a considerably larger distance from the probe volume. For the measurements in the XZ- or YZ-planes this distance ranged from 0.40 in. to 2.60 in. (measured from the inner wall) while the that for the XY-plane measurements ranged from 6.00 in. to 9.20 in.. Since the beams must travel farther the effective change in the beam angle due to thickness variations or scratches becomes more pronounced, resulting in an increase in the signal loss.

The solution to this problem was the replacement of the plexiglass side walls with 0.25 in. thick glass plates. These plates facilitated unimpeded beam traversal due to very uniform thickness as well as high resistance to scratching.

The annular jets were constructed out of stainless steel, with a length of 9.55 in. and inner and outer radii of 1.084 in. and 1.459 in., resulting in a length-to-effective diameter ratio of 25. The swirlers are actual engine hardware currently being used in the Allison 570-K turboshaft gas turbine engine, which can be seen in figure (3.5). These swirlers, also constructed from stainless steel, are vane-type with 12 flat vanes at blade angles of 60 degrees. From equation (1.5) the approximate swirl number is calculated to be 1.52. A diagram of the annular jet can be seen in figure (3.6), while a separate diagram of the swirler can be seen in figure (3.7).

In order for this experimental apparatus to successfully model an annular combustor the five annular jets must pass the same mass flow. Since the pressure drop across a jet can be related to the mass flow, or average velocity, through the jet,

$$\Delta p = \frac{k}{2}\rho U_{ave}^2 \tag{3.1}$$

where

U_{ave} = mass averaged velocity in the jet,

k = loss coefficient of the jet,

Δp = pressure drop across the jet.

Two pressure taps were installed on each jet, the distance between the taps being as large as geometrically possible

to allow the measurement of the largest pressure drop. The larger the measured pressure drop the smaller the percent uncertainty of the calculated velocities.

Control of the pressure drop, and the corresponding mass flow, is allowed by the throttle valves mounted at the inlets of the annular jets. These throttles ,which also can be seen in figure (3.6), are infinitely adjustable to allow either an increase or decrease in mass flow. The calibration of the annular jets was performed by a researcher on previous similar project, Dean Barron. Those results can be found in [2].

Figure (3.9) shows the installation of the annular jets and swirlers to the head plate of the duct. One may notice that the swirlers are recessed a small distance from being flush with the head plate. Initially the swirlers were mounted flush, as in figure (3.8), but preliminary flow visualization by Barron [2] showed that upon exiting the swirler the flow attached to the head plate in the manner shown.

This type of flow phenomena is not desirable in gas turbine combustors since the fluid would transfer a large amount of heat to the combustor liner with the main flow losing energy. The increased heat transfer rate, as well as increased surface shear stress due to the larger velocity gradients near the wall, would serve to reduce the life of the combustor, increasing the maintenance

costs. The loss in energy from the main flow results in reduced available turbine inlet temperature and a corresponding loss in power. The desired type of swirler exit flow pattern can be seen in figure (3.9). This pattern produces a highly stable flame and regions of high combustion intensity. From these flow visualization results the swirlers were recessed in the annular jets a distance of 0.25 in. in order to produce the desired flow pattern at the test section inlet.

The preliminary flow visualization by Barron [2] was performed in the single swirler apparatus which, as stated before, operated at a smaller annular pressure drop than the model combustor. Further flow visualization in the single swirler apparatus of the test section inlet flow pattern (with the swirler installed in the recessed position) was performed by this author. These studies indicated that a bi-stable flowfield pattern existed for a small annular jet pressure drop range very near the maximum of the apparatus.

For pressure drops less than 0.0178 psi the desired flow pattern existed, while for pressure drops greater than 0.0190 psi the attached flow pattern existed. In the range 0.0178 psi< <0.0190 psi the flow pattern was bi-stable, switching between the two established flow patterns in a seemingly random fashion. From these flow visualization results one can assume that model combustor,

operating at a pressure drop of 0.040 psi, exhibited the attached flow pattern. Due to time constraints further modifications of the test section inlet to produce the desired flow pattern were not possible. All the measurements were therefore conducted with the attached inlet flow pattern.

The primary cross flow jets were constructed from stainless with a length of 10.75 in. and an inside diameter of 0.43 in., also resulting in a length-to-diameter ratio of 25. As with the annular jets the primary jet mass flow balance was maintained by balancing the pressure drops on the jets; the pressure taps were mounted to give the largest possible pressure drop and the inlets of the jets were fitted with throttle valves to allow the tailoring of the pressure drops. A diagram of a sample primary cross jet and throttle valve can be seen in figure (3.10).

An important characteristic in the analysis of a combustor of this type is the primary jet-to-annular jet mass flow ratio. Originally, the desire was to have a primary jet mass averaged exit velocity of 300 ft./sec. and an annular jet mass averaged exit velocity of 150 ft./sec.. These velocities give the desired mass flow ratio of 0.81, a total duct mass flow of 0.517 lbm./sec. and a duct average velocity of 21.6 ft./sec.

Although the five annular and ten primary cross jets appeared identical to each other some inconsistencies did exist. Differences in the maximum measured velocities were discovered during preliminary testing. Since the jets were required to have the same mass flow the maximum pressure drop was limited to the lowest measured maximum of all the jets.

The maximum average velocity for the annular jets was 93.4 ft./sec., while for the cross jets 250.0 ft./sec. was the maximum. These measurements were made with a pitot tube and the Laser Doppler Velocimeter. The original mass flow ratio could have been obtained by adjusting the throttles valves on the cross jets to reduce their mass flow; the decision was made to have the highest possible jet exit velocities in order to keep the turbulence levels as high as possible. The resulting mass flow ratio was 1.08, with a total duct mass flow of 0.371 lbm./sec. and a duct average velocity of 15.8 ft./sec..

In order to draw the ambient laboratory air into and through the test section some type of fan or blower had to be utilized. A 30-hp Chicago Blowers centrifugal blower was selected due to its ability to pass the large required mass flow. Connecting the test section duct to the fan was a large volume plenum chamber. The large volume was chosen to minimize the possible effects of feedback of larger scale fluctuations into the test section. Preliminary

tests indicated that some large scale feedback, in the form of large scale velocity fluctuations, did exist, prompting the use of screens and straws at the end of the test section. The additions did not cause a significant loss in mass flow and did eliminate the previously observed feedback. The plenum chamber and the centrifugal fan can be seen in figure (3.11).

3.2 Theory of Laser Doppler Velocimetry

Laser Doppler Velocimetry (LDV) is a non-intrusive technique used to detect the velocities of particles in a particular flowfield. Several modes of LDV operation have been developed and each mode has its own advantages and disadvantages. The mode chosen for use in this experiment is the burst, or individual realization, mode of operation. In this mode the velocities of individual particles residing in the flowfield are detected as they traverse the probe volume. If naturally occurring particles do not produce a strong enough signal to allow a measurement marker particles which will allow a measurable signal must be added to the flowfield.

One particular advantage to this mode of operation is that measurements can be made no matter how low the data rate; measurements are only made when particles are crossing the probe volume. This is of particular

importance in gas or air flows where high seeding density is often very difficult to achieve.

The particular LDV mode used in this experiment is the dual-beam, or fringe-type, mode. The basic element of this system, which can be seen in basic form in figure (3.12), is the probe volume that is formed by the intersection of two coherent laser beams of the same frequency. The dual-beam mode is based on the wave character of light; as the two beams intersect, usually by the focussing of two parallel beams into a common volume by a single lens, a pattern of constructive and destructive interference fringes are formed. An illustration of this phenomena can be seen in figure (3.13).

As a particle traverses the probe volume, it passes through these constructive (bright) and destructive (dark) fringes, scattering light in all directions at the frequency at which it crosses these fringes. The scattered light, in general a function of the particle size and shape, is collected by some type of detector, usually a photomultiplier. This collection can be made from any angle, but the direction of the strongest intensity of the scattered light is along the direction of the propagation of the incident beams, with the direction of the weakest intensity along the opposite direction.

In general one would prefer to collect the scattered light in the direction of maximum intensity. This is known as forward scatter light collection and can be seen in figure (3.14(a)). The advantage of this type of collection is that the signal is much stronger than in any other direction. The disadvantages are that a more complex optical system must be utilized as well as the fact that, in some cases, forward scatter collection is impossible due to geometrical restrictions.

Collection of scattered light along the direction of weakest intensity is known as backscatter and can be seen in figure (3.14(b)). The main advantage of this type of collection is that (for 180 degree backscatter) a simple optical system is required since components of the transmitting optics are also used as the collection optics. The disadvantage of this type of collection is that for air flows where high seeding density is difficult the signal is usually very weak, an order or two of magnitude smaller than for forward scatter.

At the probe volume the intersecting beams, with gaussian intensity profiles, are focussed to the diffraction limited diameter given by

$$2b_o = \frac{4}{\pi}\frac{f}{2b}\lambda \qquad (3.2)$$

where

f = the focal length of field lens,

2b= beam diameter entering field lens.

The diameter 2b is usually defined as the radial contour of light intensity $\frac{1}{e^2}$ Imax. The probe volume formed is in the form of an ellipsoid with dimensions 2a, 2b and 2c (figure (3.12)),

$$2a = 2\frac{b_o}{\cos(\frac{\theta}{2})} \tag{3.3}$$

$$2b = 2b_o \tag{3.4}$$

$$2c = 2\frac{b_o}{\sin(\frac{\theta}{2})} \tag{3.5}$$

For this experiment the half-angle between the incident laser beams was measured to be in the range 2.40 degrees$<\frac{\theta}{2}<$2.60 degrees, resulting in a probe volume of dimensions (on the average)

2a=0.0480 in.,

2b=0.0021 in.,

2c=0.0021 in.

The interference fringes formed by the two intersecting beams are, assuming that the beam's minimum diameter is located at the probe volume center, planes parallel to the plane of symmetry of the intersecting beams. These planes are separated by a constant distance, δ , given by

$$\delta = \frac{\lambda}{2\sin(\frac{\theta}{2})} \tag{3.6}$$

with the number of fringes in the probe volume given by

$$N = \frac{8f}{2b}\frac{\tan(\frac{\theta}{2})}{\pi} \tag{3.7}$$

With this information the processing electronics or more specifically, the frequency counter, can be used to detect the particle velocities. The frequency counter is a device which measures the time for a particle to traverse a given number of fringes (explained more fully later), usually preset by the experimenter. The time increment, Δt , for N fringes from the counter allows the following relation for the particle velocity, U:

$$U = \frac{N\delta}{\Delta t} \tag{3.8}$$

Since $\frac{N}{\Delta t}$ is the Doppler frequency, f_D , at which the particle scatters light while crossing the fringes one finds that

$$U = \frac{\lambda}{2\sin(\frac{\theta}{2})} f_D \tag{3.9}$$

which is the general relation between particle velocity and the Doppler frequency for a Laser Doppler Velocimeter.

The actual volume from which the particle velocity is measured, the measurement volume, is usually not the same as the probe volume. The size of the measurement volume is

determined by many factors such as particle size and shape, collection optics, and laser power. The effect of collection optics on the measurement volume size can be seen in figure (3.14(a)), where it can be seen that the overall volume is limited by the pinholes (explained later). The reduction in effective measurement volume is large when the off-axis measurement angle is large. The size and shape of the scattering particles as well as the laser power affect the amplitude of the signal relative to the threshold value in the processing electronics. An increase in the signal amplitude allows particles at larger distances from the center of the probe volume to be detected, resulting in an effective increase in the measurement volume.

3.3 Optical Configuration

The laser system used in this experiment consisted of a Spectra-Physics Model 165 5-Watt Argon-Ion Laser. The complete LDV system was originally designed and intended to be used as a two-color (blue(488.0 nm), green(514.5 nm)), two velocity component measurement system. Due to technical difficulties only one channel of processing electronics was available for use, limiting data acquisition to single-component measurements. The blue line of the laser was chosen as the light frequency with which to perform the measurements. Since only a single

color line was desired a single color prism was installed in place of the broadband mirror to increase system performance.

A diagram of the LDV system can be seen in figure (3.15). The transmitting optics consisted of quarter wave plates, beam waist lens, beam splitter, beam translator, Bragg cell, beam expander, and field lens, all of which are DISA products.

The quarter wave plates were a necessity for this experiment since the beam orientations, and thus the transmitting optics (except for the beam expander), had to be rotated for the measurement of the various velocity components. The first quarter wave plate, mounted at the output of the laser, converts the linearly polarized light from the laser into circularly polarized light. The second plate, mounted to the beam waist, converts the circularly polarized light back into linearly polarized light. This conversion permits the correct plane of polarization even through the rotation of the transmitting optics.

The beam waist lens allows the adjustment for the minimum beam diameter at the probe volume. At the minimum diameter in a laser beam the wavefronts are planar, and as one moves away from this minimum diameter the wavefronts become spherical. If the minimum beam diameters are located at the probe volume the interference fringe will

be planar and the spacing will be a constant: a particle traversing the probe volume at a constant speed will scatter light at a constant frequency no matter where in the probe volume the particle is located. When the minimum diameters are not located at the probe volume this fringe spacing will not be a constant: a particle traversing the probe volume at a constant speed will scatter light at varying frequency, giving erroneous subsequent statistics.

The purpose of the beam splitter is to split the incoming beam from the laser into two beams of equal intensity. One of these beams remains on the optical axis while the other beam is translated approximately 30 mm from the optical axis. This translation occurs due to the geometrical requirements of the bragg cell.

The main purpose of the Bragg cell is to remove any directional ambiguity in the velocity measurement. The Bragg cell acousto-optically shifts the frequency of the beam travelling along the optical axis by 40 MHz. With this frequency shift the interference fringes in the probe volume move relative to the probe volume at a 40 MHz rate. This allows the measurement of both the velocity and direction of the particles; particles moving against the direction of fringe movement will have a frequency higher than 40 MHz while a particle moving in the direction of fringe movement will have a frequency less than 40 MHz. The ability to measure the flow direction is of prime

importance in flows with recirculation or high levels of turbulence, such as the flowfield studied in this research.

Another advantage of Bragg cell use concerns angle bias, also known as fringe bias. Angle bias is caused by the fact that an LDV system cannot measure all particle velocities at all angles. Since the number of fringes crossed by a particle before the signal will be validated is preset particles that traverse the probe volume with certain trajectories will not be detected. With use of a Bragg cell as long as the highest measured frequency is less than one-half the shift frequency, in this case 20 Mhz, particles with all angles can be detected. The beam translator performs the opposite task of the beam splitter: the previously translated beam is retranslated toward the optical axis due to the requirements of the beam expander. The beam expander (expansion ratio=3.75X) serves one main function: expansion of the transmitted beams before they are focussed in the probe volume, resulting in a smaller measuring volume than would have been otherwise been possible. This result can be seen in equations (3.3), (3.4) and (3.5).

The purpose of the field lens is to focus the transmitted beams to one common intersection point, the probe volume. Decreasing the focal length of the field lens decreases both the length and effective diameter of

the probe volume, which is a highly desirable feature; the smaller the probe volume the greater the spatial resolution of the measurements. The field lens used in this experiment was actually a combination of two lenses, one having a focal length of 30.0 in., the other having a focal length of 48.0 in. Using standard thin lens theory

$$f = \frac{1}{\left[\frac{1}{f_1} + \frac{1}{f_2}\right]} \qquad (3.10)$$

where

f_1 = focal length of first lens,

f_2 = focal length of second lens.

Using this relation one finds the focal length of the combination to be 18.46 in.

The receiving optics, as discussed previously, were operated in the forward scatter mode due to the much stronger available signal. The receiving optics consisted of several elements manufactured by DISA: receiving lens, beam expander, spatial filters and photomultiplier tube. The receiving lens, focussed onto the probe volume, receives the scattered light from the probe volume and converts it into parallel light along optical axis of the receiving optics. The beam expander in the receiving optics works in reverse of the beam expander in the transmitting optics: the incoming parallel light is reduced to a smaller diameter (still remaining parallel) in order to enter the first spatial filter (pinhole).

The first pinhole is located at a the common focal point of the two lenses in the pinhole section. This setup is designed to reduce the collection of extraneous light from reflections due to light sources other than the probe volume or reflections from nearby surfaces. Due to the size of the pinhole being several times larger than the dimensions of the probe volume a small amount of stray scattered light will be passed.

The second pinhole is located immediately before the photomultiplier tube. The size of the second pinhole is roughly the same size as the measurement volume thereby removing nearly all of the extraneous scattered light.

The photomultiplier tube receives the scattered light from the measuring volume and converts the fluctuations in light intensity into electrical signals which will be input to the processing electronics. The photomultiplier tube is built by RCA and has a high level of quantum efficiency which corresponds to a high current signal-to-noise ratio.

3.4 Light Scattering Particles

As discussed before, the traversing of a seed particle across the interference fringes and the subsequent scattering of the incident light is what allows the measurement of velocity. These seed particles must have certain characteristics in order to ensure the

validity of the measured velocities:

(1) ability to follow the flow,

(2) ability to scatter adequate light,

(3) non-toxic nature,

(4) convenience of generation,

(5) inexpensive.

The most important of these qualities are the first and the second. If the particles cannot adequately follow the fluid motion the measured velocities will not accurately represent the existing flowfield. If the particle can follow the flow but cannot scatter adequate light to allow the photomultiplier tubes to detect the motion the measurement of velocity cannot be made. The second characteristic is usually not difficult to achieve, while the first is a problem in all types of turbulent flows or flows with high speeds and large or sudden changes in direction.

In this experiment the ability of the seed particle to follow the fluid motion was paramount. With the high levels of turbulence, strong swirling motion, and opposing primary cross jets generating a stagnation point region a more complex flowfield is difficult to find.

The major problem encountered related to the particle trajectories involved the flow upon exit from the swirlers. Due to the large amount of swirl, and the resulting large centrifugal accelerations, applied to the

inlet annular jet flow the flow path had a radial component. Near the test section walls the flow turned to become parallel to these walls. For larger particles, or groups of particles that had coagulated, this turning near the walls presented a great difficulty. This was readily evident when light oil was atomized and used as the seed: the particles collected on the test section walls, hindering data acquisition.

Various types of seed particles were tried: solid particles such as salt crystals and titanium tetrachloride; atomized solutions such as water, fog juice, dioctylpthalate, and propylene glycol. Of all these seed particles fog juice gave the best results but still did not allow adequate time for a large amount of data acquisition since these particles still collected on the test section walls, although much less than the other particles.

The solution was to combine a small amount of the fog juice to a large amount of ethyl alcohol, atomize this mixture, then run the mixture through a series of evaporation chambers. The result was a sub-micron particle size, small enough to allow confidence in the particle's ability to follow the flow. This confidence was a result of the fact that 15 hours of actual data acquisition could be performed before cleaning of the test section walls became necessary.

3.5 Data Acquisition

A general schematic of the data acquisition system can be seen in figure (3.16). The output signal from the photomultiplier tube, assumed to be generated by single particles in the probe volume at any instant of measurement (low burst density), contains the Bragg cell shift of 40 Mhz plus the doppler frequency shift of the particles passing through the probe volume. Since this output signal, on the order of 40 MHz, is at much too high a frequency to be handled by the processing electronics the signal is mixed, or heterodyned, with a selected frequency in the range of 31 MHz to 49 MHz. This process is known as frequency downshifting and is performed by a DISA 55 N 12 Mixer Unit.

The selected mixing frequency is chosen to allow the processor to receive the signal in the optimum operating frequency range while keeping the instantaneous signal (average plus fluctuation) from crossing the zero frequency level. This is a real problem with turbulent flows since the levels of turbulence can sometimes be very high. If the frequency is downshifted too much a large turbulent fluctuation could cause the signal to cross the zero frequency level, and since frequency is non-negative errors are introduced into the statistics.

Upon downshifting, the signal is sent to a TSI Counter Processor consisting of a Model 1994 Input

Conditioner and a Model 1995 Timer. Since the LDV is a fringe-type or dual-beam system the processor unit makes a measurement on a frequency burst, created by a particle traversing the probe volume, by counting the time for the particle to cross N interference fringes. The input conditioner makes an envelope of the time to be measured and the Timer Unit measures this time interval by use of a high speed clock.

The Input Conditioner also allows the experimenter high- and low-pass filter control, adjustable gain control, and the choice of the number of cycles to be measured. The Timer Unit also allows for a time comparison check for purposes of data validation.

In the Input Conditioner the pedestal level in a frequency burst (see figure (3.17)) is removed by the use of high pass filtering, while the low-pass helps to remove some of the high-end noise. Removal of the pedestal is crucial as it causes errors in the statistics if not removed; the processing electronics are designed for an input signal which is symmetric about a fixed level. The gain control is used to amplify the input signal.

For the choice of the number of fringes, N, over which to measure the time interval two options are generally available for counter processors: N-Cycle or Total Burst mode. The Total Burst mode allows the processor to accept any number of fringes (above a certain

minimum), or cycles, depending on the length of the frequency burst. The N-Cycle mode allows the experimenter to choose the number of cycles, usually either 4, 8, or 16.

The advantage of the Total Burst mode is that since the different samples have different envelope lengths the knowledge of the time interval and the number of cycles for each sample allows the possibility of velocity bias correction. The main disadvantage of operation in the Total Burst mode is that storage space is greatly increased due to the necessity of storing the number of cycles for each sample. Since the object of this project was to perform measurements in a full three-dimensional flowfield , and since no form of velocity bias correction was to be performed, the extra information obtained in the Total Burst mode was viewed as extraneous and the N-Cycle mode of operation was chosen. A setting of 8 cycles/burst was chosen as the number of cycles as the envelope over which the measurements were to be taken.

In the Timer Unit the leading edge of the burst envelope produced by the Input Conditioner starts a very high speed clock. This clock is arrested by the trailing edge of the envelope, and thus the total time for the envelope is known. A second function of the Timer Unit is to form a comparison of the envelope times for N cycles to the envelope times for N/2 cycles. Since this method of

data acquisition is based on the assumption of single particle residence in the probe volume at any one measurement time this comparison aids in the removal of signals generated by multiple particles in the probe volume. The timer allows the choice of the percent comparison. Thus, if the percent difference between the measured times is larger than the chosen comparison the data is rejected and the processor accepts another input signal. If the percent difference is less than the preset comparison the data is sent to the PDP 11/73 minicomputer, and the processor begins the cycle over with a new sample.

Aside from data acquisition and reduction tasks, the minicomputer controls the three-dimensional movement of the measurement volume in the test section. The laser, transmitting optics, and assorted electronics (mixer units, power supplies, and Bragg cell unit) are mounted to a 3/4-inch thick aluminum slab table (30.0 in. x 60.0 in.). Mounted to this table is a boom assembly which extends under the test apparatus. The table and boom assembly, which can be seen in figure (3.18), is directly mounted to a steel structure (figure (3.19)) which moves the table and boom assembly in the vertical and horizontal directions through the use of stepping motors. The third dimension of measurement volume movement is accomplished through the movement, also by use of stepping motors, of the field lens and receiving optics, a single unit

connected to the table and boom assembly by a roller slide and zoom traverse. The field lens and receiving optics are designed as a single unit so as to allow the measurement volume to always remain in focus, independent of measurement volume location. The sensitivities of the movements by the stepper motors in the three directions are listed below

Horizontal Movement: 1/1000 inch/pulse

Vertical Movement: 1/22574 inch/pulse

Zoom Movement: 1/1000 inch/pulse

These sensitivities allow very accurate placement of the measurement volume in the test section.

3.6 Results and Discussion

3.6.1 Main Flow

Three-dimensional information on the main flowfield has been obtained through the use of a single-component LDV system. Distributions of U, V, W, U', V', W', U'V', and K are calculated from the individual data samples. The description of the actual measured quantities and the method of calculation of the above characteristics can be found in Appendix A.

The choice of a measurement grid depends on the character of the fluid motion. More detailed measurements are needed in regions of large gradients and complex flow

patterns, with less detail necessary in regions of simpler, less complex flow. Due to the three-dimensionality of the flowfield a choice was made as to the regions of the flow in which to concentrate the measurements. The YZ-plane was in need of a measurement grid with greater spatial resolution than that for the XY-plane due to the smaller scale structures to be found in the YZ-plane. Thus measurements were to be made in YZ-planes for various downstream locations, with these downstream locations chosen so as to also be more concentrated in the more complex regions.

Another consideration in measurement grid sizing involves the probe volume size; the resolution of the grid should be such that probe volume overlap from one data point to the next does not occur. From Appendix A the rotation of the test section to allow the measurement of the W characteristics is illustrated. Due to this rotation the length of the probe volume, on the average being 0.05 in., is the driving factor for the grid spacing in both the Y- and Z-directions, which was chosen to be 0.20 in., or 4 probe volume lengths, for both directions.

The spacing in the X-direction of the various planes was chosen as 0.50 in. in the region of the more complex flow, 0.0 in.<X< 4.00 in., with larger spacing thereafter. The downstream locations of the YZ measurement planes were: X=1.00, 1.50, 2.00, 2.50, 3.00, 3.50, 4.00, 4.50,

6.00, and 9.00 in.. The YZ-plane and XY-plane measurement grids can be seen in figures (3.20) and (3.21).

Although a complete scan in the YZ-plane from one wall to the other was desired, limits on the vertical travel of the probe volume were imposed. A fully detailed explanation can be found in Appendix A. The range of vertical probe volume travel was, therefore, limited to 0.40 in.<Y< 2.60 in. Since data pertaining to only one cell was desired, the limits on the travel of the probe volume in the Z-direction were 5.80 in.<Z< 9.00 in., where the Z=5.80 in. location allows comparison to a geometrically similar station at Z=8.80 in..

In the measurement of the W characteristics some geometrical restrictions were encountered at X=2.50, 3.00, and 3.50 in., necessitating the removal of the cross jet throttles and mounting plate; very little resulting flowfield alteration occurred. The measurements at the X=2.50 in. and X=3.50 in. locations were then able to be made while those at X=3.00 in. were not due to the necessary removal of the cross jet supporting structure. A further explanation can be found in Appendix A.

Mean Flowfield

The mean flowfield found in the model combustor is best represented by vector plots in the XY- and YZ-planes. These vector plots allow one to see the relative values of

the velocities at points in the flowfield, thus illustrating the general mean flow characteristics. The XY-plane vector plots can be found in figures (3.22-3.27) while the YZ-plane vector plots can be found in figures(3.29-3.34).

From the XY-plane vector plots two main characteristics can be seen: the formation of a general toroidal recirculation zone and the influence of the primary cross jets. A great amount of interaction exists between the recirculation zone and the cross jets. As a consequence of this interaction, the recirculation zone and the cross jet interaction must be discussed together, not separately.

The recirculation zone is generated by the application of swirl to the inlet annular jet flow and the step change in area at the inlet to the test section; this zone is created in order to enhance the combustion process. The general character of this zone can be seen in the XY-plane vector plots. This region of backflow exists over a large portion of the cell cross-section, showing asymmetric behavior.

The purpose of the primary jets is to shorten the recirculation zone in order to decrease the overall length of the combustor. This goal has been achieved as no backflow exists past the X=3.00 in. station, but while the length of the recirculation region is shortened by the

addition of the jets, the strength of recirculation has been enhanced by the radial jet effect from the cross jet stagnation point. The location of the stagnation point is controlled by the relative strength of the two opposing jets; if the jets had equal mass flows (pressure drops), the stagnation point would be located in the vertical center of the duct. From figures (3.24(c)) and (3.25(a)) one can see that this location is not in the vertical center of the duct, but at roughly Y=1.35 in. Preliminary flow visualization had illustrated large scale fluctuations of the location of the cross jet stagnation point in the range 1.00 in.<Y<2.00 in., indicating the unsteadiness present in the flowfield.

The influence of the cross jet stagnation point on the recirculation zone, and the downstream flow, is easily seen in figures (3.24) and (3.25). The flow can be imagined to flow out of the jets, reach the stagnation point, and be forced to move in a radial type motion in the XZ-plane, as in figure (3.28). The recirculating backflow thus receives a driving force which generates stronger recirculation.

Previous studies on similar experimental apparatus' ([8],[47],[37]) show a recirculation region which is symmetric about the duct centerline in the XY-plane. These studies, though, used axisymmetric (cylindrical) test section geometries, whereas the geometry used in this

study was of rectangular cross-section, with a square cell cross section. With a square cross section, as one moves equal distances away from the centerline location, Z=7.50 in., one would expect the vector profiles to be the inverse of one another. Since all of the cells are assumed geometrically similar, a necessary condition is that the flow conditions at the plane boundaries separating the cells be the same. At the Z=6.00 in. and Z=9.00 in. boundaries the flow conditions should be the same.

Figures (3.29) illustrates the regions of recirculating flow in the YZ-plane at X=1.00, 1.50, 2.00 and 2.50 in. The recirculation zone at X=1.00 in. appears to be located off-center in the positive Z direction with strong recirculation existing into the upper right corner; a smaller amount of recirculating mass flow exists in the upper left corner. This backflow existing in the upper left corner could be part of the recirculation zone from the adjacent cell. From the vector plots for 7.40 in.<Z< 8.00 in. the effect of the attached inlet flow pattern is evident; the recirculation is strong across the duct height with positive axial flux occurring only near the walls. Strong positive axial flux can be found to exist in the lower left and lower right corners. The profiles at the Z boundaries are roughly similar in form with larger magnitudes existing at Z=9.00 in.

The vector plots indicate the structure of the flow patterns at X=1.50 in. to be very similar to that at X=1.00 in. The recirculation can be seen to extend the entire width of the cell cross section with a larger portion of this backflow existing in the upper Y range; nearer the Z=6.00 in. and Z=9.00 in boundaries the lower Y range is dominated by strong positive axial flux. The profiles at the Z boundaries, like those at X=1.00 in., are similar in form but with much larger magnitudes existing at Z=9.00 in.

Except in the range 7.00 in.<Z<8.40 in. the vector profiles at X=2.00 in. and X=2.50 in. are very similar. Near the center of the cell the strong influence of the cross jets on the recirculated mass flow is illustrated. The extent of the backflow in the cell cross section can be seen to be reduced for the X=2.50 in. location than for the X=2.00 in. location; the backflow is more concentrated near the center of the cell cross section. This can be attributed to the flow from the cross jet stagnation point region; the strongest influence of the stagnation point on the recirculated mass flow is in the center of the cell cross section. For both the X=2.00 in. and X=2.50 in. stations the vector plots on the Z boundaries are very different in shape and magnitude.

The behavior of the mean flowfield for stations downstream of the cross jet injection plane is relatively

simple compared to that of the upstream stations. The main characteristic is the influence on the local flowfield from the radial jet flow pattern formed at the cross jet stagnation point; this effect is best seen in figures (3.24) and (3.25). As one moves in the Z direction, either positive or negative, the vertical spread of the radial jet can be seen. This spread is an effect of viscous dissipation and is strong enough that, for the X=3.50 in. plane, no influence of the cross jets can be seen at either the Z=6.00 in. or the Z=9.00 in. boundary. The dissipation of this effect occurs in the axial direction, as well, as no vertical variation of any consequence in the axial velocity profile can be seen at X=6.00 in. or X=9.00 in..

The YZ-plane vector plots (figures (3.30-3.34)) allow the illustration of the flow developing in the various cross-stream planes. At all of these stations some type of smaller scale swirling motion exists, with the largest concentrated near the cross jet injection location. Unexpected, however, was the absence of overall swirl; some amount of overall swirl was expected in the first duct height of the test section due to the large amount of swirl (S=1.52) applied to the inlet flow.

As with the vector plots in the XY-plane the vector plots in the YZ-plane show the effect of the cross jets on the flowfield. The far downstream locations, X=6.00 in.

and X=9.00 in., show very little motion in the cross-stream plane, illustrating the large amount of dissipation present.

The vector plots of most interest are those of the X=2.50 in. and X=3.50 in. downstream locations. At both of these stations one can see the strong effect of the cross jets on the combustor model flowfield. The flow pattern in the YZ-plane can be seen to be dominated by four cells of vortex-type motion. For both of these locations the left side of the plane (looking downstream, Z<7.50 in.) shows a much more symmetric (with the Y=1.50 in. centerline) pattern than the right side.

The driving force behind this type of motion is, as in the case of the XY-plane, the flow resulting from the cross jet stagnation point region. The flow can be seen exiting the cross jets, reaching the stagnation region, and flowing in a radial type motion in the XZ-plane. This radial motion exhibits itself in the YZ-plane as fluid motion in the positive and negative Z directions. Thus, with generally no cross flow between the adjacent swirler cells this jet effect drives this vortex-type cell motion.

Further upstream of the X=2.50 in. station one can still see the swirling motion, although not nearly as structured as the X=2.50 in. or X=3.50 in. cases. The X=2.00 in. location shows two regions of vortex-type motion, with a more structured flow pattern possibly

altered by the existence of the large amount of cross-flow at the Z=9.00 in. boundary. This type of cross-flow is not seen at the Z=6.00 in. boundary, and thus is a probable cause of the asymmetry in the flowfield. This cross-flow is unexpected since all the swirler cells were assumed to be geometrically similar, resulting in similar flowfields for the different cells. This cross-flow is partially responsible for the asymmetries found in the right half of the grid at the X=2.50 in. and X=3.50 in. locations.

This cross-flow can be seen to exist at the X=1.50 in. plane and, to a lesser extent, at the X=1.00 in. plane. These two locations share similarities in flow patterns other than afore-mentioned cross-flow from the adjacent cell. In each of the vector plots of these two locations two regions of vortex-type motion can be observed, one in the upper right corner, and a second, much weaker, vortex motion located near the mid-Z and lower-Y ranges. The behavior in the lower-Z range for the full Y-range at both the X=1.00 in. and X=1.50 in.stations is rather undefined. At X=1.00 in. scattered or bad data seems to obscure flow details, while at the X=1.50 in. station no prevalent type of motion exists.

As stated earlier, no overall swirling motion is found in the first duct height of the test section, as would be expected from the large amount of swirl applied to the inlet flow. The combination of the primary cross

jets, attached flow pattern and large step change in area at the test section inlet (area ratio=12.02), serve to reduce the swirl velocities to negligible levels in this region. The effect of the cross jets on the swirl is the same as that of flow straighteners: the radial jet issuing from the cross jet stagnation point serves as a boundary (porous in this case, solid in the case of flow straighteners) across which mass flow is inhibited.

The effect of the attached flow pattern and large step change in area can be explained by angular momentum concepts. As the fluid issues from the swirler it possesses a certain amount of swirl, or angular, momentum. Since the flow is a wall jet the fluid moves towards the cell boundaries upon exit from the swirler. When the fluid turns in the downstream direction the large change in area will cause a large reduction in the particle velocities due to the law of conservation of angular momentum. These velocities may be further reduced due to viscous effects from the cell boundaries but this would be a small effect.This absence of swirl, and the corresponding absence of the decay of swirl, indicates that the recirculation is formed and driven by the step change in area.

Further downstream of the Z=3.50 in. location, at X=4.00 in., the well-defined 4 cell flow pattern is seen to deteriorate. Four vortex-type motions are still

evident, but the cores of the vortices have translated while their strengths have been reduced. The 4.50 in. location shows almost complete breakdown of the 4 cells, with only one very weak region of vortex motion sill existing.

The X=6.00 in. plane illustrates the decay of nearly all motion in the cross-stream plane, the only motion being a small amount of flow in the negative Z and positive Y directions in the lower Z range. The X=9.00 in. plane shows no detectable motion of any type; this shows the large amount of dissipation present in the flowfield as only 6.00 in. upstream existed a very complicated, high speed flow pattern.

Turbulence Flowfield

The turbulence flowfield of the combustor model is best represented by contour plots of the characteristics in the YZ-planes for the various downstream locations. The turbulence quantities calculated from the individual data samples are the three root-mean-square velocities, Urms, Vrms, and Wrms, and the corresponding turbulence kinetic energy, K, as well as the XY-component of the Reynold's shear stresses, $\overline{U'V'}$.

RMS Velocities and Turbulence Kinetic Energy

The root-mean-square velocity and turbulence kinetic energy distributions for the various downstream stations

can be found in figures (3.35-3.86). The data for the X=3.00 in. case consists of only the Urms and Vrms, since Wrms was not measurable due to geometric restrictions (see Appendix A).

The profiles for X=1.00 in. can be seen in figures (3.35-3.38). The three rms velocities seem to exhibit similar behavior with flat contours near the center of the duct. Urms and Vrms show a large amount of data scatter for most of the plane, especially the lower Z range, while the Wrms contour is relatively flat for most of the plane, with scatter only found in the 5.80 in.<Z<6.40 in. range.

The K distribution, as well, shows a well-defined central region of reduced magnitude extending into both corners on the Z=9.00 in. boundary. The intensity of the turbulence peaks up near the walls and near the mid-Y range at the Z=9.00 in. boundary. This flat (nearly constant magnitude) central region corresponds to the strong region of backflow found at the X=1.00 in. plane, as seen from the mean flowfield data, while the peaking near the walls corresponds to the shear layer produced by the strong axial flow along the walls. This pattern of reduced levels of turbulence inside the backflow region as compared to the shear layer was seen also in the work of Brum and Samuelson [9] and Vu and Gouldin [53].

Another characteristic of the K distribution at the X location is the formation of a circular shape, high

gradient region found in the lower Z range. This appears to be the result of the high shear zones from the annular jet flow. This ridge of high K extends around the central zone only for the lower Z range and does not exist in the upper Z range.

At X=1.50 in. (figures (3.39-3.42)) the Urms, Vrms, and Wrms contours all display relatively flat distributions, resulting in a flat K contour. The circular, high gradient region found at X=1.00 in. is barely visible in the lower Z range, while a peak is evident near Y=2.0 in. on the Z=9.00 in. boundary. This peak results from both Urms and Vrms showing general peaks in that region. One characteristic of Vrms illustrated in the contour is the magnitude deficit in the lower right corner.

Moving to the X=2.00 in. station one observes some interesting flow characteristics (figures (3.43-3.46)). Regarding the line plots one can see that all three rms terms (except for Vrms in the upper Z range) and K show very similar behavior across the cell width with nearly equal magnitudes (peaking near the mid-Y region) and a trailing off of the magnitudes near the walls; the velocity gradients are larger in the Y direction than in the Z direction. This behavior seems to be a combination of isotropy (all three rms terms being equal) and homogeneity in the Z direction (rms terms at a constant value).

The contours of the turbulence characteristics at X=2.50 in. show general similarity to those at X=2.00 in. with general peaking in the central region of the cell cross-section and larger gradients in the Y direction than the Z direction. The larger gradients result from the close proximity of the measurement plane to the stagnation point; the radial jet fluid is concentrated in a thin layer in the Y direction while spreading in all direction in the XZ-plane.

The behavior of Urms at X=3.00 in., seen in figure (3.51), does not show much effect from the cross jet injection as most of the contour displays a flat profile, with a small peak in the lower right corner. The effect of the jets is clearly evident, though, in the Vrms distribution, with a clear and sharp peak occurring near the center of the cell cross section.

Unlike that at the X=3.00 in. location, the Urms contour for X=3.50 in. (figure (3.53) shows a large central peak with the magnitude dropping off at the cell boundaries. The Vrms distribution shows magnitudes nearly equal to those at X=3.00 in., with a central peak trailing off at the boundaries and walls. The Wrms contour, on the other hand, shows a very asymmetric behavior, with a general peaking located off center in the negative Z direction. Due to this behavior in Wrms, the K distribution also shows an asymmetric peaking in the same

general location. Other than this abnormality the distribution shows the turbulence kinetic energy to be highly concentrated in the central region of the duct.

The behavior of the Urms, Vrms, Wrms, and K at the X=4.00 in. station, seen in figures (3.57-3.60), follows that of the data at X=3.50 in., although with reduced magnitudes due to dissipation and decay. The asymmetric Wrms behavior exists in the same general form as at X=3.50 in., thus reducing the probability of measurement error. The contour of the turbulence kinetic energy again shows the high concentration near the center of the duct, trailing off to nearly constant values at the upper and lower walls and showing smooth profiles, peaking at mid-Y, on the two Z boundaries. The characteristics at X=4.50 in. display the same general behavior as the data at both the X=3.50 in. and the X=4.00 in. planes, only with reduced magnitudes.

The contours of data at X=6.00 in. indicate near isotropy and homogeneity, although some scatter of the data is evident and the Wrms contour does show a slight gradient in the negative Z direction. The same behavior is seen at X=9.00 in., with the magnitudes of all three rms terms reduced from those at X=6.00 in. Regarding the K contours at both the X=6.00 in. and X=9.00 in. planes, one can see that the distributions at X=9.00 in. allow a better approximation of isotropy and homogeneity than at

X=6.00 in.; since the magnitudes at these stations are so much less than at X=3.50 in., say, isotropy and homogeneity can be assumed to be valid assumptions. Although the values of the rms velocities and K at these two downstream stations are much lower than the values at the upstream stations the values are still very high when compared to fluid flows such as channel or pipe flow.

$\overline{U'V'}$ Behavior

The contour plots of the Reynold's stress component, $\overline{U'V'}$, can be found in figures (3.73-3.82). Higher levels, either positive or negative, of $\overline{U'V'}$ are found in regions of high shear or momentum transfer in the XY-plane. This component of the Reynold's shear stresses was the only one measured.

From the $\overline{U'V'}$ contour at X=1.00 in., seen in figure (3.73), one can immediately see the circular ridge of increased $\overline{U'V'}$ in the left half of the plane (looking downstream). This ridge was also seen in the K contour at X=1.00 in., and corresponds to the high speed flow issuing from the swirlers creating a region of high shear and momentum transfer. This ridge appears to indicate that the flow exiting the swirler is not of the wall jet variety and appears to possess some type of swirling motion. Near the center of the duct one also sees a region of near zero magnitude, also shifted in the positive Z direction, signalling a region of low or zero shear; this region

corresponds to the strong backflow found at this location.

The X=1.50 in. station exhibits behavior similar to X=1.00 in. only in the sense that a slight ridge is visible for the lower Z range. In general the contour is rather flat but asymmetric with a peaking on the Z=9.00 in. boundary. Also peaking at this same location were Urms and Vrms (and also K), indicating the occurrence of some strong turbulence interaction.

Some interesting behavior appears at X=2.00 in.. From figure (3.75) one can see regions of large, positive $\overline{U'V'}$ in most of the right half plane and in the lower left corner, while between these two peaks a region of large, negative $\overline{U'V'}$ can be found. Regarding the XY- and YZ-plane vector plots the largest gradients of U and V can be seen to occur at these locations. At X=2.50 in. the behavior of $\overline{U'V'}$ is very asymmetric, showing a strong positive peak towards the Z=9.00 in. boundary. The rest of the $\overline{U'V'}$ contour shows small local peaking but, in general, a flat profile.

The effect of the cross jets on the turbulent shear can be clearly seen at the X=3.00 in. location. The central portion of the cell cross-section can be seen to display large negative values of $\overline{U'V'}$, while the lower-Y region shows a trend towards near zero values. The line plot in figure (3.77) shows a general levelling off near the Y boundaries at the Y=7.20 in. location with large

slopes occurring near the center of the duct. These slopes, and their changes in sign, indicate the strong effect of the cross jet stagnation point on the local flowfield. The magnitude of the turbulence stress can be seen to decrease near the cell walls and boundaries, where the influence of the cross jets is much reduced.

The $\overline{U'V'}$ contour at X=3.50 in. shows two very sharp, positive peaks near the center of the cell cross section, the two sharp positive peaks being separated by a region of much reduced turbulence stress. At the X=3.00 in. plane the positive peak was found in the lower Y range, with the much larger negative peak occurring near the center of the duct. For the X=3.50 in. case the positive peaks are found near the middle of the duct with the negative peaks occupying the lower Y range. Again the values are seen to trail off near the cell walls and boundaries.

The behavior of the turbulence stress contours at the X=4.00 in. and X=4.50 in. planes is much the same. The twin positive peaks occurring at X=3.50 in. are no longer evident as one large peak of nearly the same magnitude has developed at X=4.00 in.. The location of this peak has translated to the Y=1.80 in. location, while the negative peak, of much reduced magnitude, remains at the same vertical location. The X=4.50 in. location shows a much dissipated peak near Y=2.00 in., with the negative peak remaining at the same location and strength as at

X=4.00in.. As with the other cases, the turbulence stress drops off near the walls and boundaries.

Dissipation and mixing has a large effect on the downstream flowfield, as the X=6.00 in. station shows a general spread of the peaks resulting in a flatter $\overline{U'V'}$ profile. The negative peak is no longer evident and, as before, the turbulence stress goes to zero at the walls and boundaries. By X=9.00 in., the turbulence stress can be seen to be almost completely dissipated.

3.6.2 Cross Jet Flowfield

In figures (3.85-3.100) can be found flow profiles showing the development of the primary jet flow into the test section. These profiles, showing only the vertical (Y direction) velocity component (corresponding to the jet axial velocity), are measured at the vertical locations Y=0.06, 0.25, 0.50, 0.75, 1.00, 1.25, and 1.50 in. These mean and rms velocity distributions should show profiles similar to pipe flow with substantial variations with vertical distance. A discussion of the beam orientations for these primary jet measurements can be found in Appendix A.

The measurement grids in both the XY-(same as YZ-) and XZ-planes can be seen in figures (3.83) and (3.84). The XY-plane grid shows a change in the number of grid points in the X direction (with a corresponding change in

the Z direction) at the third vertical station from 11 to 13 points, which was instituted since the jet flux would spread at the larger Y distances. The XZ-plane grids corresponding to these various Y locations also show the change in the grids with figure (3.84(a)) illustrating the grid for Y=0.06 in and Y=0.25 in. and figure (3.84(b)) illustrating the grid at Y=0.50, 0.75, 1.00, 1.25, and 1.50 in. Both of these grids use a spacing of 0.05 in. in both the X and Z directions.

At the Y=0.06 in. station one would expect a close comparison to classic pipe flow data such that from Laufer [32]. A comparison of Laufer's data for both the mean and rms quantities, at Reynold's numbers (based on maximum velocity and jet diameter) of 50,000 and 500,000, to the data from the current experiment (Reynold's number= 75,000) can be seen in figures (3.87) and (3.88). The data from both Laufer and the combustor model are both non-dimensionalized by the centerline (maximum) velocity. From figure (3.87) one can see the experimental V profile from the combustor model shows better agreement with the R=500,000 data than the R=50,000 data. Slight differences are to be expected, such as the slight spread of the flow due to the dissipation of the sharp gradients near the jet wall, since the combustor model measurements were made 0.06 in. from the jet exit.

Figure (3.88) shows plots of turbulence intensity (the rms velocity divided by the centerline mean velocity) for both the combustor model data and Laufer's two cases. As can be seen both of Laufer's cases show strong peaks near the walls of the jet with maximum values near 9%. The combustor model data shows a maximum near 13%, but the peak could be larger due to the rather poor resolution of the measurement grid (compared to that of Laufer). The centerline value for the combustor model is also larger, by nearly a factor of two, than both of Laufer's data sets. This large difference between the data sets is mainly attributed to the effect of the opposing cross jet as well as the effect of the local main flow.

As discussed before, flow visualization of the jet stagnation point region indicated that the location of the stagnation point fluctuated, in a rather random fashion, within a 0.75 in. range between the exits of the two jets. The region between the two jets is evidently highly turbulent and unsteady, resulting in high levels of turbulence intensity across the test section, even near the cross jet exits.

From the XY-plane vector plots at Z=7.40 in. and Z=7.60 in. one could see the positive axial flux occurring at the upper and lower walls (Y=0.00 in. and Y=3.00 in.). Since the centerline of the cross jets was located at Z=7.50 in., the jet flow issued into a region of cross

flow of velocity of roughly 10% of the maximum jet velocity. Although this is a relatively small magnitude crossflow velocity, this effect also resulted in an increase of the turbulence intensity.

At the Y=0.25 in station, figure (99), the V distribution shows a slight spread in the jet flux with not much reduction in the maximum velocity. The Vrms velocity shows a large increase in the turbulence fluctuations over those found at Y=0.06 in.; the values measured at this location in the combustor model are much larger than the values that would be expected from pure jet flow, again due to the opposing cross jets creating a region with very high levels of turbulence.

At Y=0.50 in., the V distribution can be seen to be translated in both the X and Z directions; this skewness corresponds to a bending of the centerline of the jet flow due to the main flow acting as a cross flow, exerting a shear force on the jet flux. The spread of the jet flux is increased over at Y=0.25 in. , with the maximum velocity remaining near 325 ft./sec.. The Vrms distribution shows overall increases across the grid, with the peak levels, relatively sharp at the Y=0.25 in. location, being dissipated to give a smoother contour.

The V distributions at Y=0.75, 1.00, and 1.25 in. indicate a decrease in the maximum vertical velocity as well as continued spread in the vertical jet flux with

distance from the jet exit. The location of the center of the vertical jet flux can also be seen to show little translation in the XZ-plane. The Urms distributions show the decay of the circular peak region into a concentrated peak at the Y=1.25 in. station with an XZ-plane location at the center of the vertical jet flux. This peak occurs in the stagnation point location fluctuation region, resulting in a very high level of turbulence.

The Y=1.50 in. plane is located in the middle of the stagnation point fluctuation region and, thus, shows high levels of turbulence as at Y=1.25 in. with the RMS velocity contour displaying a much smoother distribution than the previous stations. The main point of interest is the reduction in the vertical jet flux; the main fluid motion in this region is in the XZ-plane as seen in the XY-and YZ-plane vector plots. Also, from these vector plots the location of the stagnation point was illustrated to be near Y=1.35 in.; from these results the stagnation point is not evident even at Y=1.50 in.. Since the different data sets for the primary jet and for the main flow were measured at different times the operating conditions could have been slightly altered. The peak vertical velocity has been reduced from 180 ft./sec., at Y=1.25 in., to 50 ft./sec., indicating that the stagnation point is in close proximity to the Y=1.50 in. location.

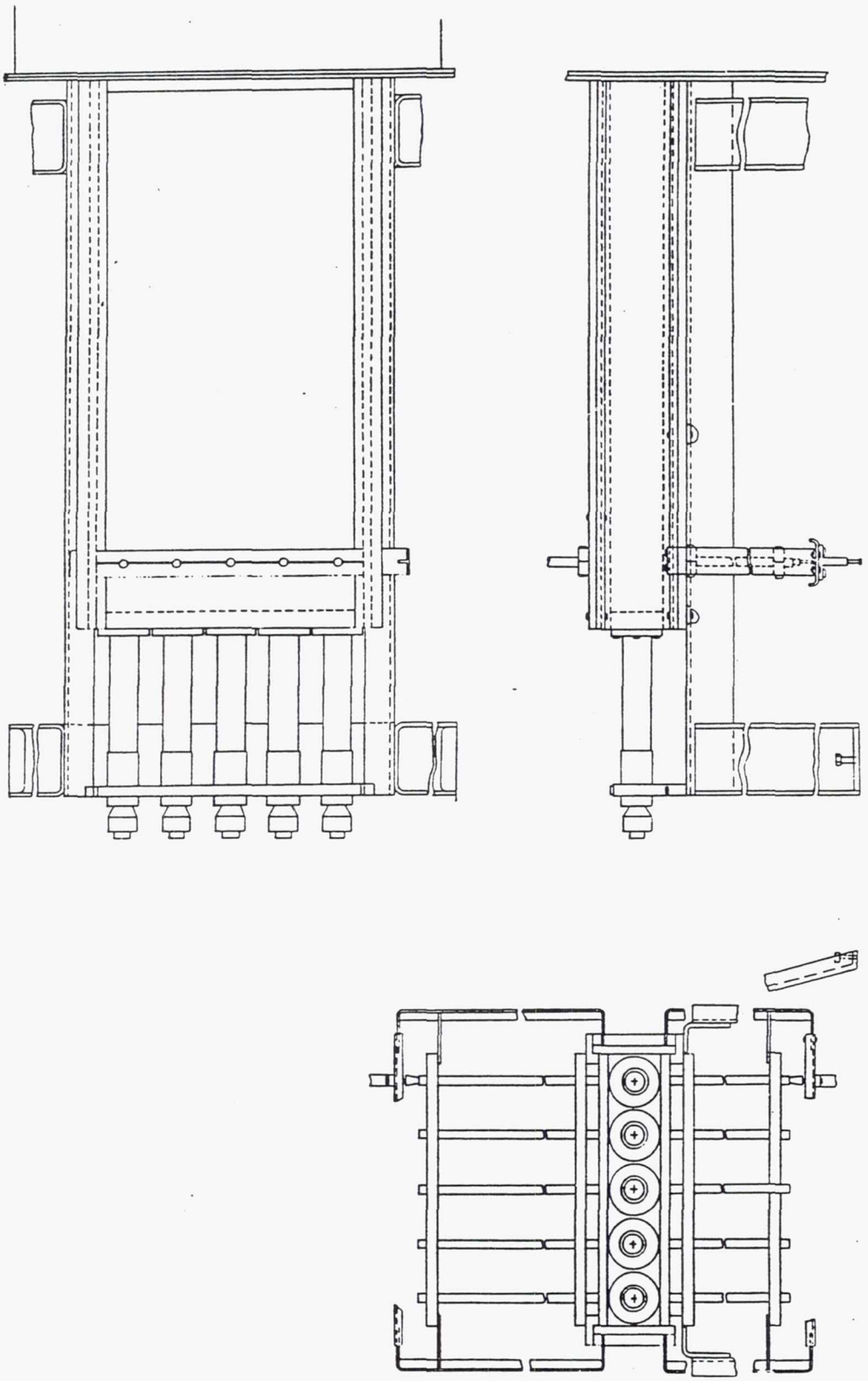

Figure 3.1 Three View Drawing of Annular Combustion Chamber Model

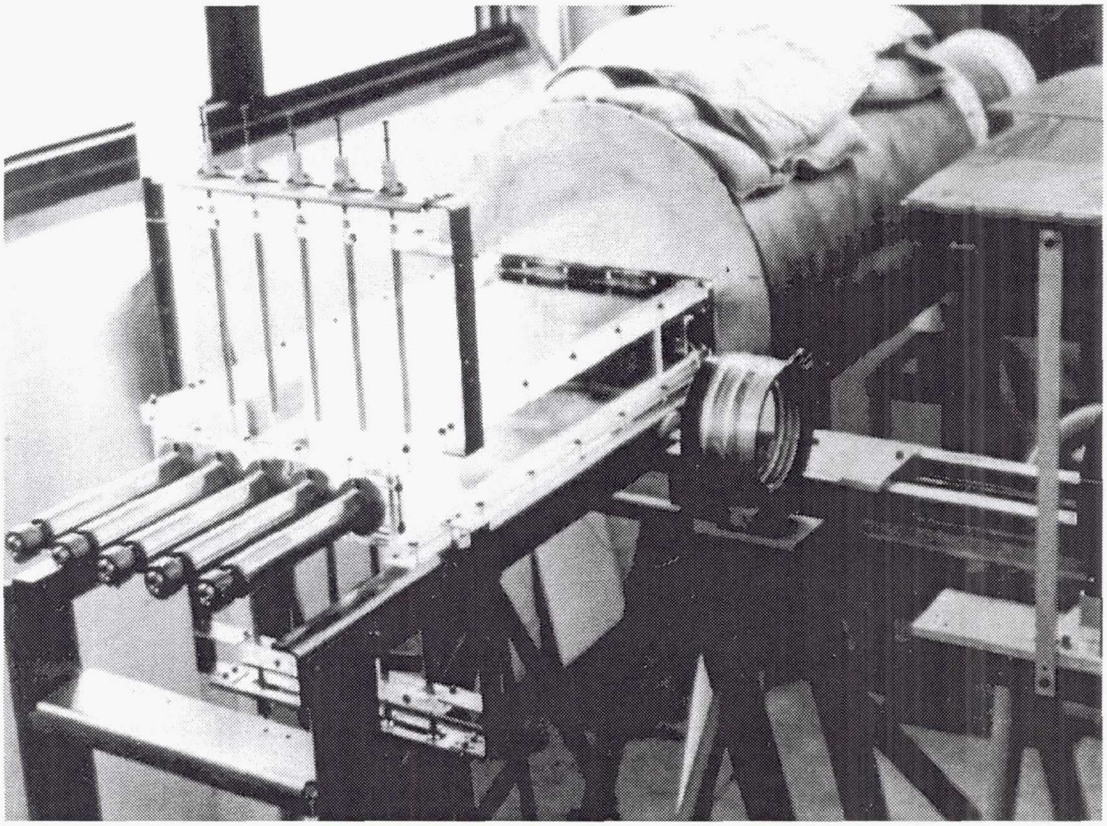

TE92-2255

Figure 3.2 Photograph of Annular Combustor Chamber Model

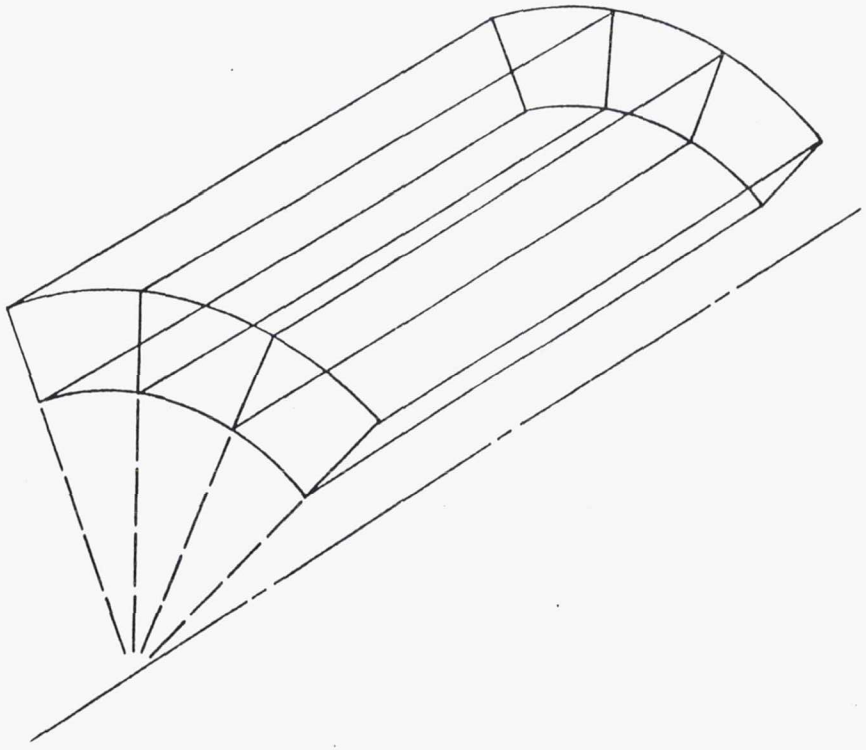

Figure 3.3 Arrangement of the Swirler Cells

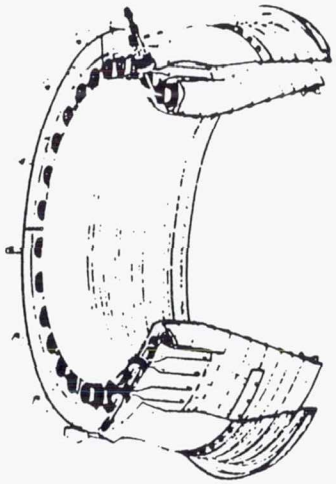

Figure 3.4 Actual Annular Combustor (After Gupta, et al[27])

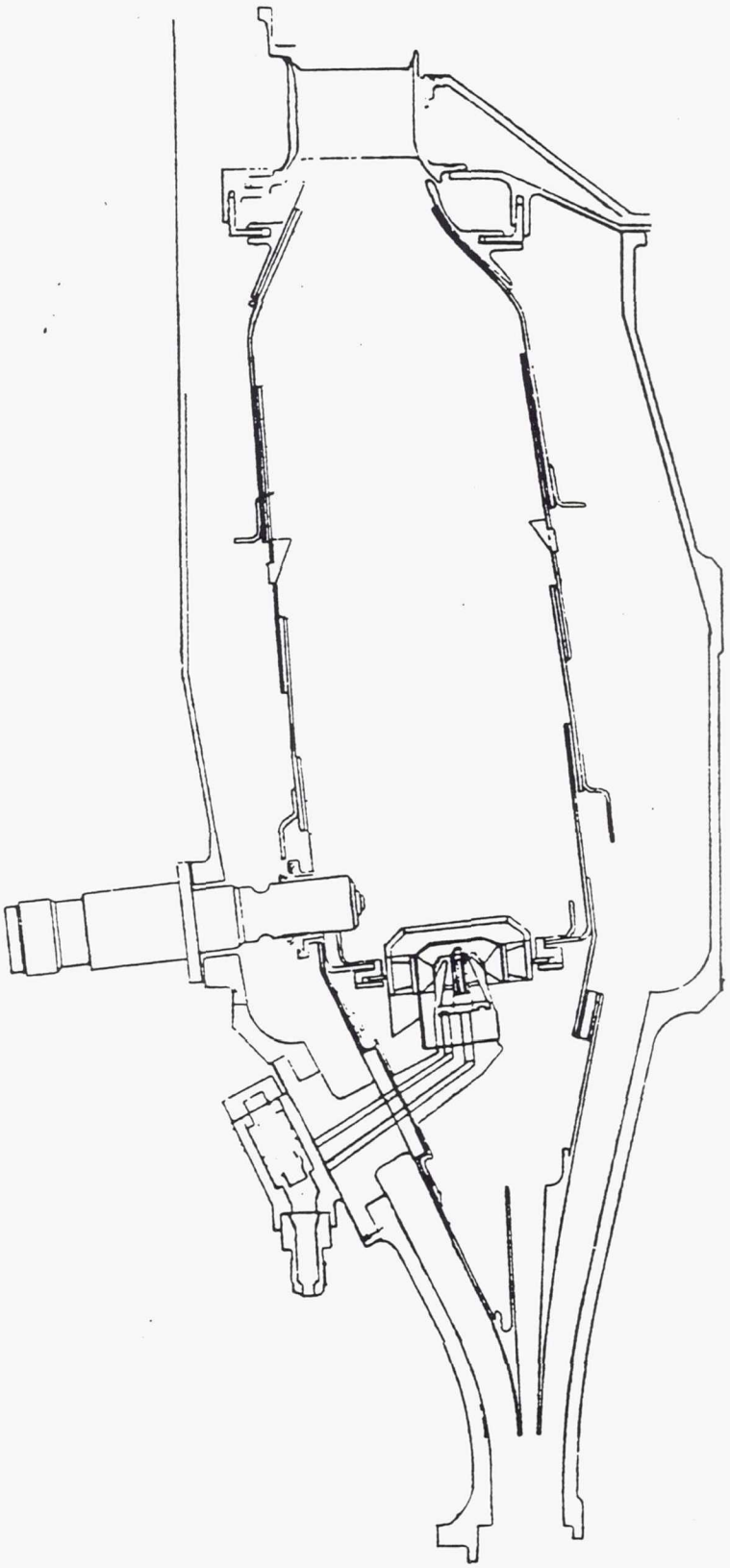

Figure 3.5 Allison Gas Turbine 570-K Annular Combustor

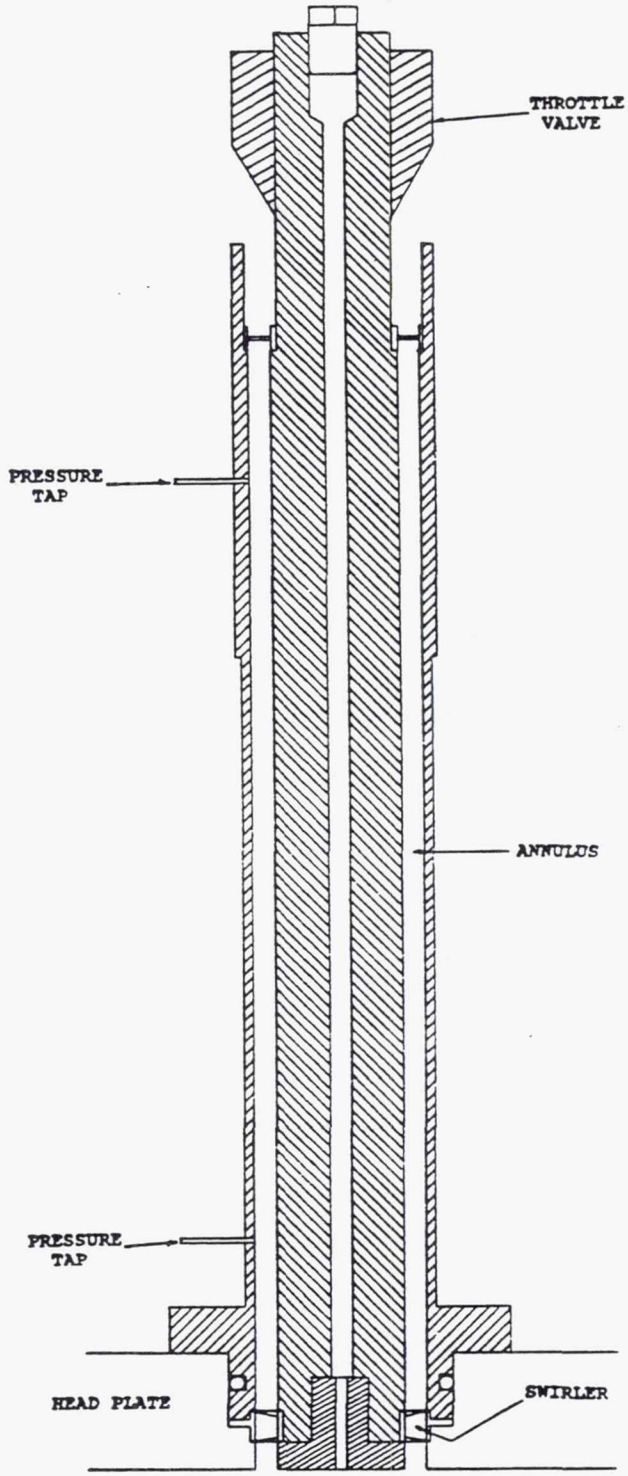

Figure 3.6 Annular Jet and Throttle Valve

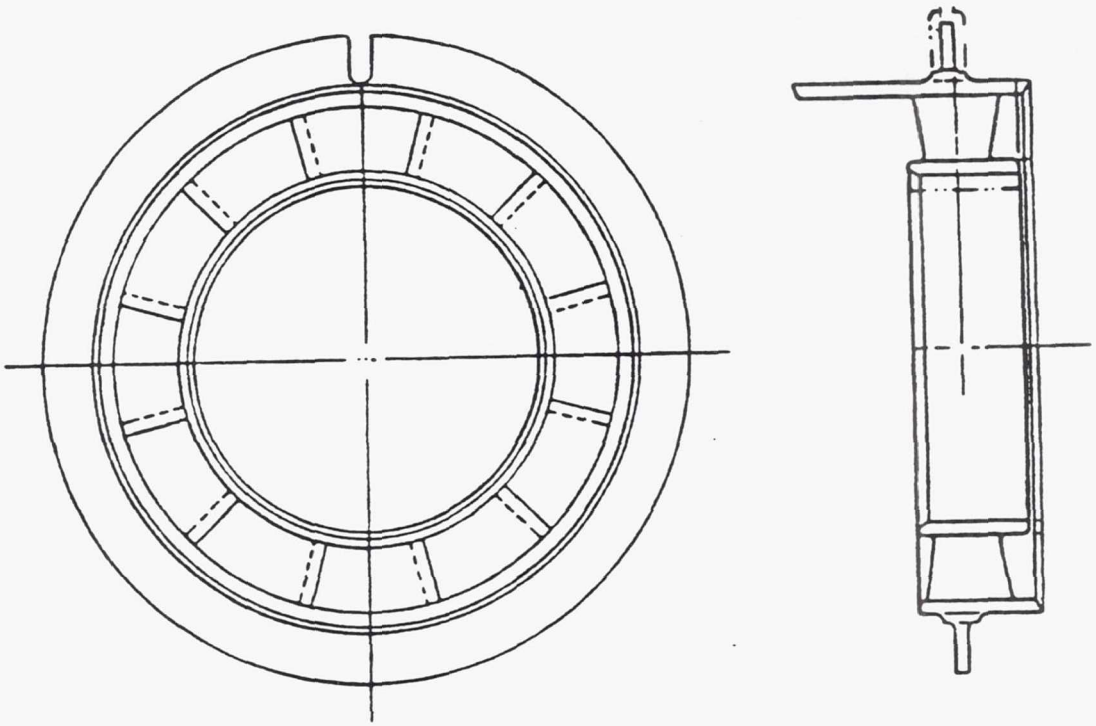

Figure 3.7 Vane Swirler from Model Combustor

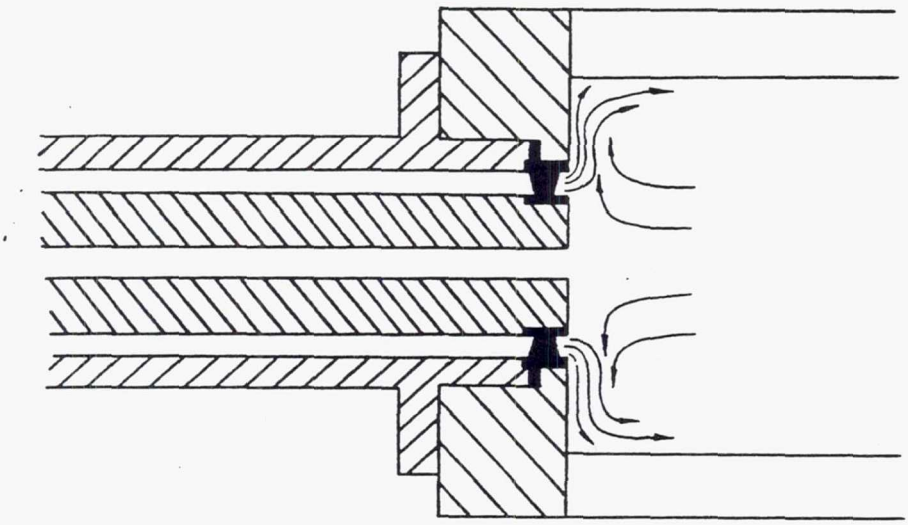

Figure 3.8 Original Swirler Orientation and Flow Pattern

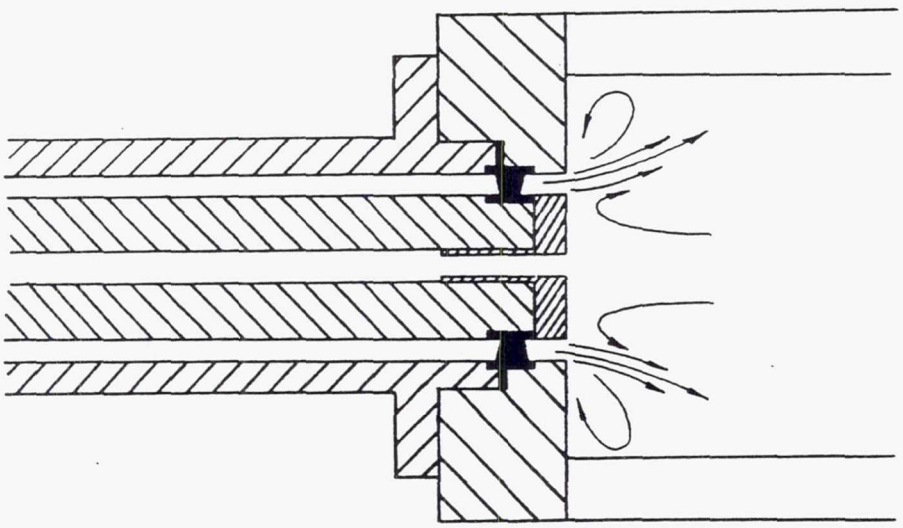

Figure 3.9 Modified Swirler Orientation and Flow Pattern

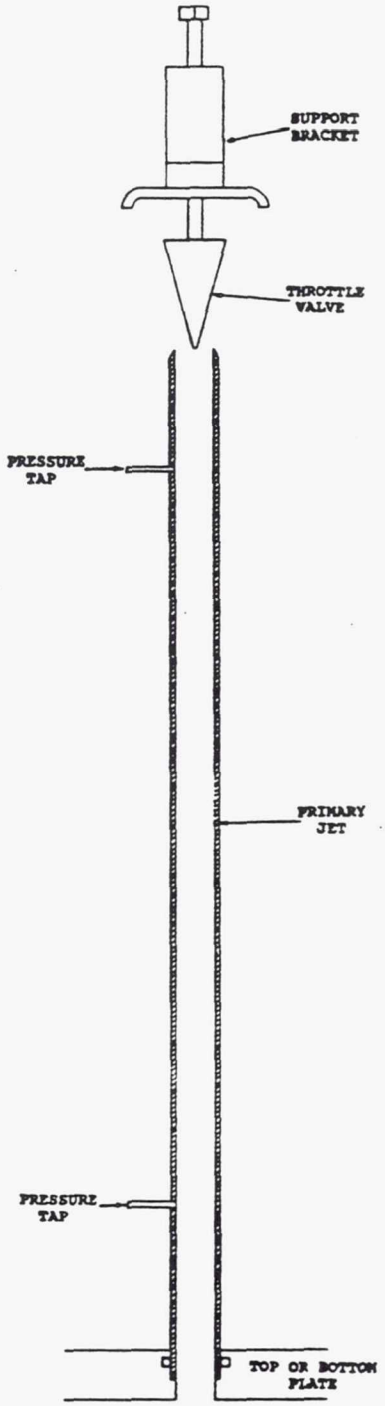

Figure 3.10 Primary Cross Jet and Throttle Valve

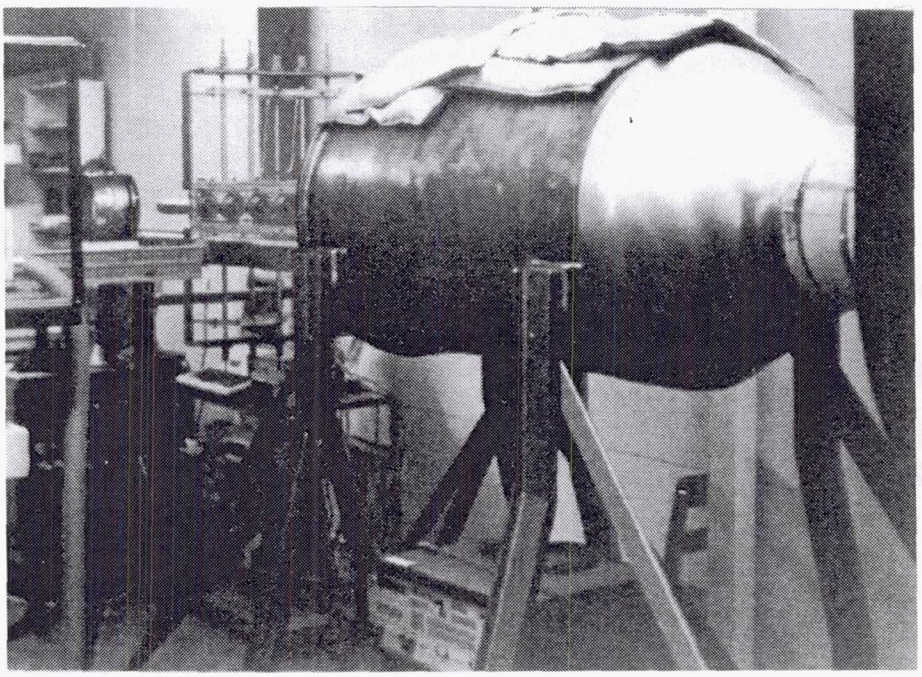

TE92-2263

Figure 3.11 Plemnum Chamber and Centrifugal Fan

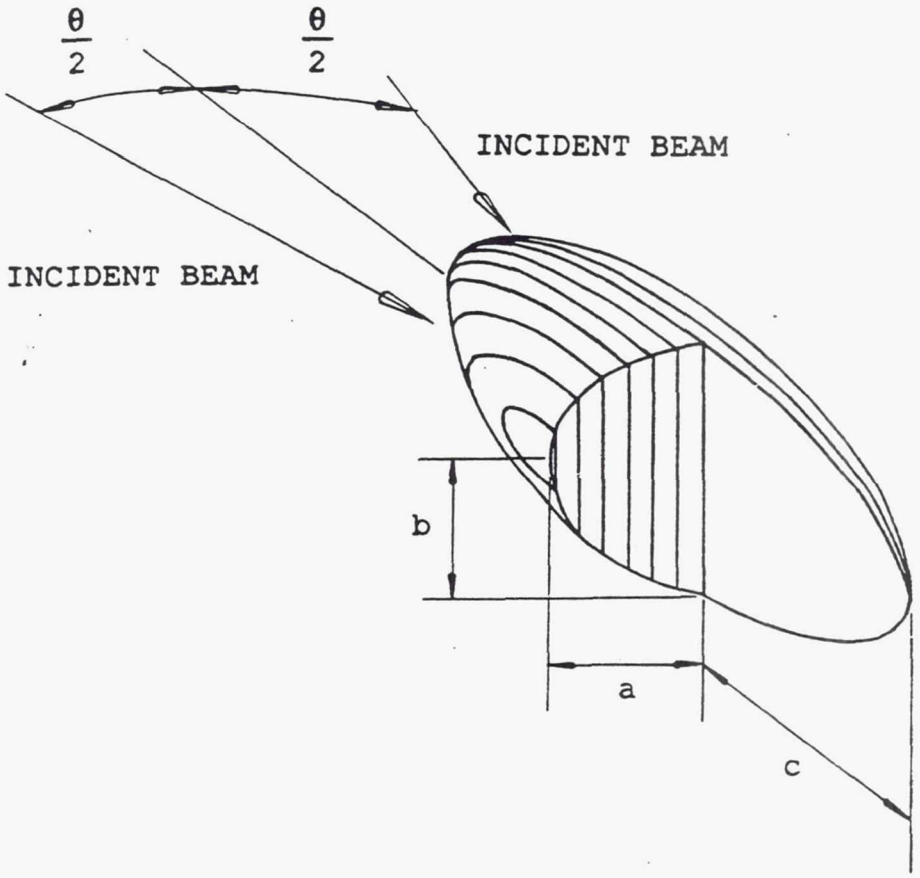

Figure 3.12 Laser Doppler Velocimeter Probe Volume

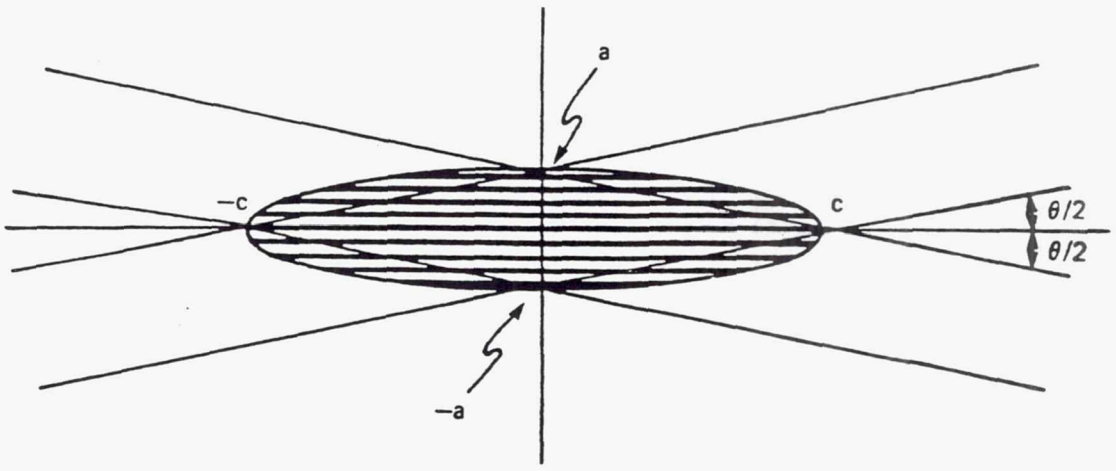

Figure 3.13 Interference Fringes Formed in Probe Volume (After Buchhave [10])

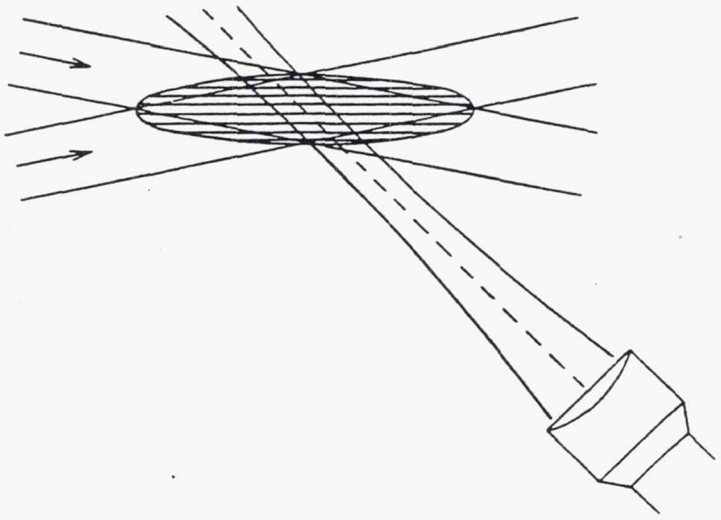

(a)

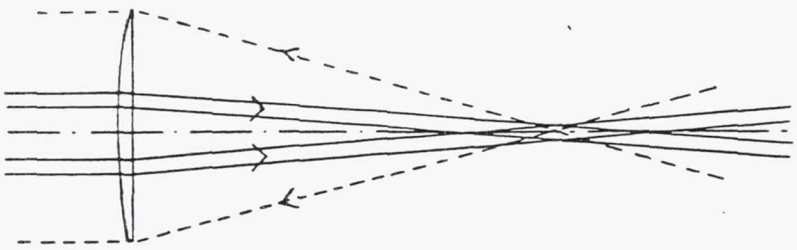

(b)

Figure 3.14 Orientation of Receiving Optics: (a) forward scatter; (b) backscatter (After Buchhave [10])

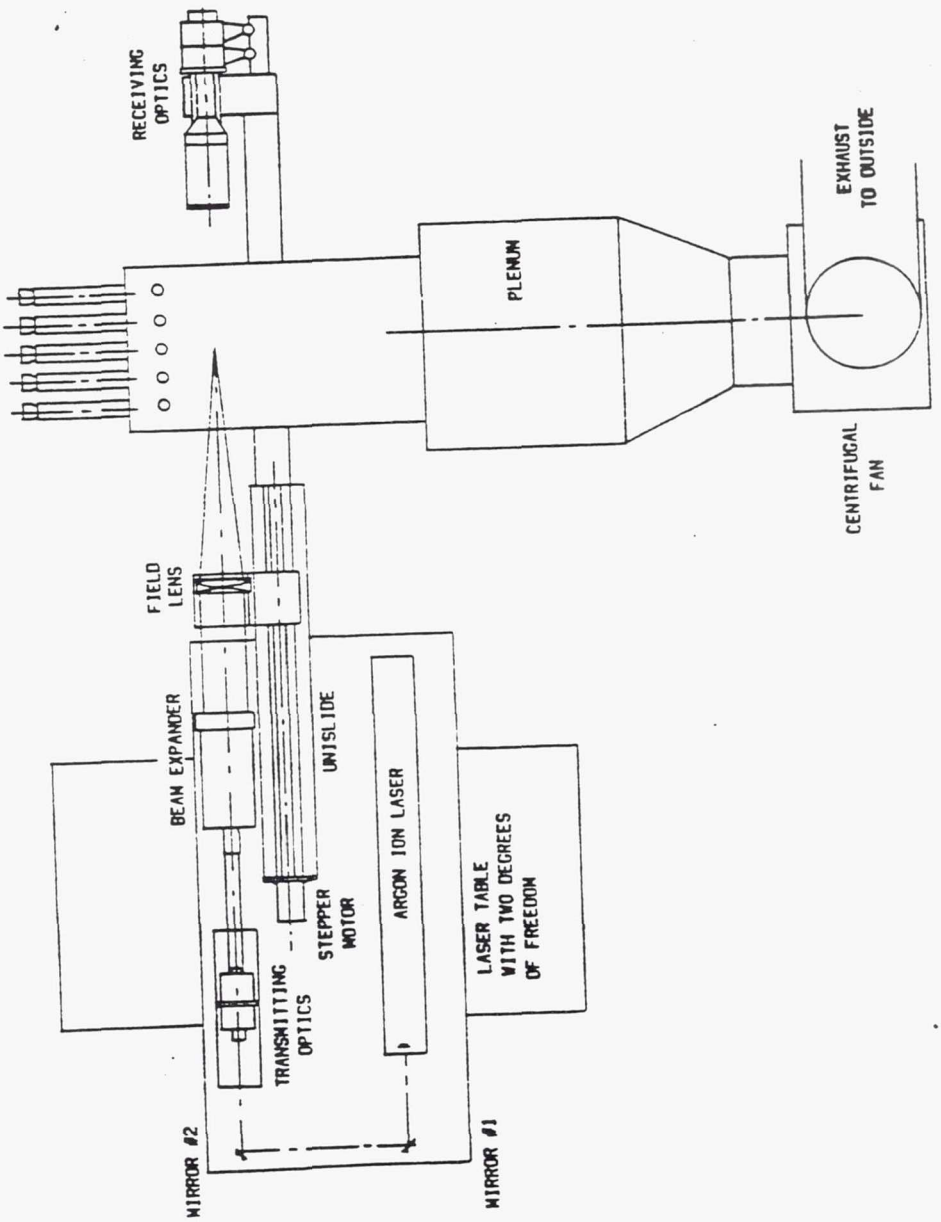

Figure 3.15 General Diagram of LDV System

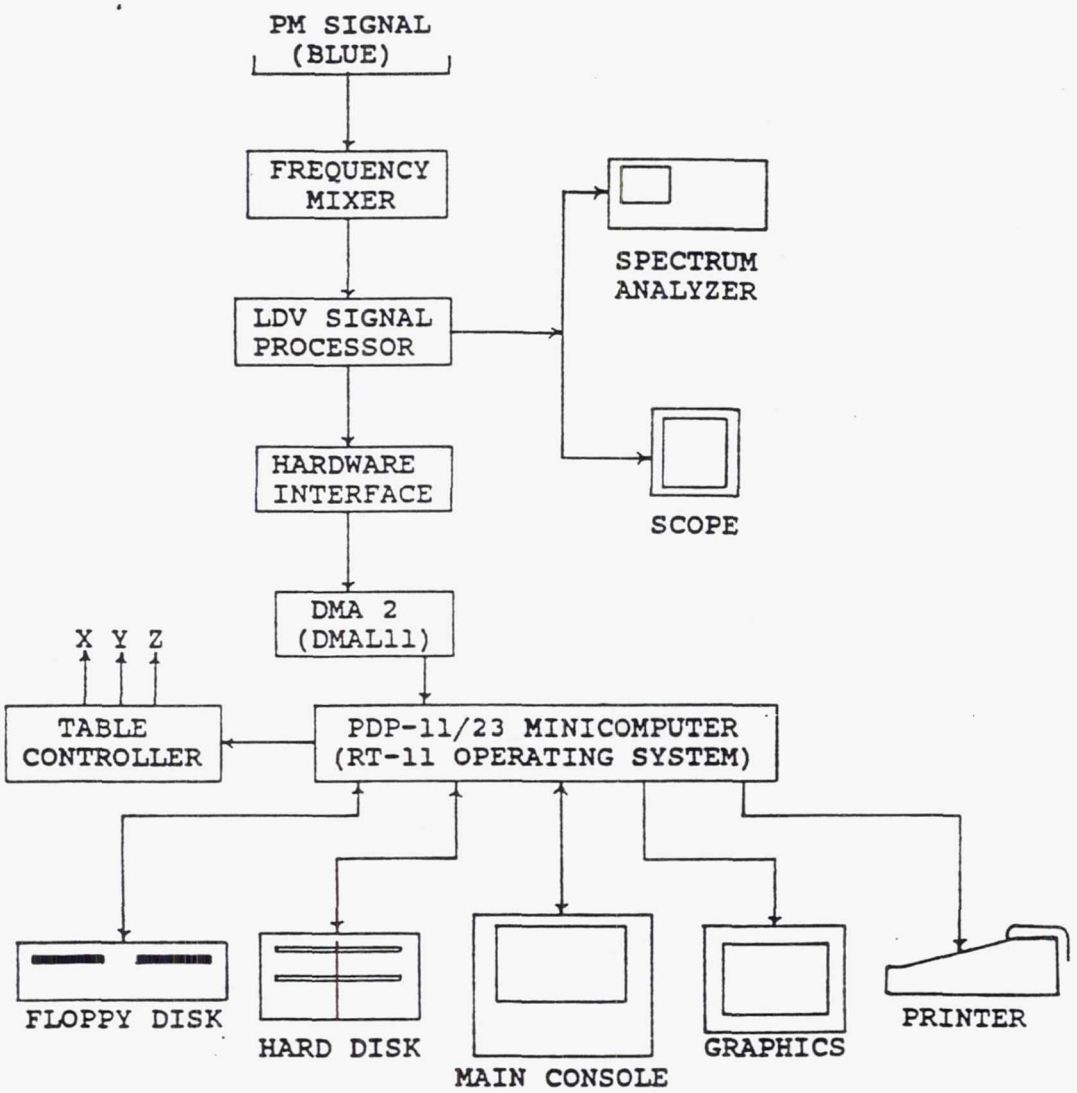

Figure 3.16 LDV Data Acquisition System

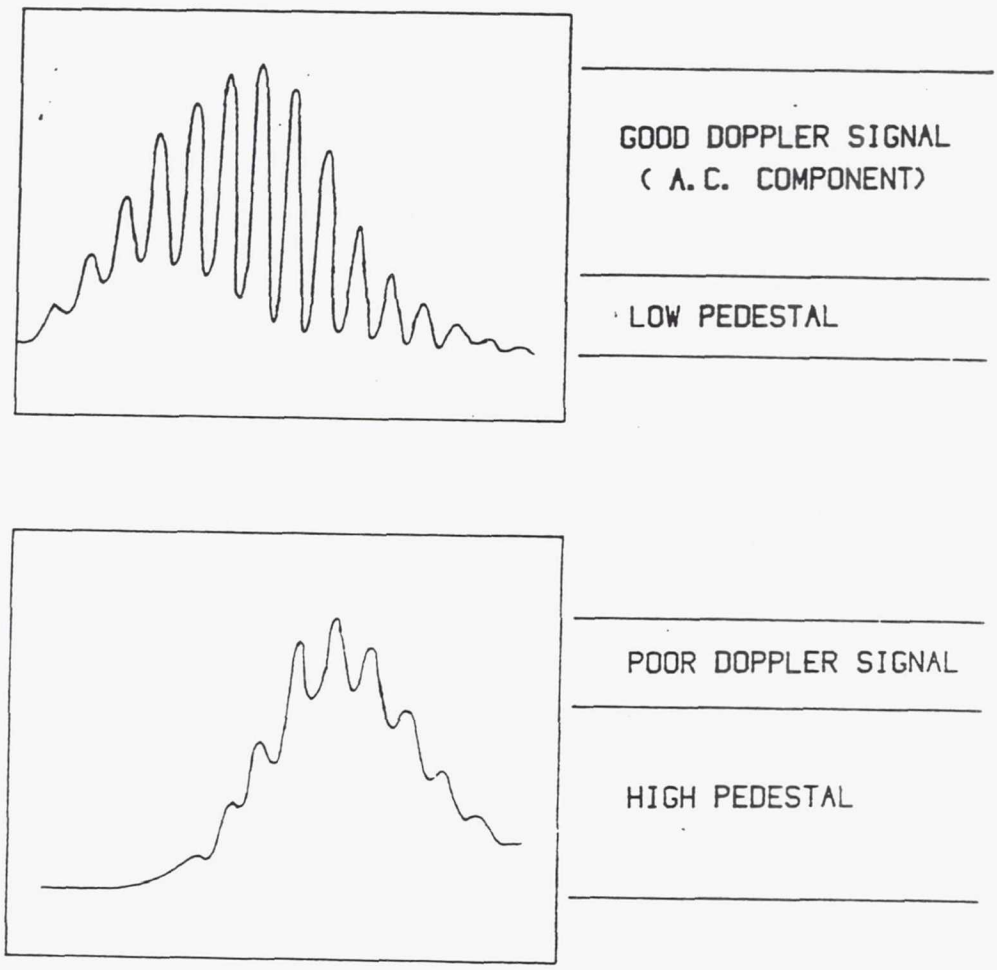

Figure 3.17 Pedestal of Frequency Burst

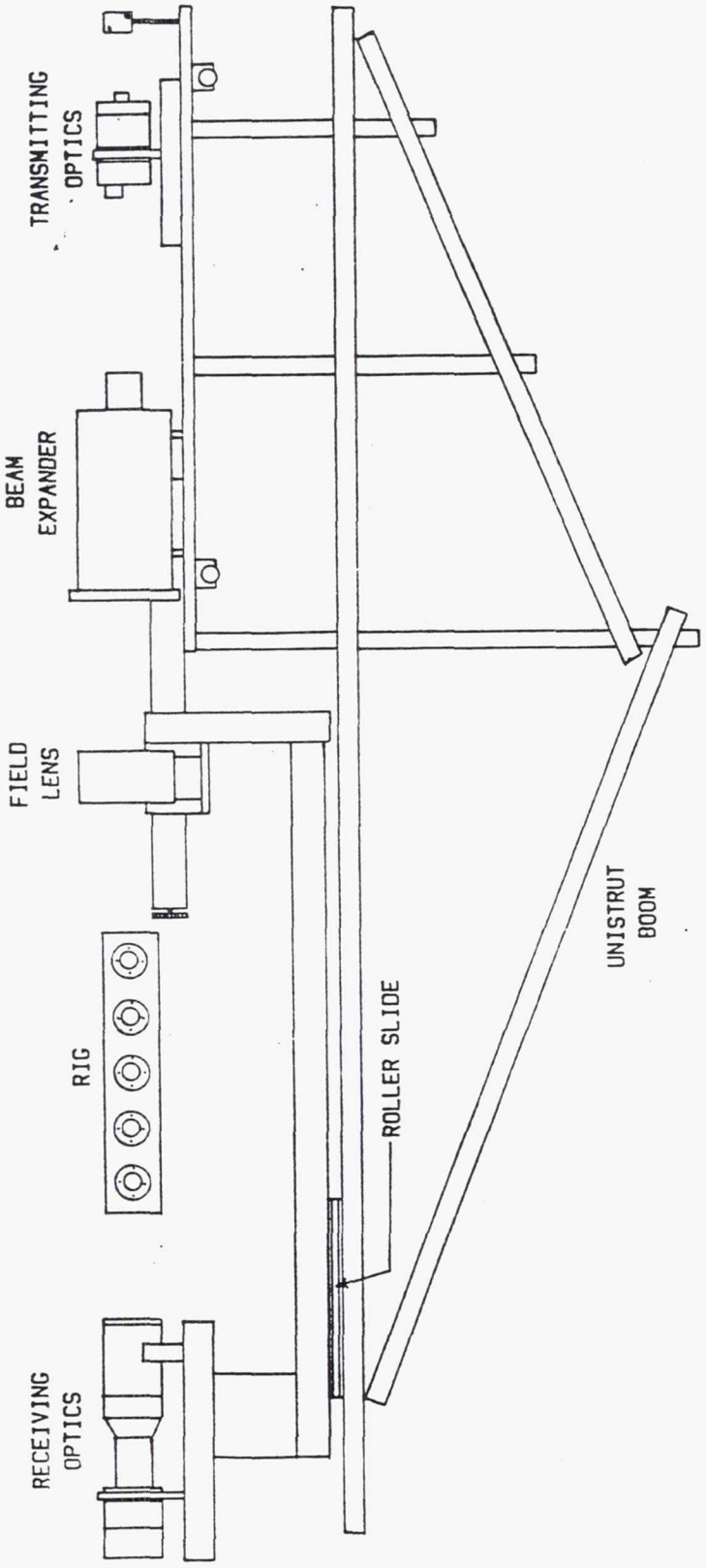

Figure 3.18 Laser Table and Boom Assembly

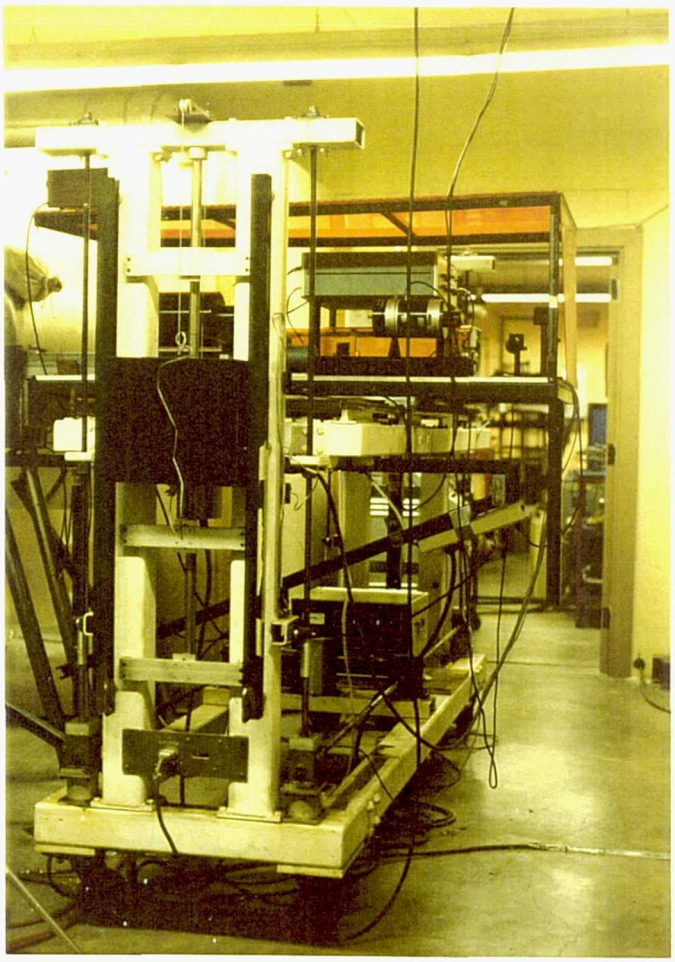

Figure 3.19 Laser Table Support Structure

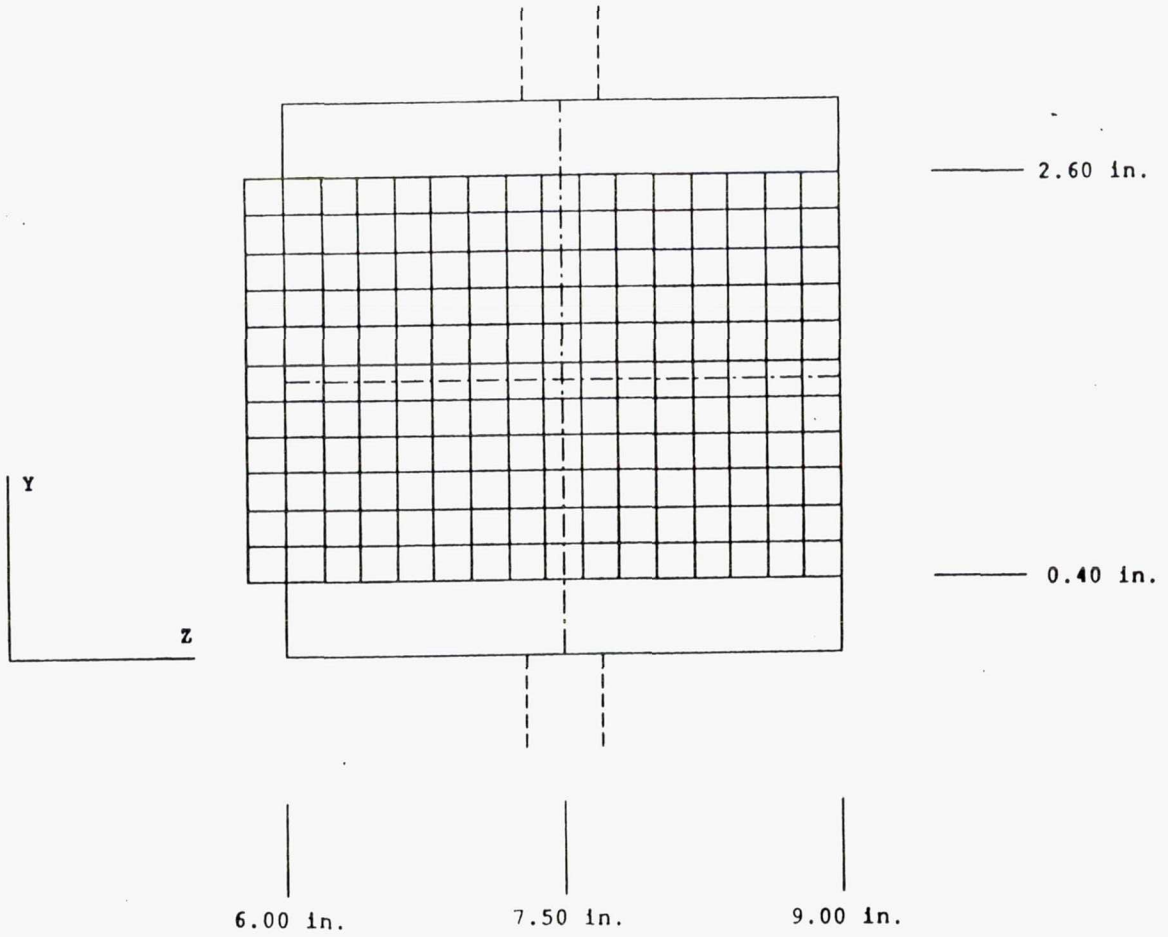

Figure 3.20 YZ-Plane Measurement Grid

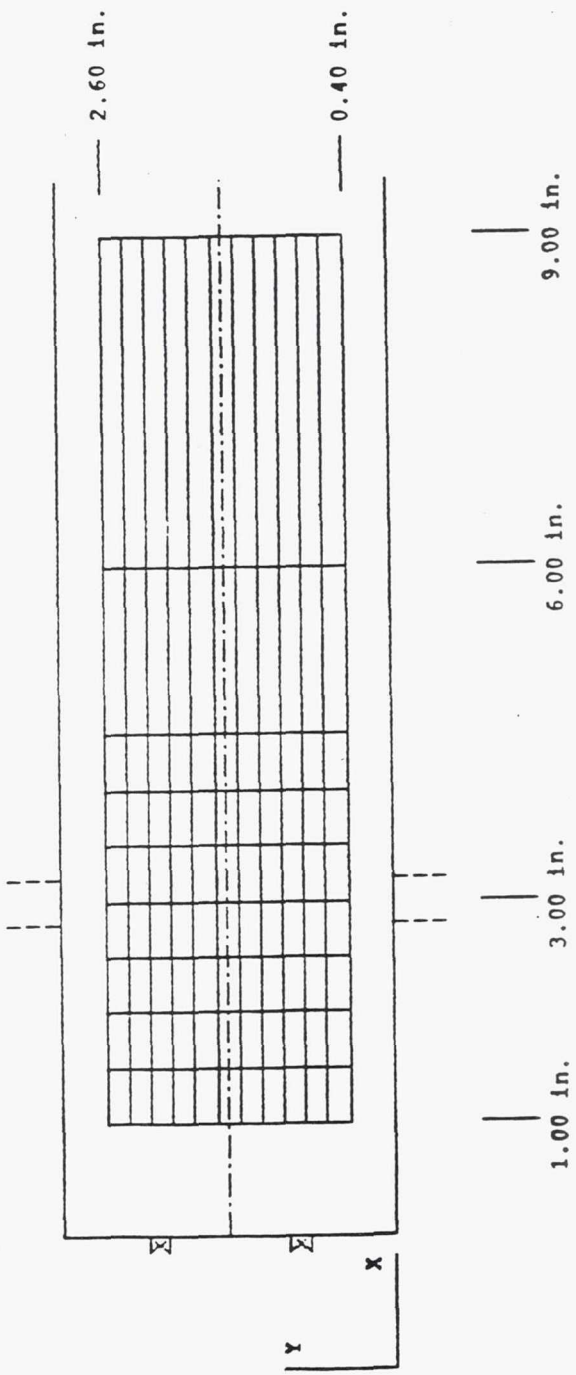

Figure 3.21 XY-Plane Measurement Grid

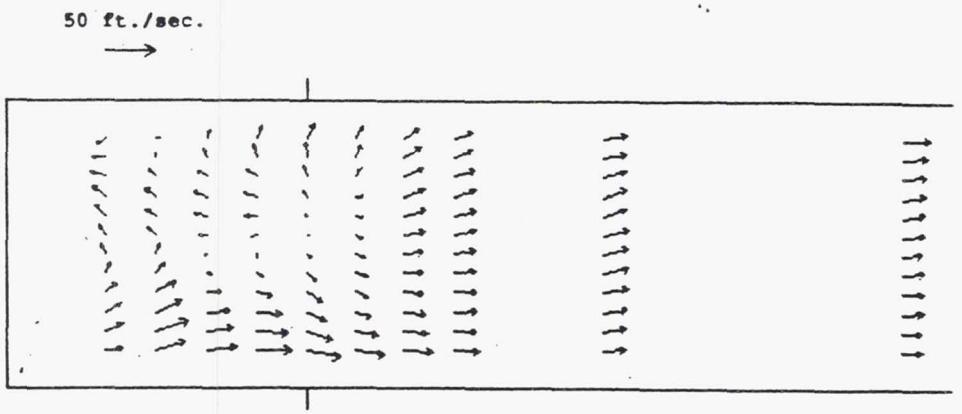

(a)

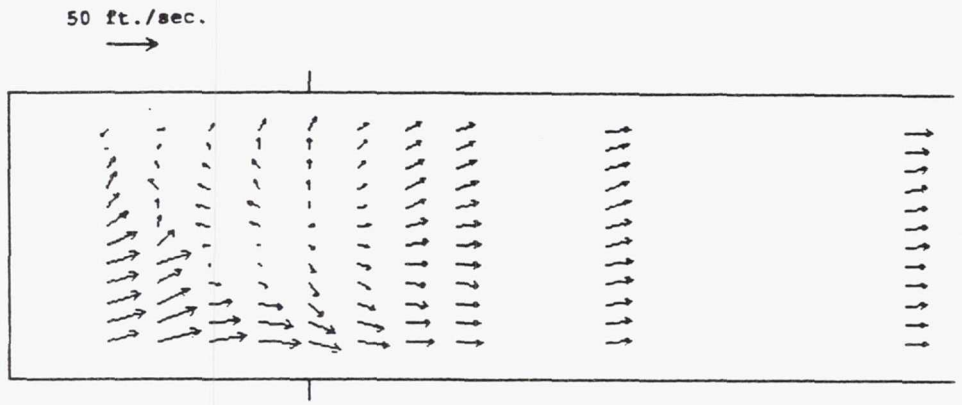

(b)

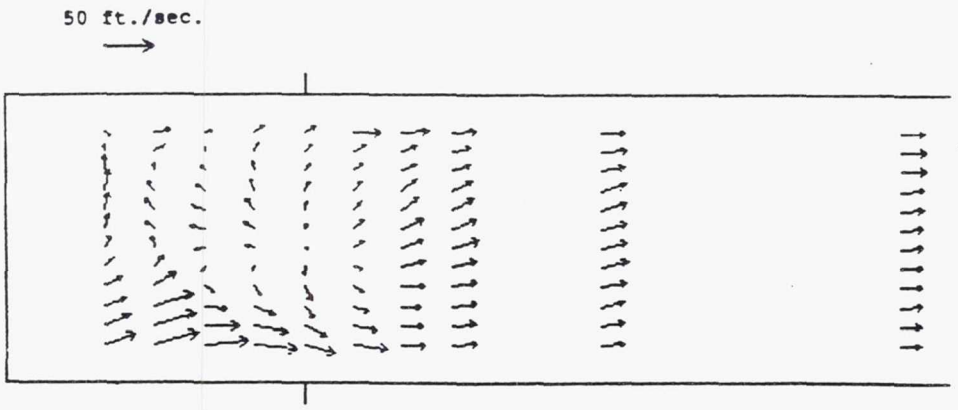

(c)

Figure 3.22 XY-Plane Mean Velocity Vector Plots: (a) Z=5.80 in.; (b) Z=6.00 in.; (c) Z=6.20 in.

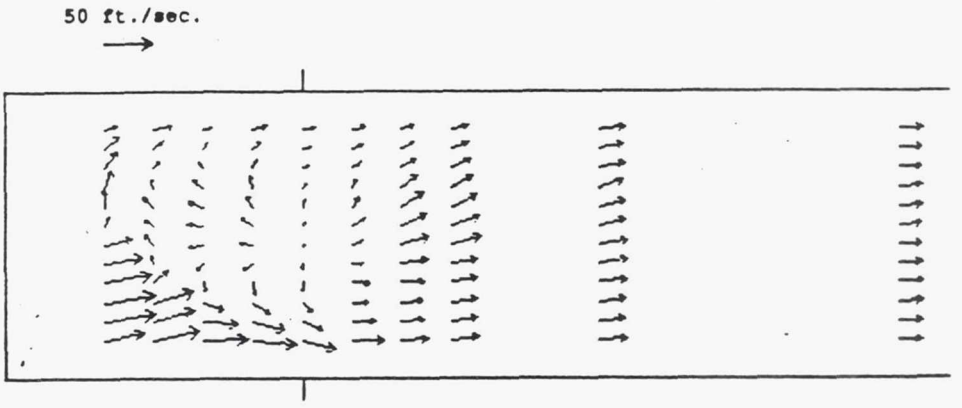

(a)

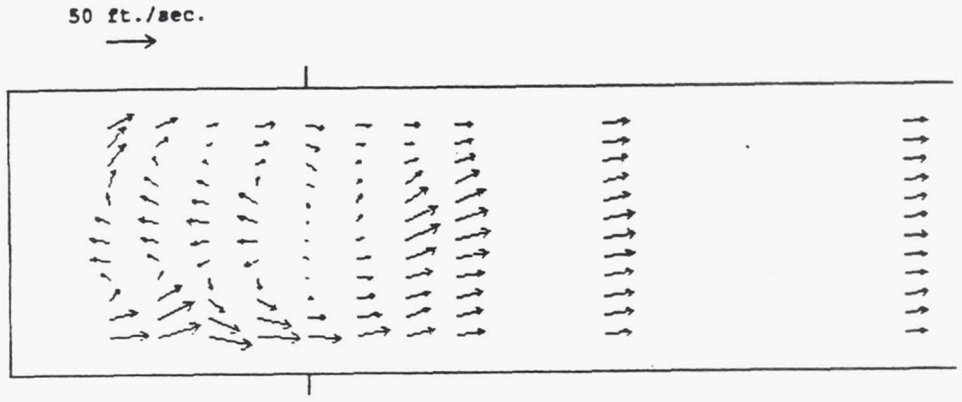

(b)

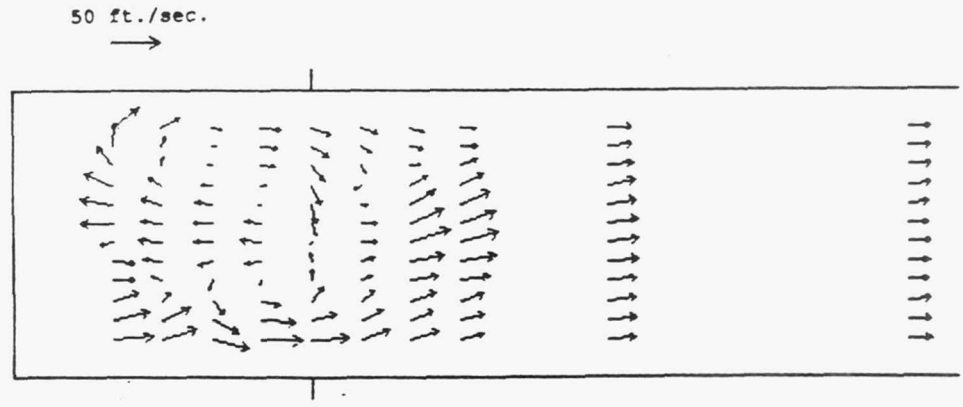

(c)

Figure 3.23 XY-Plane Mean Velocity Vector Plots: (a) Z=6.40 in.; (b) Z=6.60 in.; (c) Z=6.80 in.

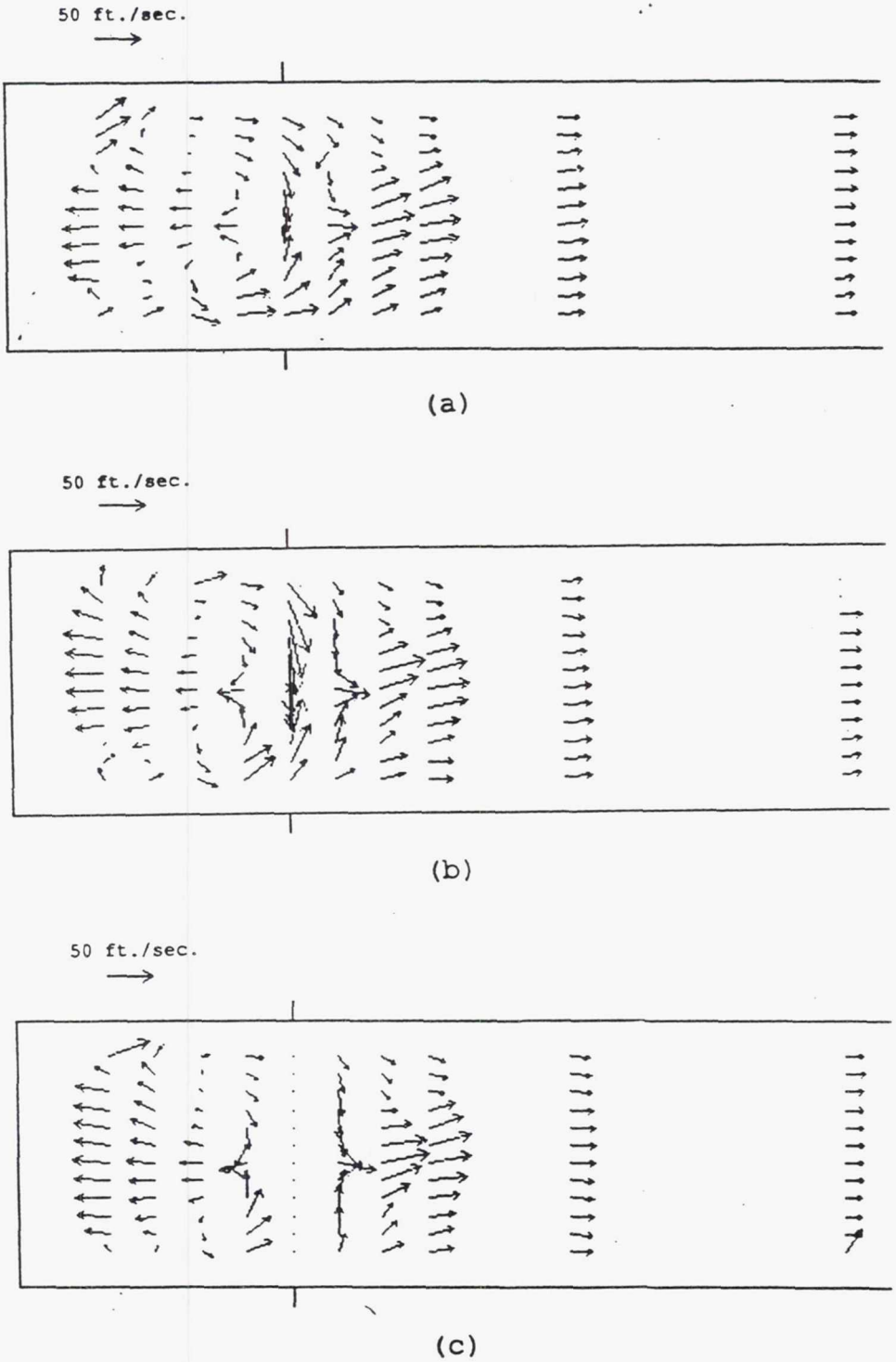

Figure 3.24 XY-Plane Mean Velocity Vector Plots: (a) Z=7.00 in.; (b) Z=7.20 in.; (c) Z=7.40 in.

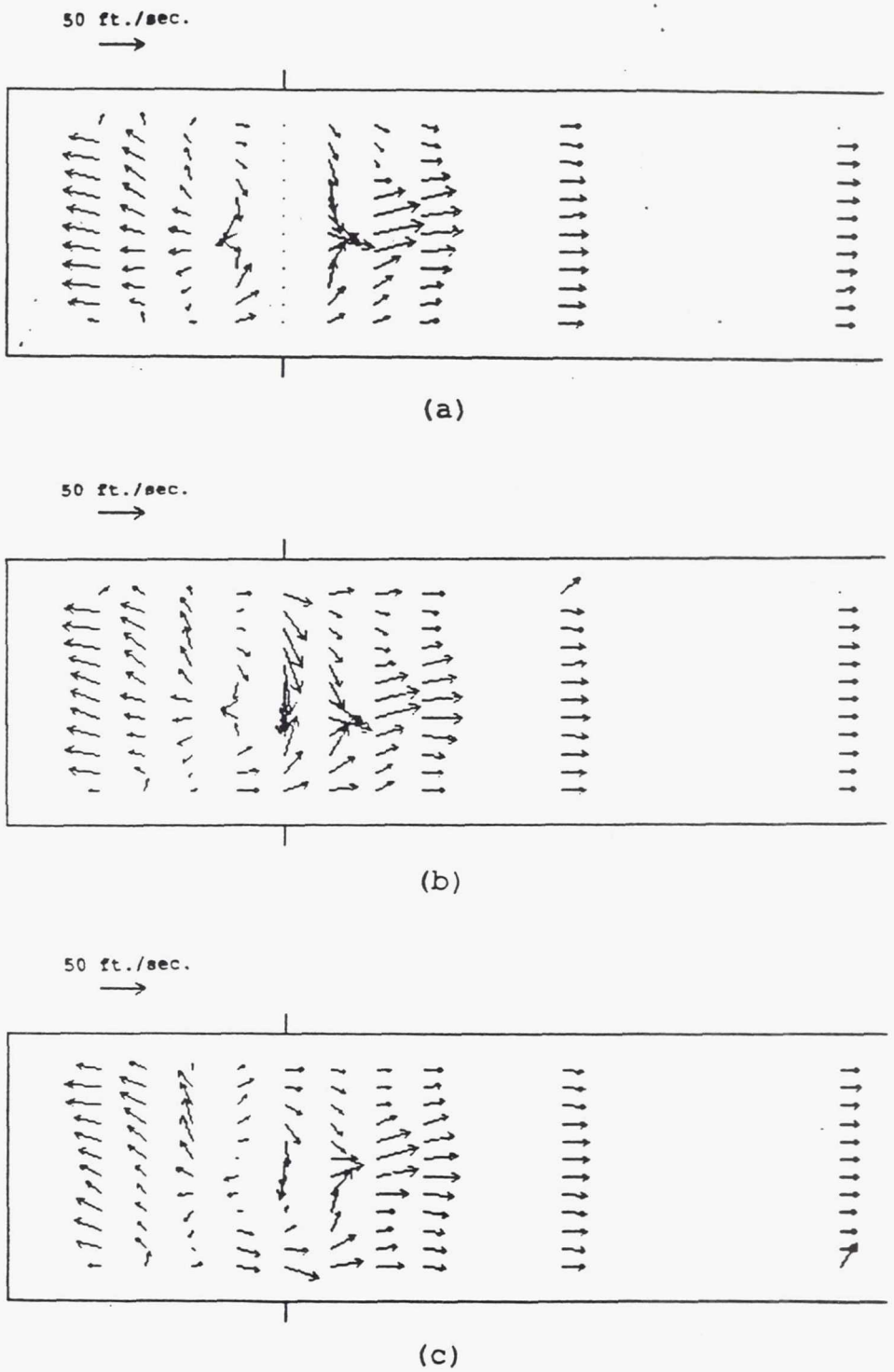

Figure 3.25 XY-Plane Mean Velocity Vector Plots: (a) Z=7.60 in.; (b) Z=7.80 in.; (c) Z=8.00 in.

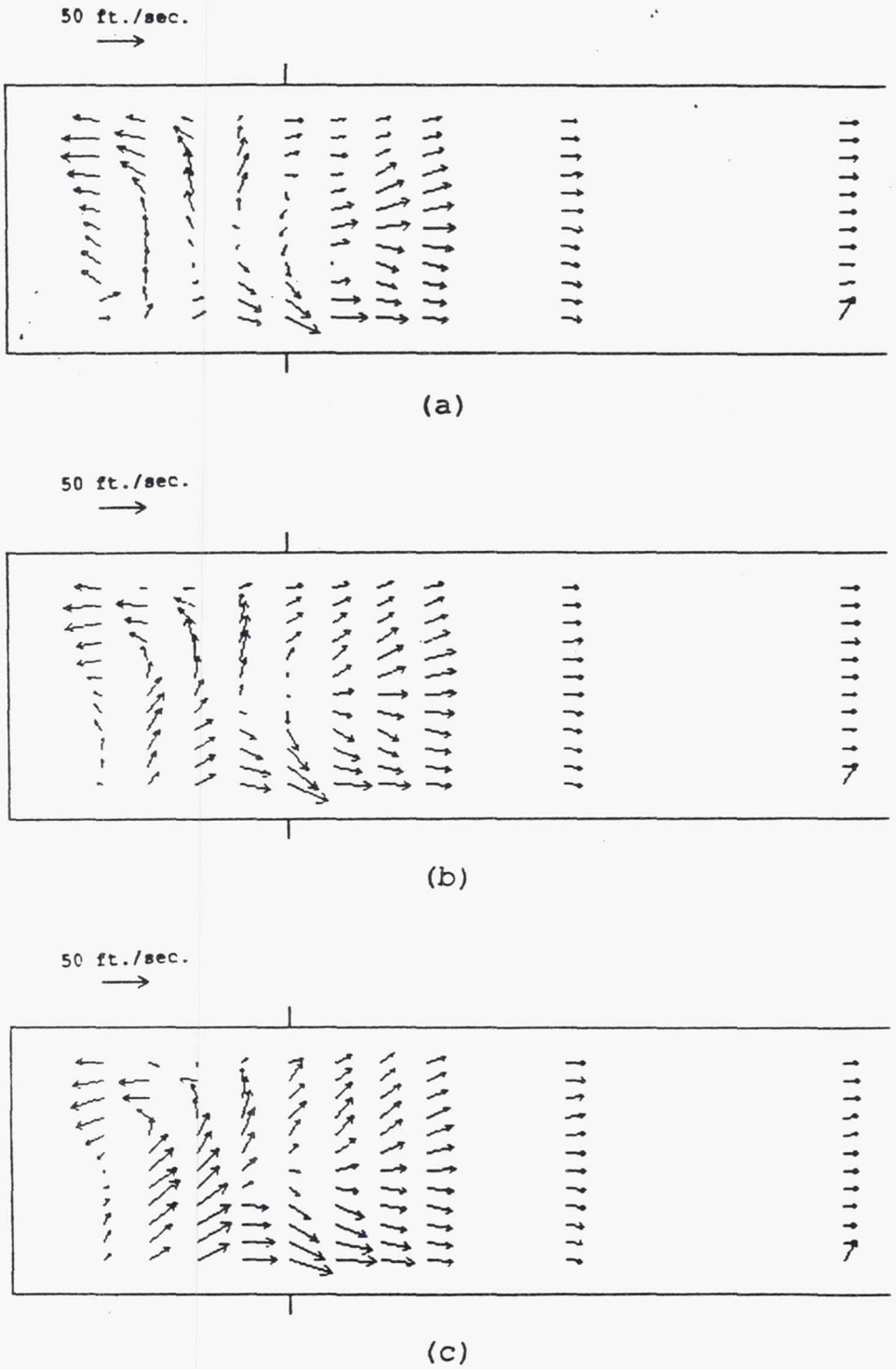

Figure 3.26 XY-Plane Mean Velocity Vector Plots:
(a) Z=8.20 in.; (b) Z=8.40 in.;
(c) Z=8.60 in.

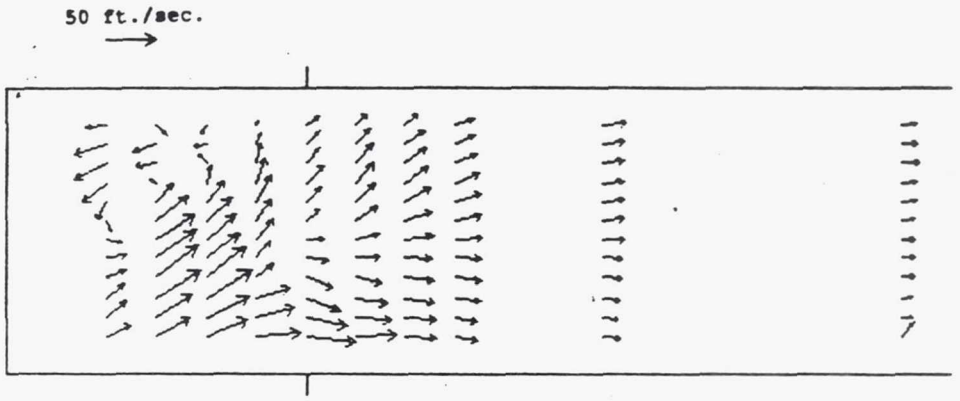

(a)

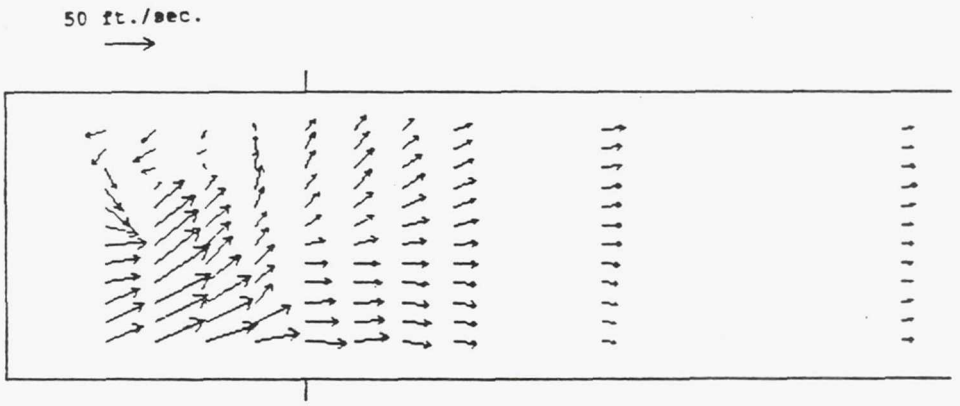

(b)

Figure 3.27 XY-Plane Mean Velocity Vector Plots; (a) Z=8.80 in.; (b) Z=9.00 in.

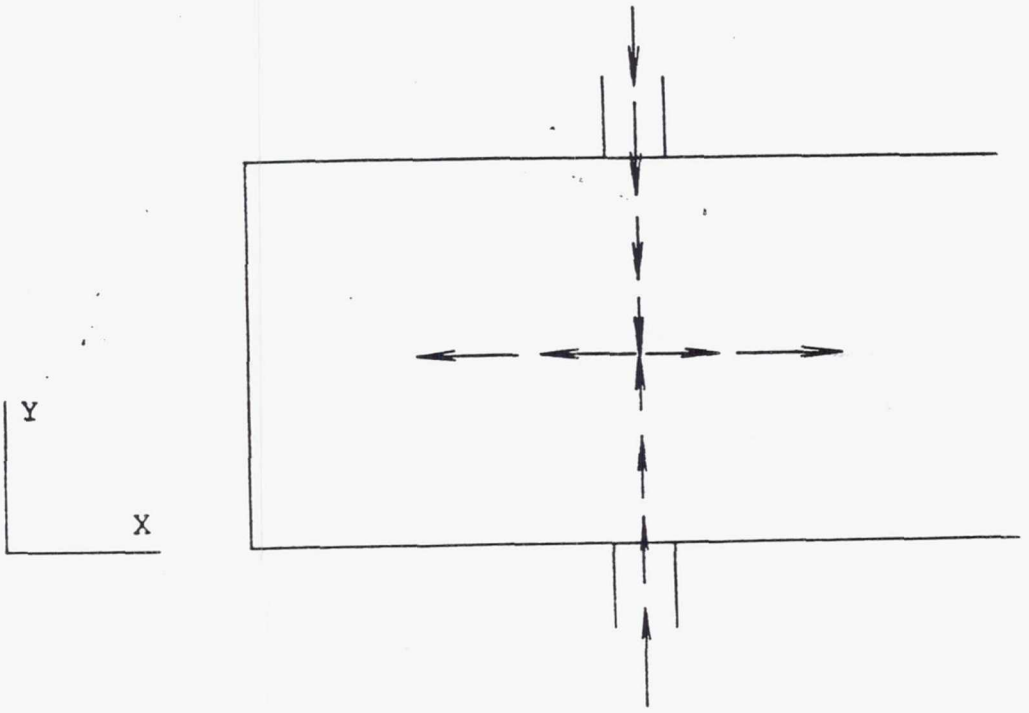

(a)

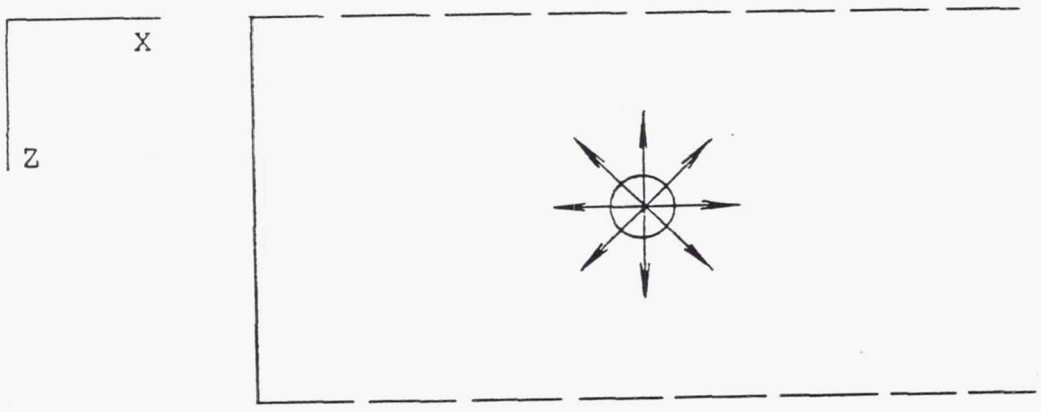

(b)

Figure 3.28 Radial Jet Flow Pattern: (a) XY-Plane View; (b) YZ-Plane View

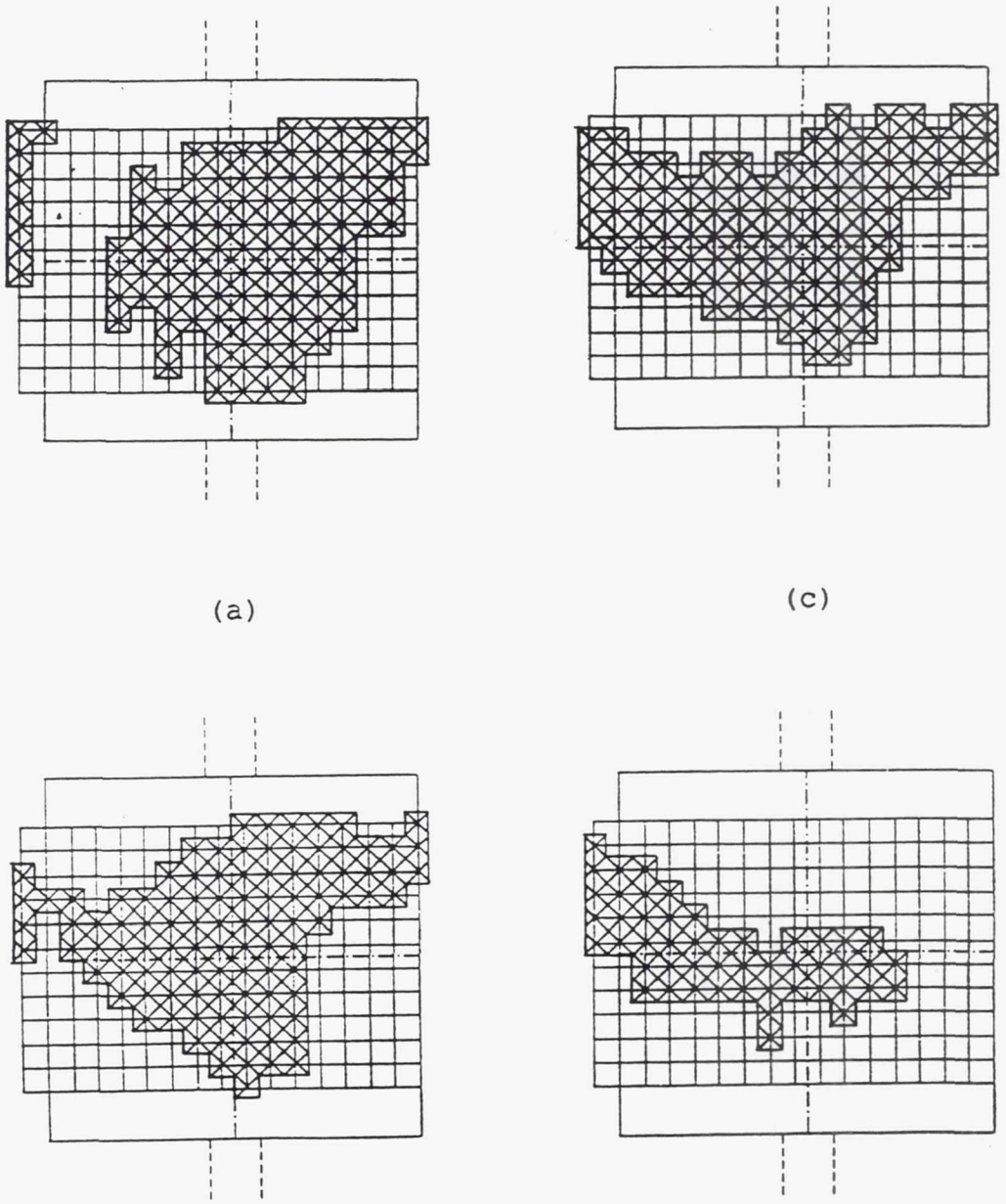

Figure 3.29 Recirculation Zone Cross-Sections: (a) X=1.00 in.; (b) X=1.50 in.; (c) X=2.00 in.; (d) X=2.50 in.

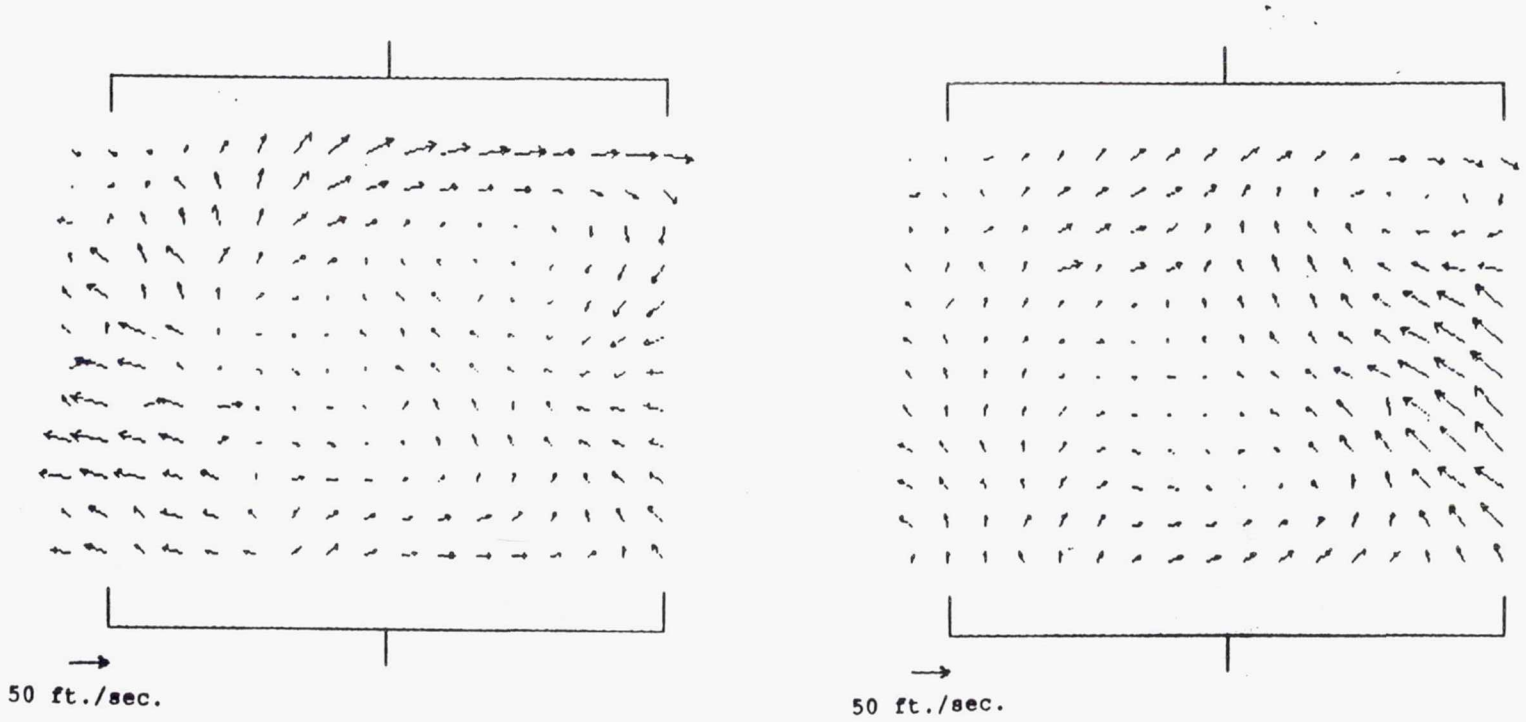

(a) (b)

Figure 3.30 YZ-Plane Mean Velocity Vector Plots:
(a) X=1.00 in.; (b) X=1.50 in.

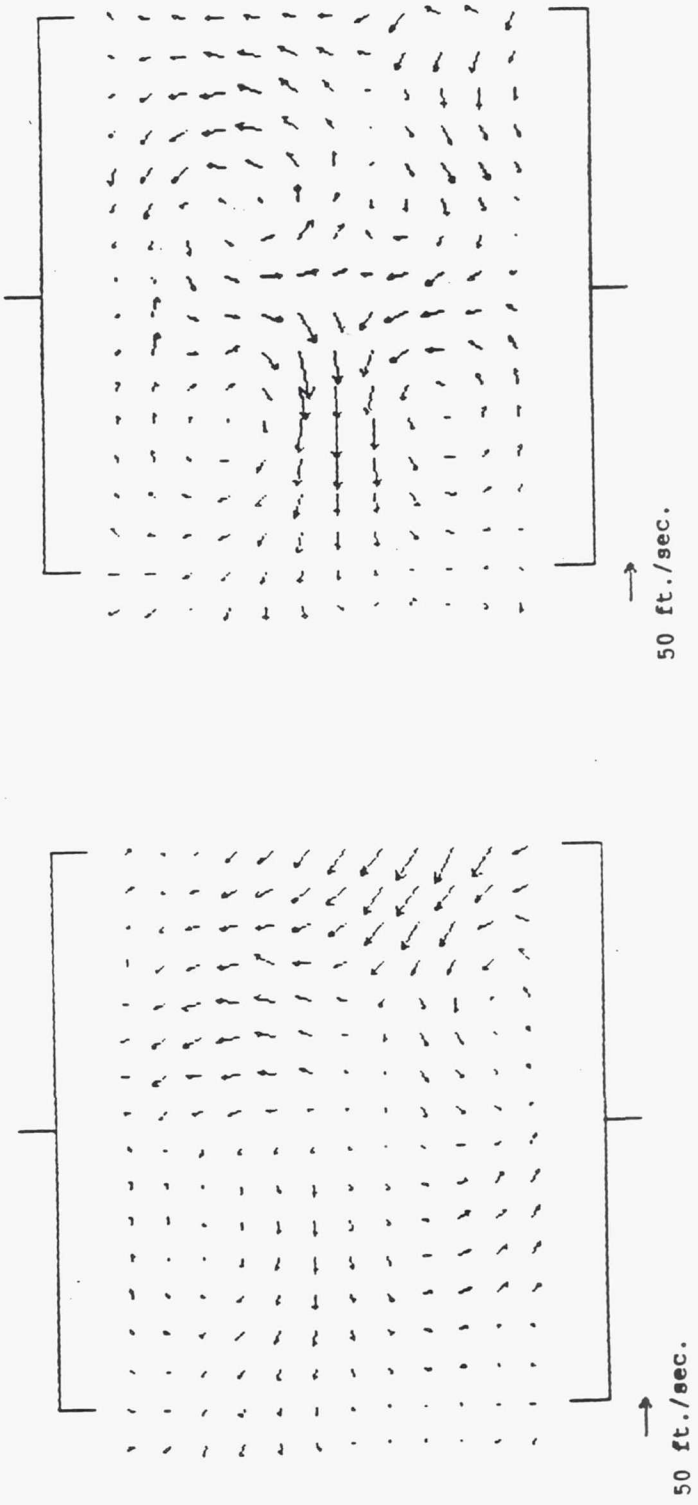

Figure 3.31 YZ-Plane Mean Velocity Vector Plots:
(a) X=2.00 in.; (b) X=2.50 in.

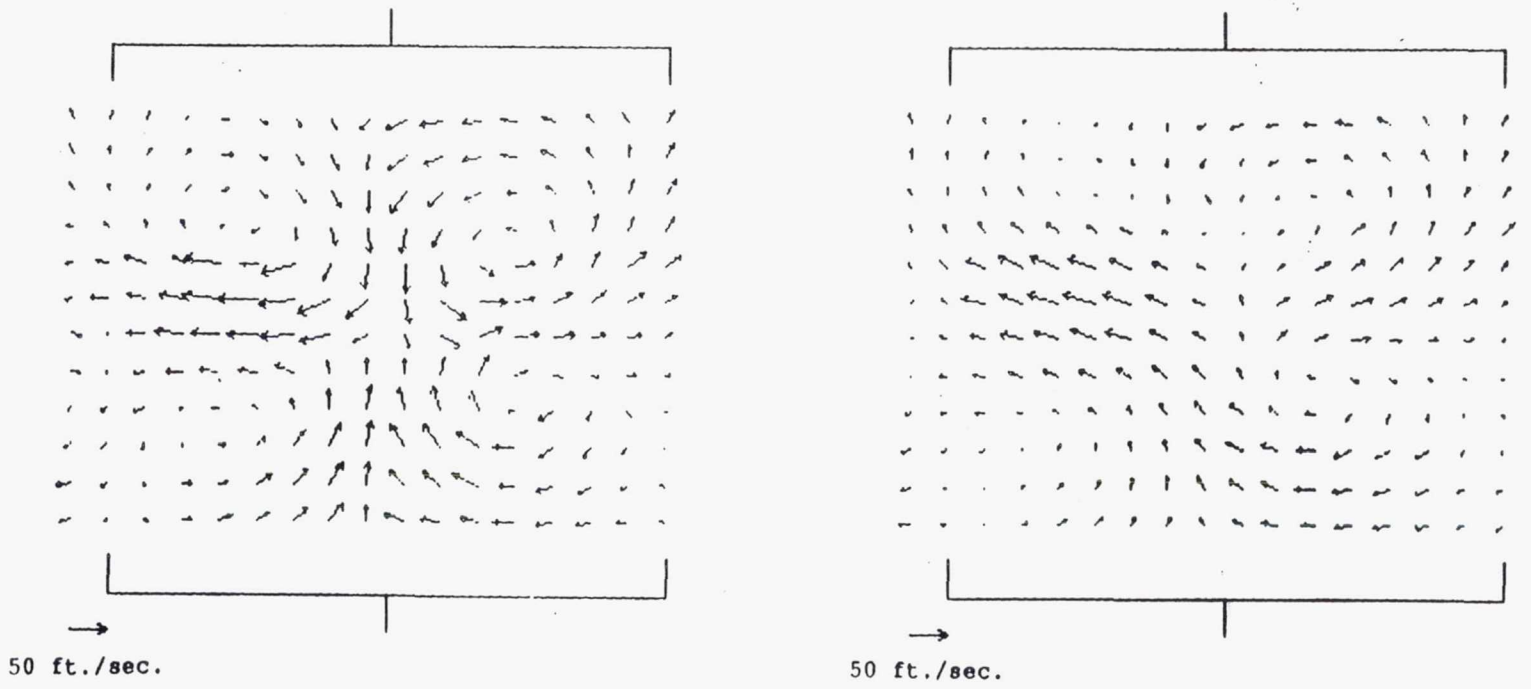

Figure 3.32 YZ-Plane Mean Velocity Vector Plots:
(a) X=3.50 in.; (b) X=4.00 in.

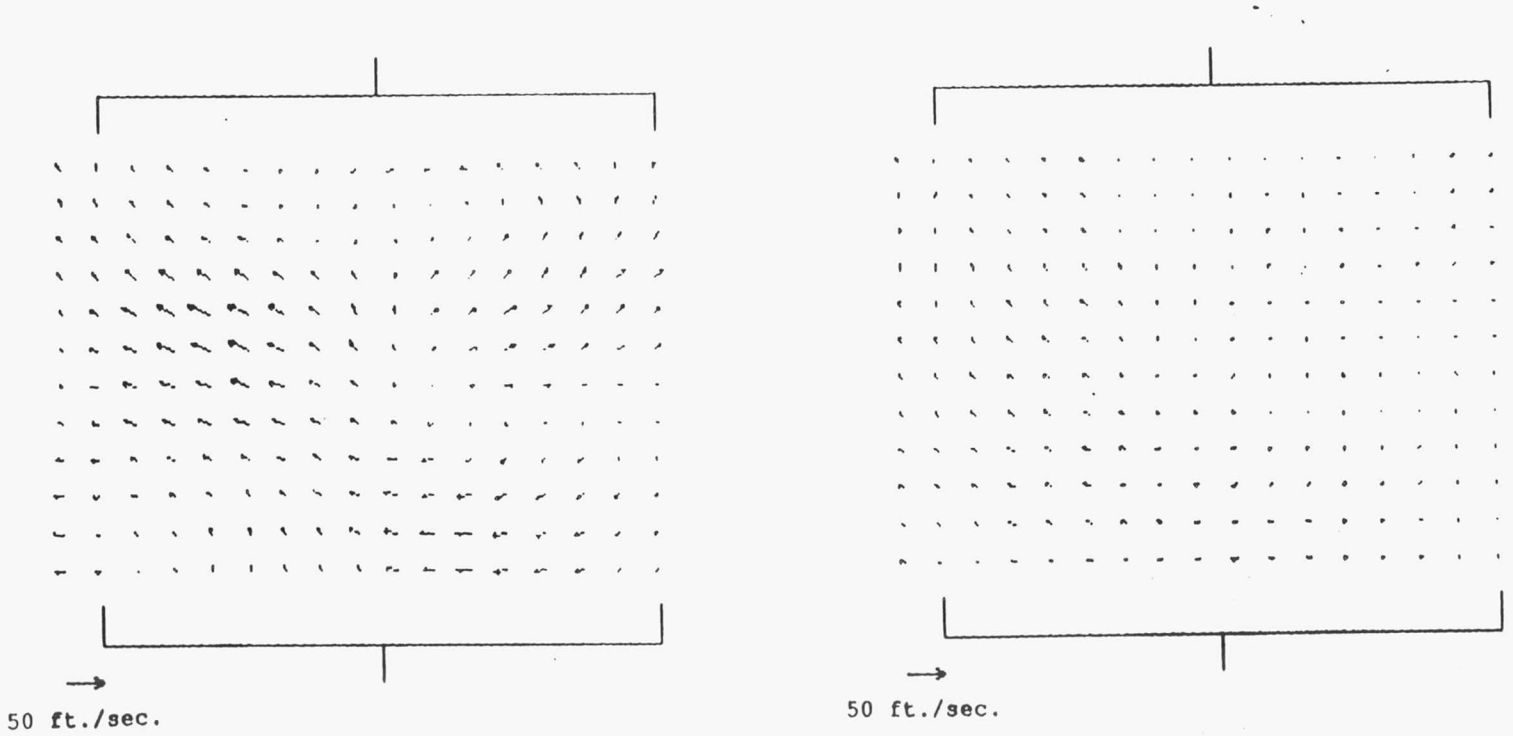

Figure 3.33 YZ-Plane Mean Velocity Vector Plots:
(a) X=4.50 in.; (b) X=6.00 in.

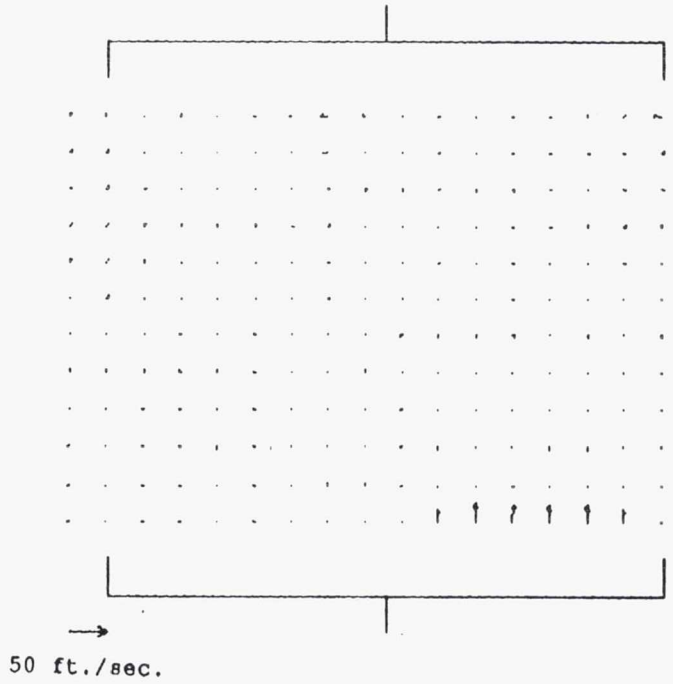

Figure 3.34 YZ-Plane Mean Velocity Vector Plot at X=9.00 in.

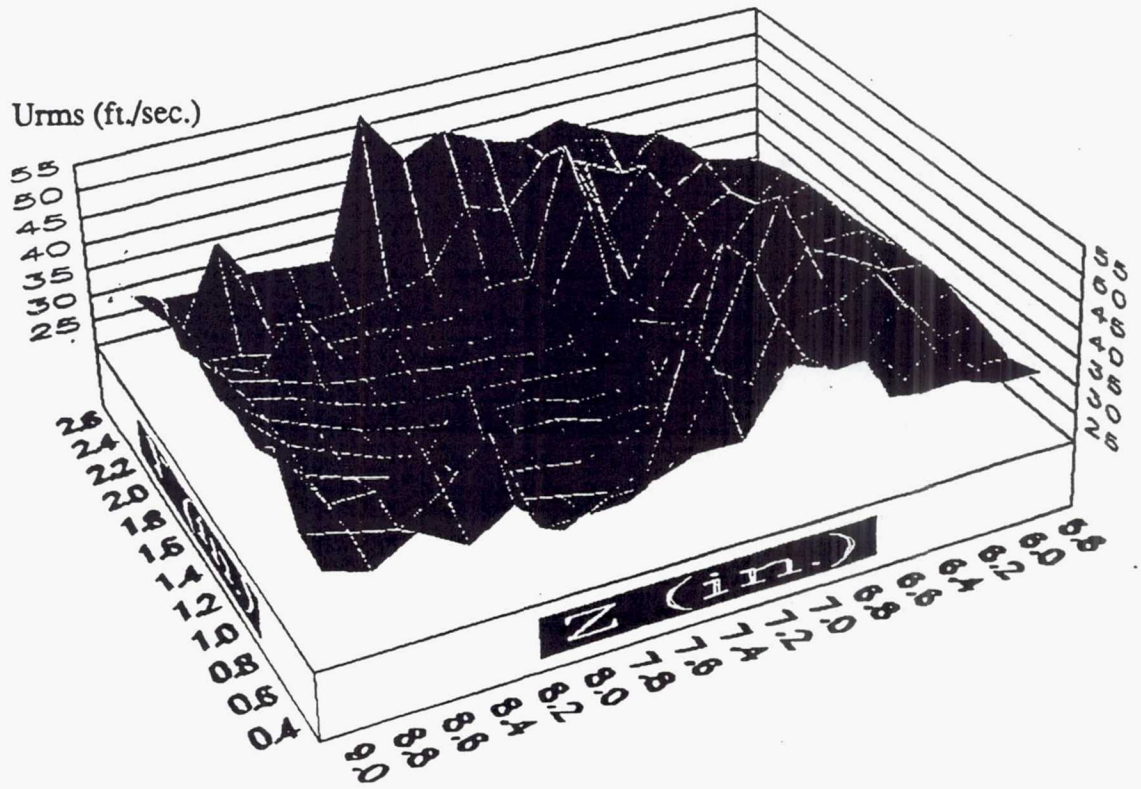

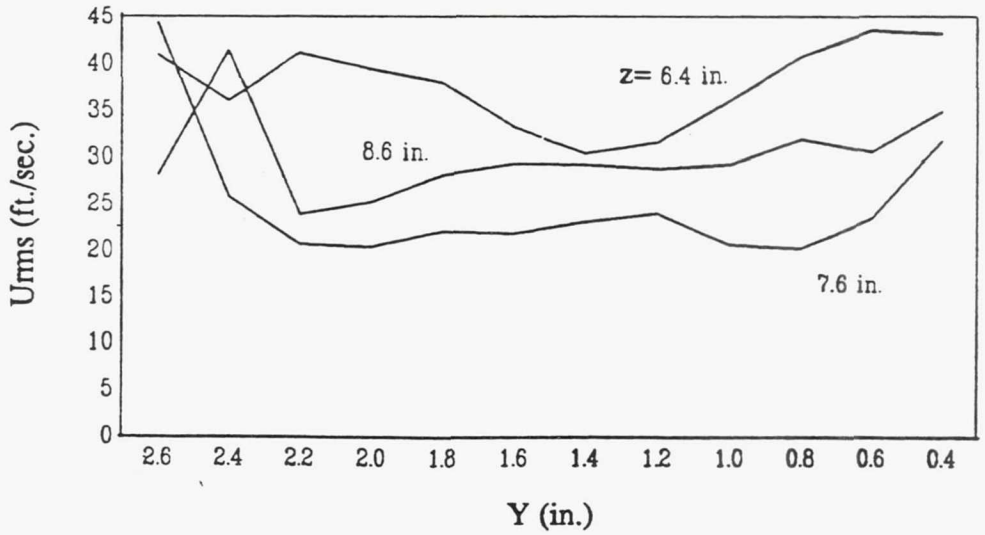

Figure 3.35 Contour and Line Plots of Urms at X=1.00 in.

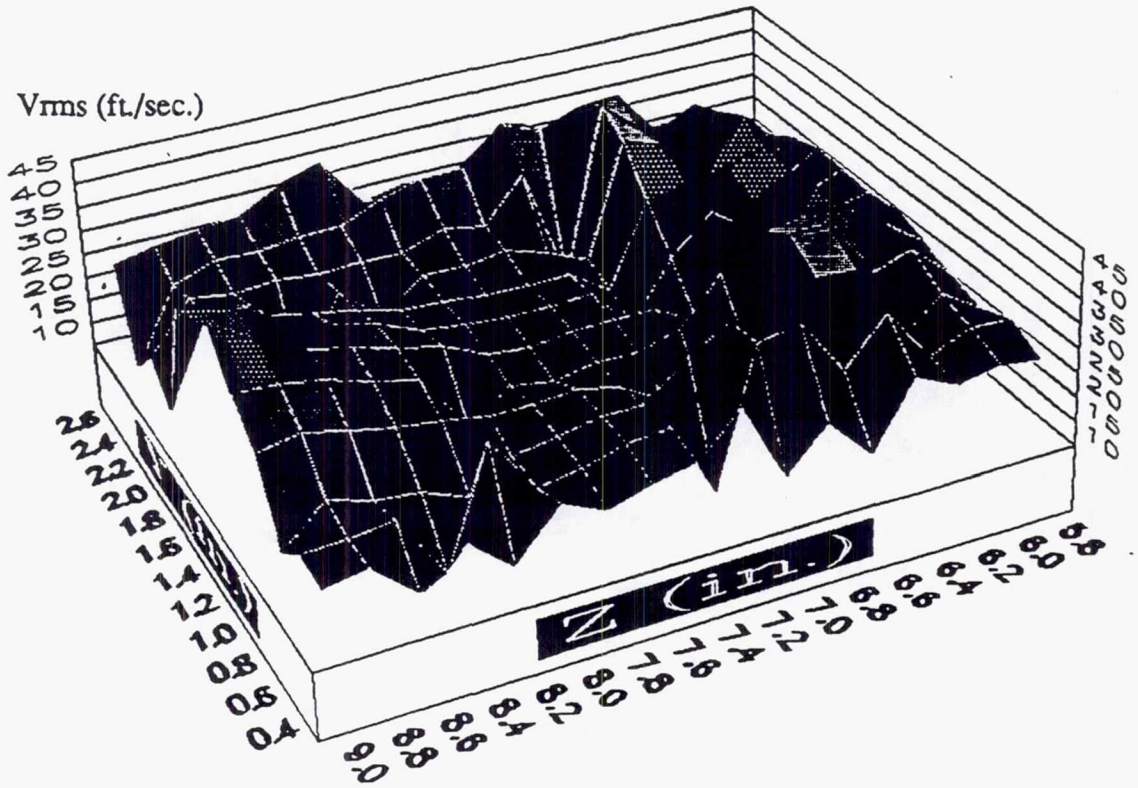

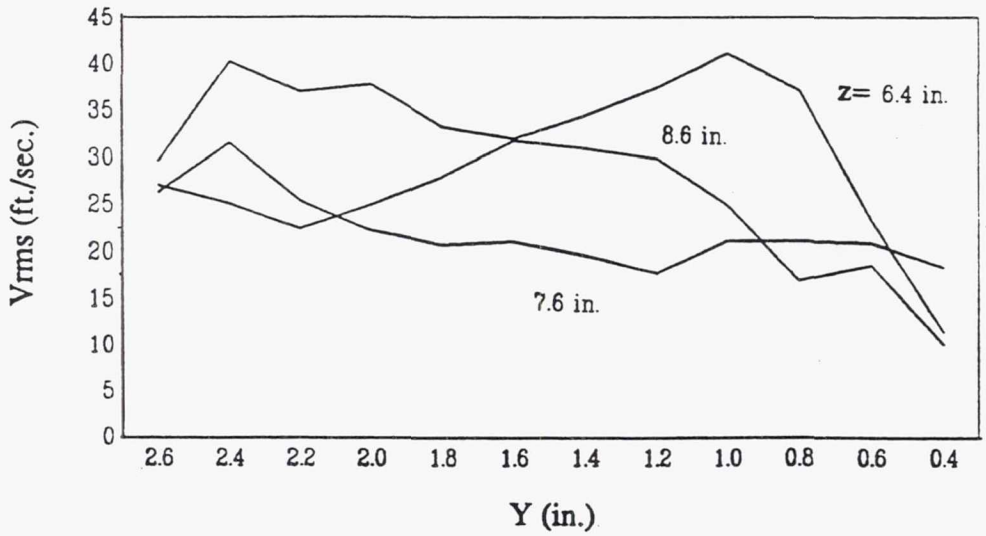

Figure 3.36 Contour and Line Plots of Vrms at X=1.00 in.

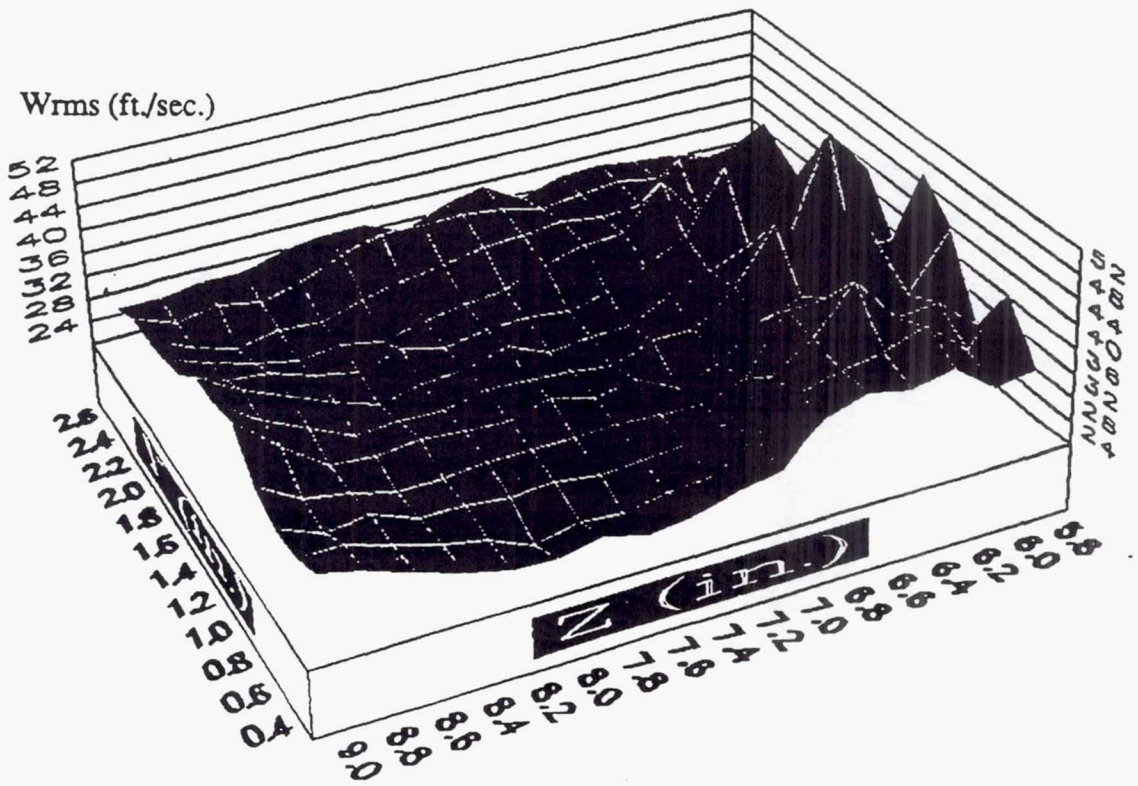

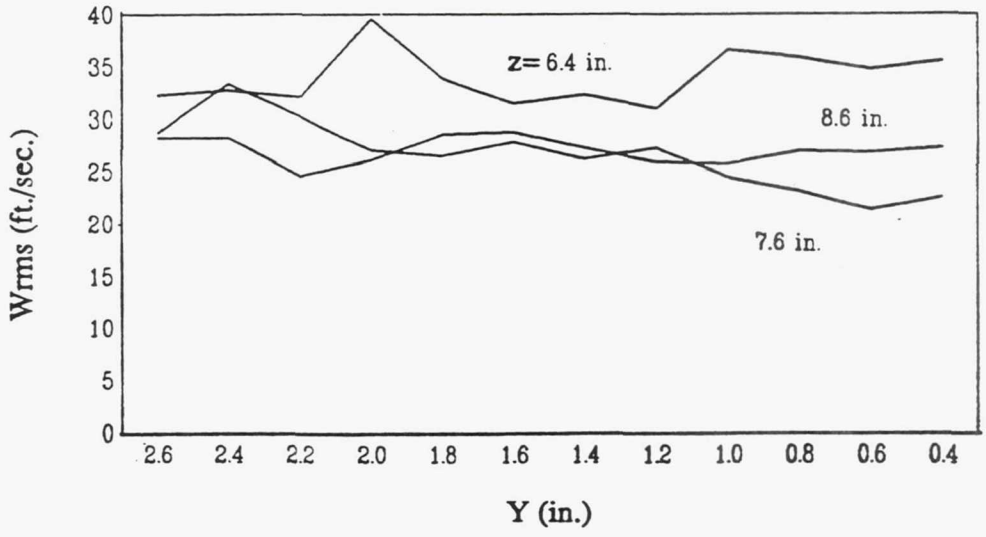

Figure 3.37 Contour and Line Plots of Wrms at X=1.00 in.

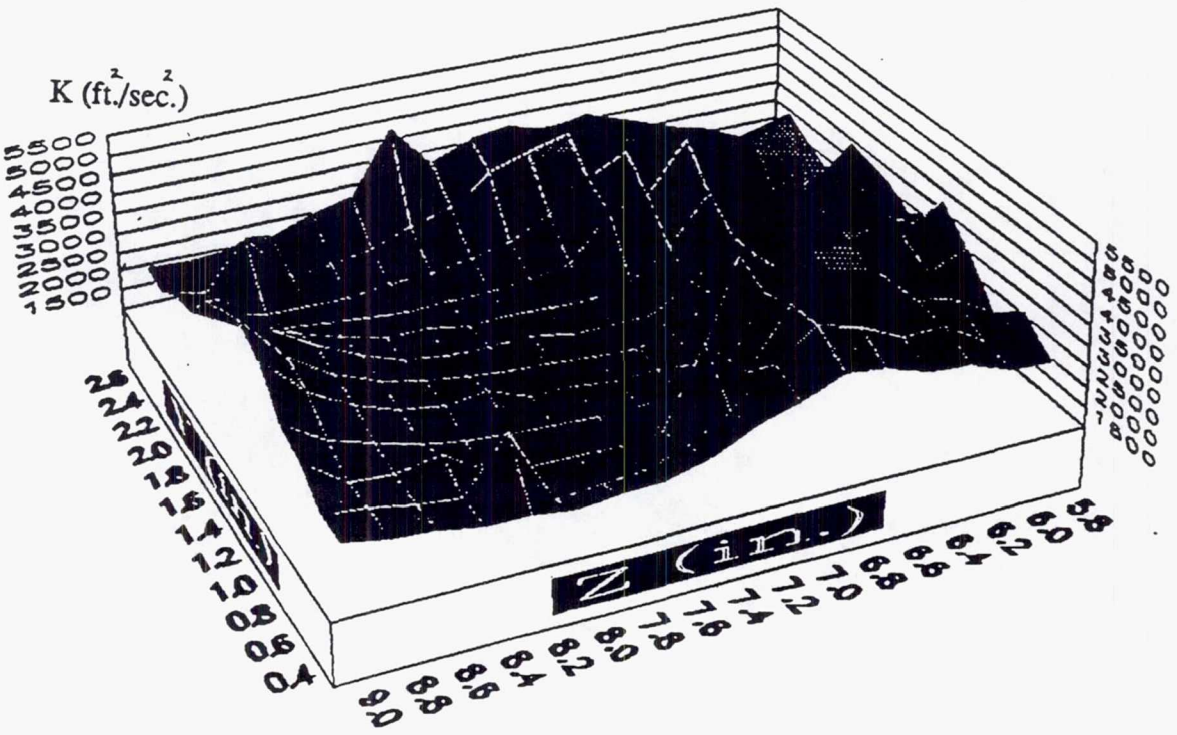

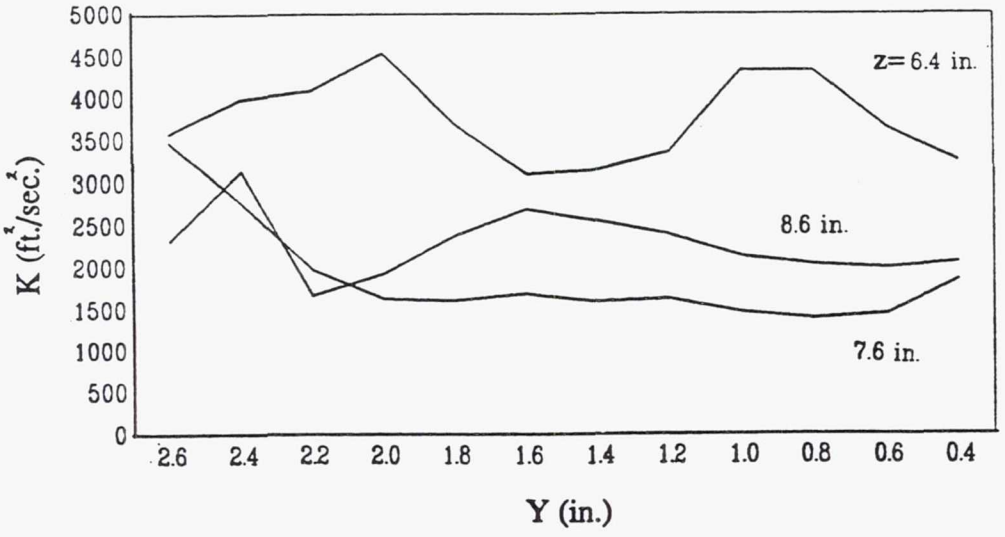

Figure 3.38 Contour and Line Plots of K at X=1.00 in.

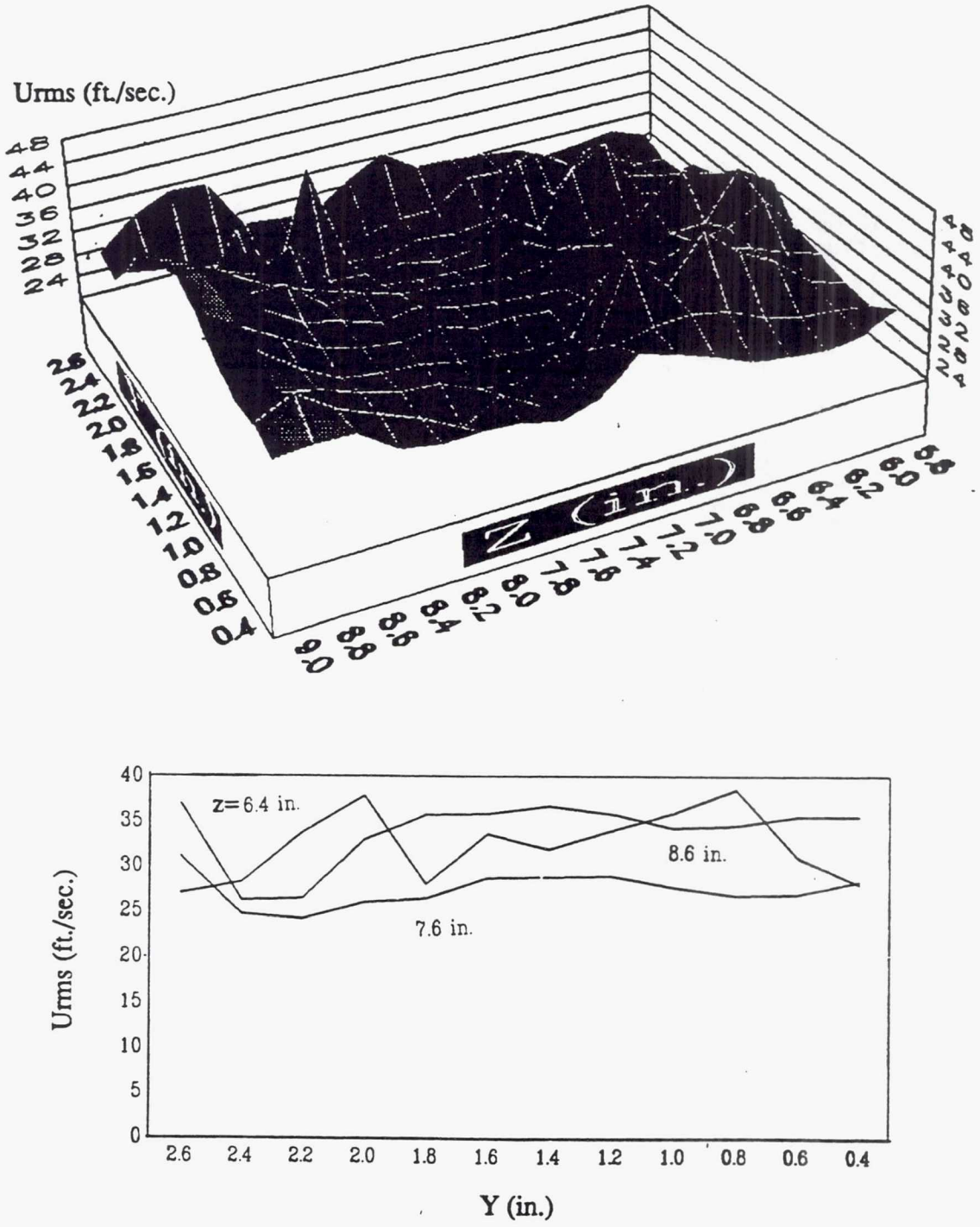

Figure 3.39 Contour and Line Plots of Urms at X=1.50 in.

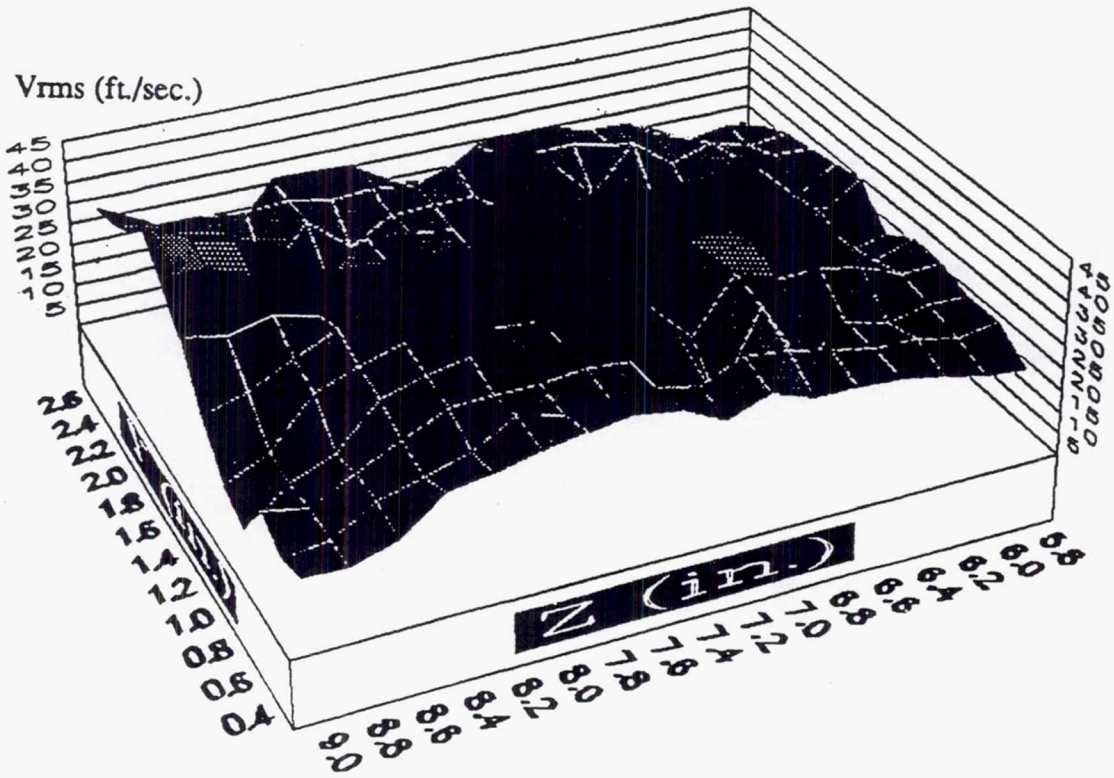

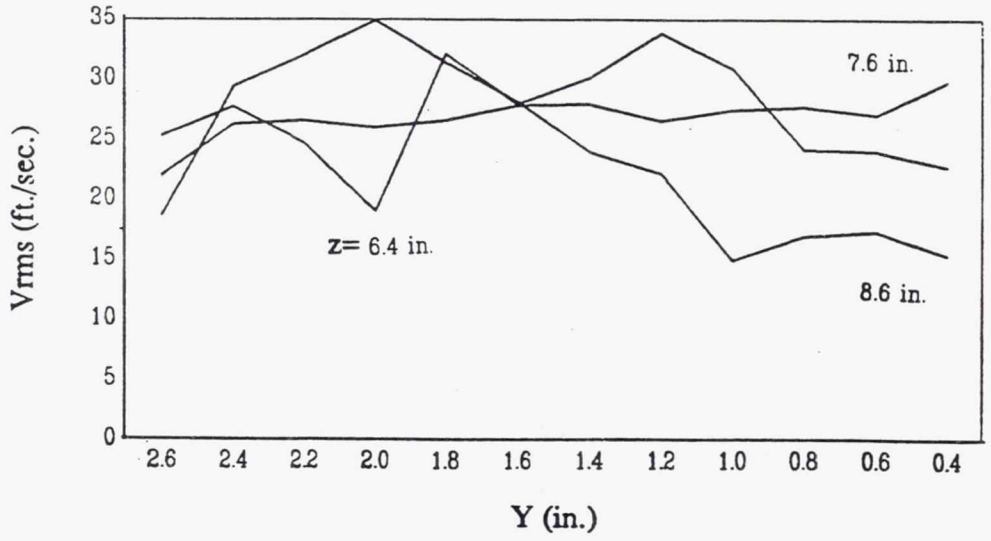

Figure 3.40 Contour and Line Plots of Vrms at X=1.50 in.

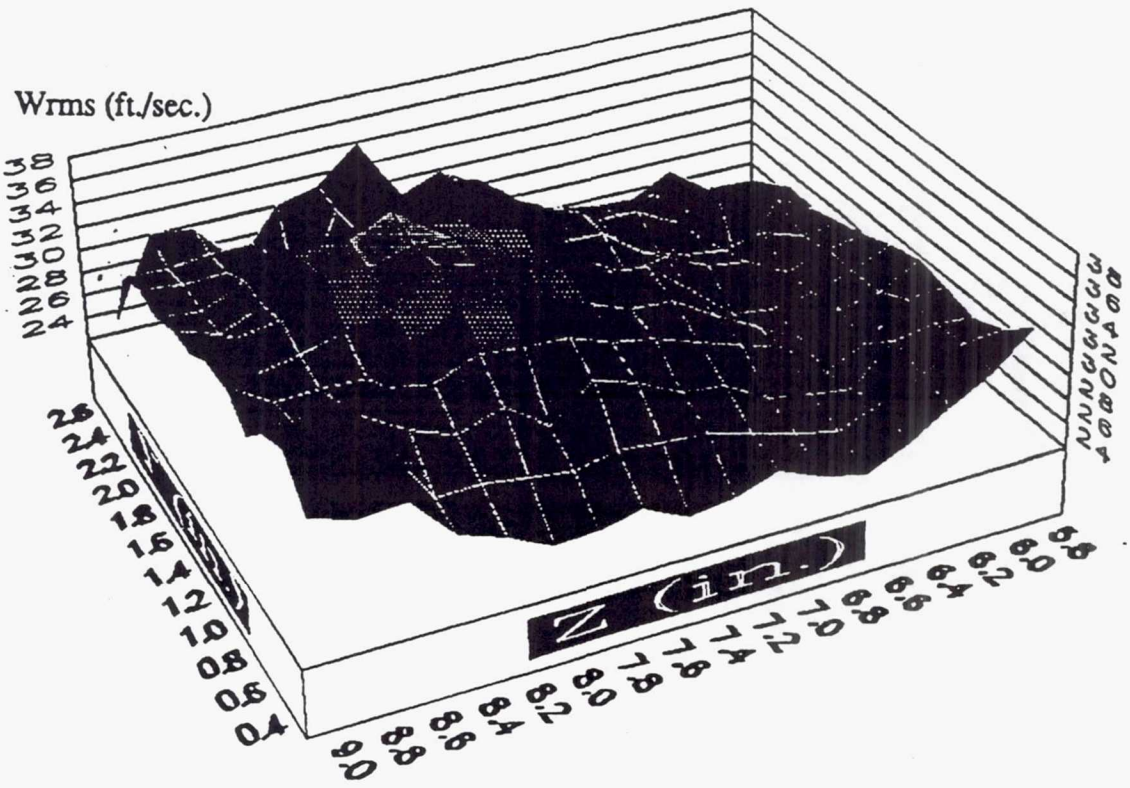

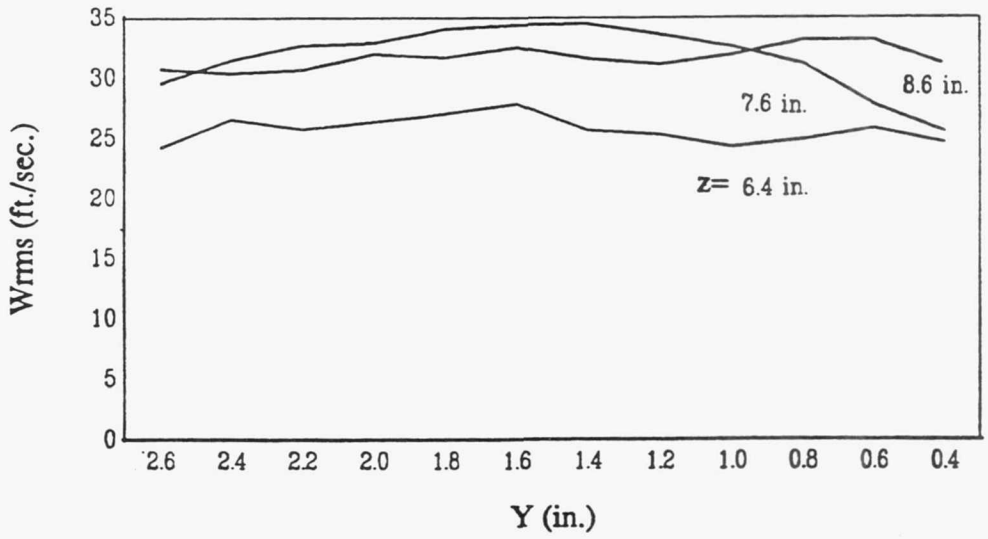

Figure 3.41 Contour and Line Plots of Wrms at X=1.50 in.

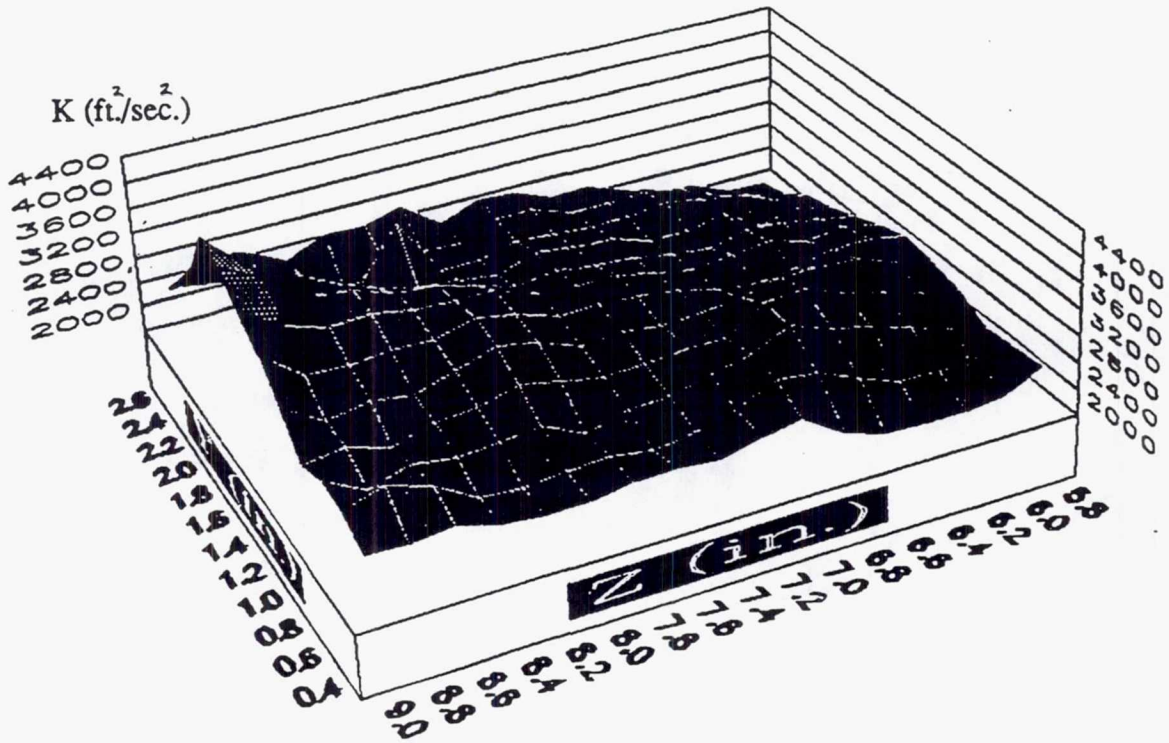

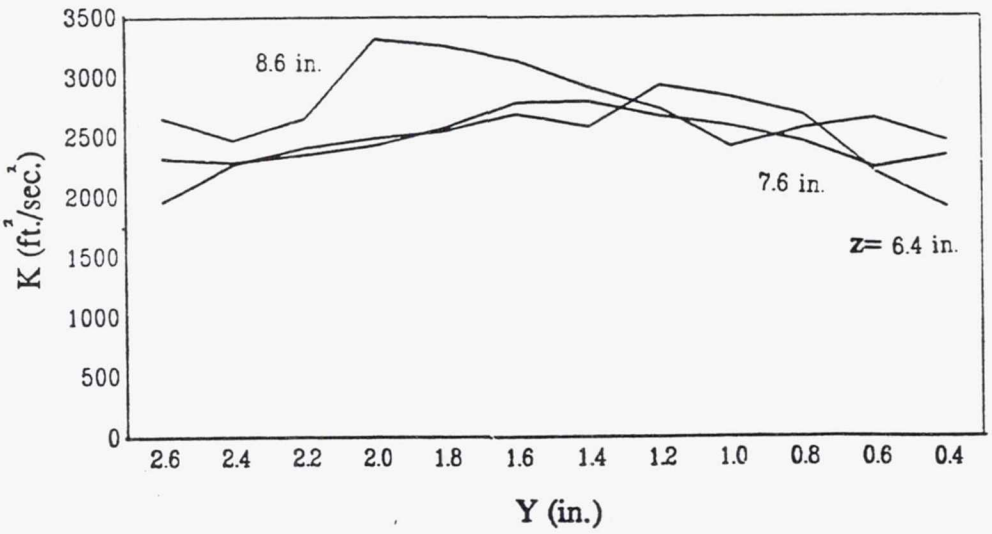

Figure 3.42 Contour and Line Plots of K at X=1.50 in.

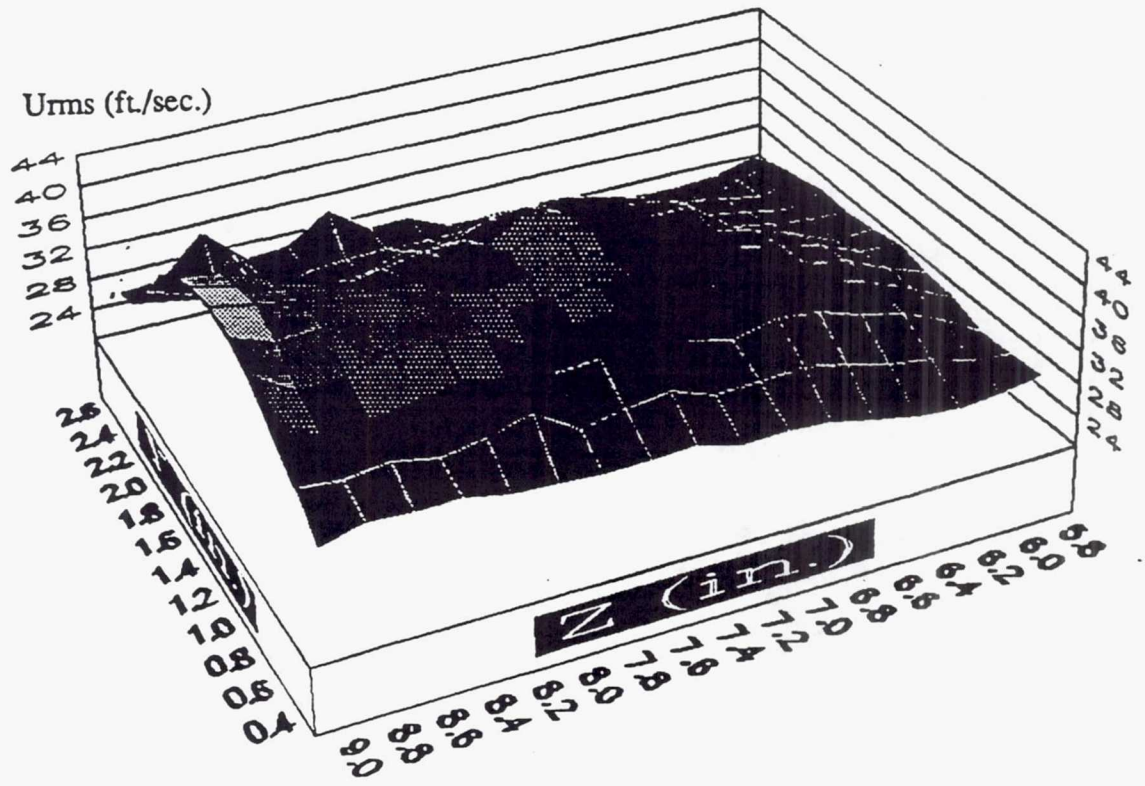

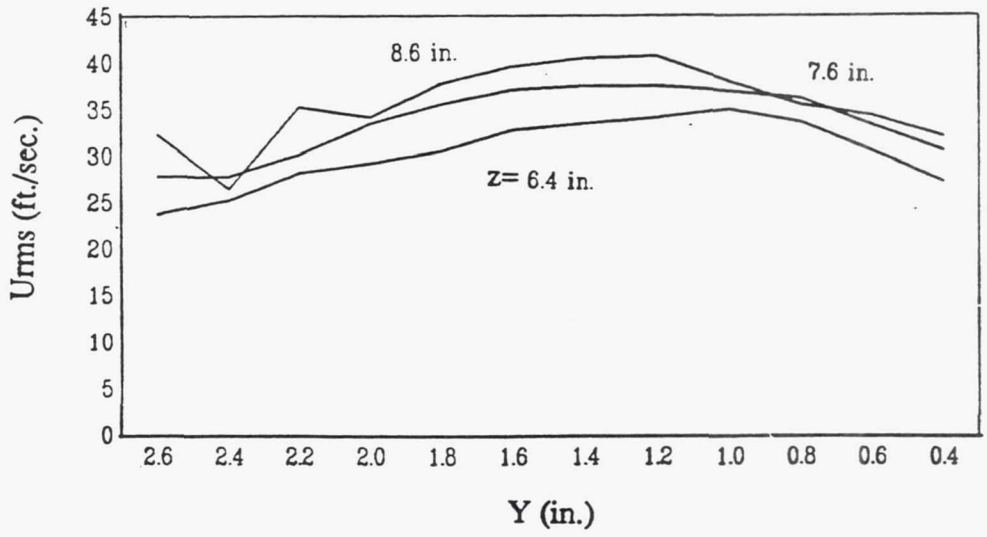

Figure 3.43 Contour and Line Plots of Urms at X=2.00 in.

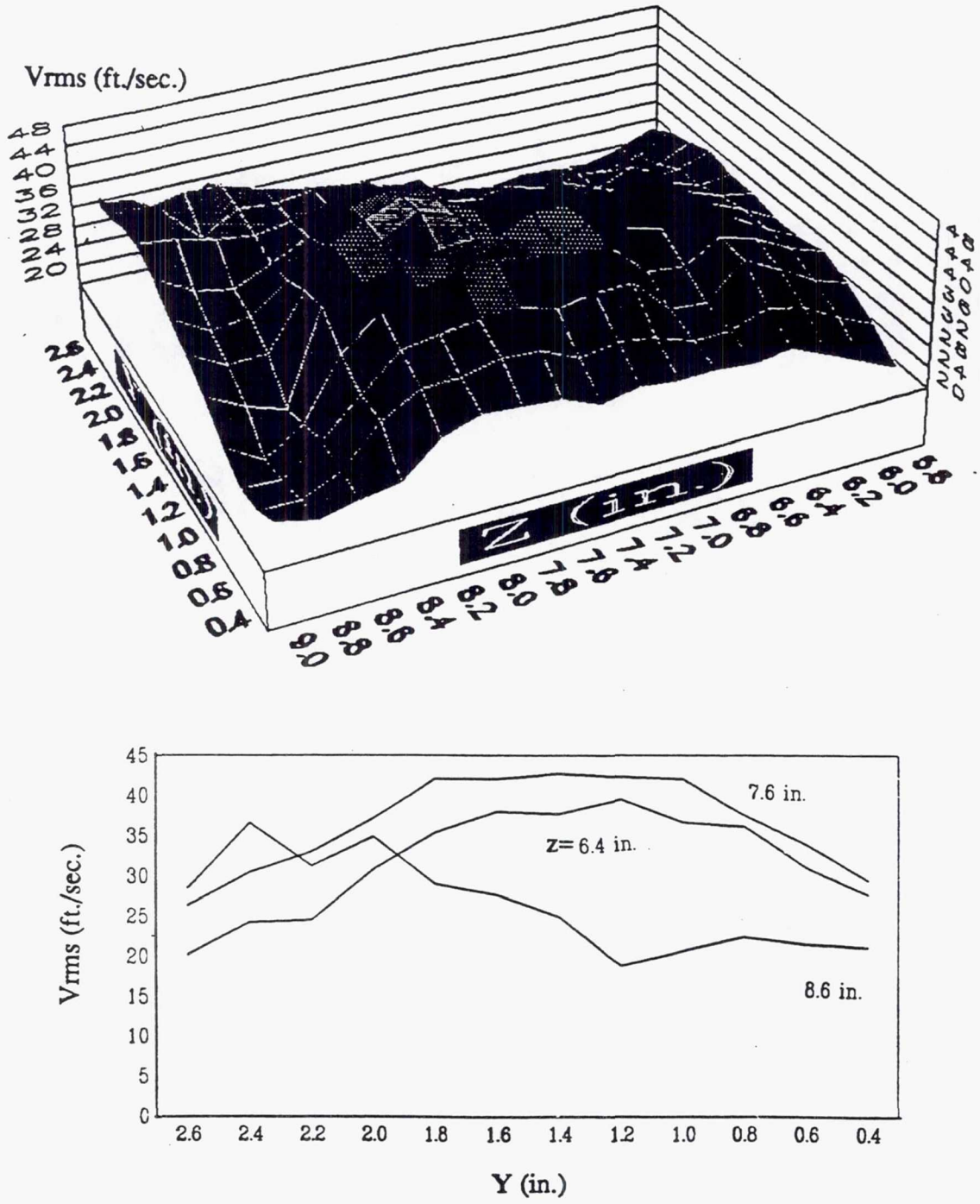

Figure 3.44 Contour and Line Plots of Vrms at X=2.00 in.

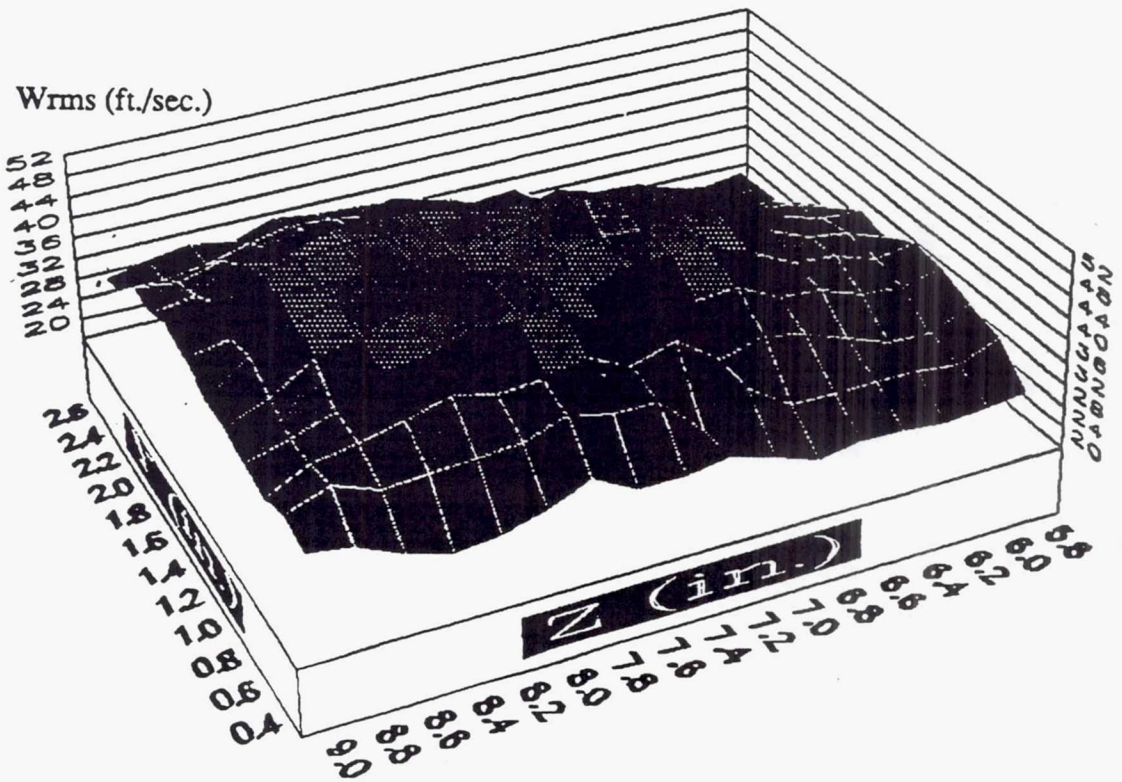

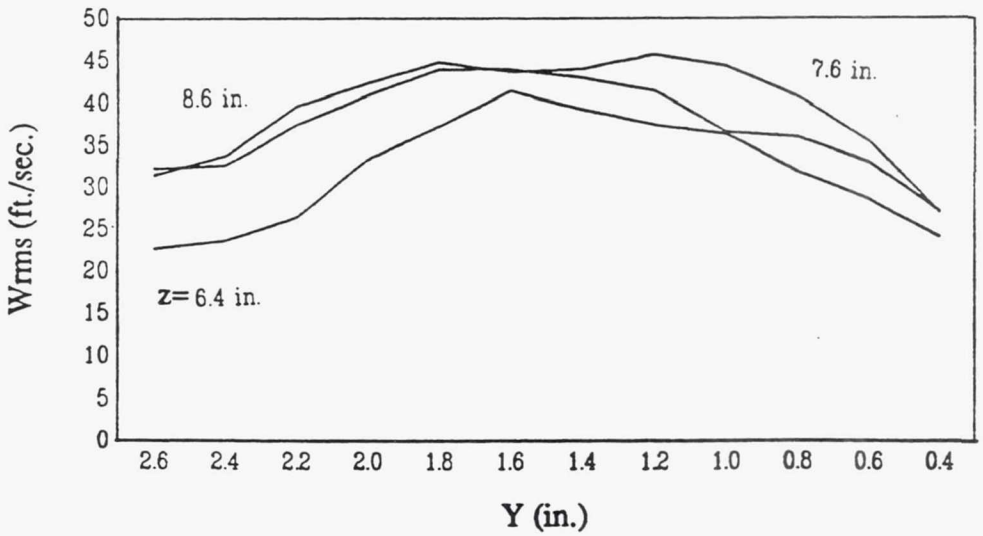

Figure 3.45 Contour and Line Plots of Wrms at X=2.00 in.

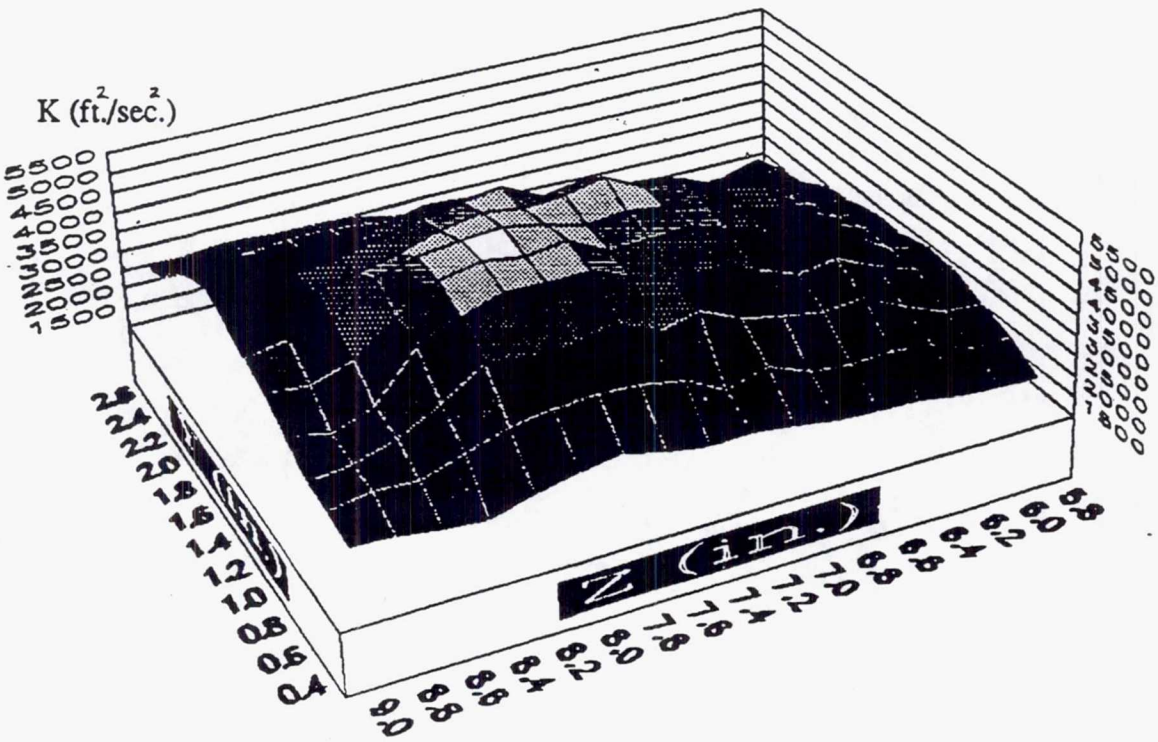

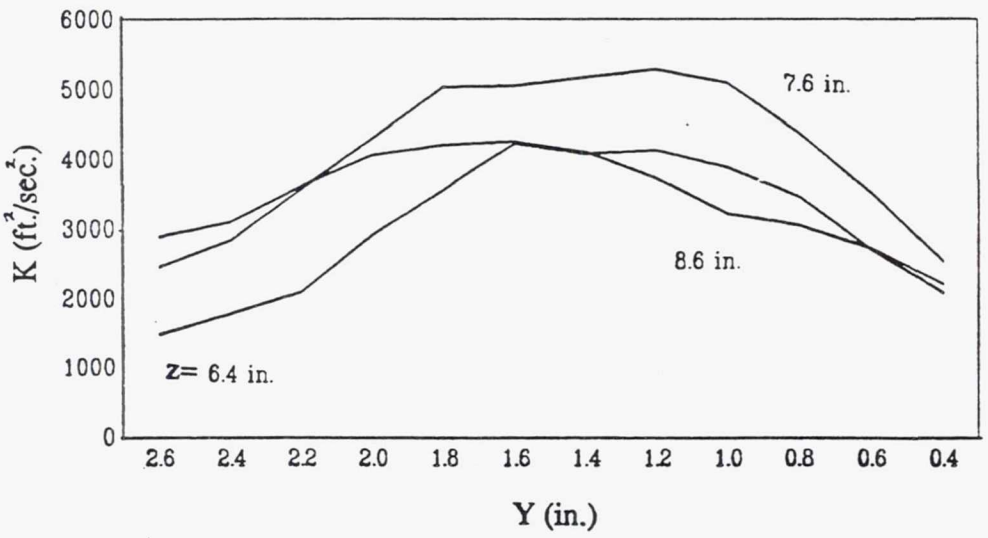

Figure 3.46 Contour and Line Plots of K at X=2.00 in.

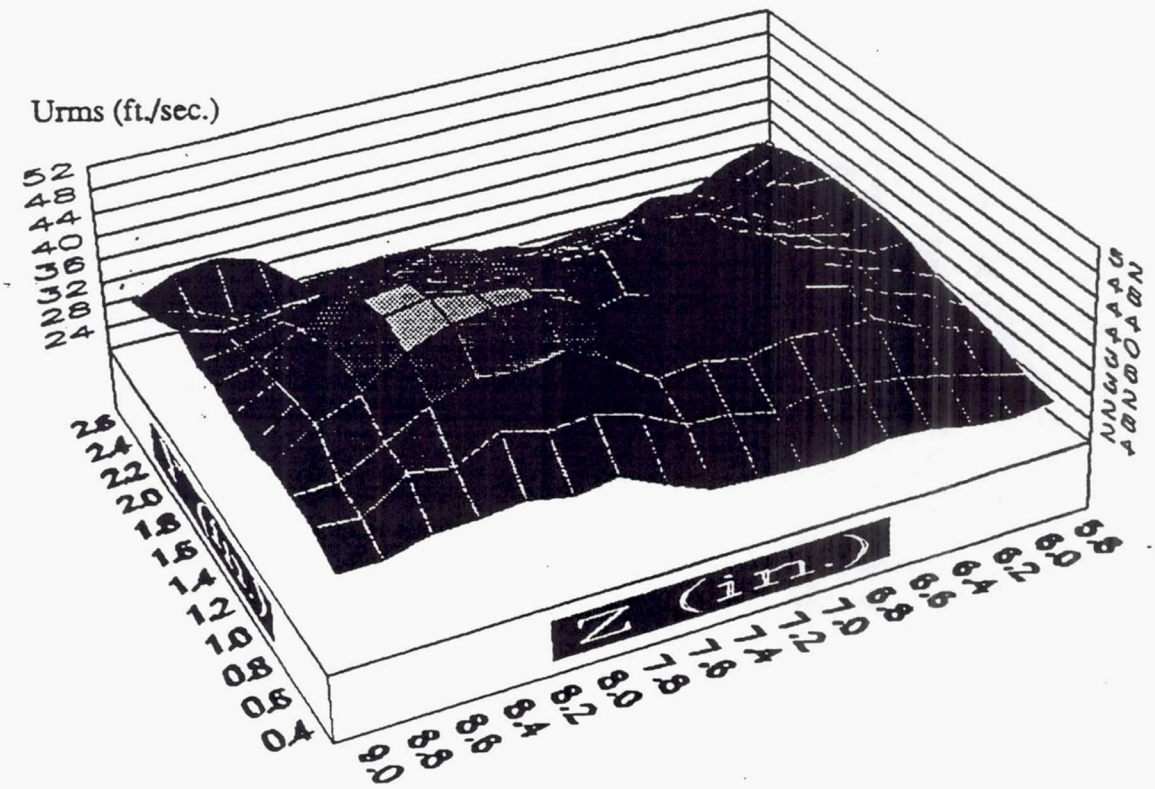

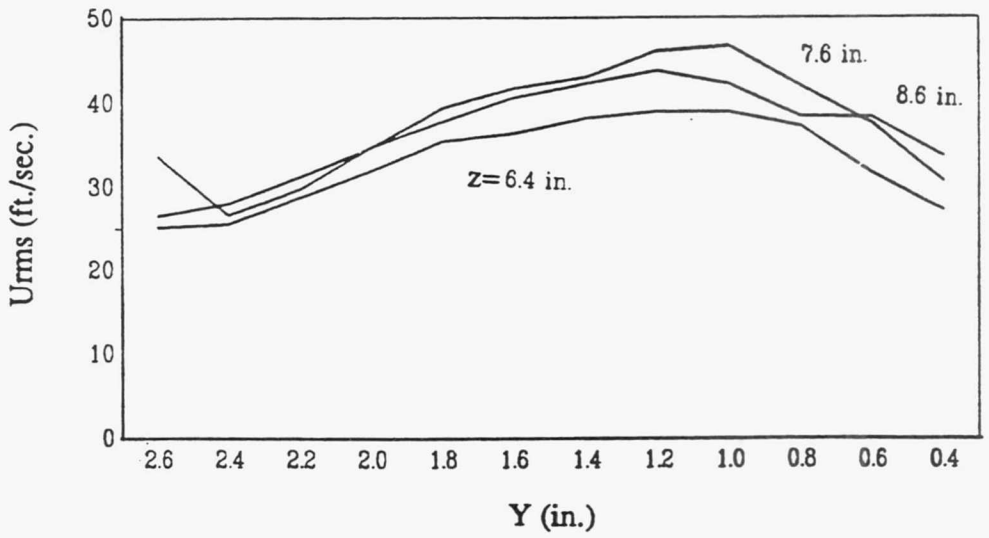

Figure 3.47 Contour and Line Plots of Urms at X=2.50 in.

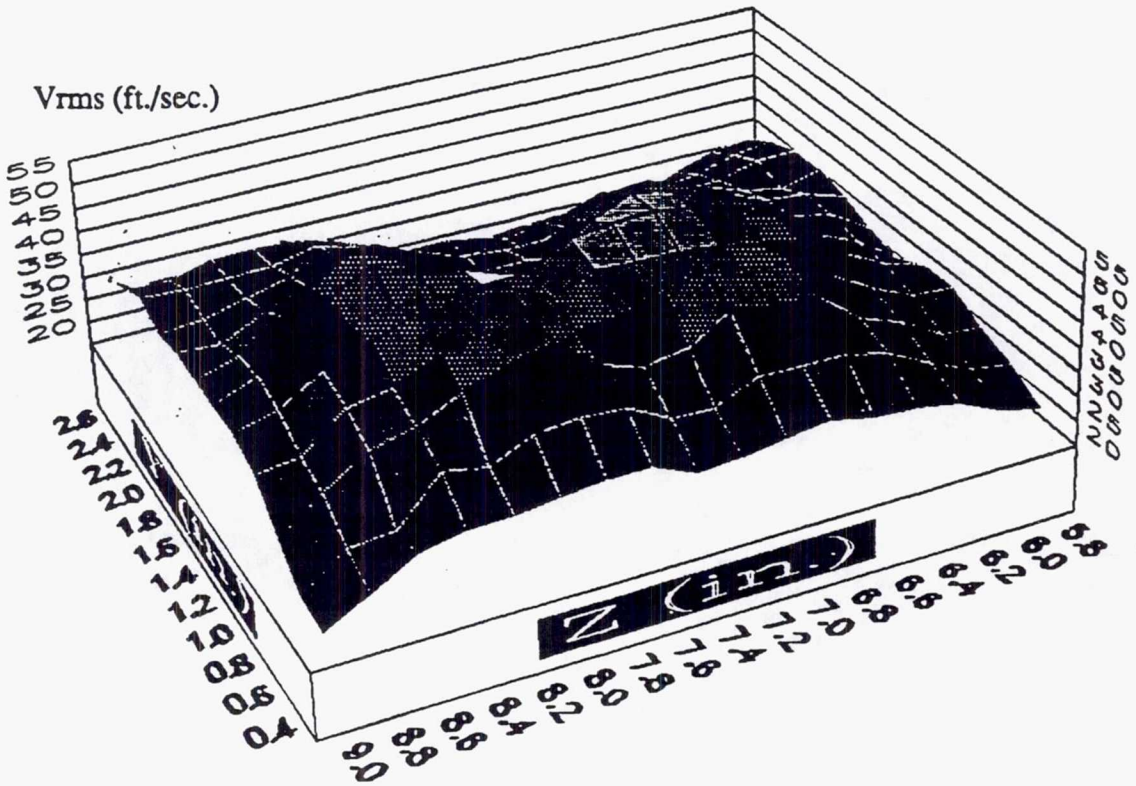

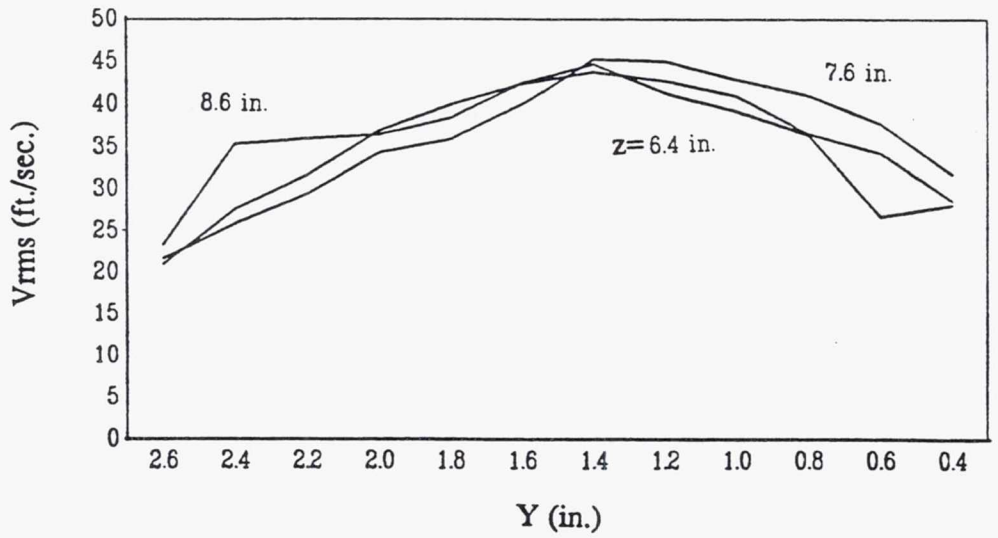

Figure 3.48 Contour and Line Plots of Vrms at X=2.50 in.

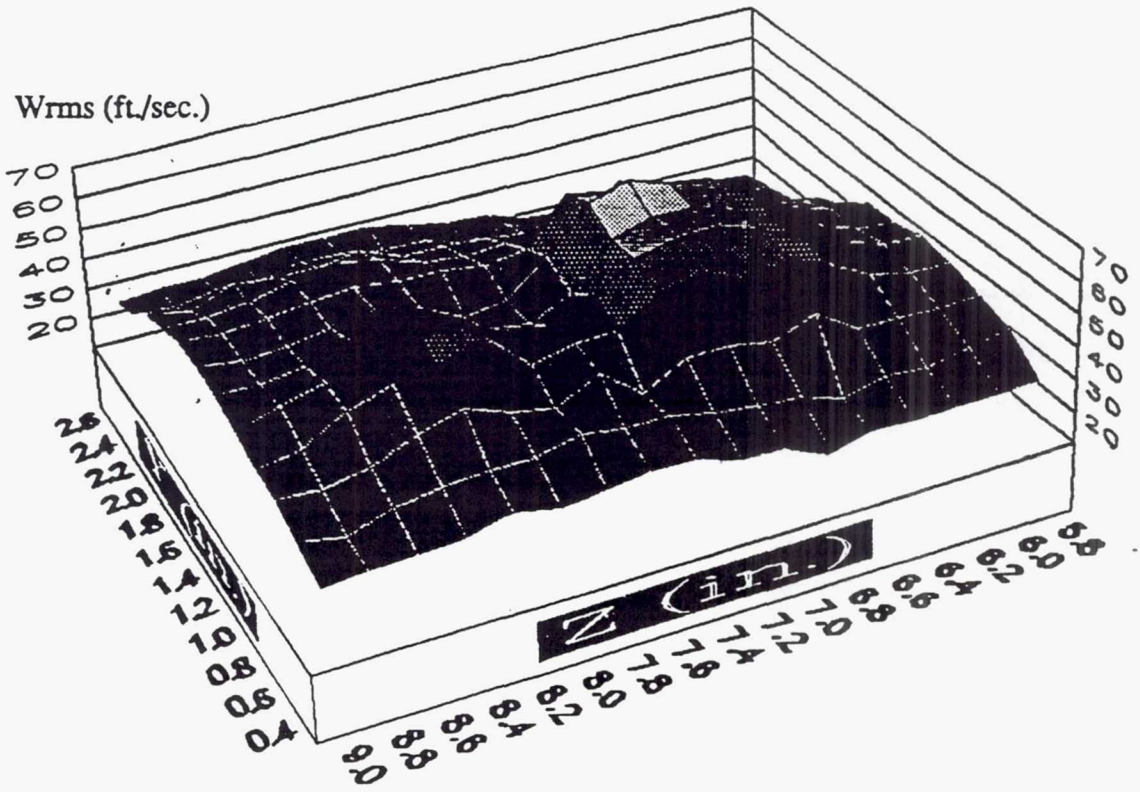

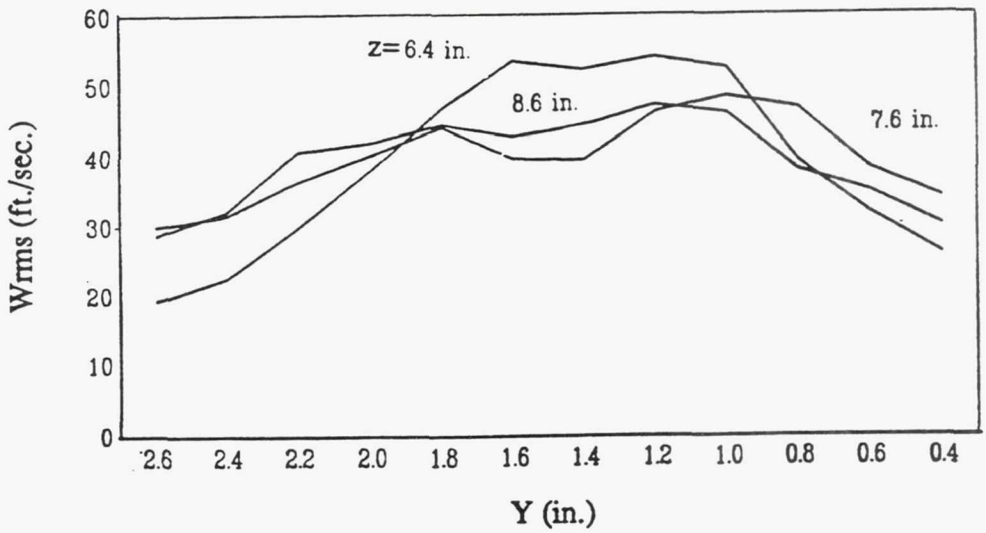

Figure 3.49 Contour and Line Plots of Wrms at X=2.50 in.

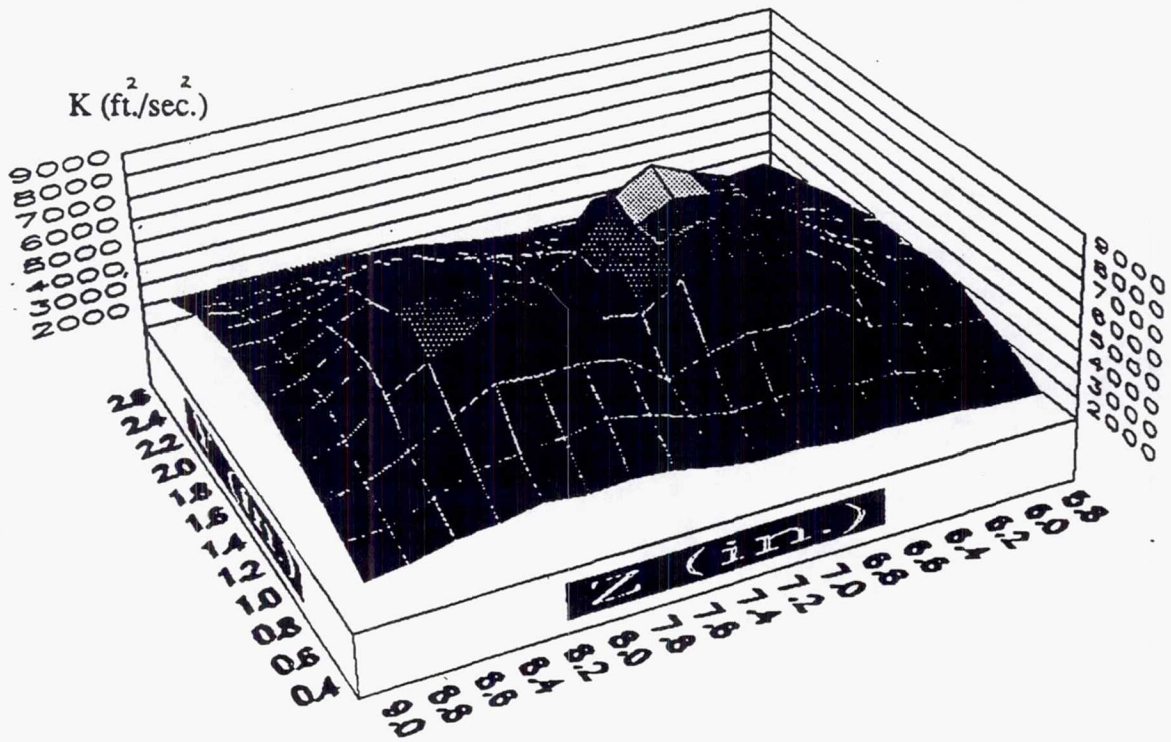

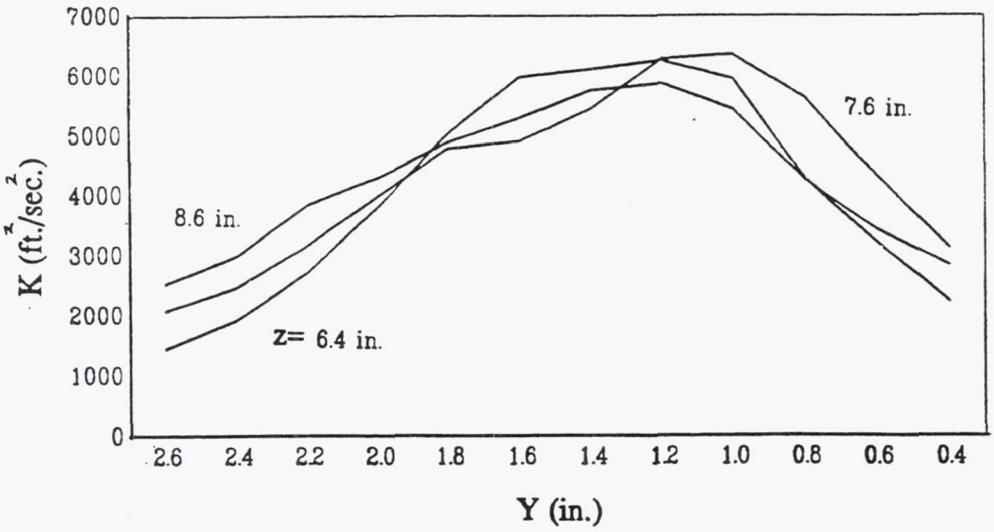

Figure 3.50 Contour and Line Plots of K at X=2.50 in.

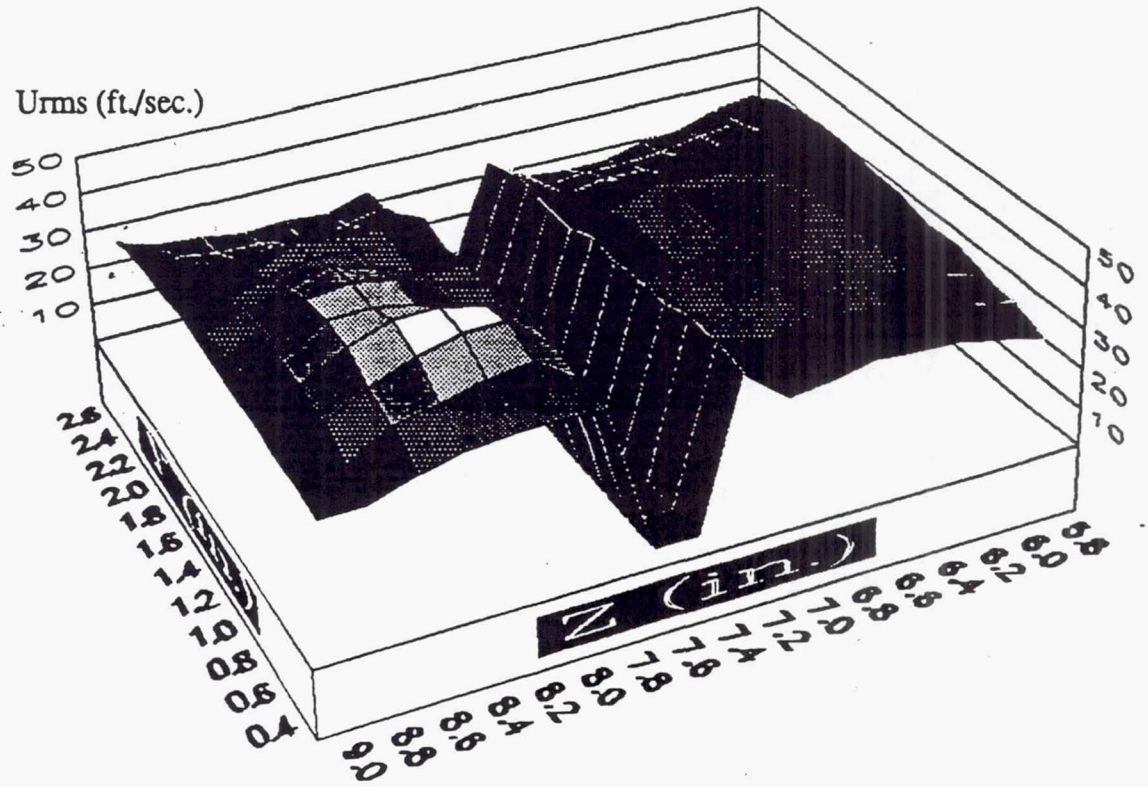

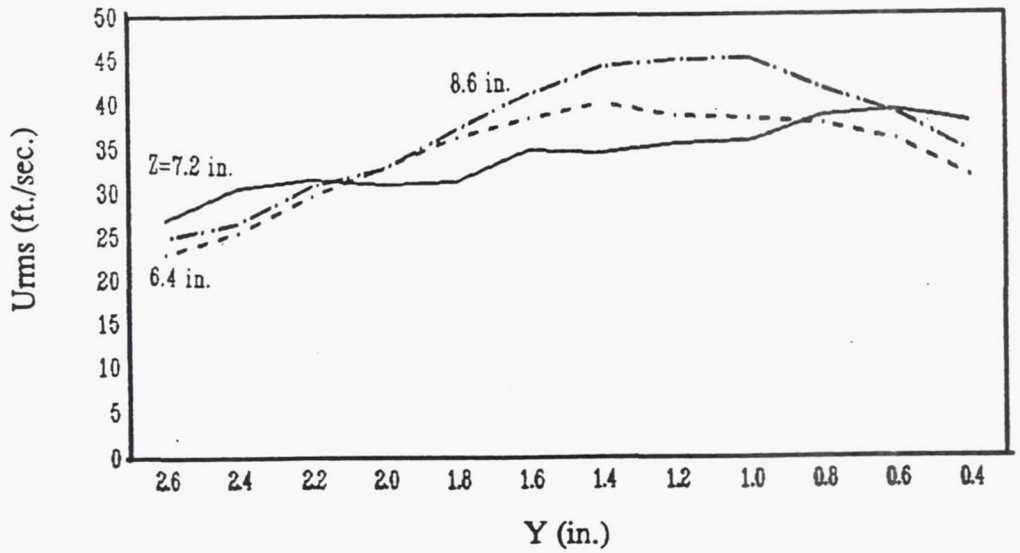

Figure 3.51 Contour and Line Plots of Urms at X=3.00 in.

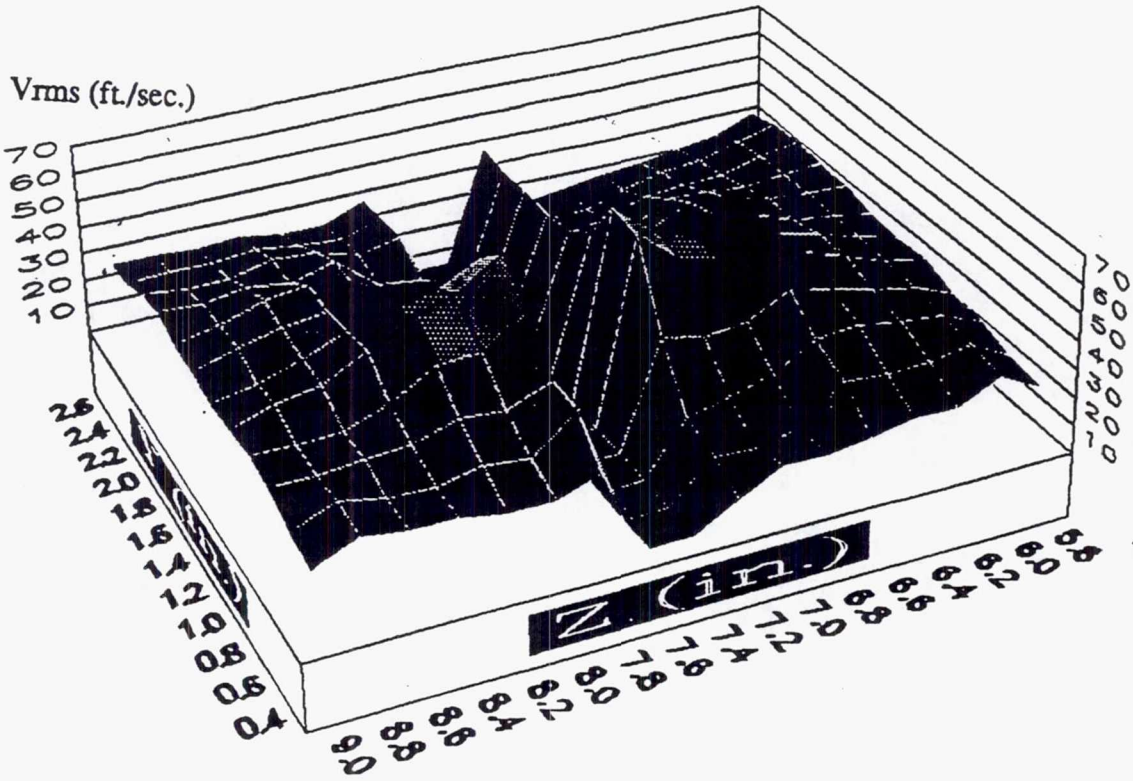

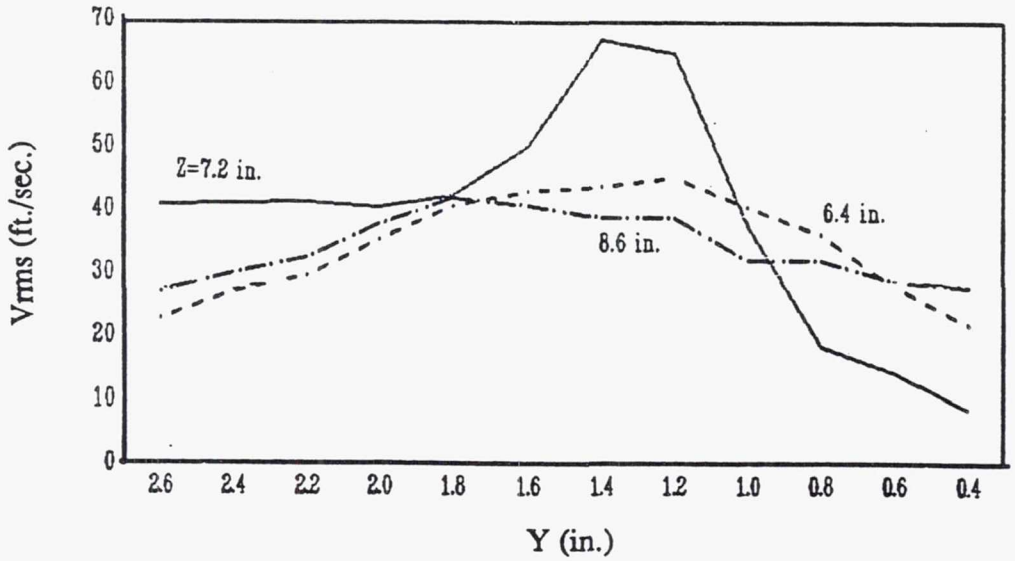

Figure 3.52 Contour and Line Plots of Vrms at X=3.00 in.

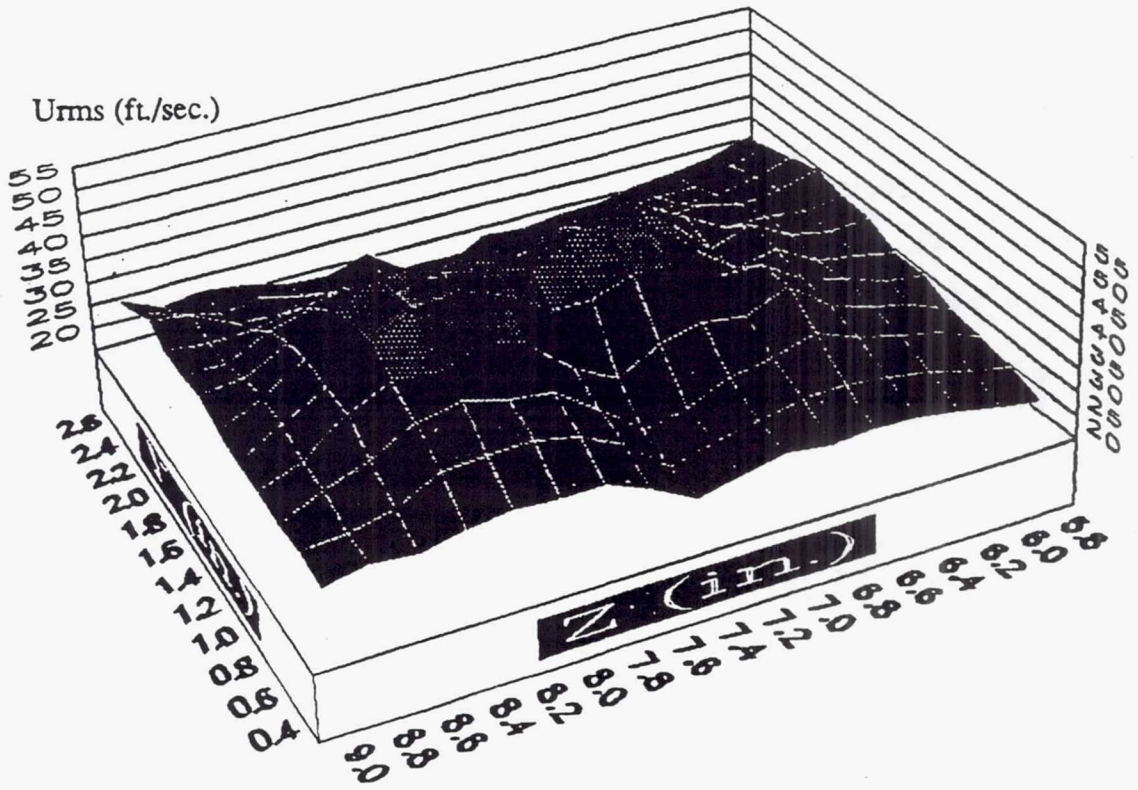

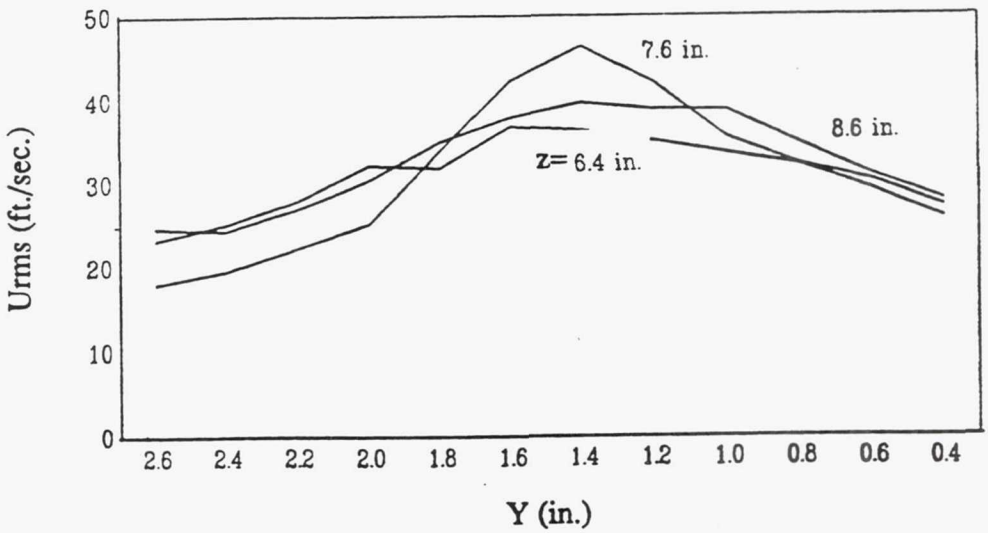

Figure 3.53 Contour and Line Plots of Urms at X=3.50 in.

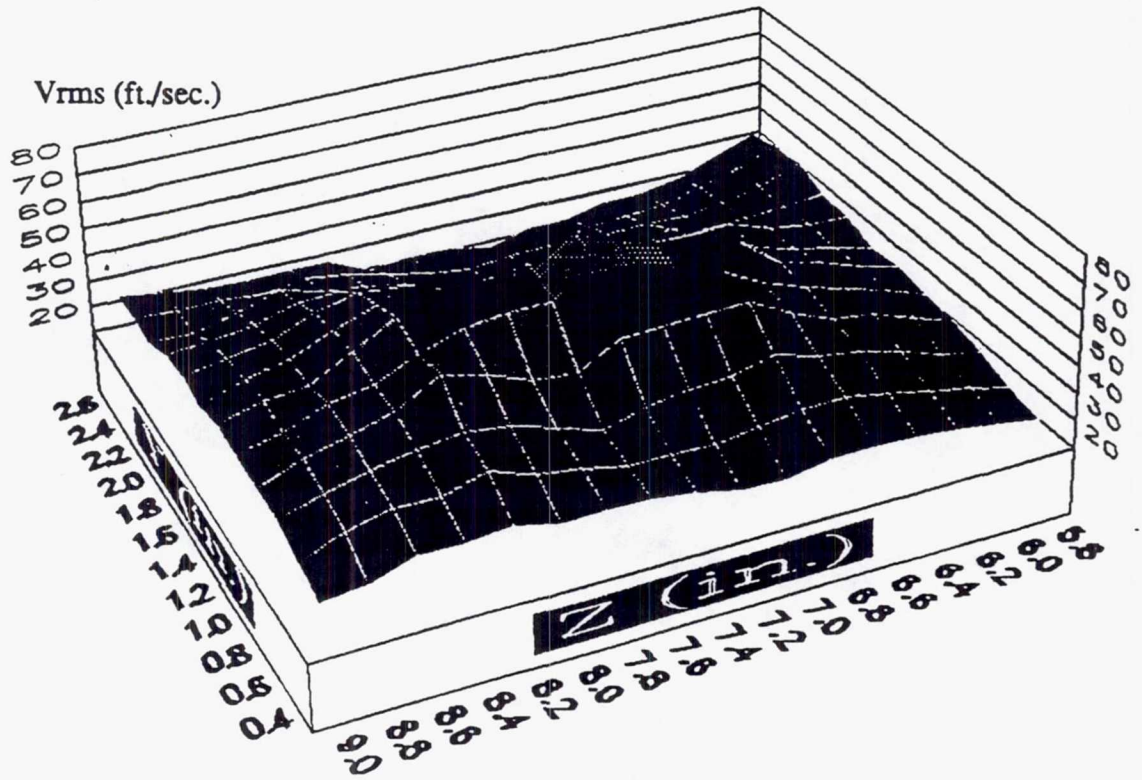

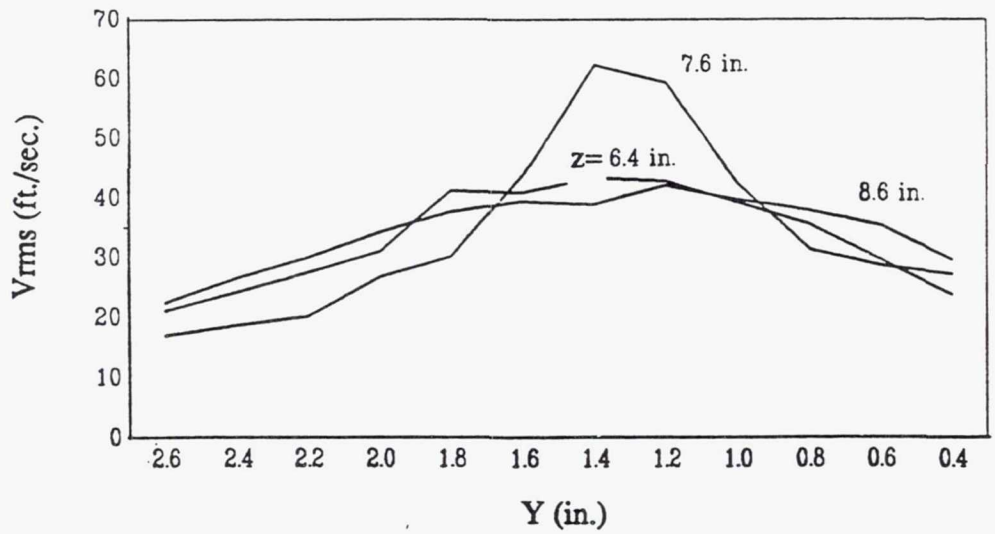

Figure 3.54 Contour and Line Plots of Vrms at X=3.50 in.

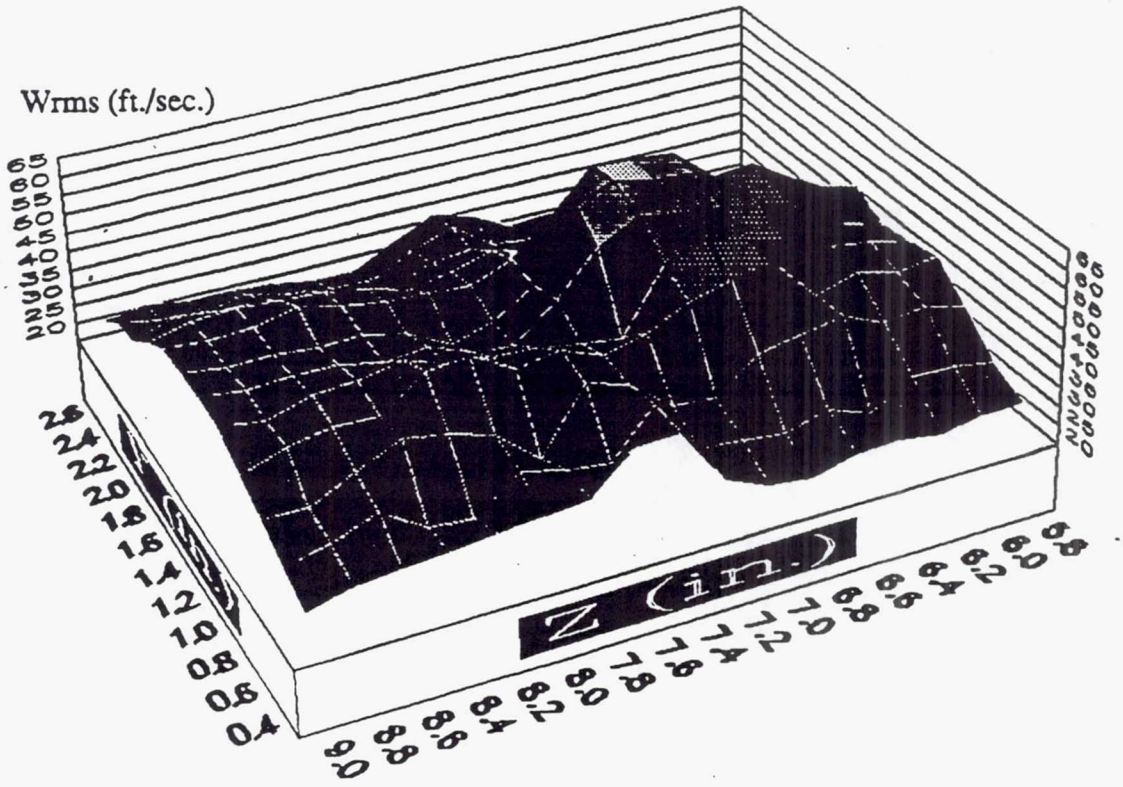

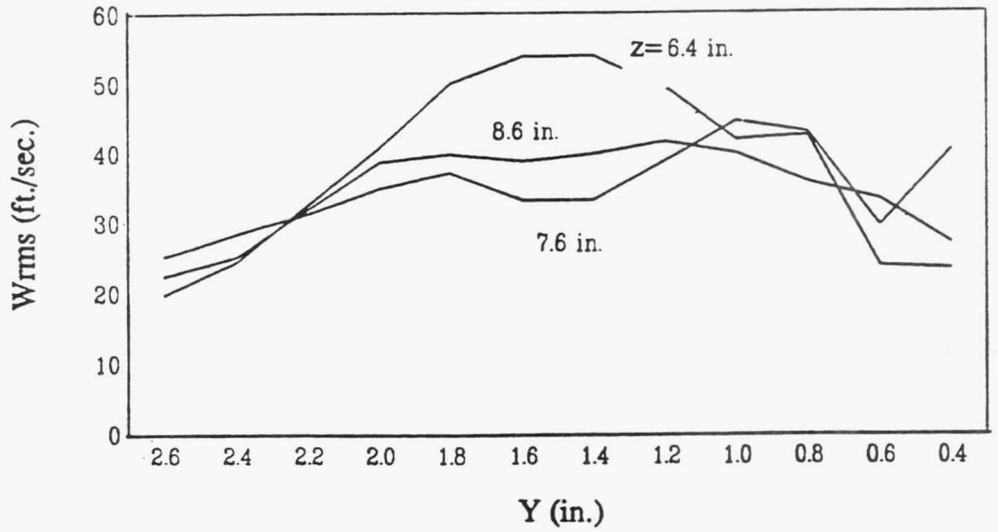

Figure 3.55 Contour and Line Plots of Wrms at X=3.50 in.

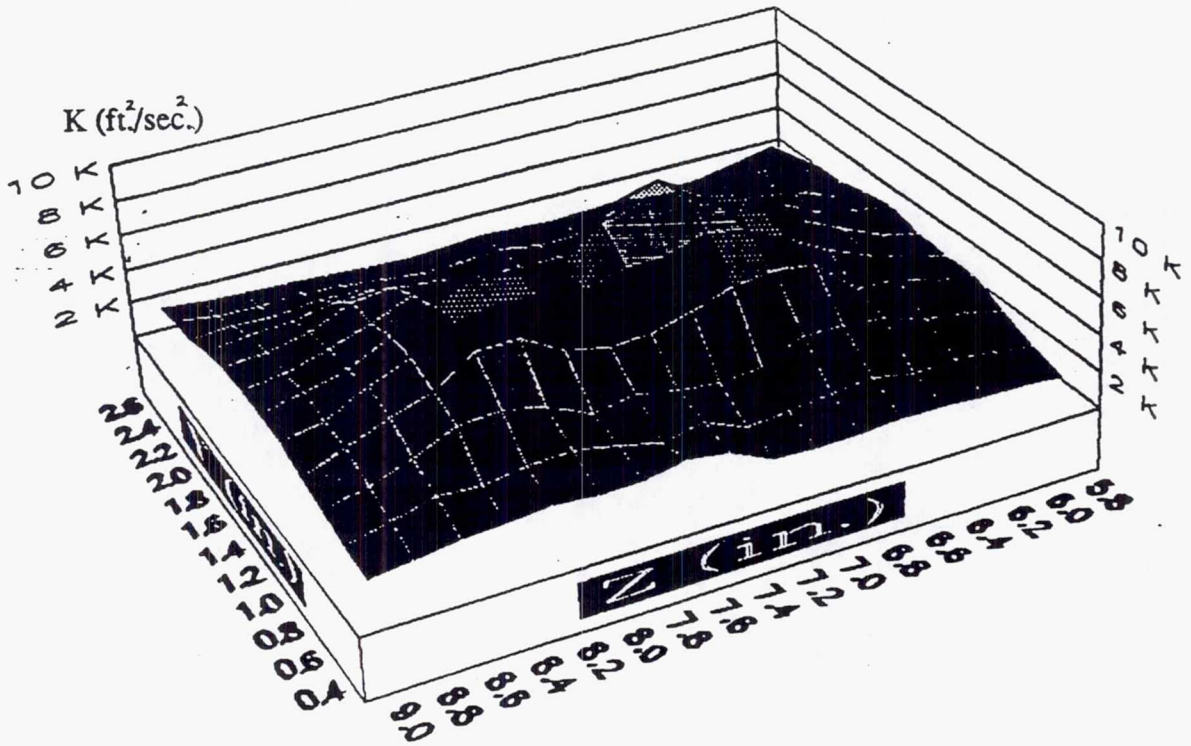

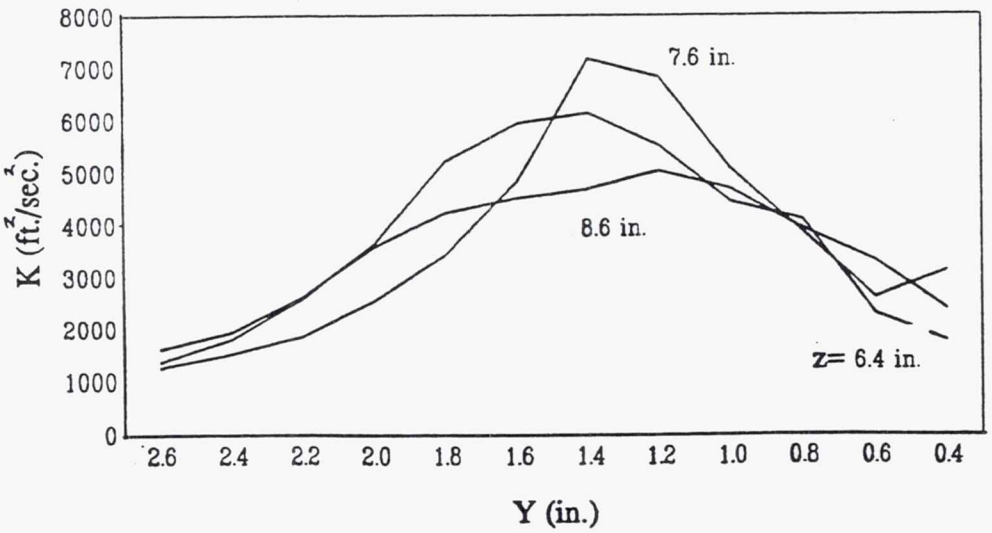

Figure 3.56 Contour and Line Plots of K at X=3.50 in.

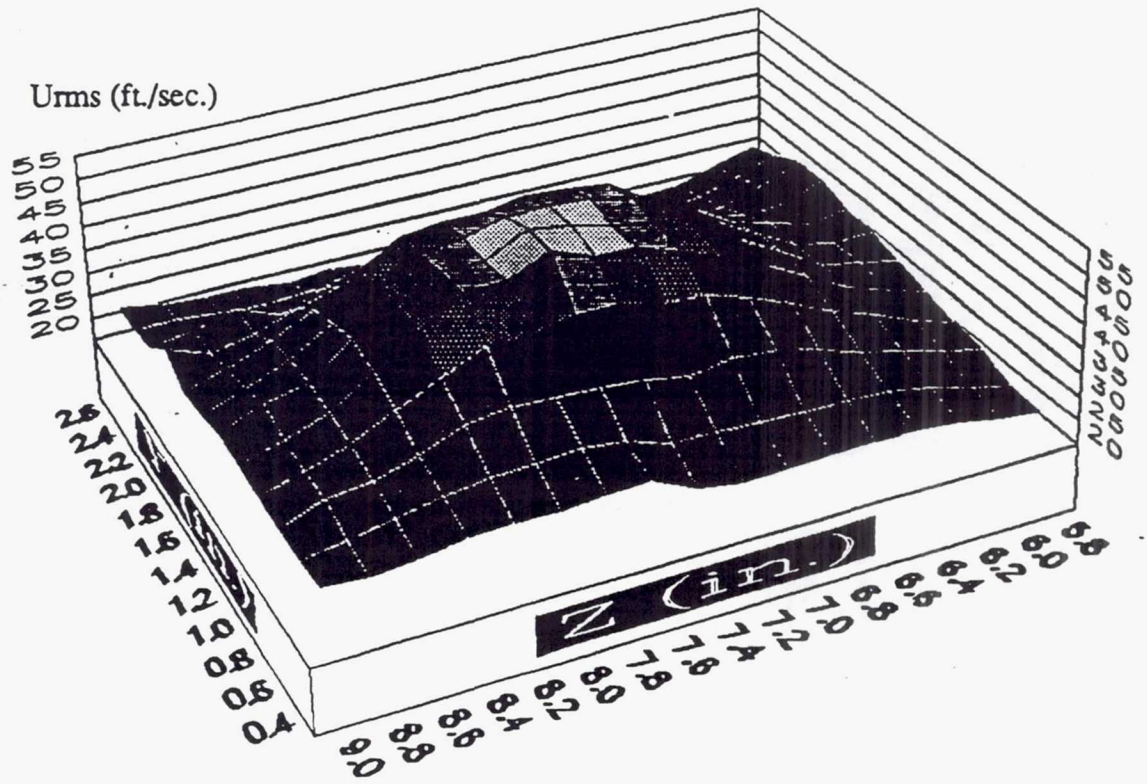

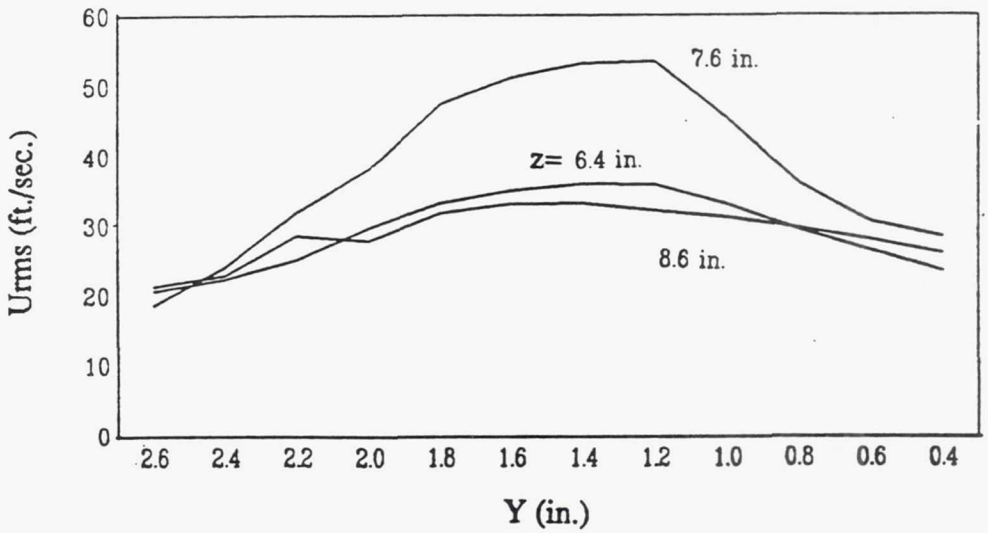

Figure 3.57 Contour and Line Plots of Urms at X=4.00 in.

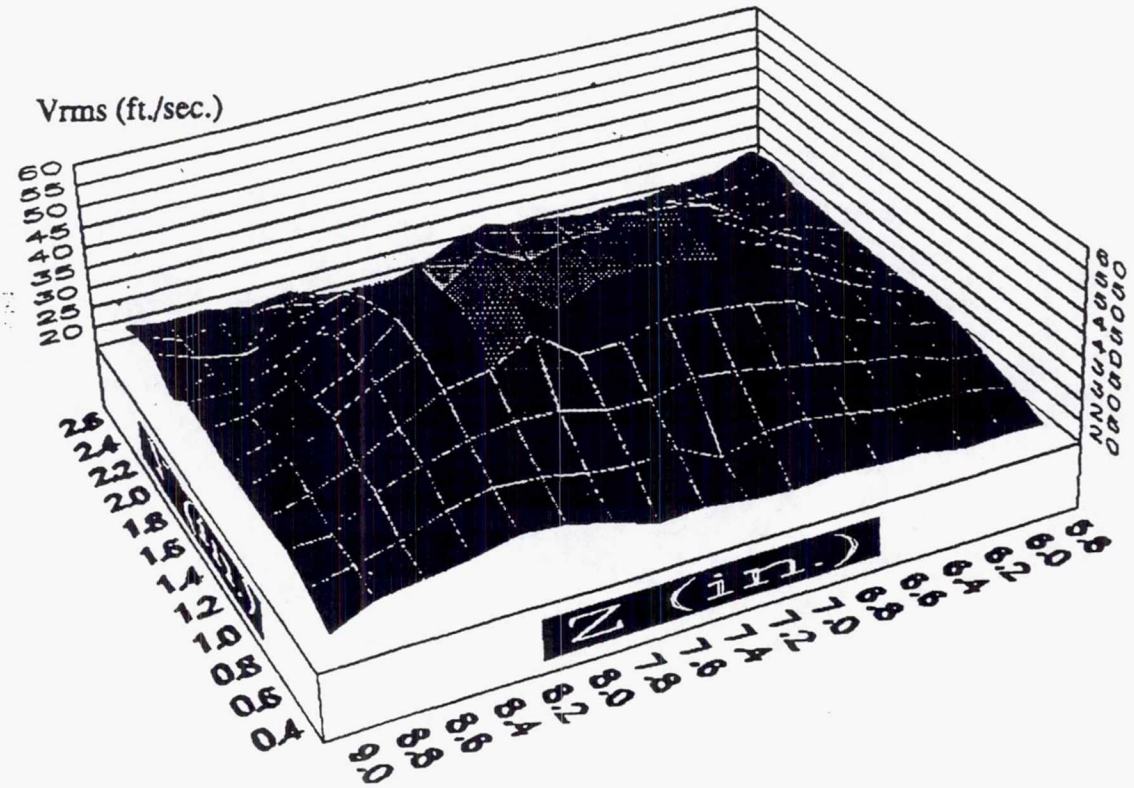

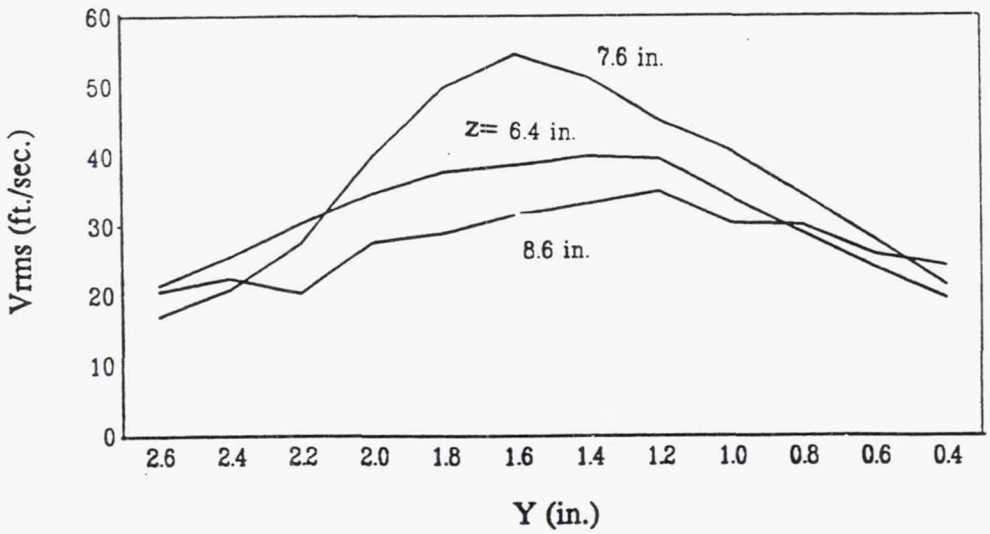

Figure 3.58 Contour and Line Plots of Vrms at X=4.00 in.

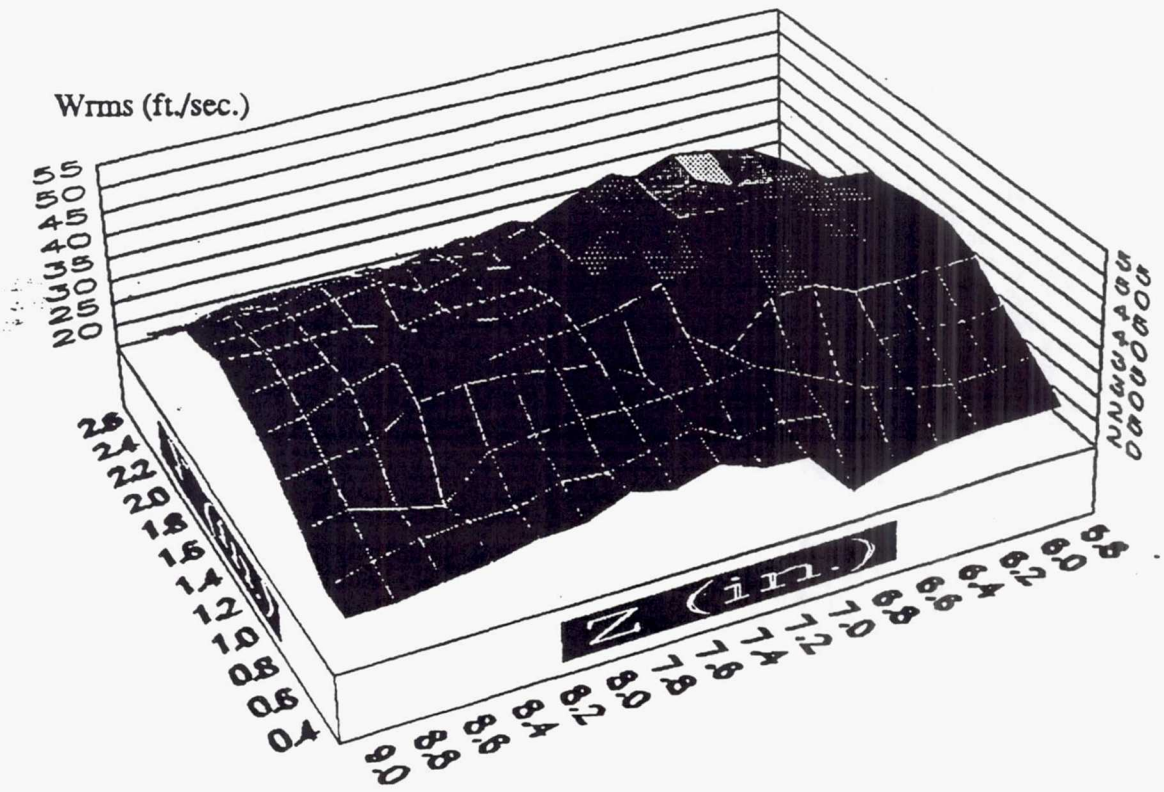

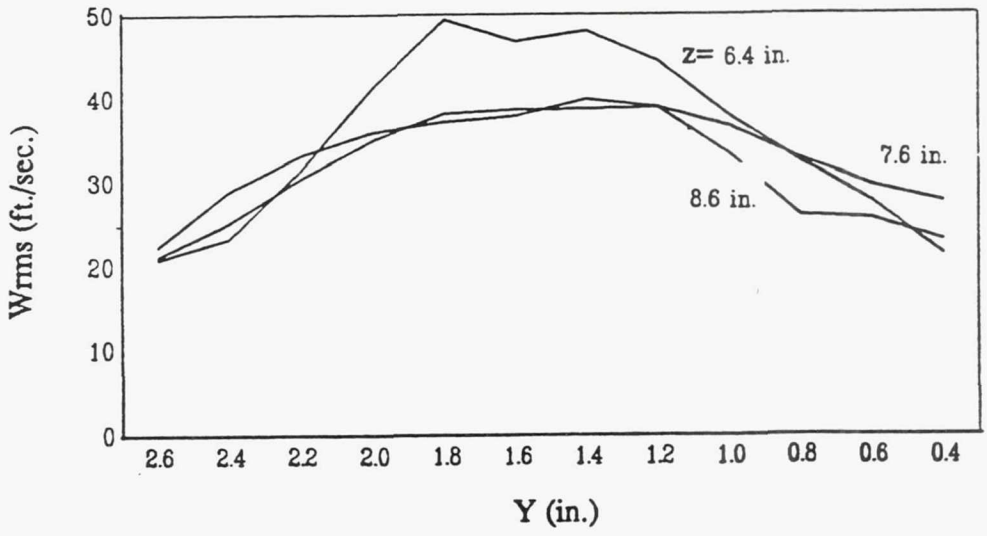

Figure 3.59 Contour and Line Plots of Wrms at X=4.00 in.

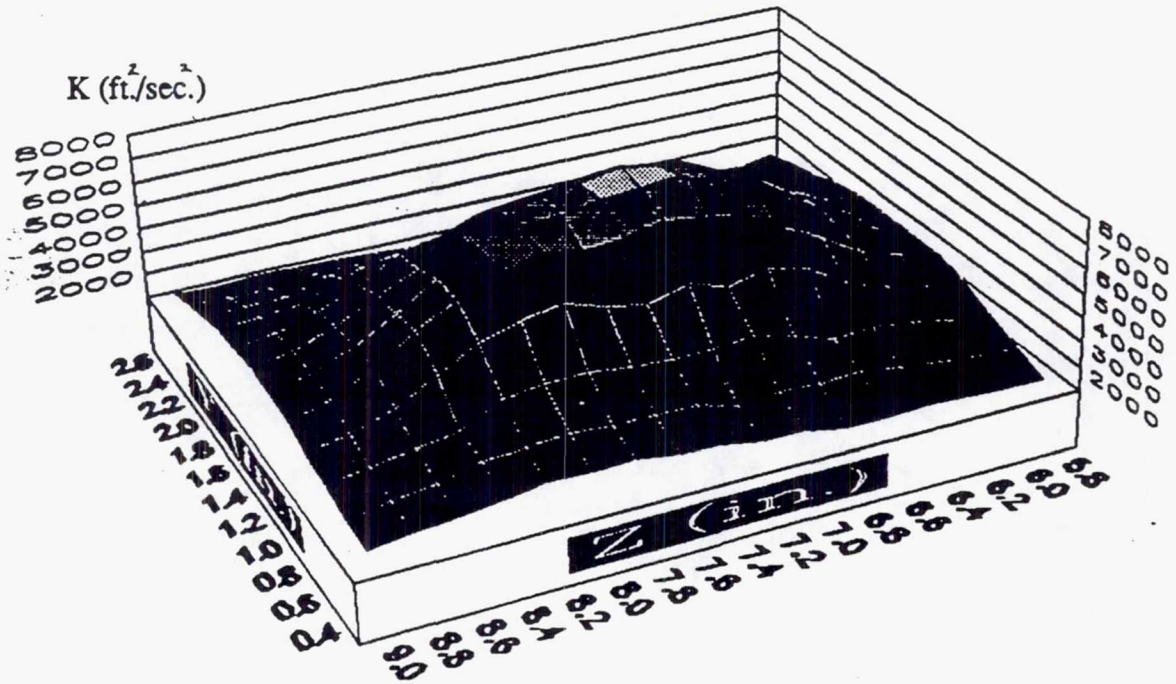

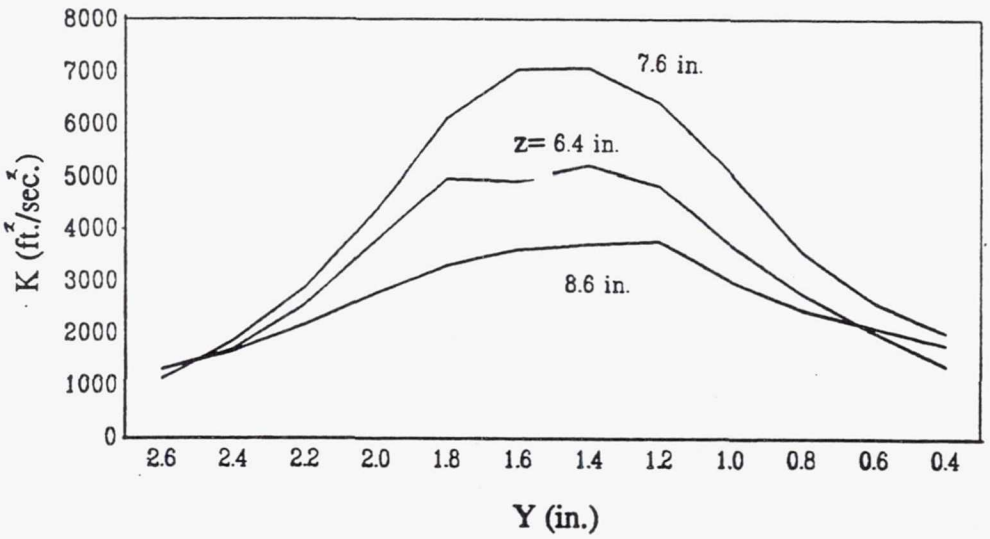

Figure 3.60 Contour and Line Plots of K at X=4.00 in.

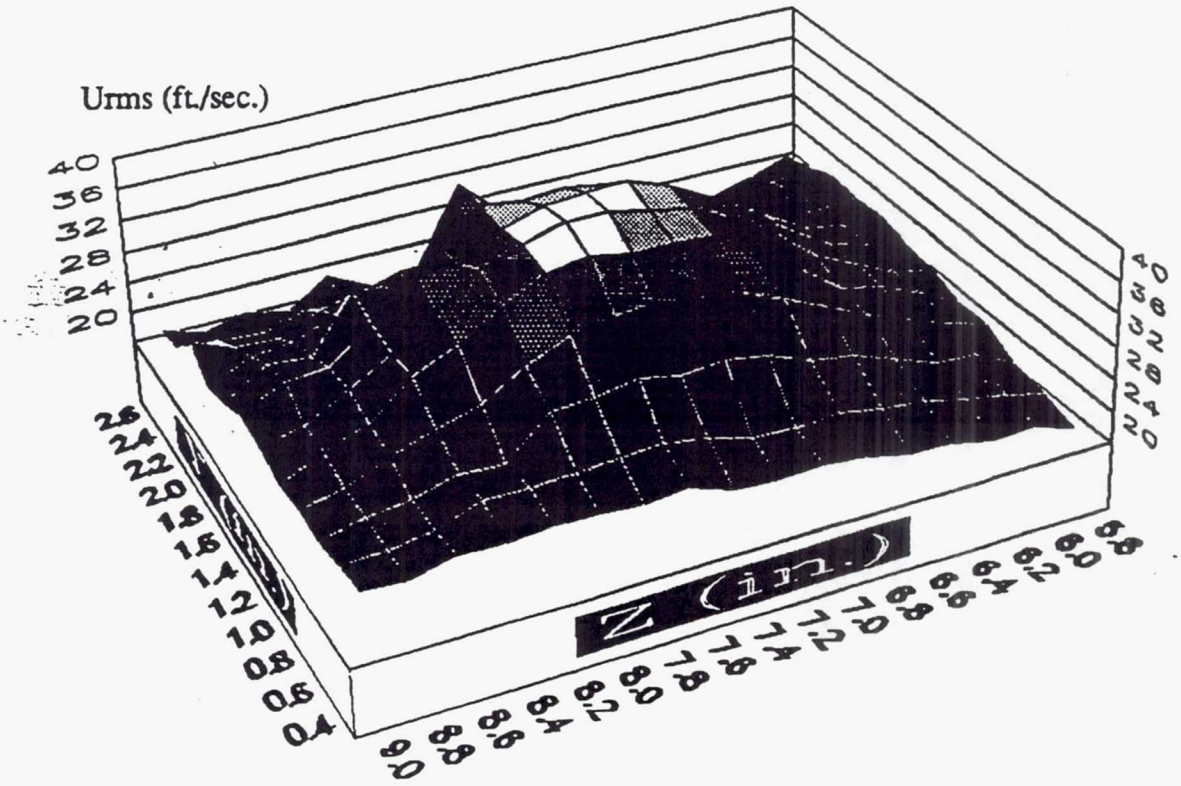

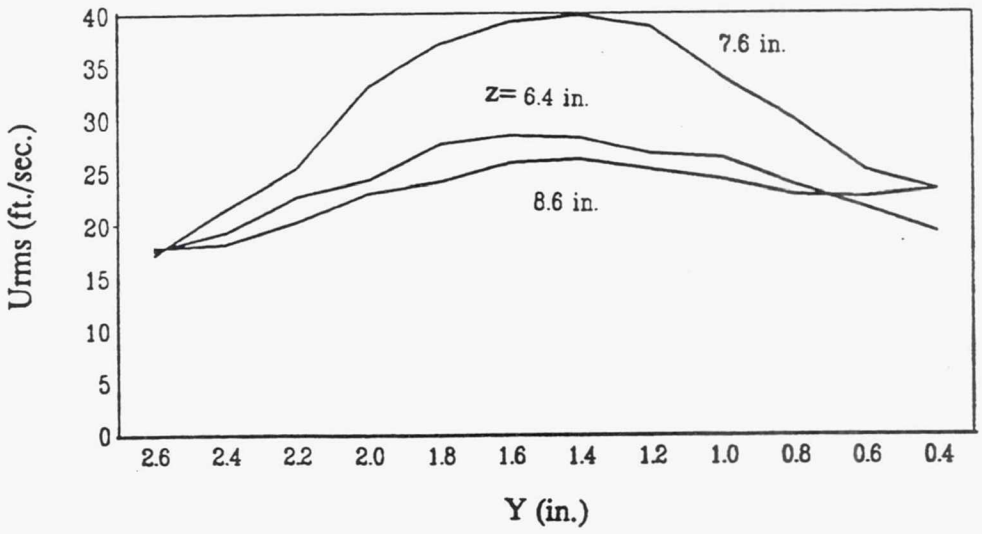

Figure 3.61 Contour and Line Plots of Urms at X=4.50 in.

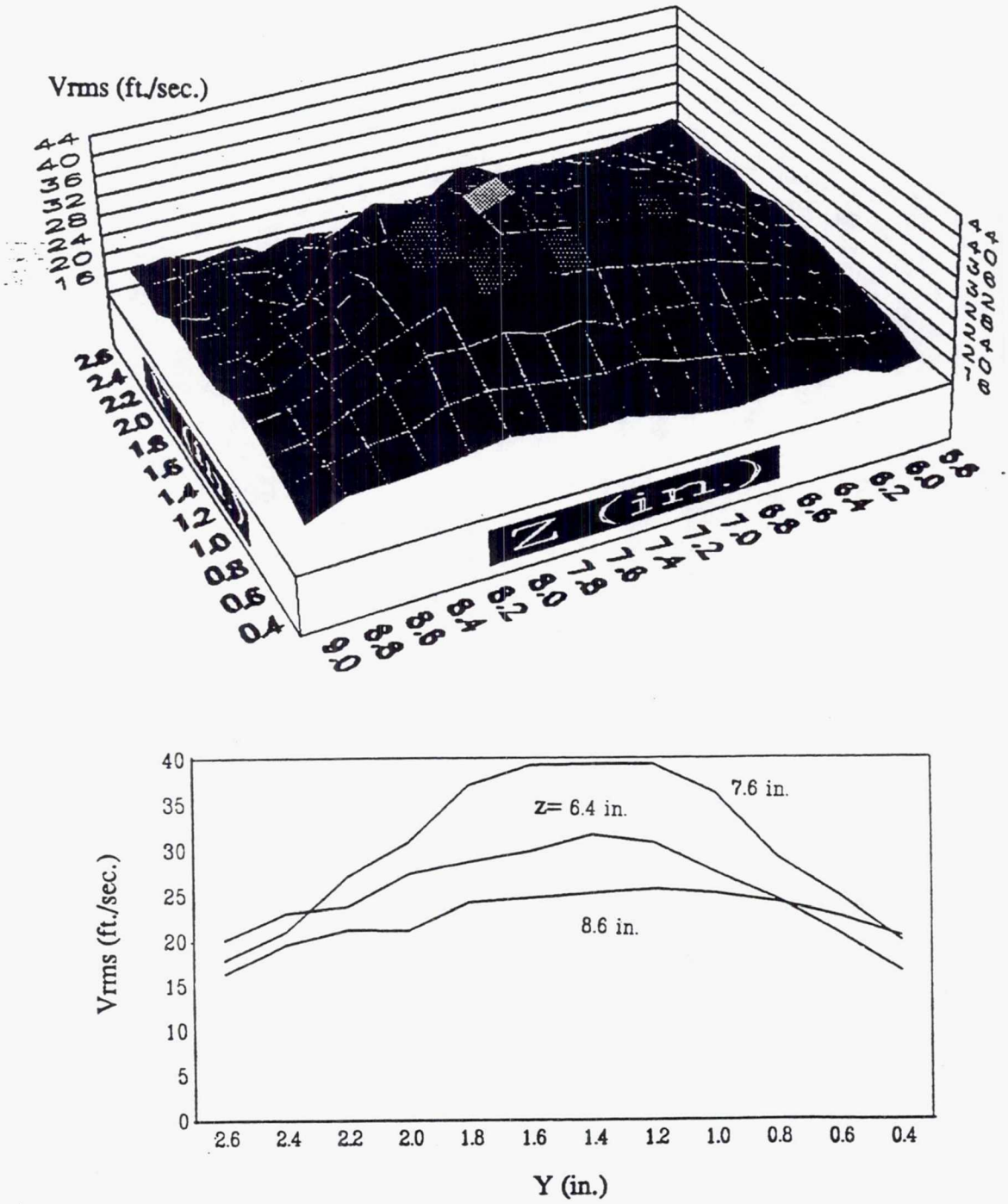

Figure 3.62 Contour and Line Plots of Vrms at X=4.50 in.

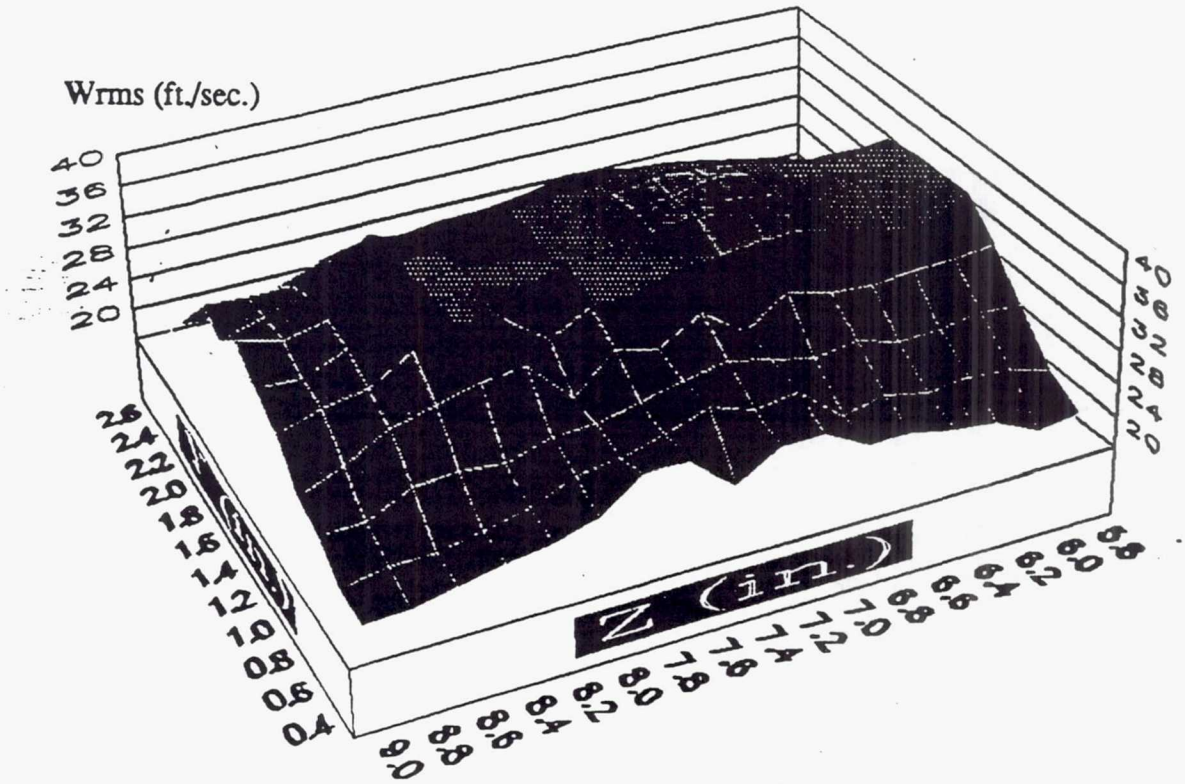

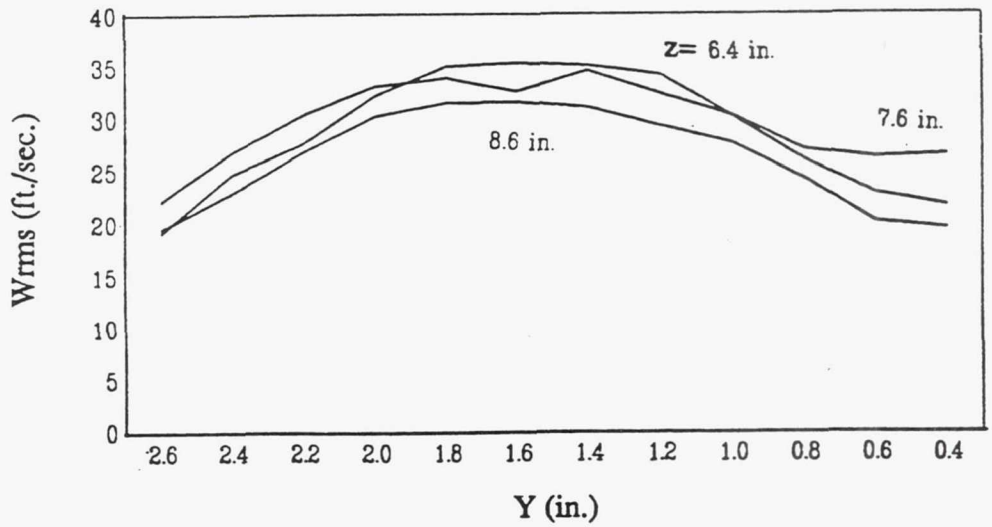

Figure 3.63 Contour and Line Plots of Wrms at X=4.50 in.

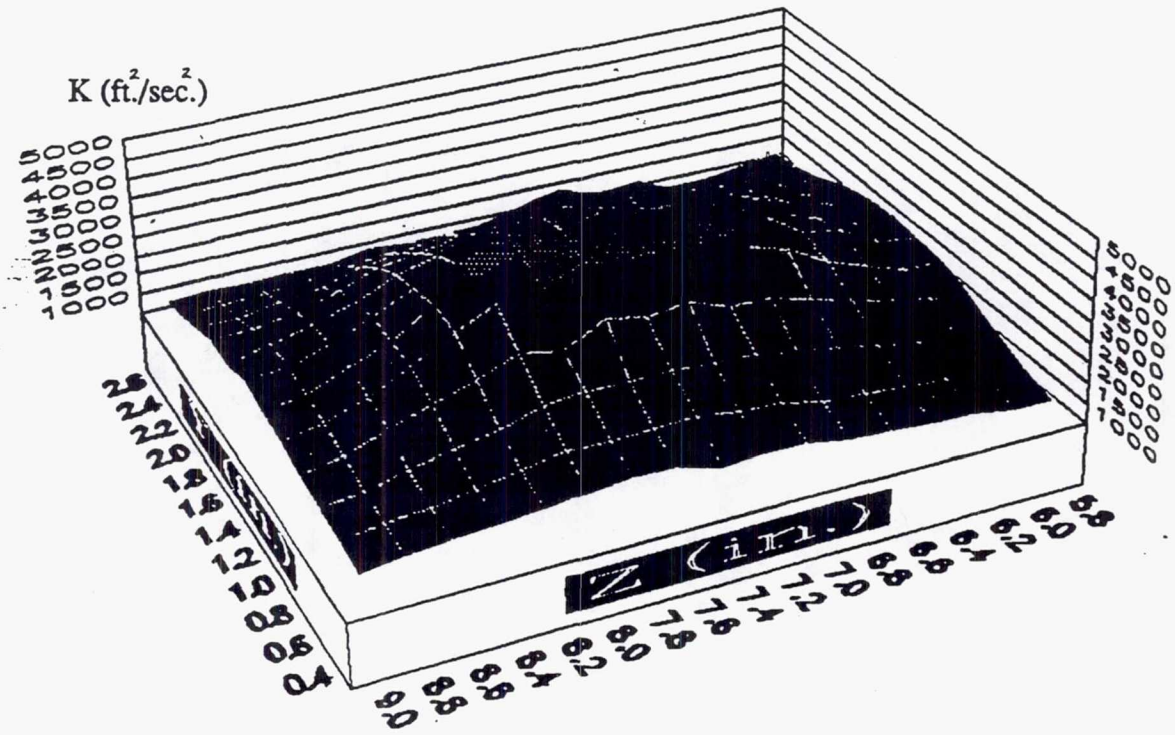

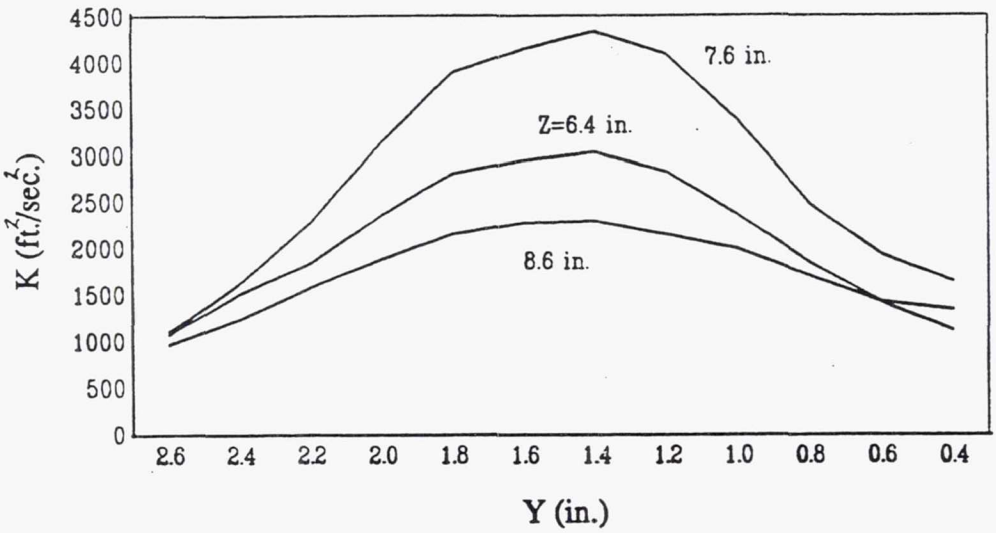

Figure 3.64 Contour and Line Plots of K at X=4.50 in.

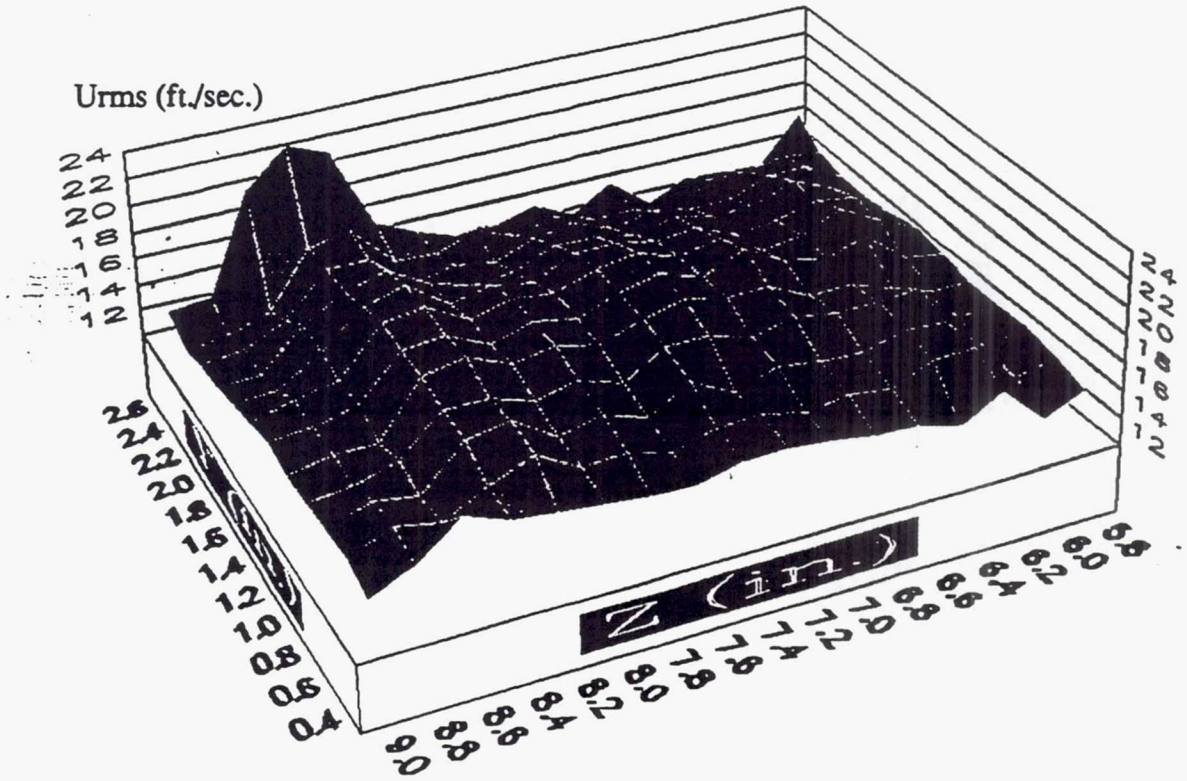

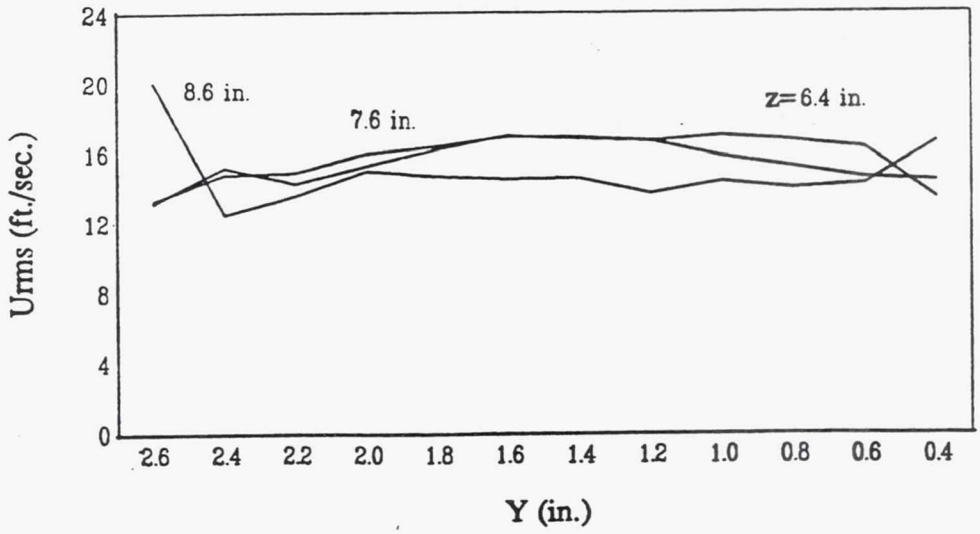

Figure 3.65 Contour and Line Plots of Urms at X=6.00 in.

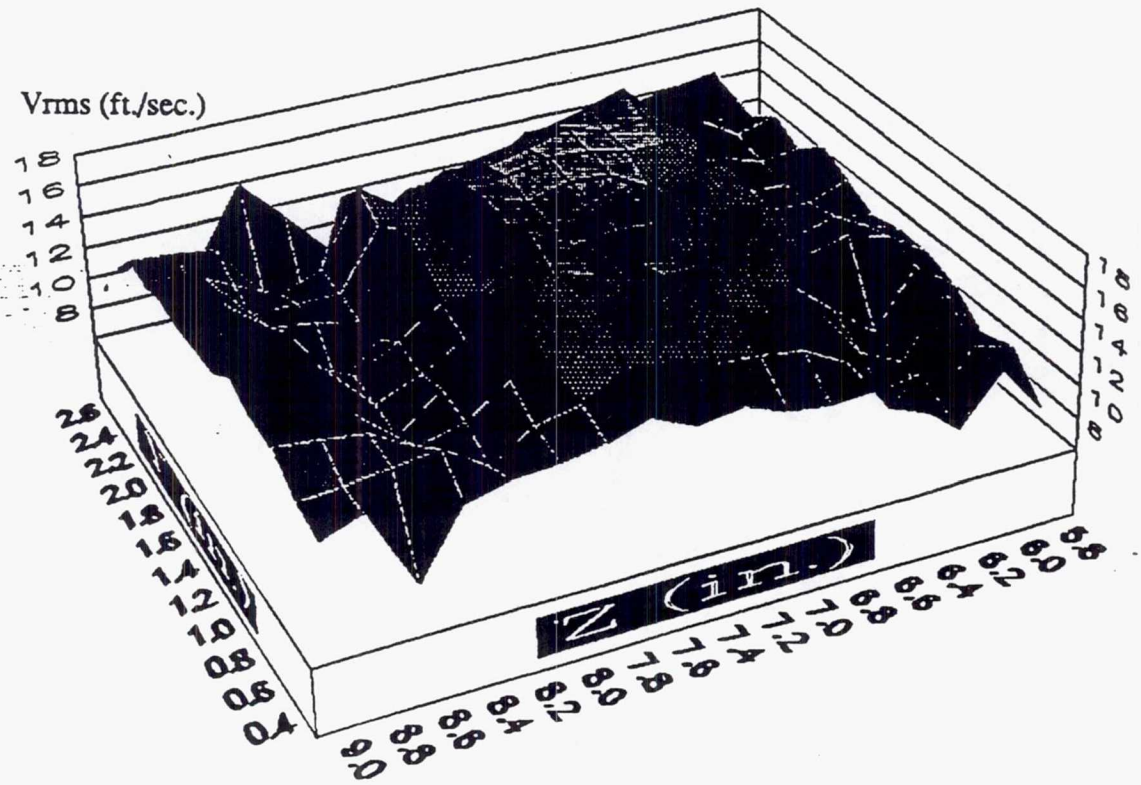

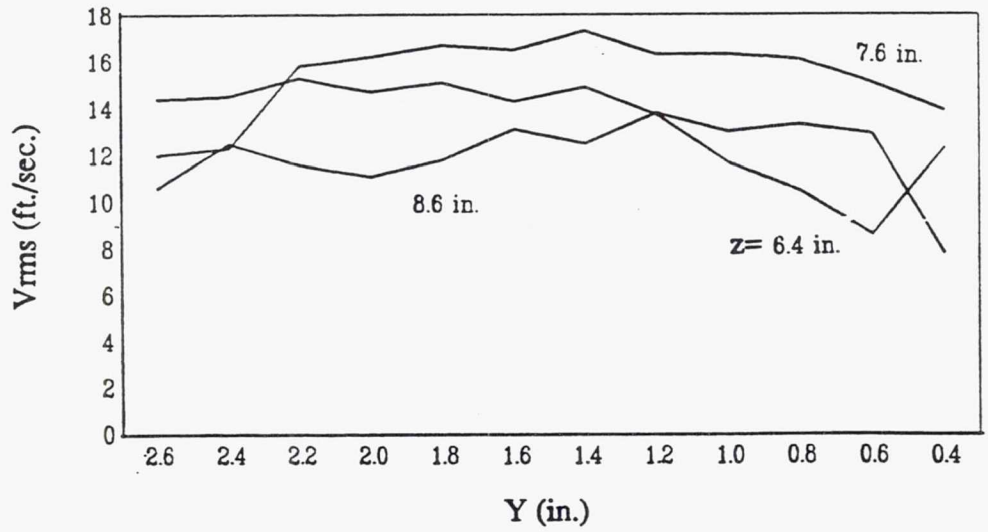

Figure 3.66 Contour and Line Plots of Vrms at X=6.00 in.

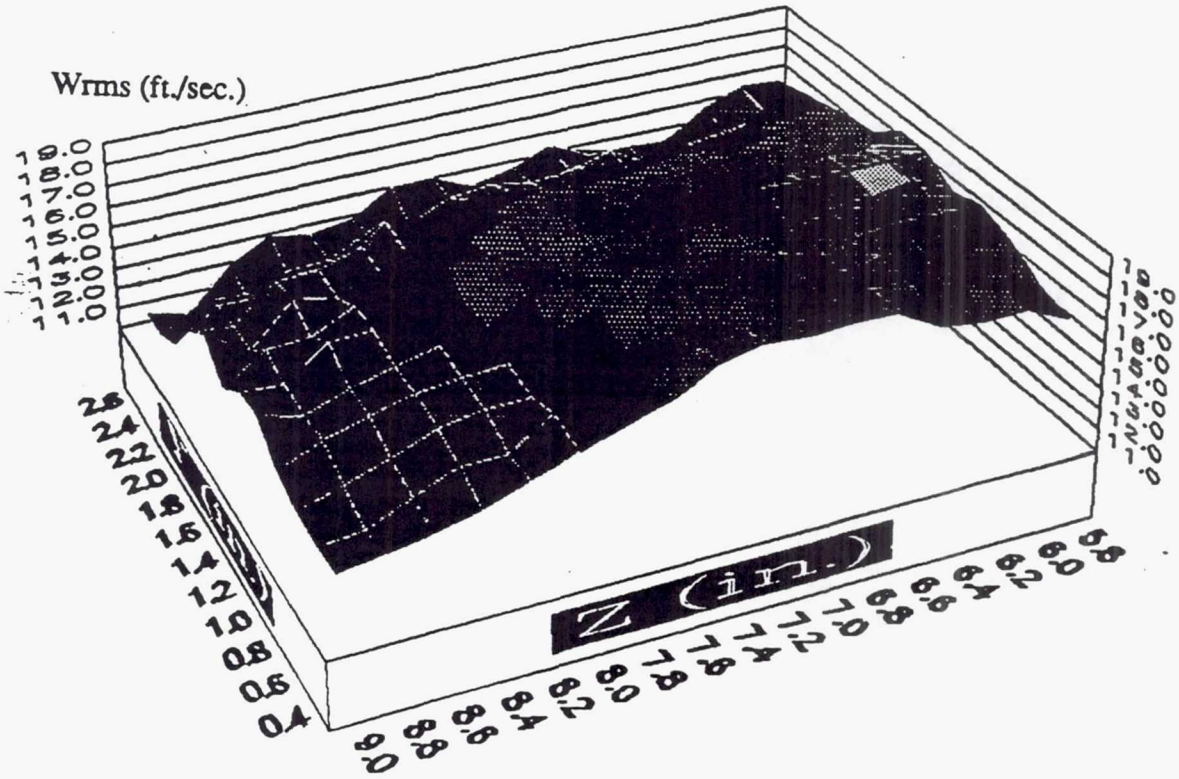

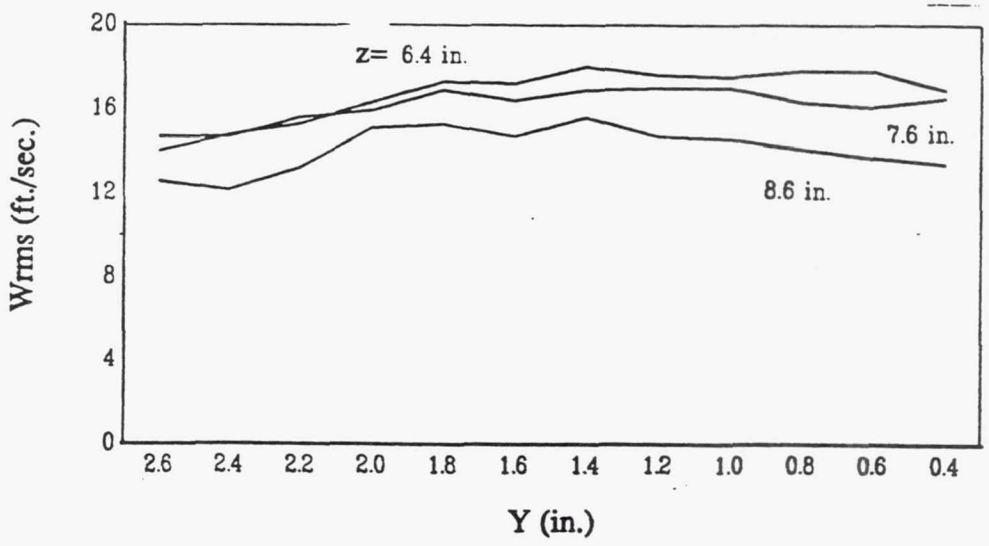

Figure 3.67 Contour and Line Plots of Wrms at X=6.00 in.

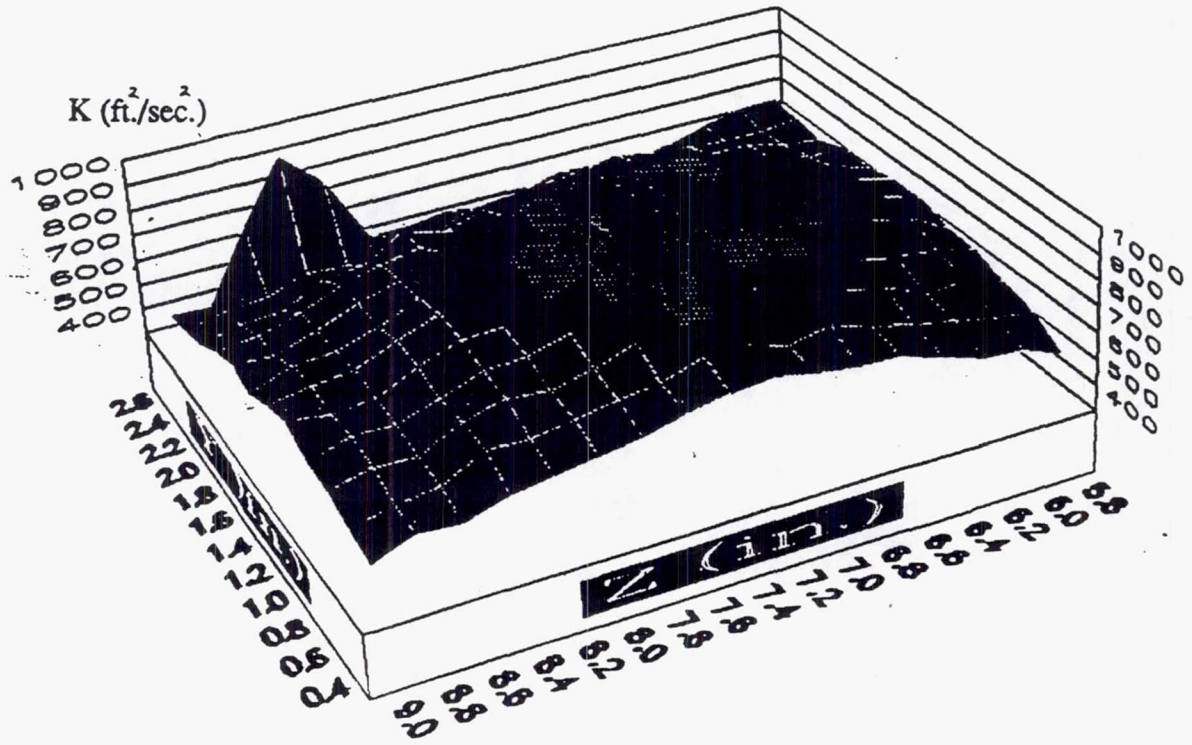

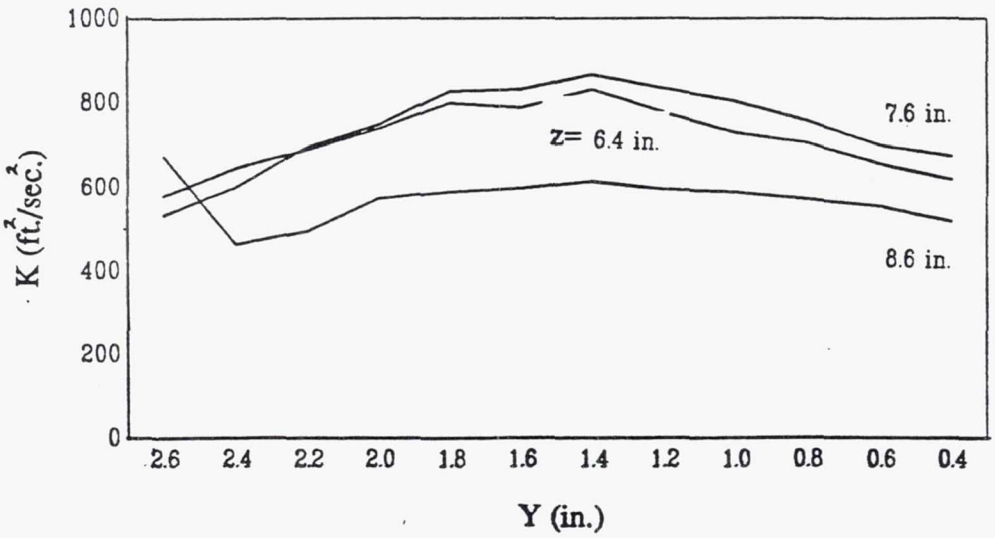

Figure 3.68 Contour and Line Plots of K at X=6.00 in.

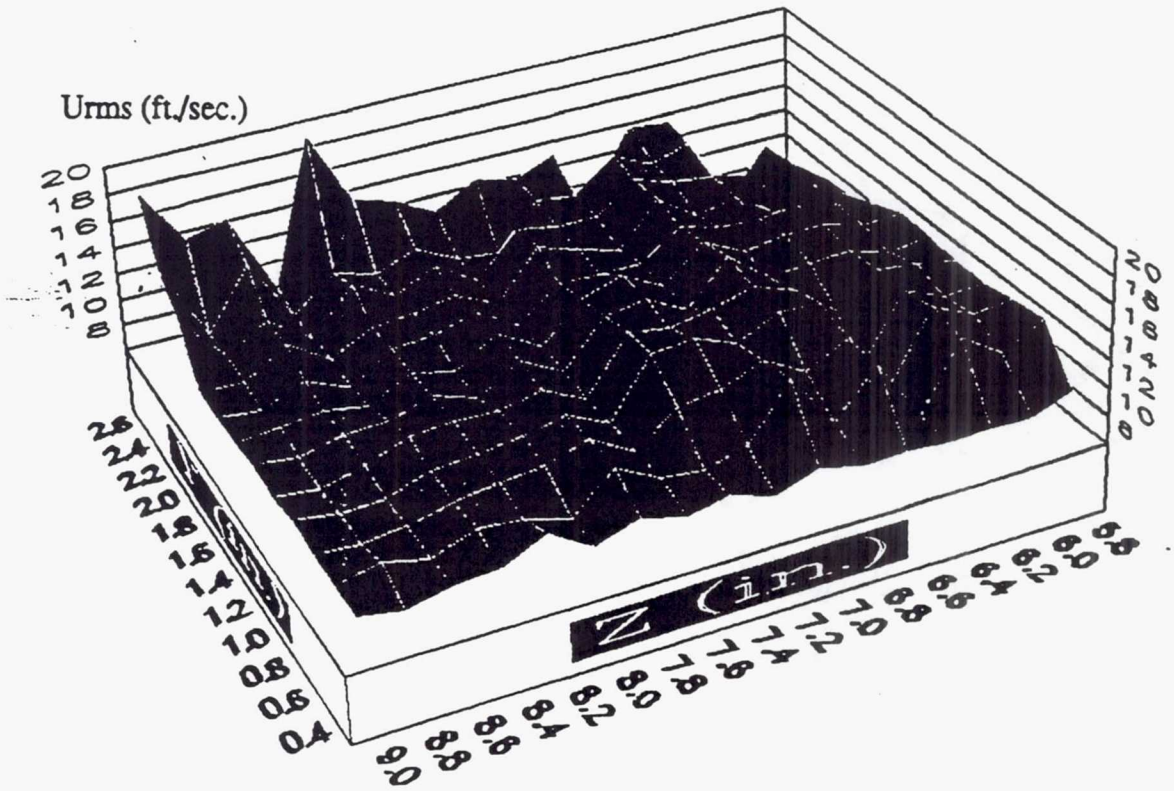

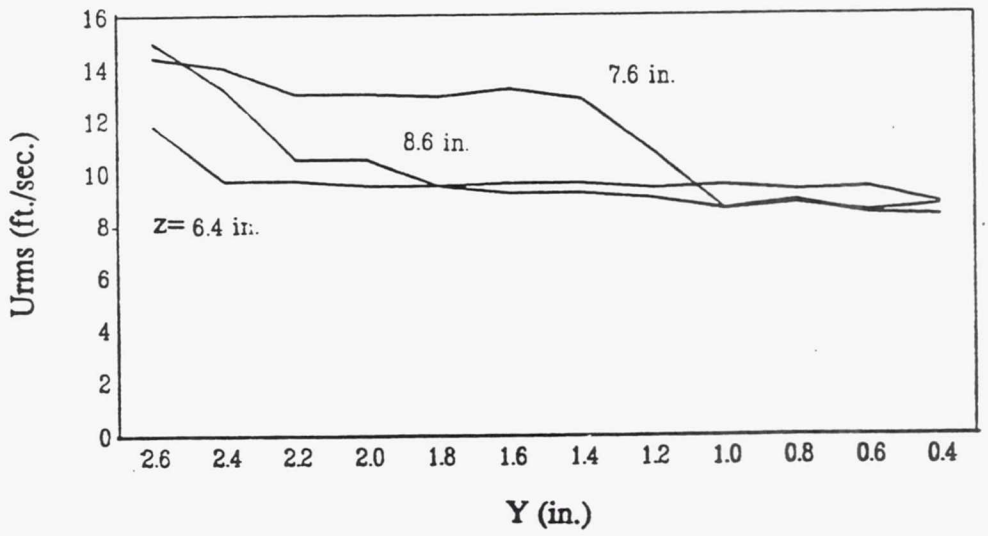

Figure 3.69 Contour and Line Plots of Urms at X=9.00 in.

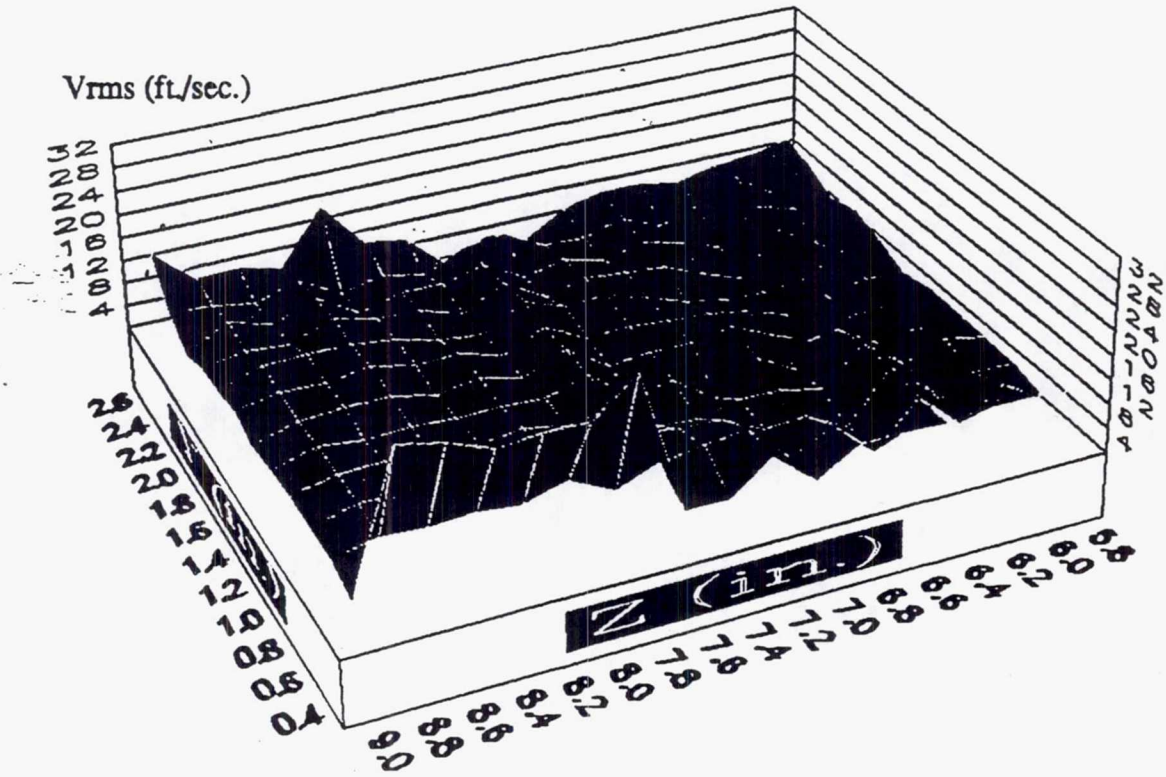

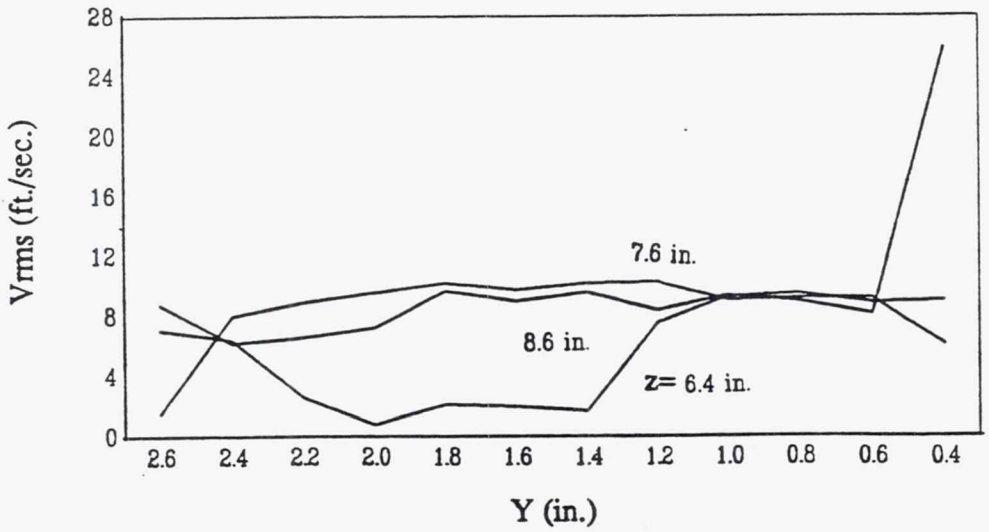

Figure 3.70 Contour and Line Plots of Vrms at X=9.00 in.

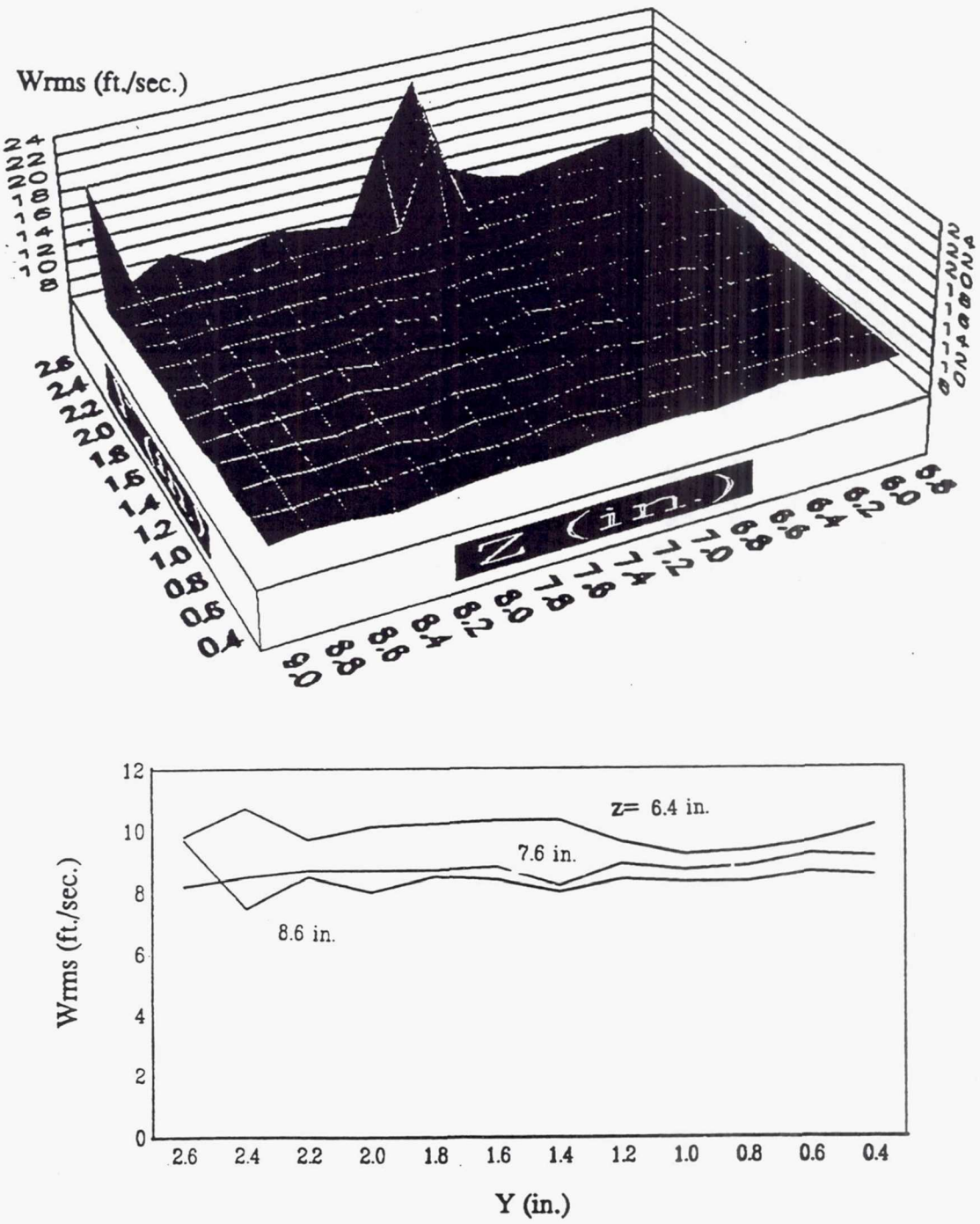

Figure 3.71 Contour and Line Plots of Wrms at X=9.00 in.

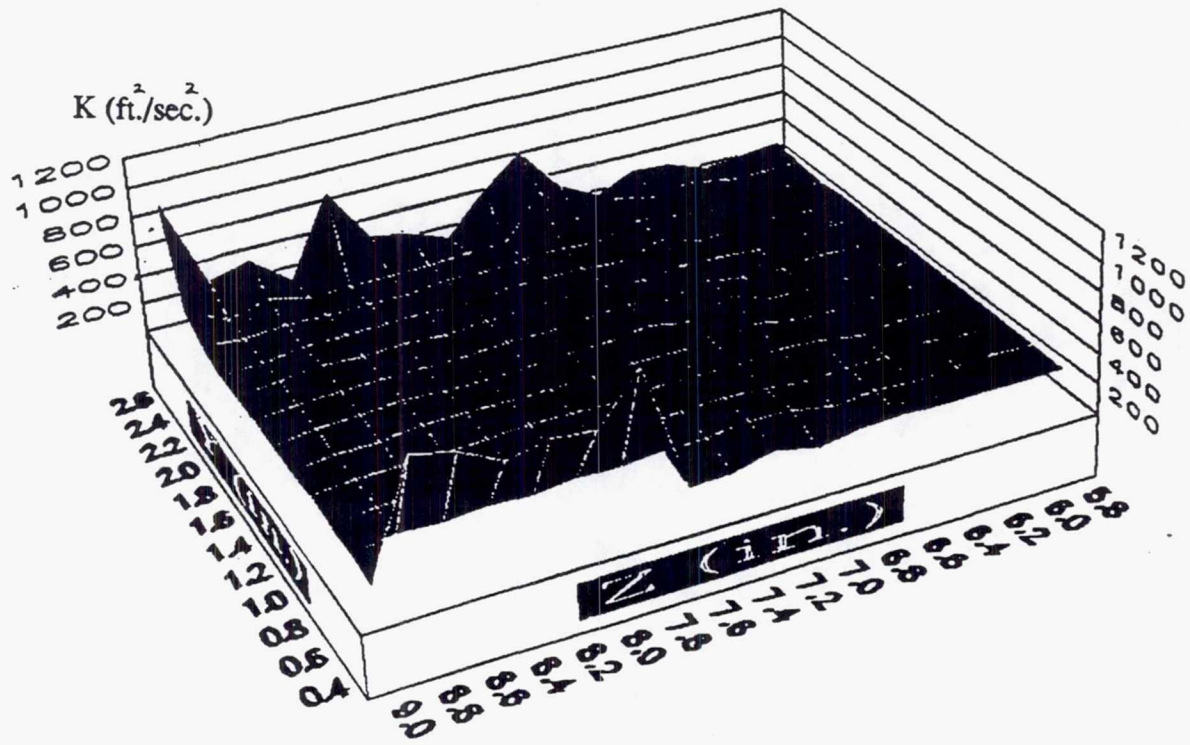

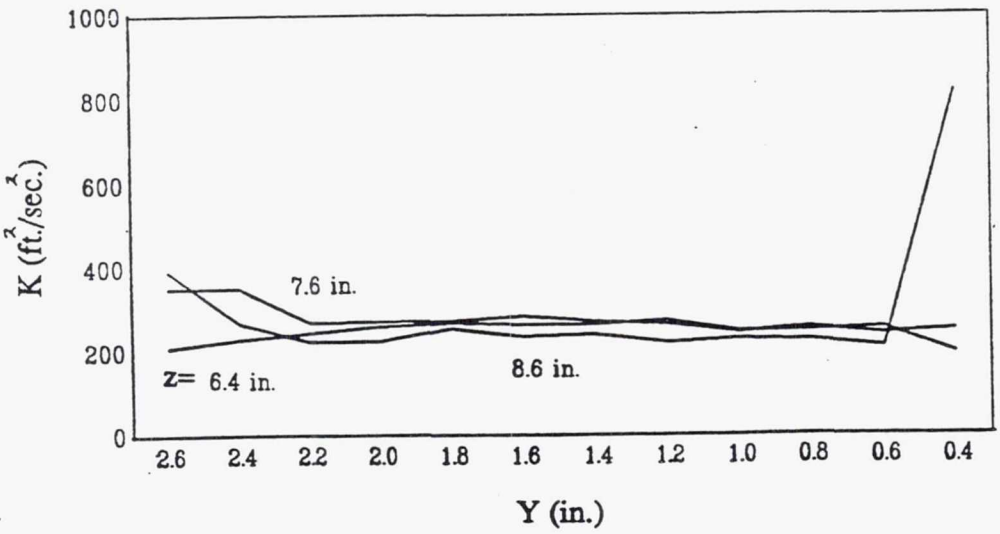

Figure 3.72 Contour and Line Plots of K at X=9.00 in.

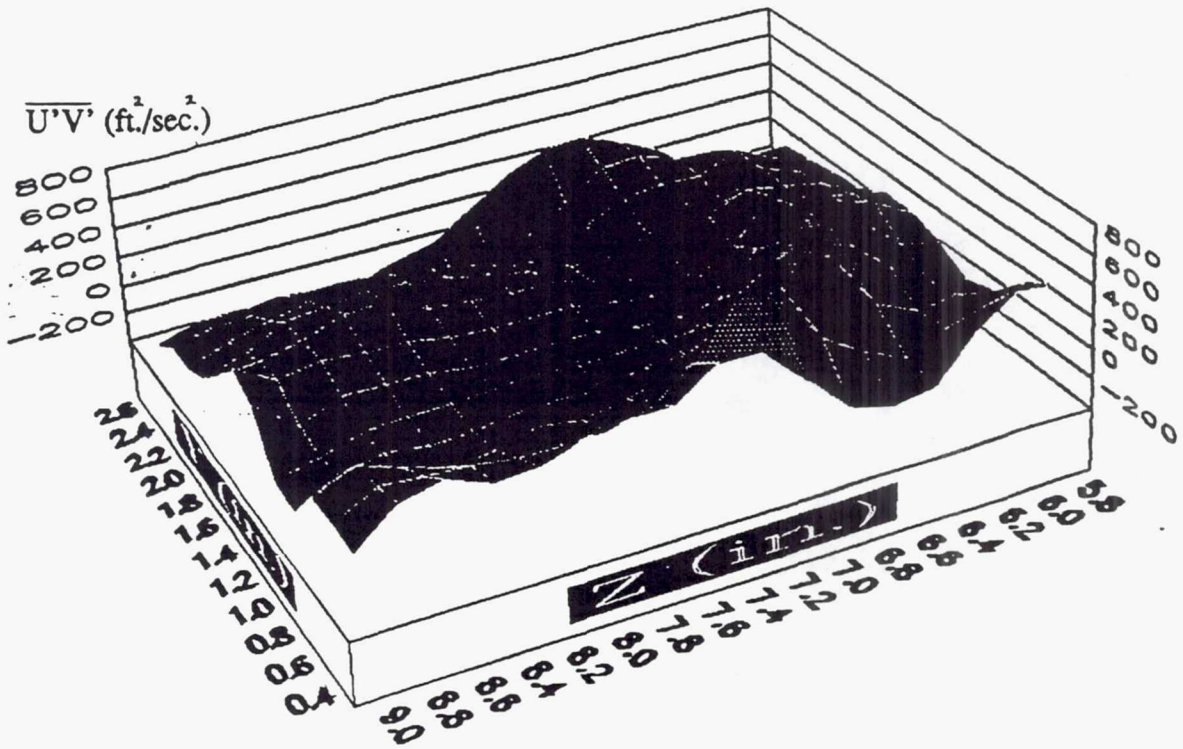

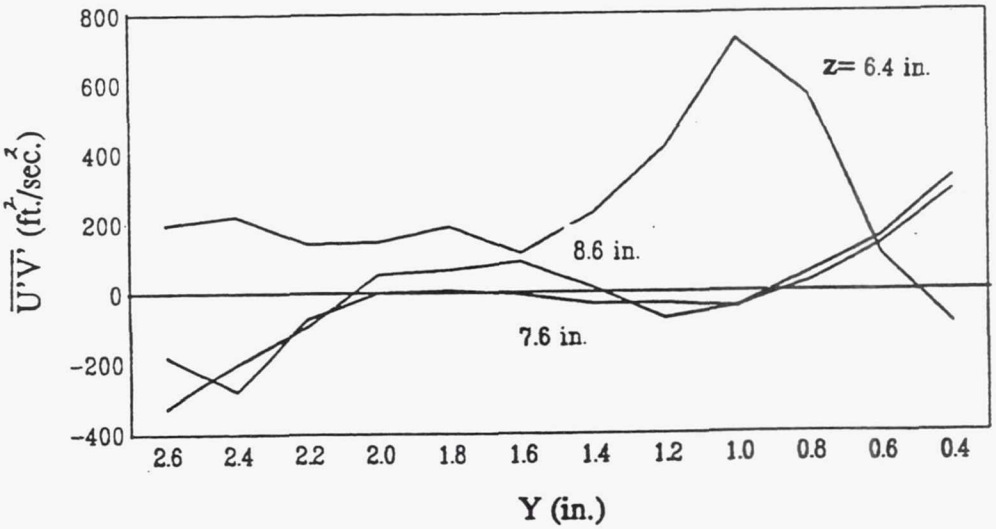

Figure 3.73 Contour and Line Plots of $\overline{U'V'}$ at X=1.00 in.

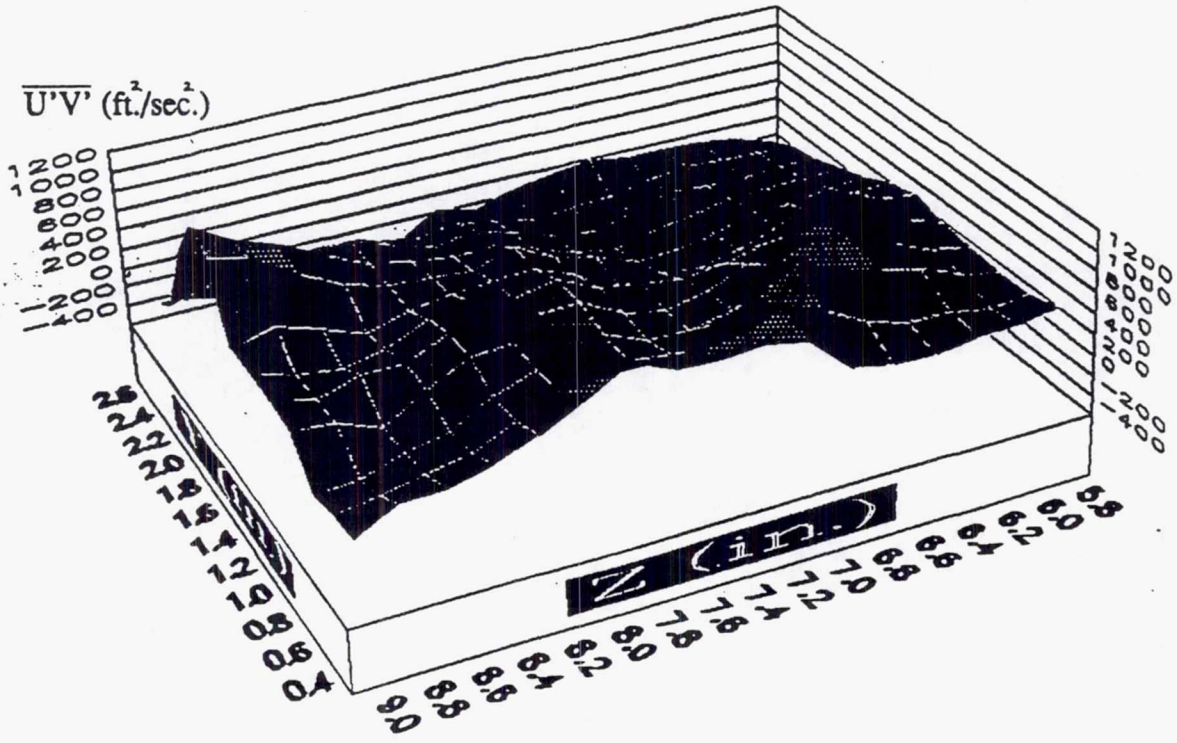

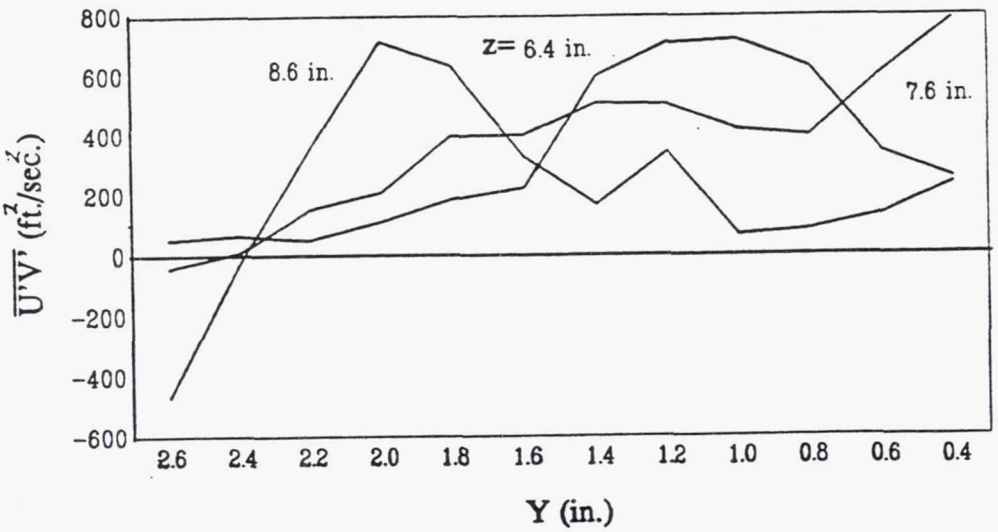

Figure 3.74 Contour and Line Plots of $\overline{U'V'}$ at X=1.50 in.

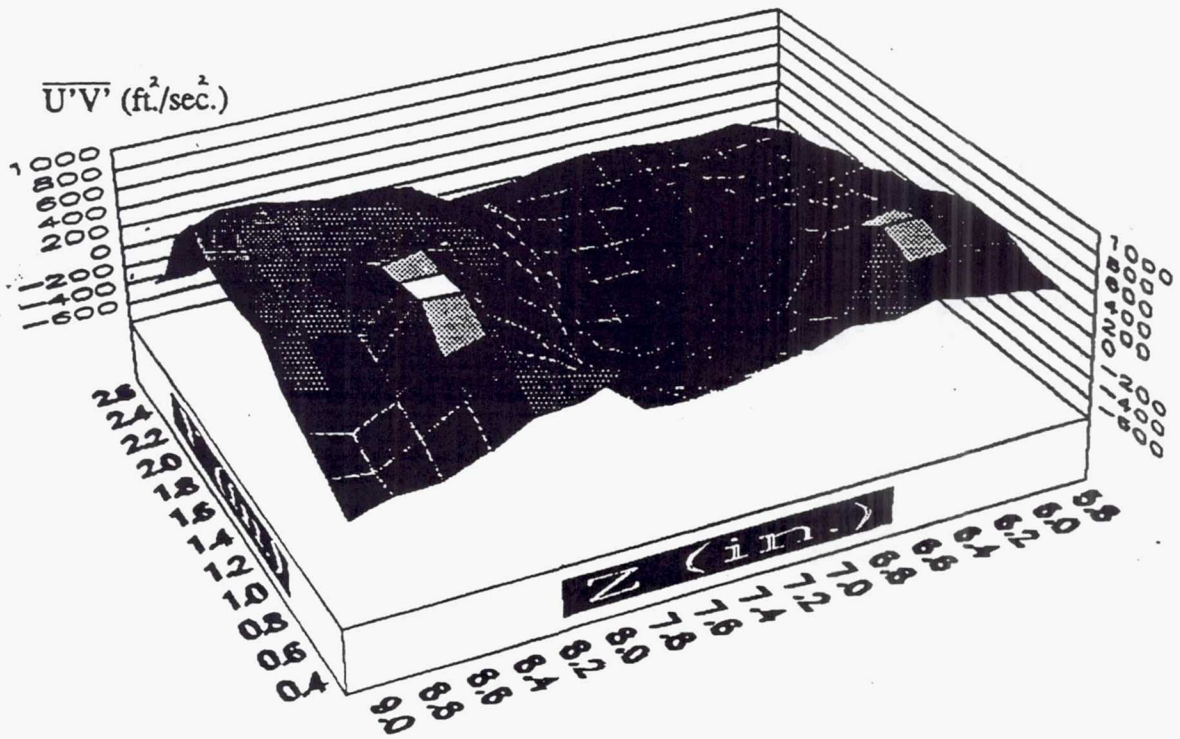

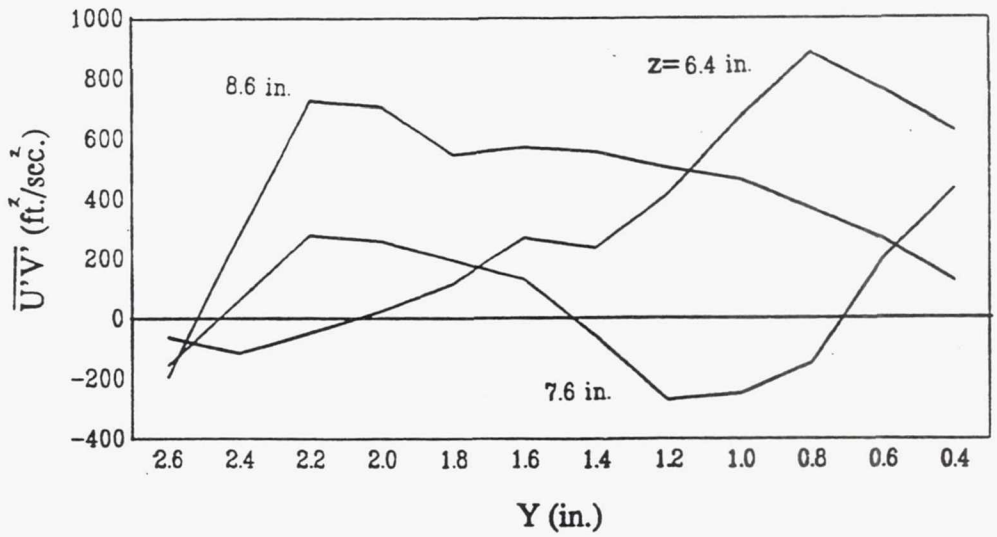

Figure 3.75 Contour and Line Plots of $\overline{U'V'}$ at X=2.00 in.

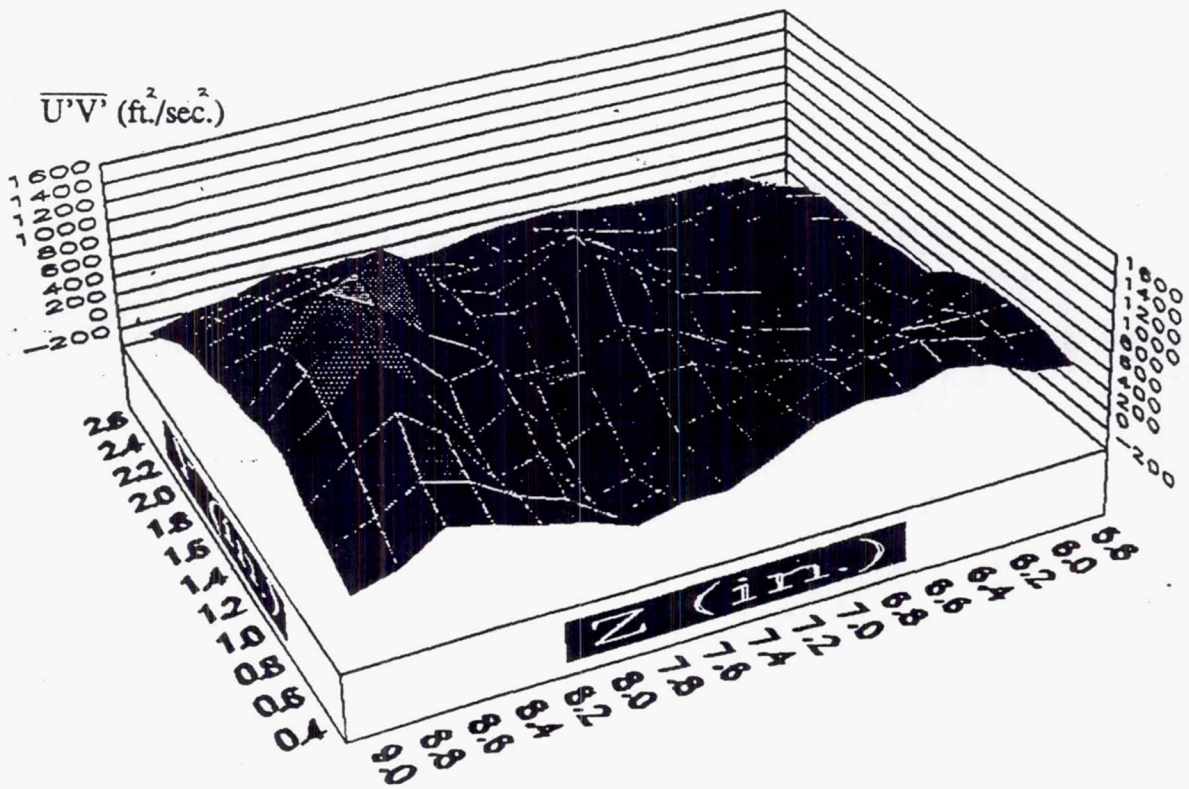

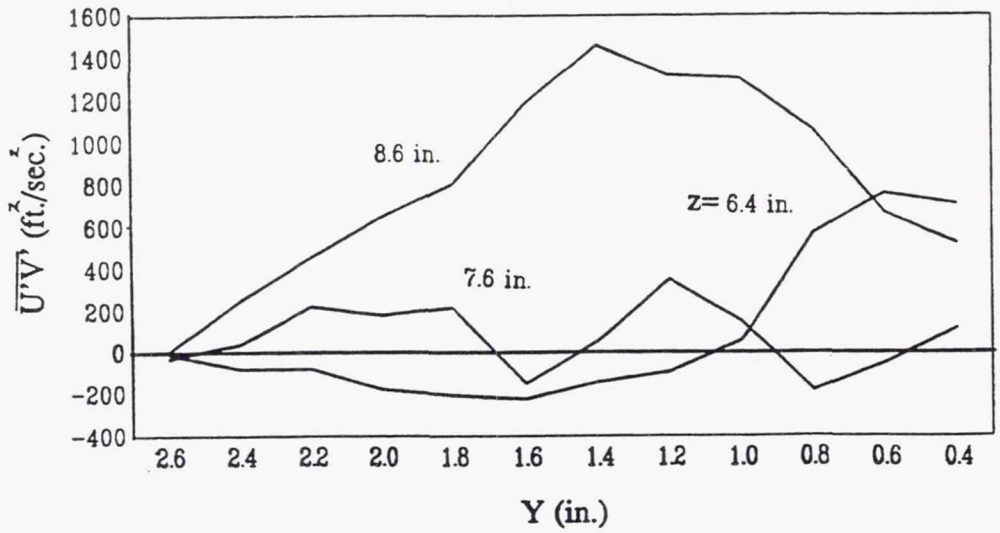

Figure 3.76 Contour and Line Plots of $\overline{U'V'}$ at X=2.50 in.

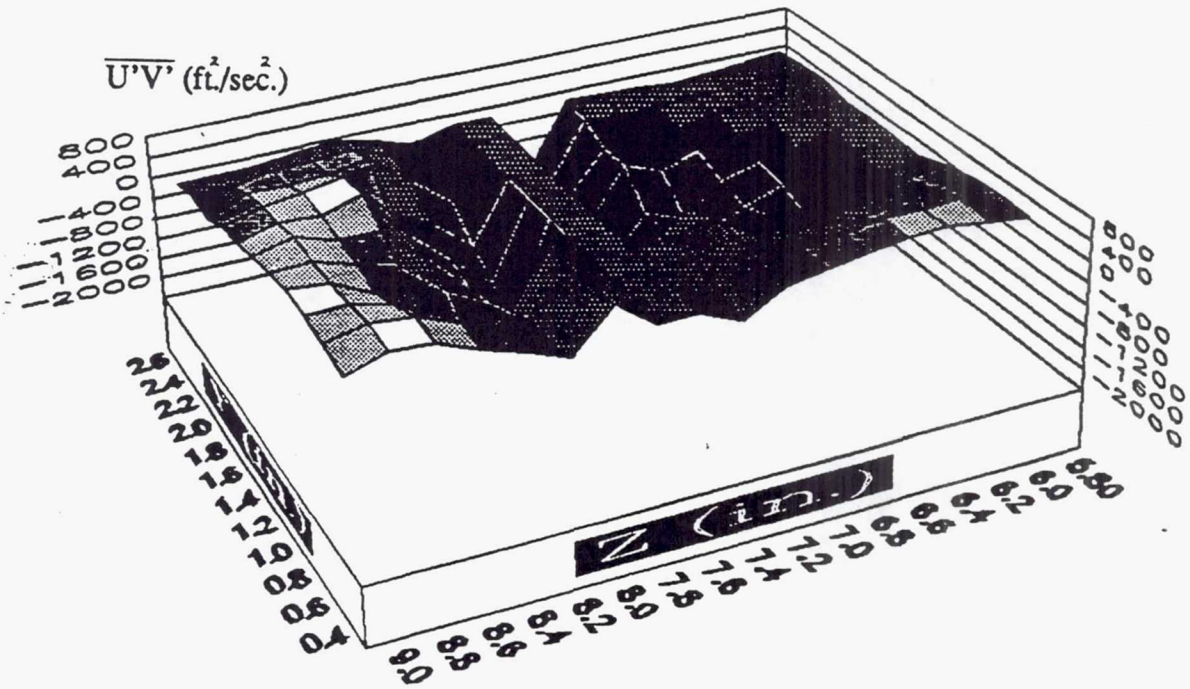

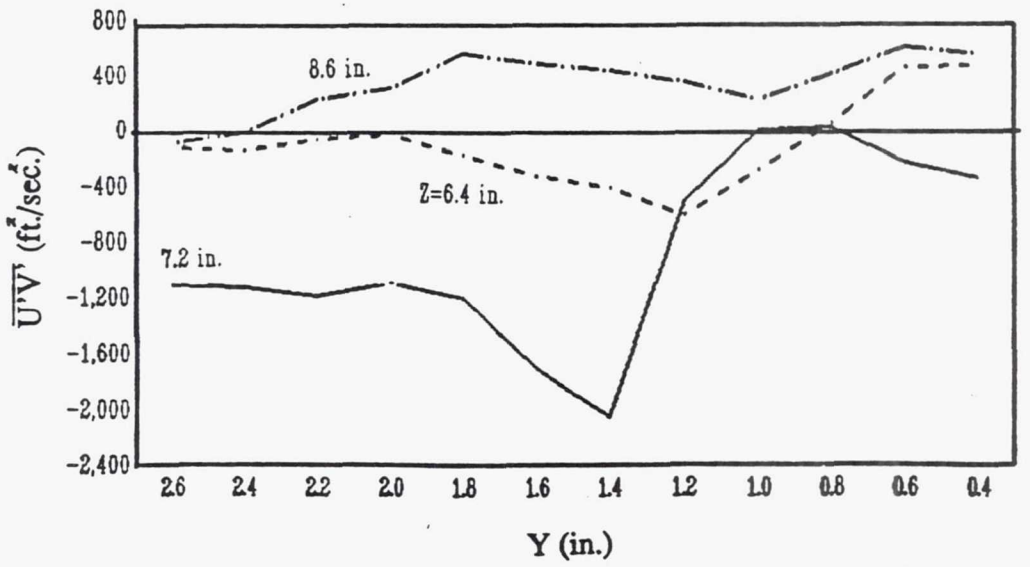

Figure 3.77 Contour and Line Plots of $\overline{U'V'}$ at X=3.00 in.

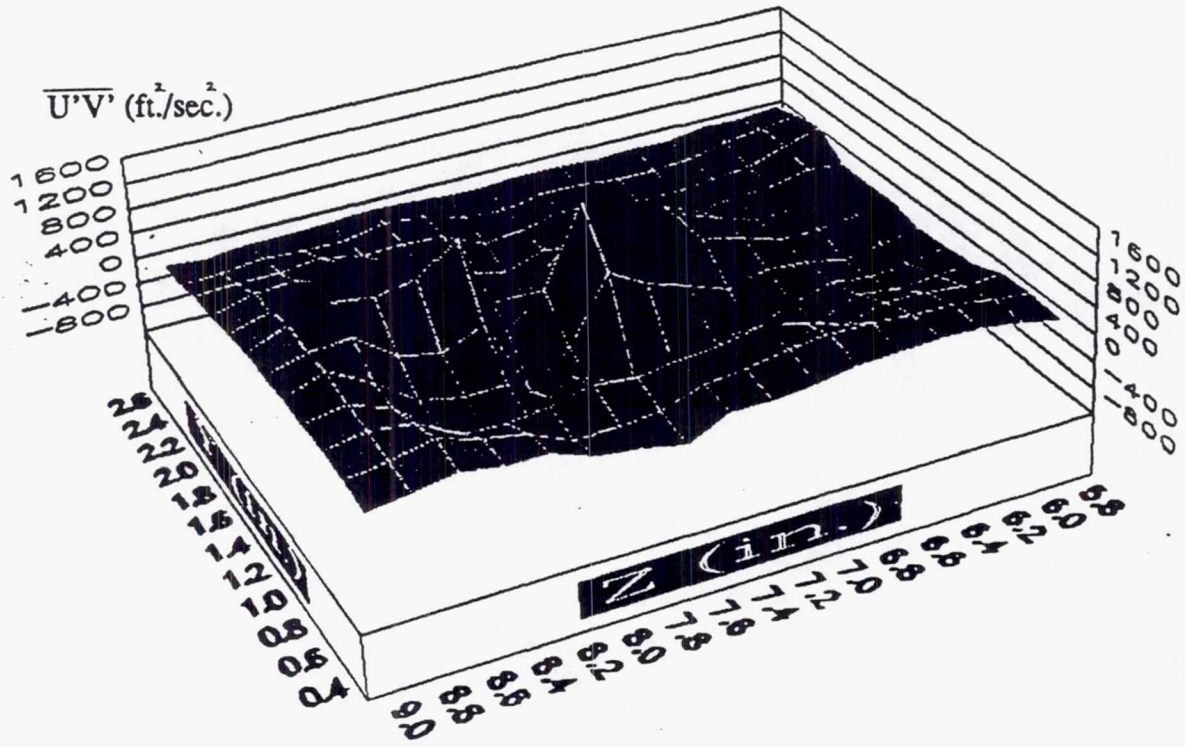

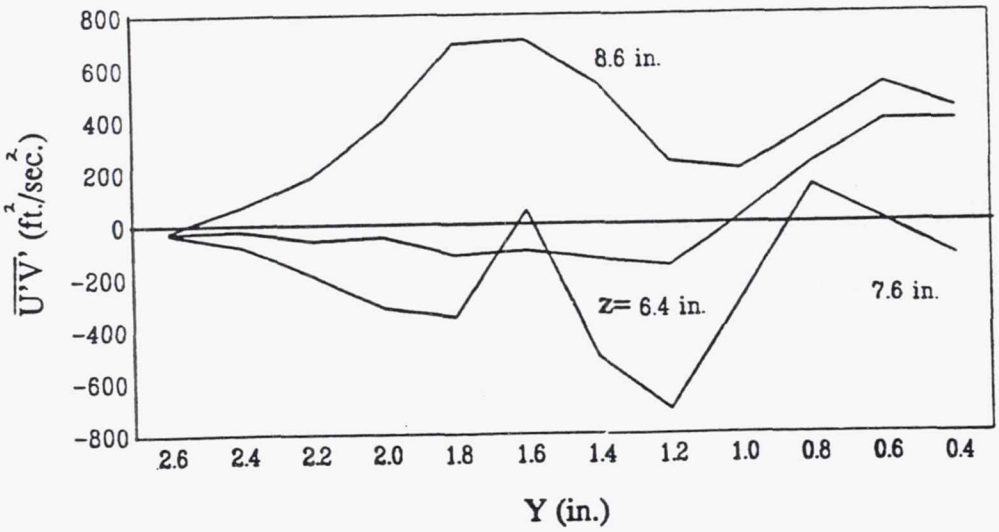

Figure 3.78 Contour and Line Plots of $\overline{U'V'}$ at X=3.50 in.

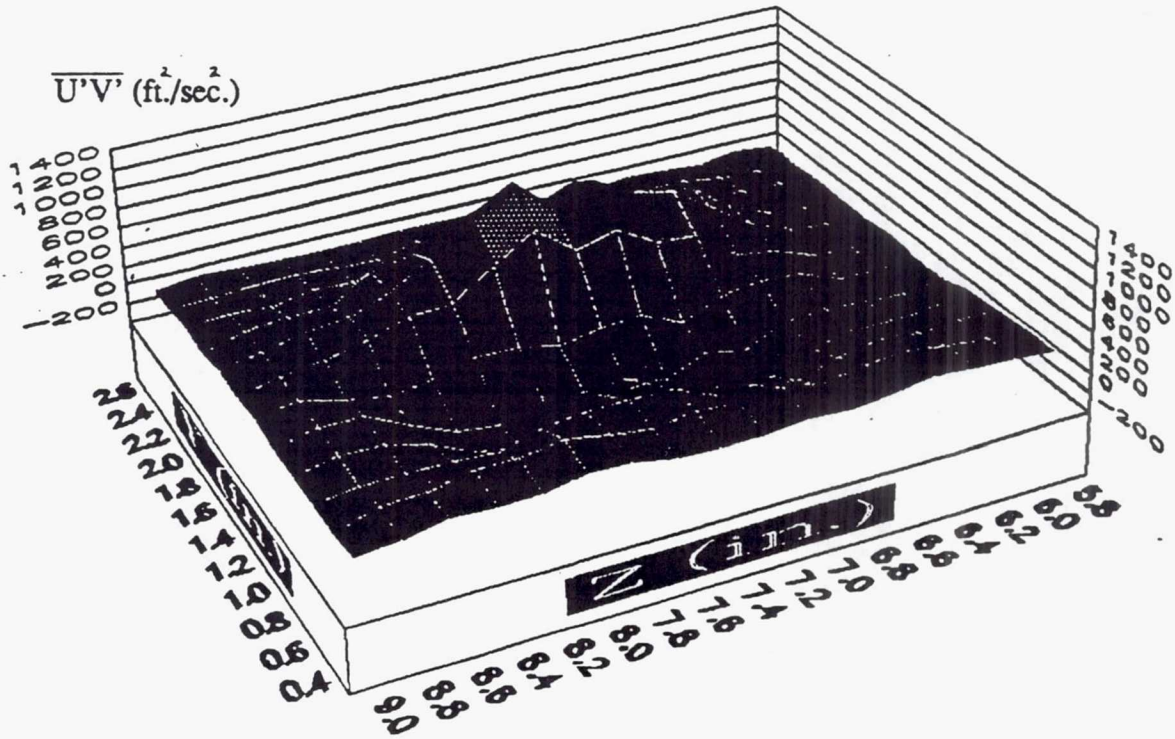

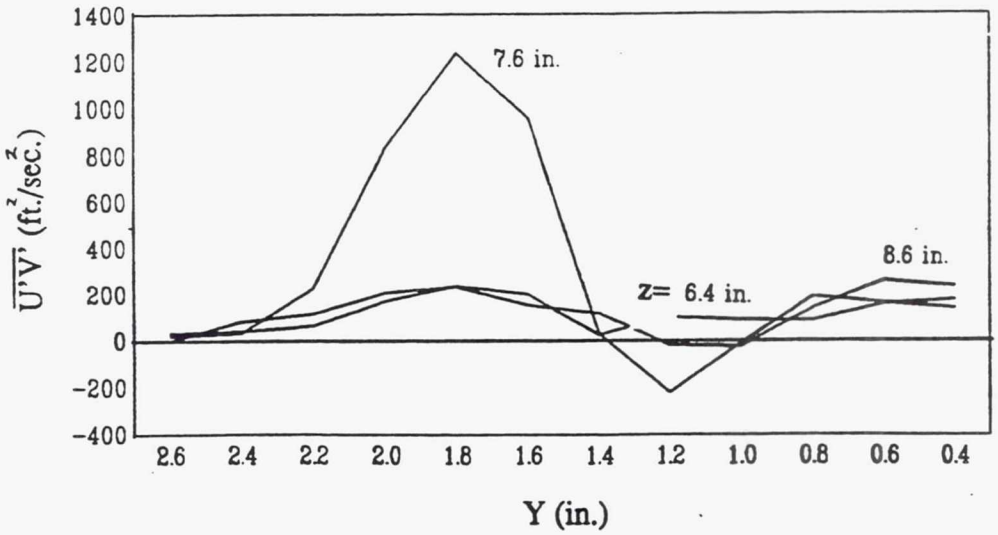

Figure 3.79 Contour and Line Plots of $\overline{U'V'}$ at X=4.00 in.

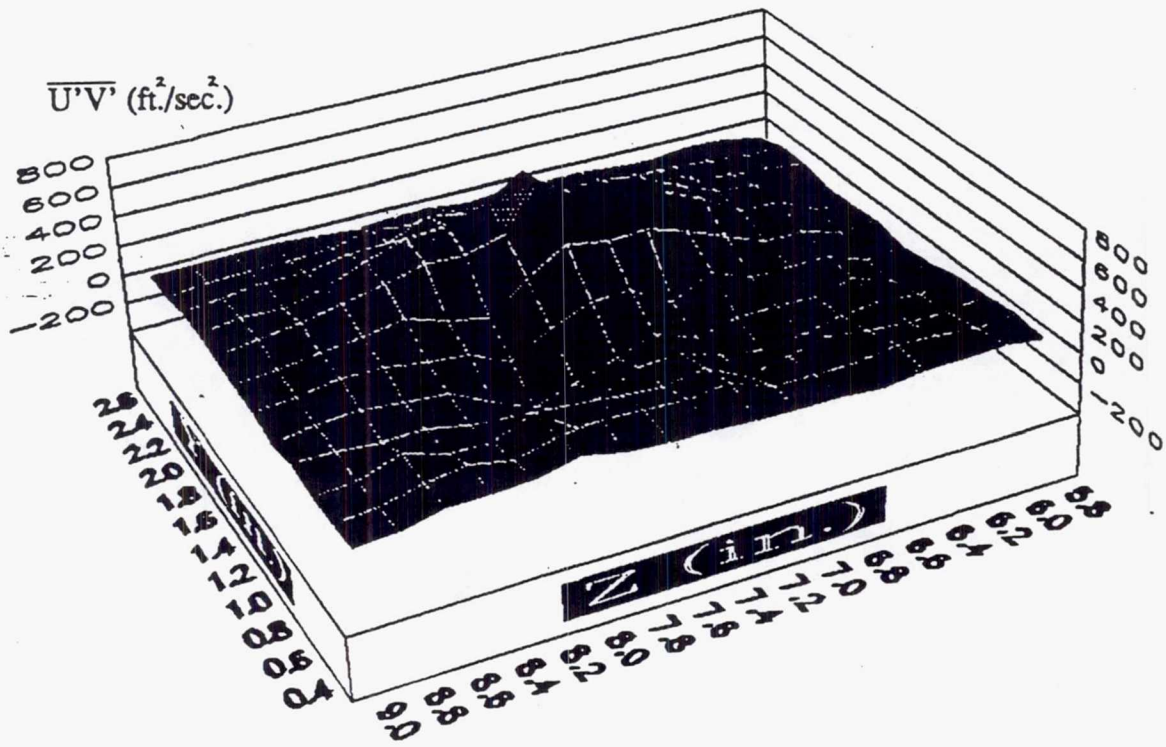

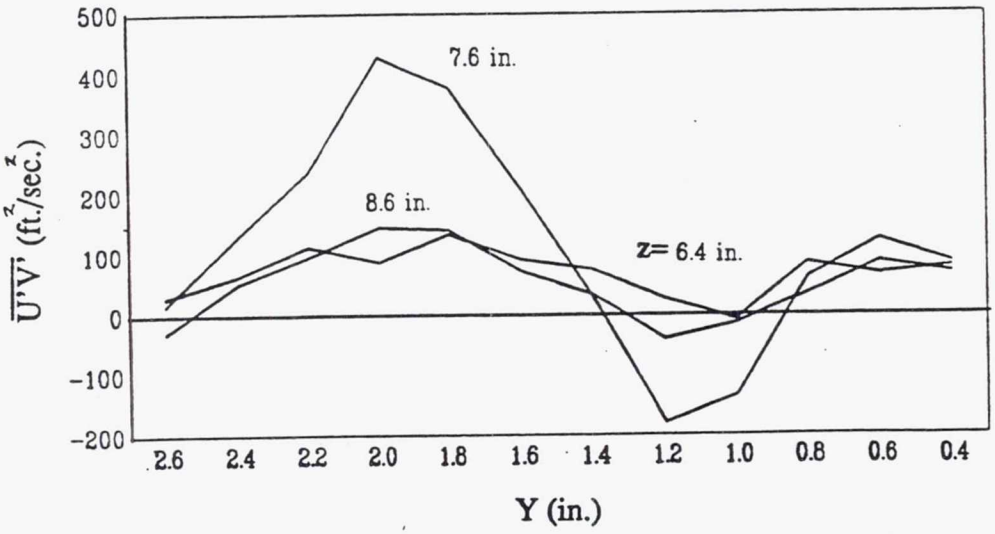

Figure 3.80 Contour and Line Plots of $\overline{U'V'}$ at X=4.50 in.

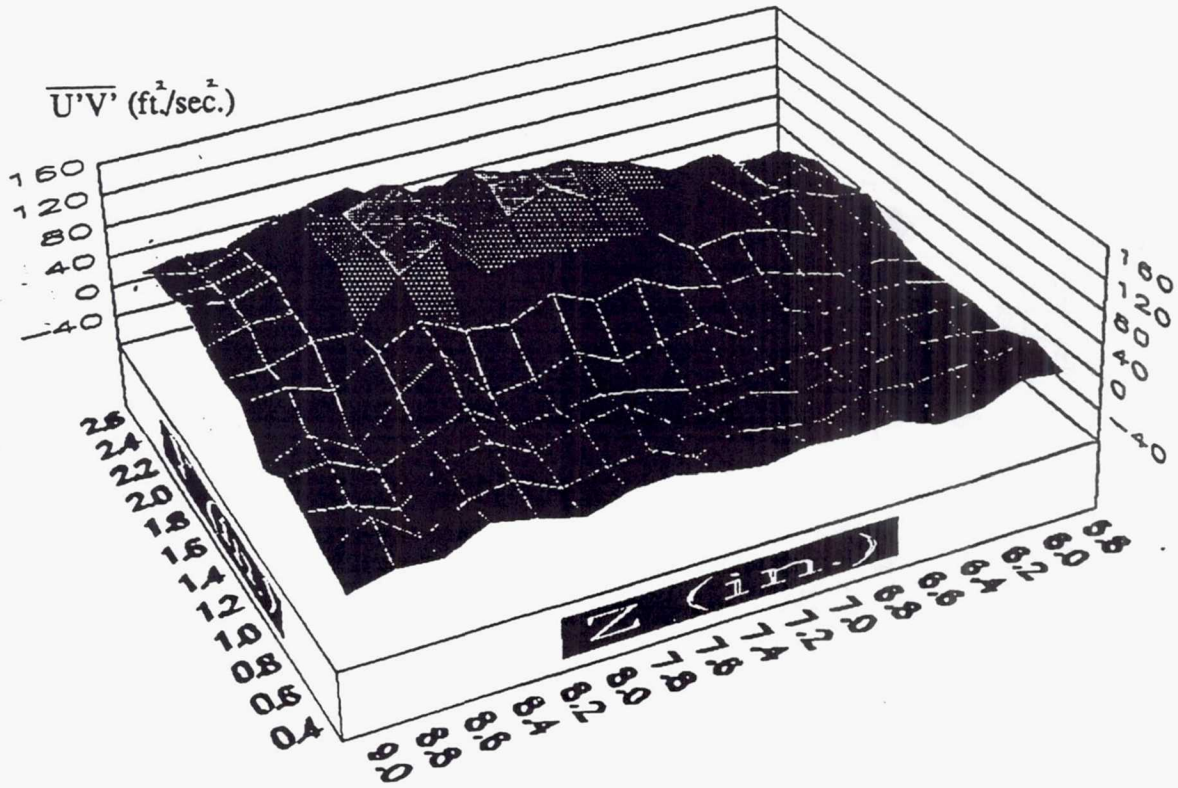

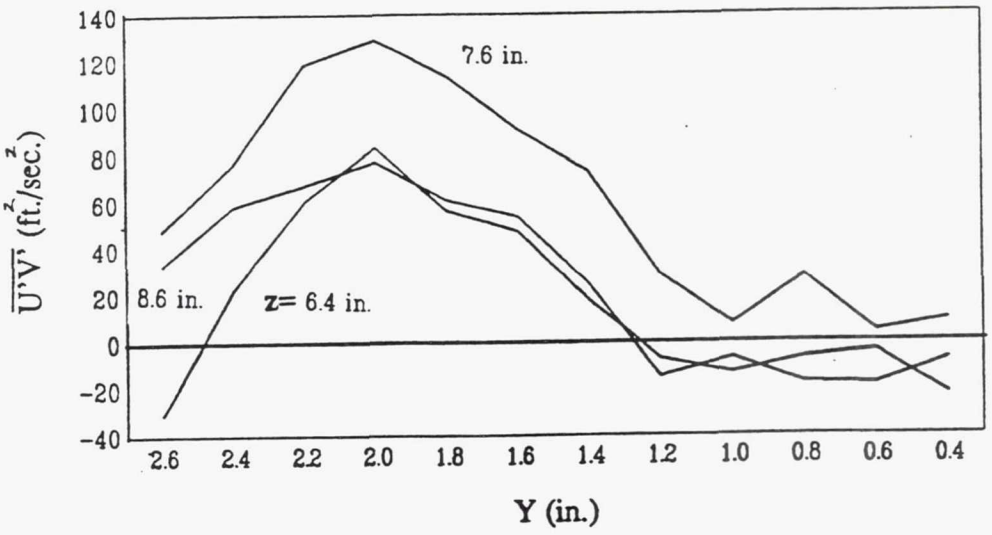

Figure 3.81 Contour and Line Plots of $\overline{U'V'}$ at X=6.00 in.

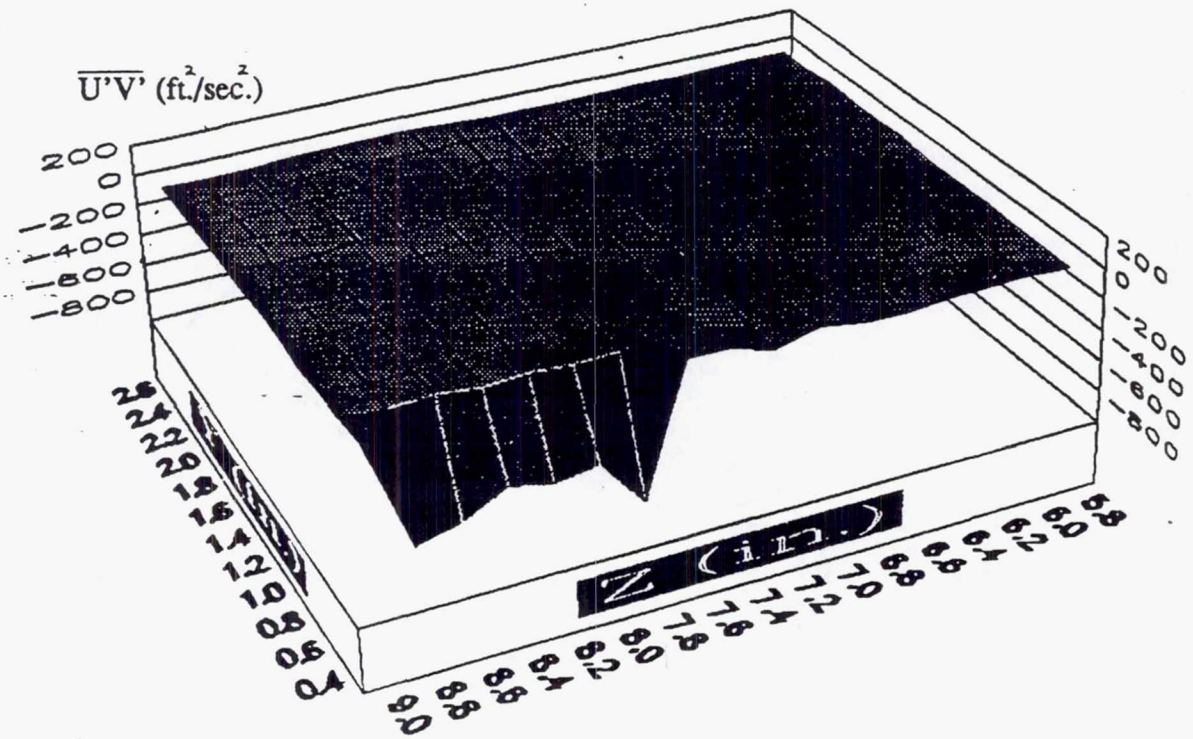

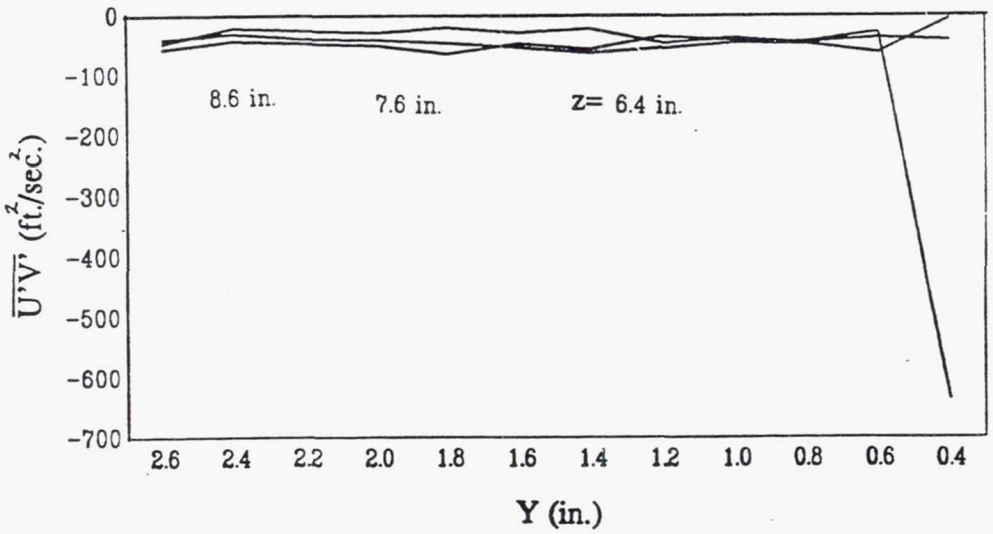

Figure 3.82 Contour and Line Plots of $\overline{U'V'}$ at X=9.00 in.

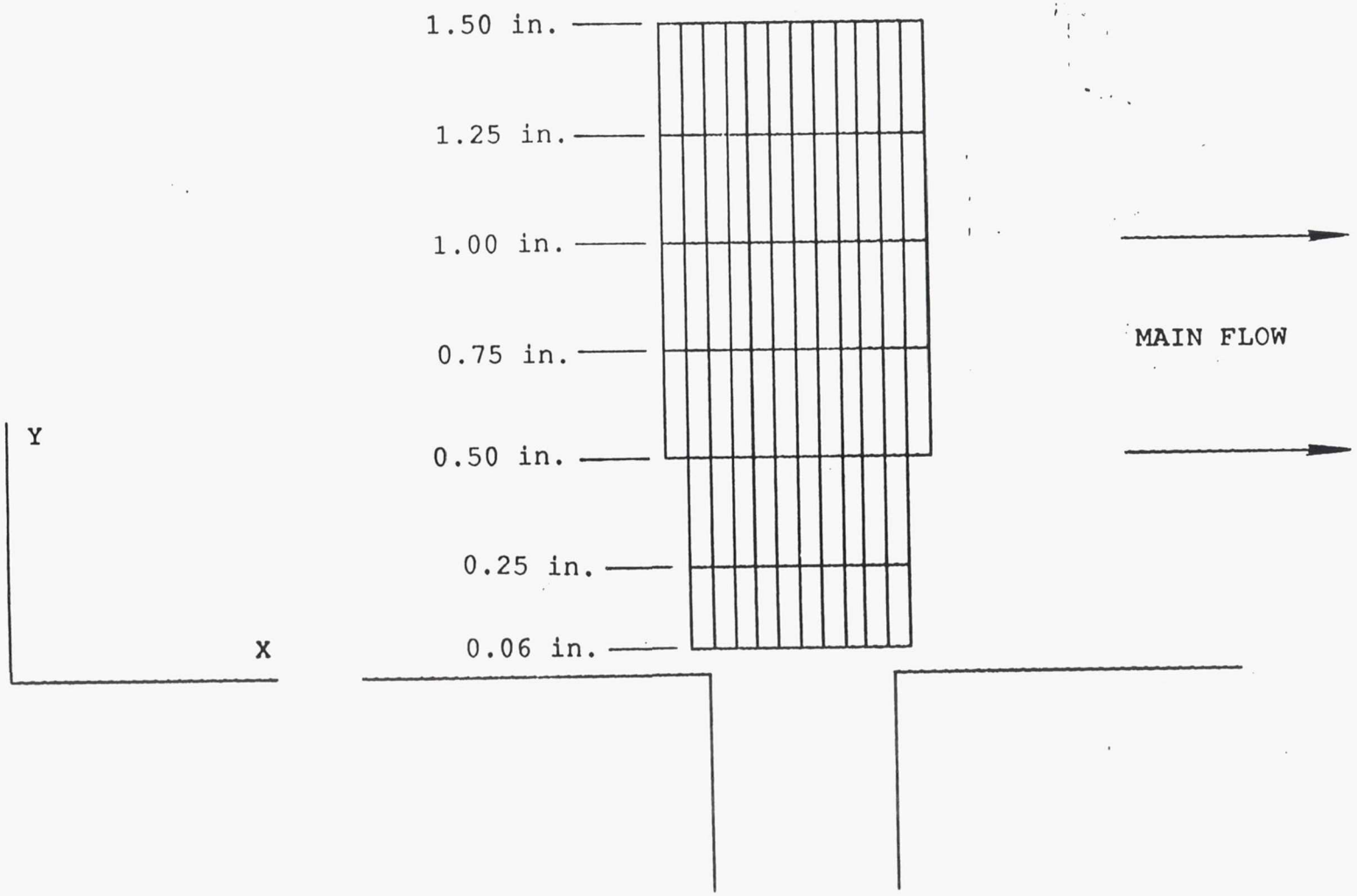

Figure 3.83 XY-Plane Measurement Grid for the Primary Cross Jets

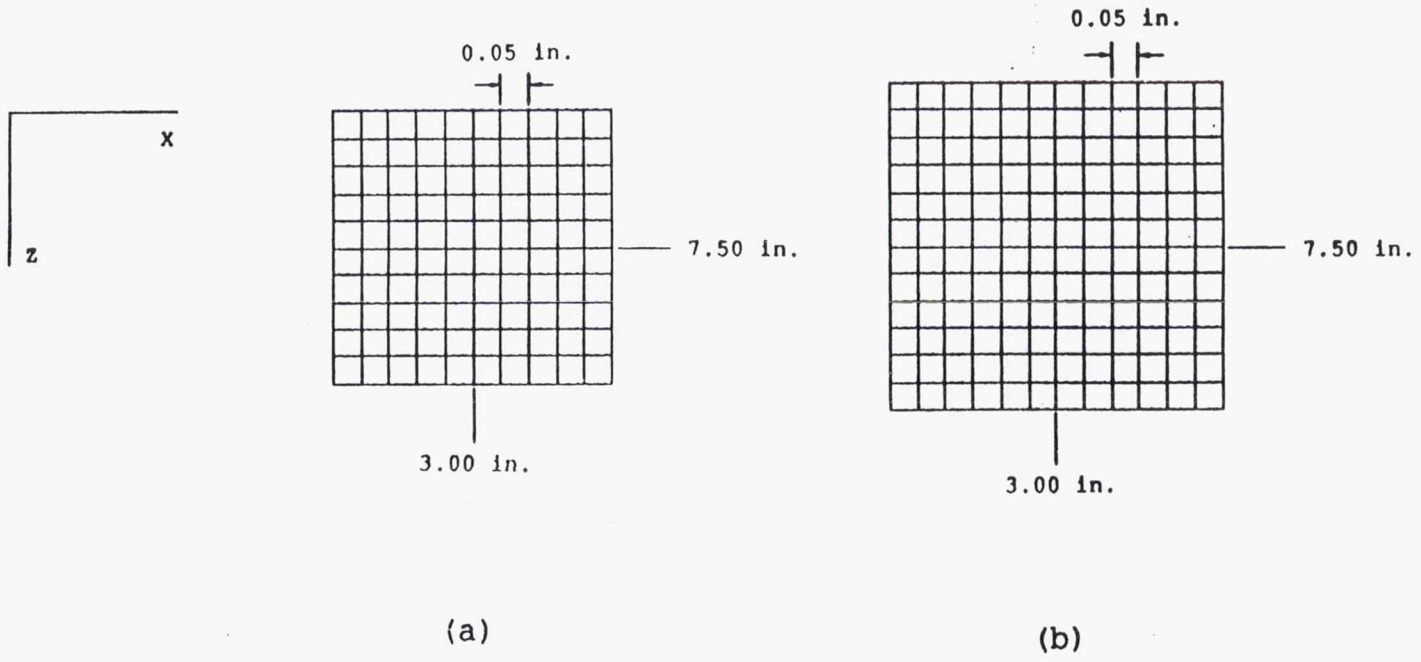

Figure 3.84 XZ-Plane Measurement Grids for the Primary Cross Jets for: (a) Y=0.06 in. and Y=0.25 in.; (b) Y=0.50, 0.75, 1.00, 1.25 and 1.50 in.

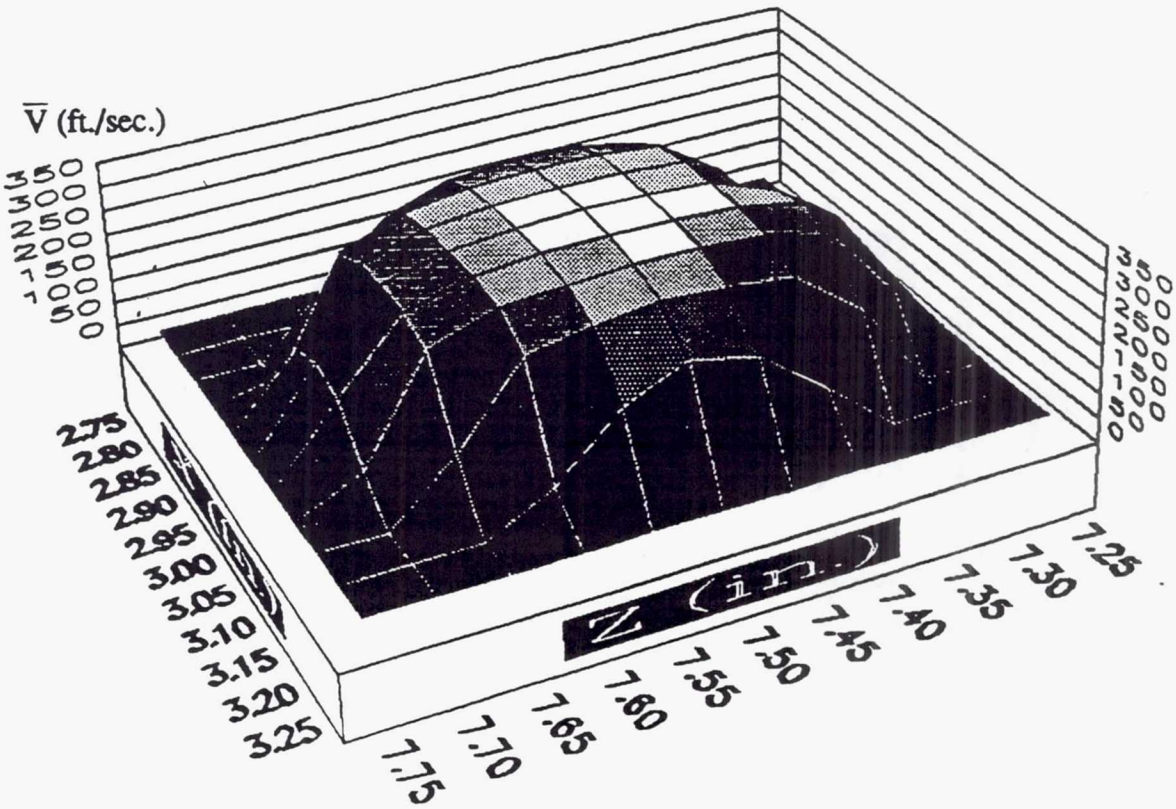

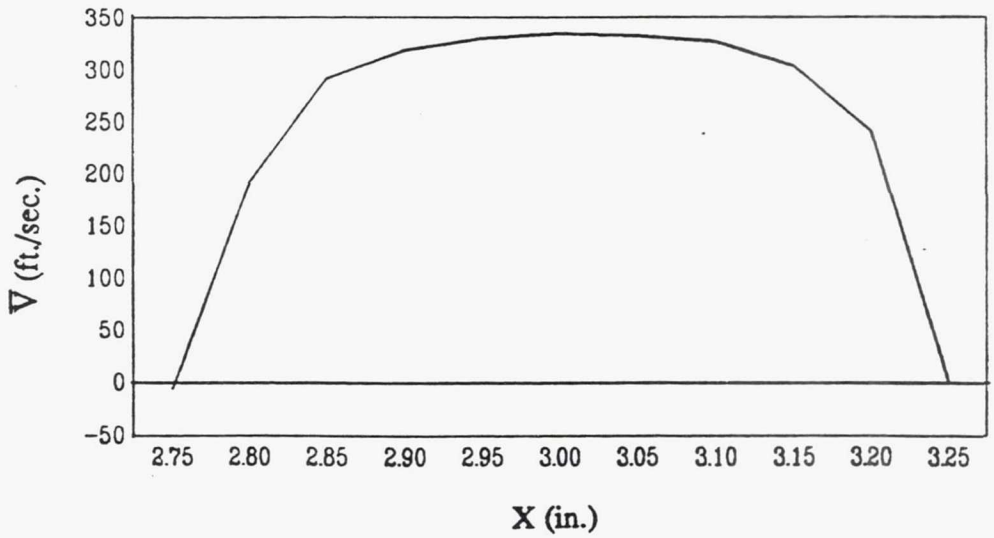

Figure 3.85 Contour and Line Plots of $\overline{V}$ for Primary Cross Jet at Y=0.06 in.

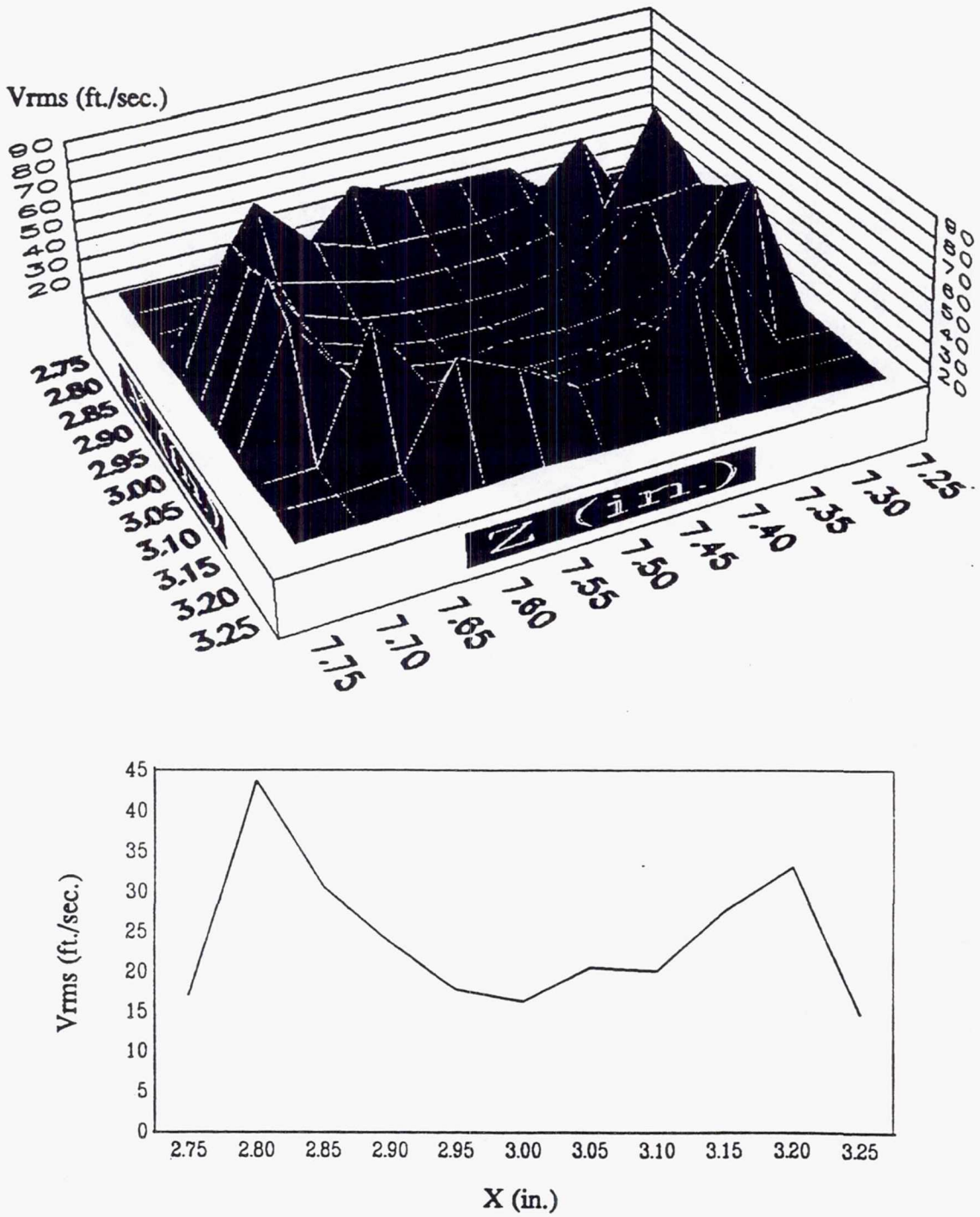

Figure 3.86 Contour and Line Plots of Vrms for Primary Cross Jet at Y=0.06 in.

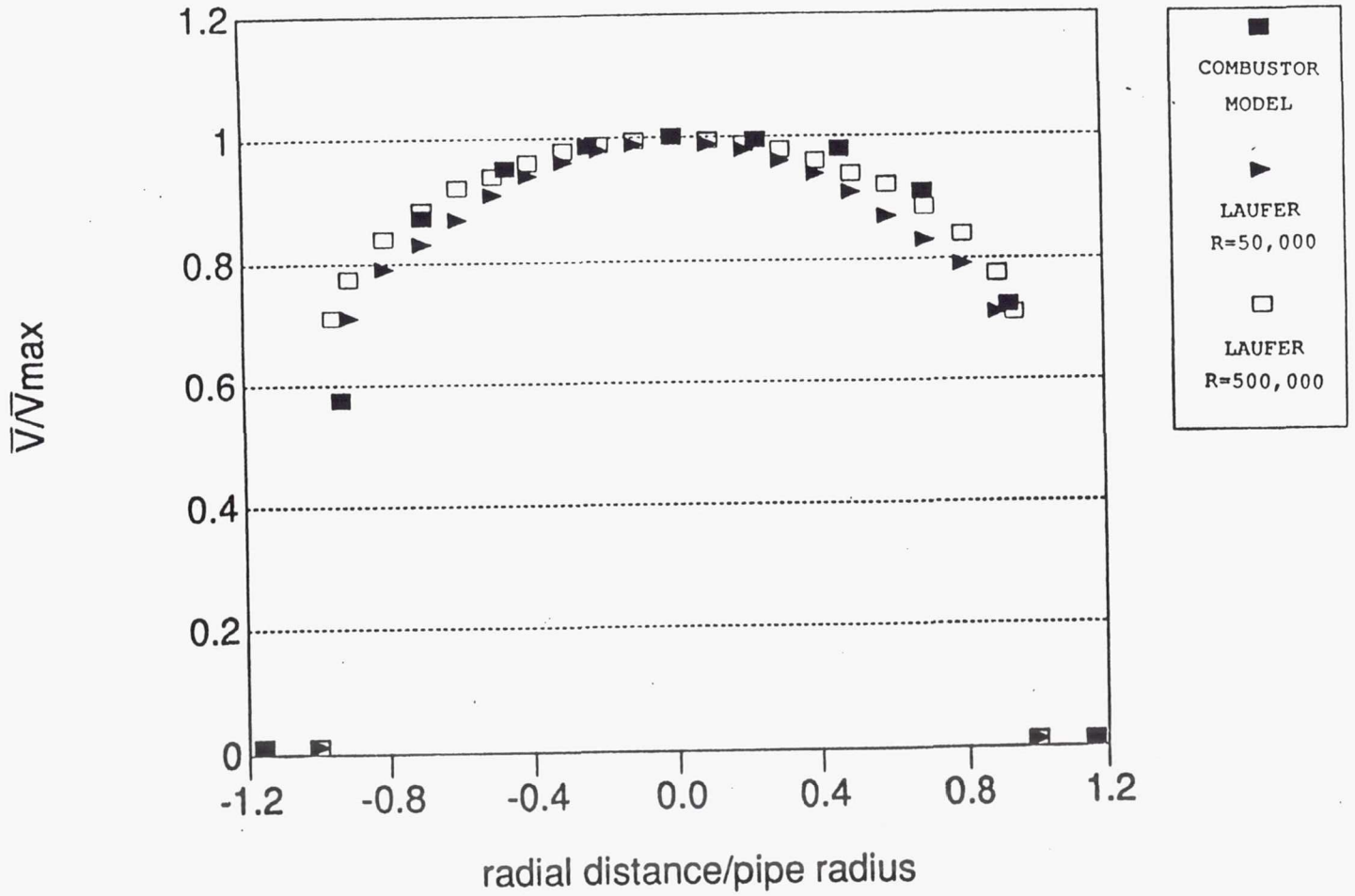

Figure 3.87 Comparison of $\overline{V}$ Data at Y=0.06 in. to Classical Pipe Flow Data of Laufer

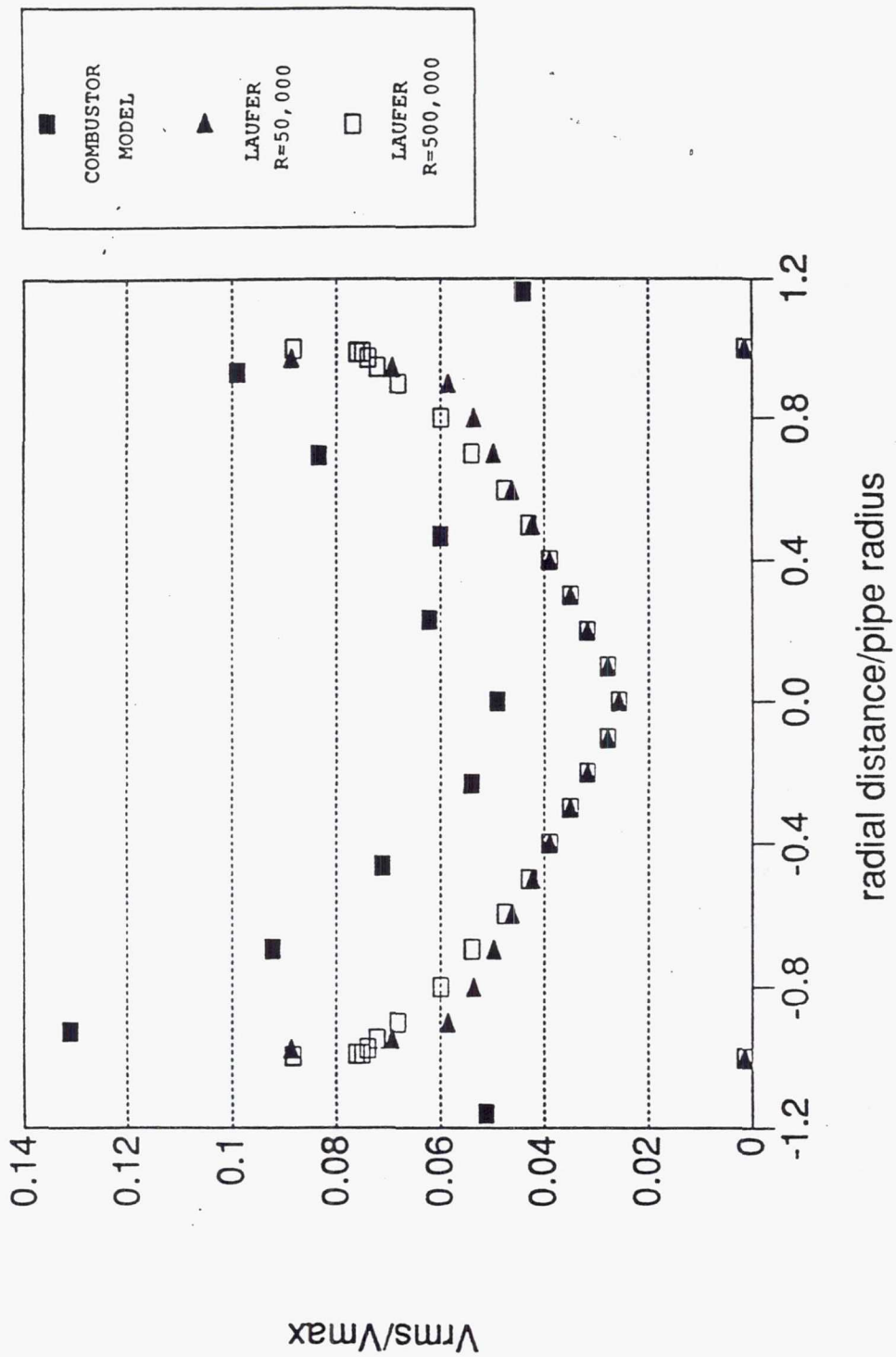

Figure 3.88 Comparison of Vrms Data at Y=0.06 in. to Classical Pipe Flow Data of Laufer

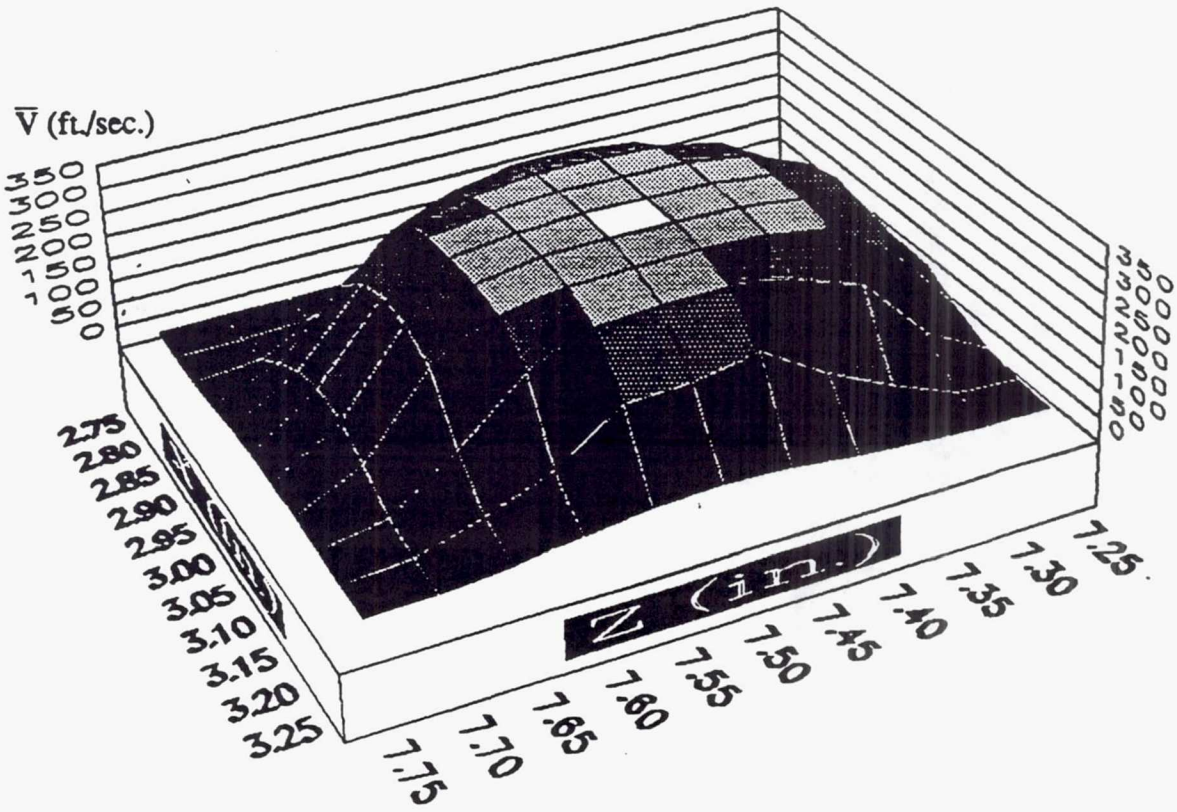

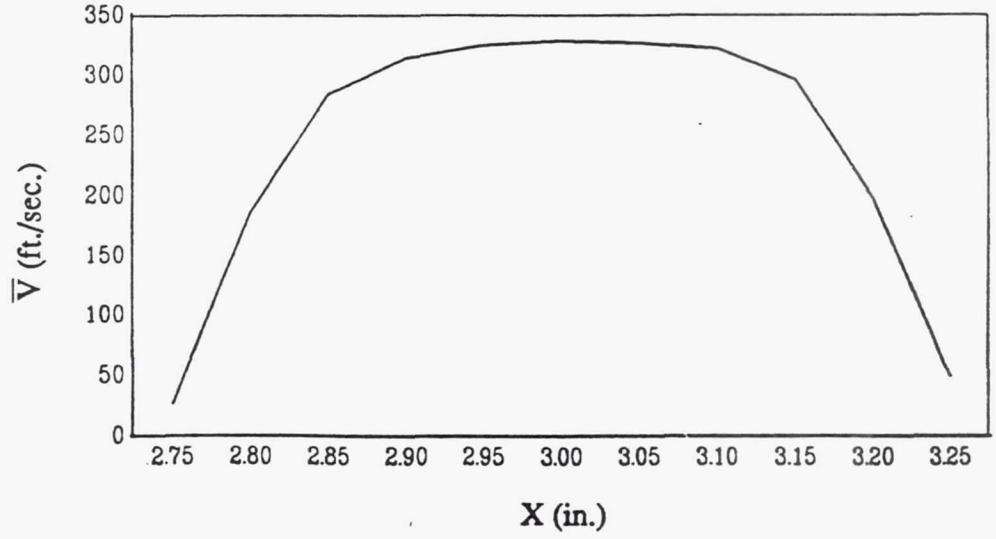

Figure 3.89 Contour and Line Plots of $\overline{V}$ for Primary Cross Jet at Y=0.25 in.

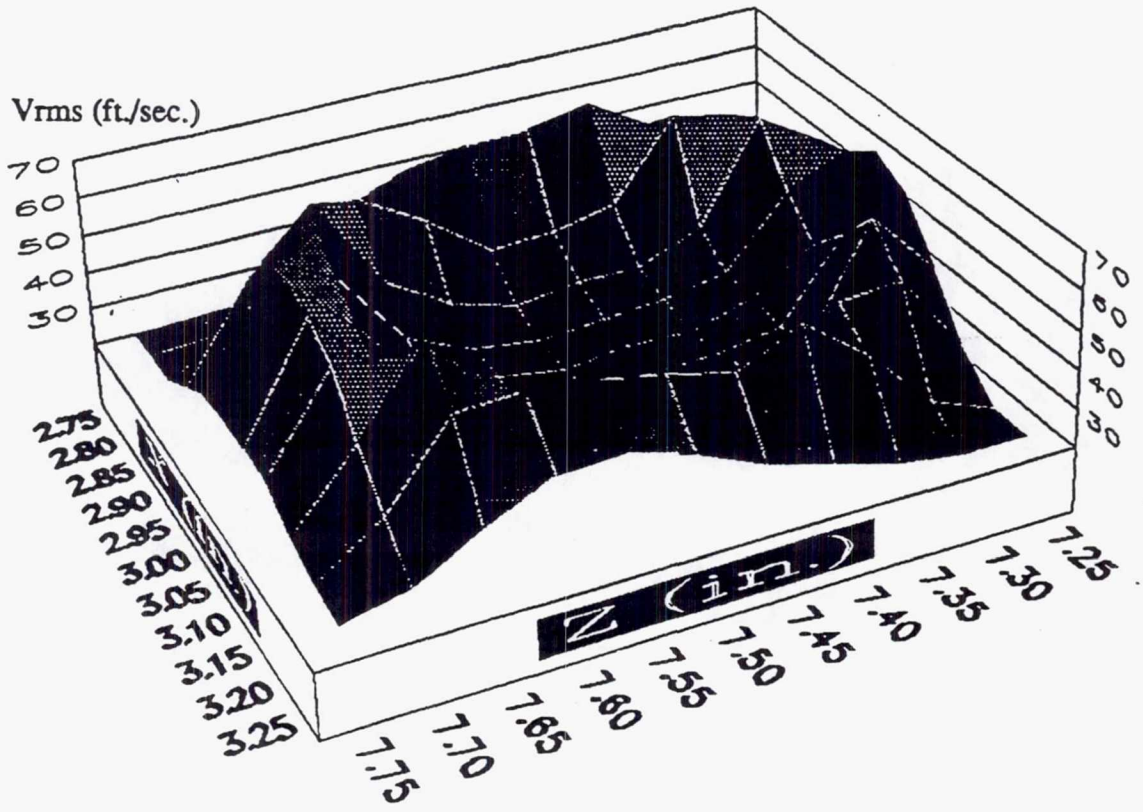

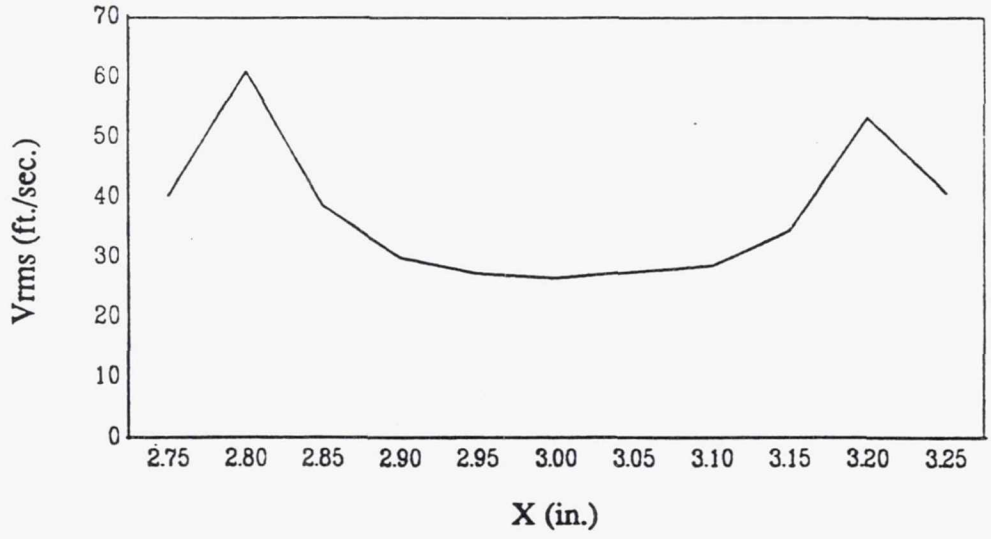

Figure 3.90 Contour and Line Plots of Vrms for Primary Cross Jet at Y=0.25 in.

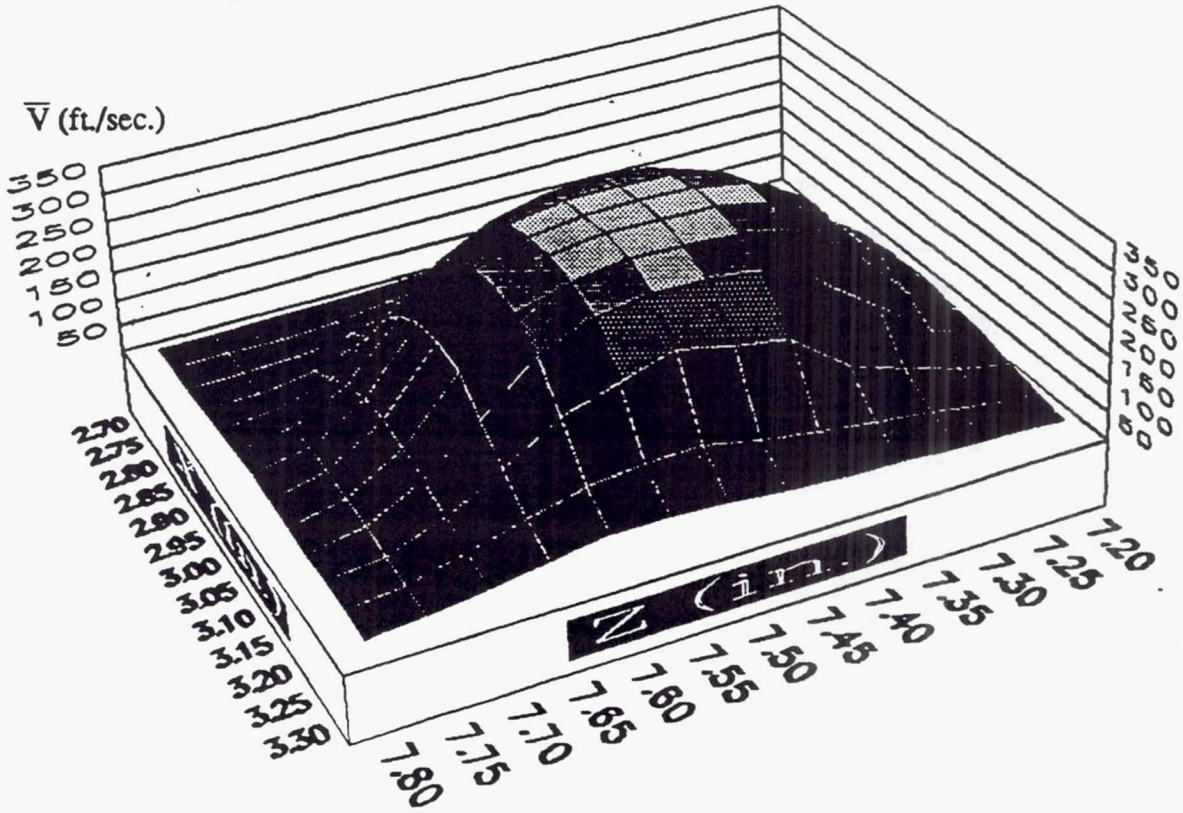

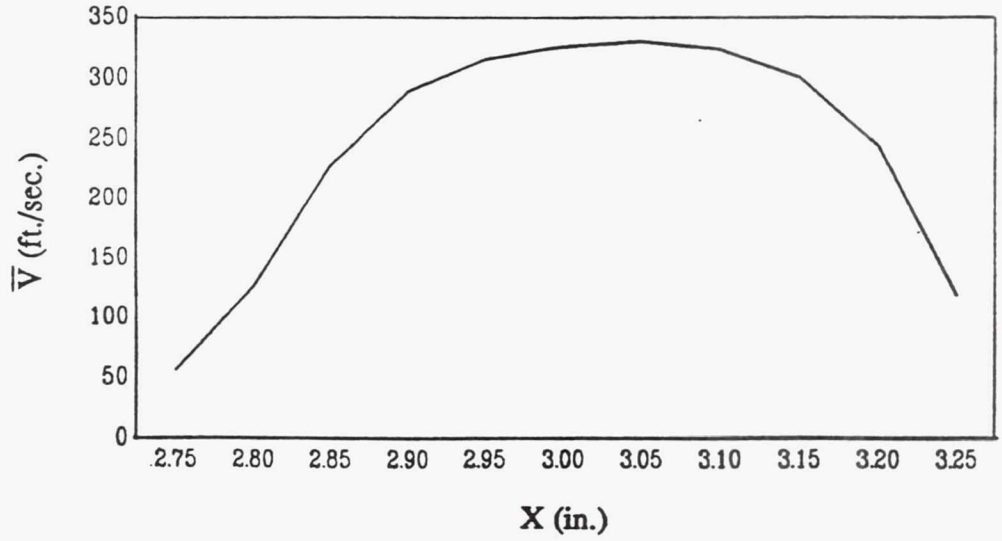

Figure 3.91 Contour and Line Plots of $\overline{V}$ for Primary Cross Jet at Y=0.50 in.

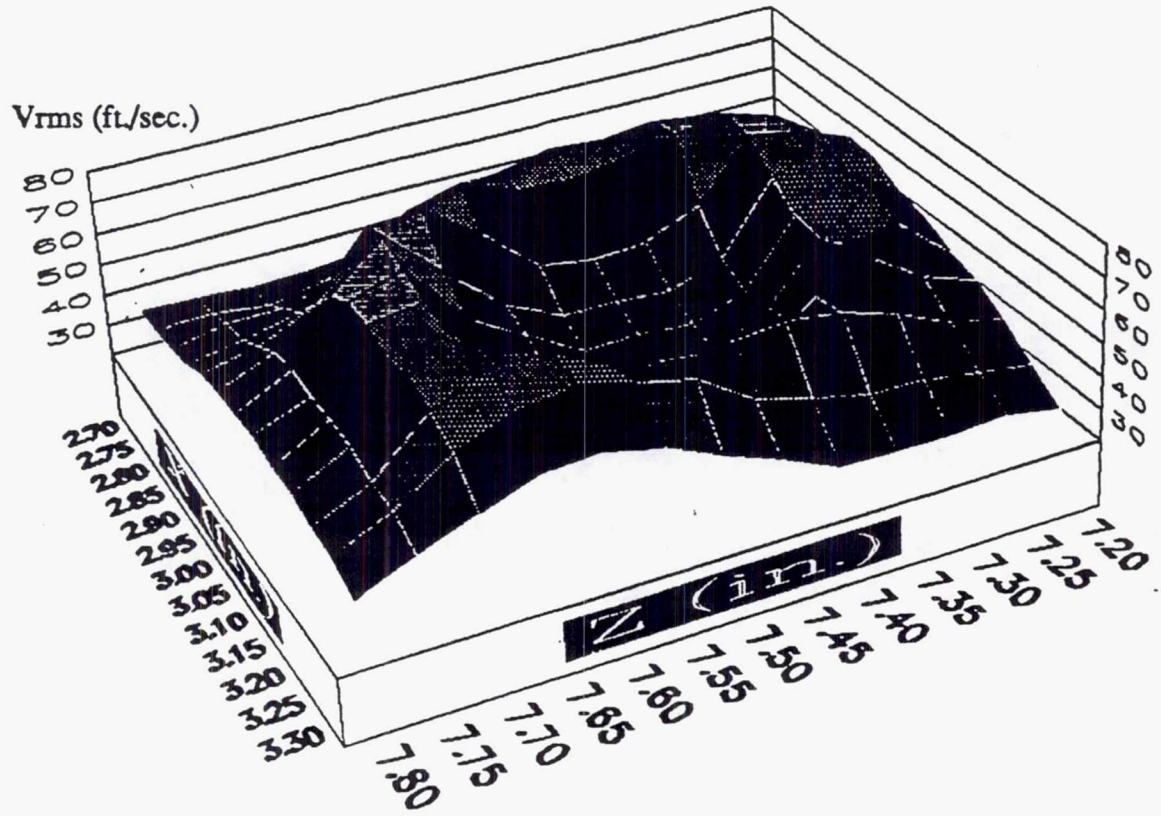

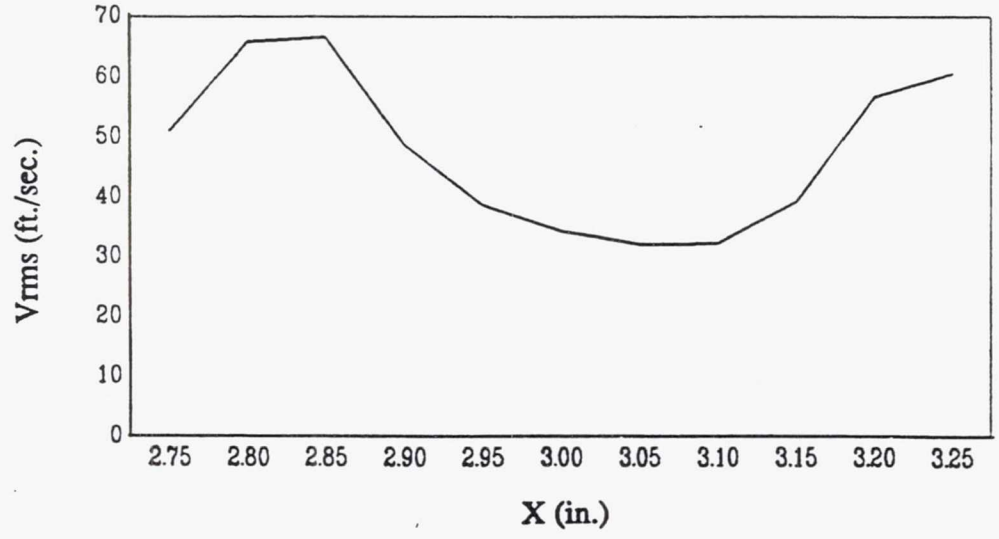

Figure 3.92 Contour and Line Plots of Vrms for Primary Cross Jet at Y=0.50 in.

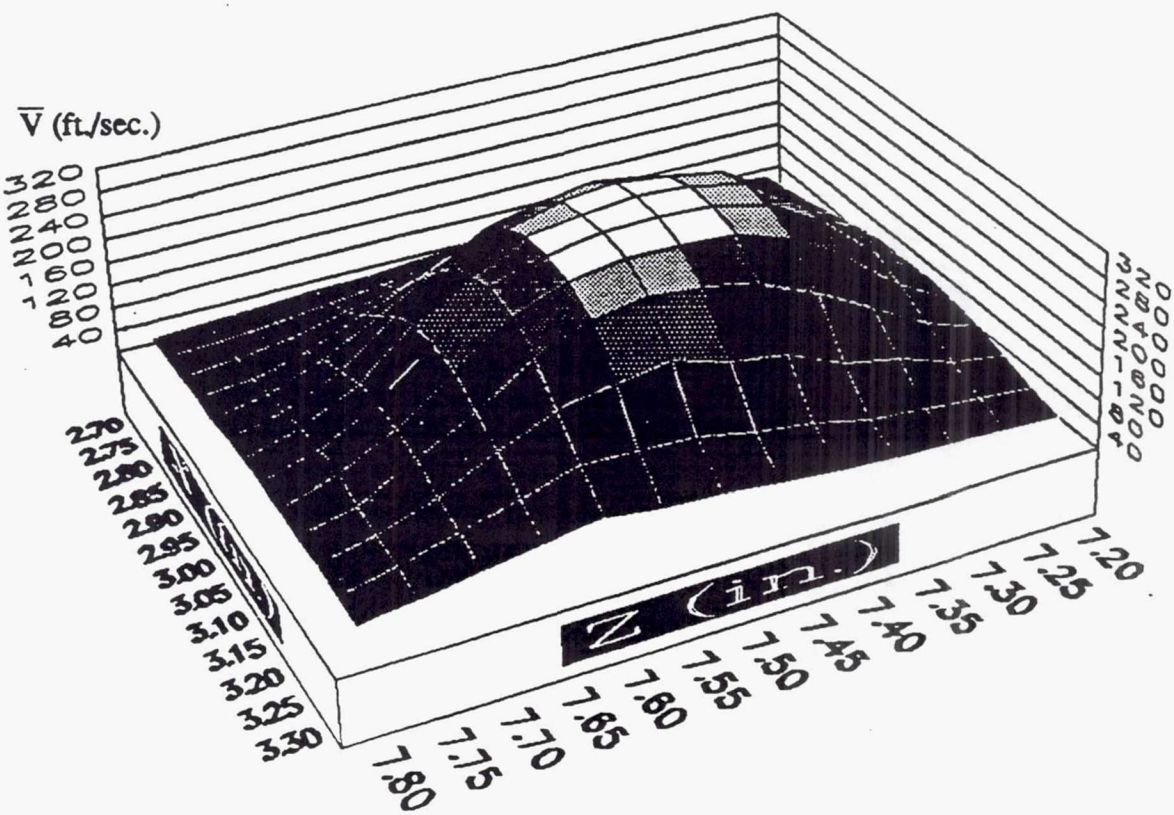

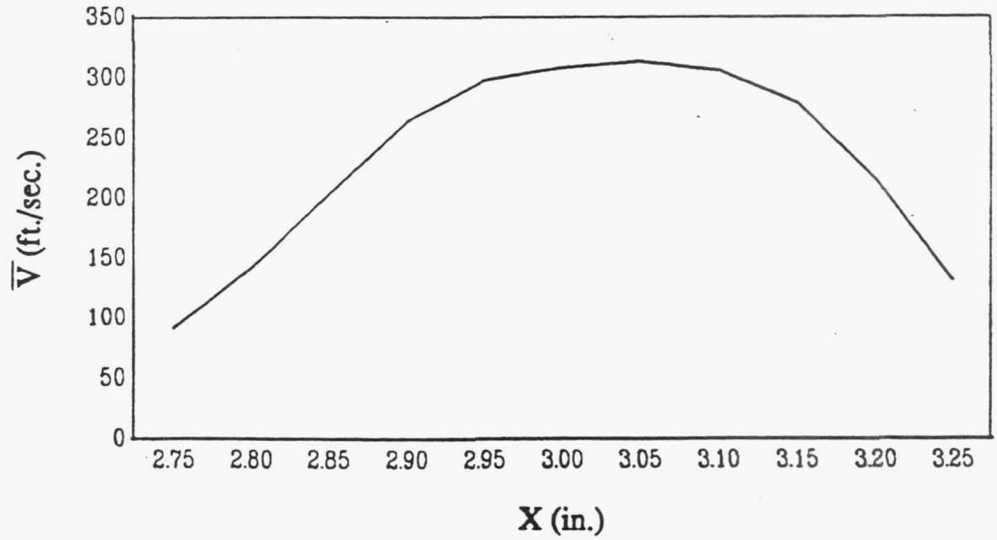

Figure 3.93 Contour and Line Plots of $\overline{V}$ for Primary Cross Jet at Y=0.75 in.

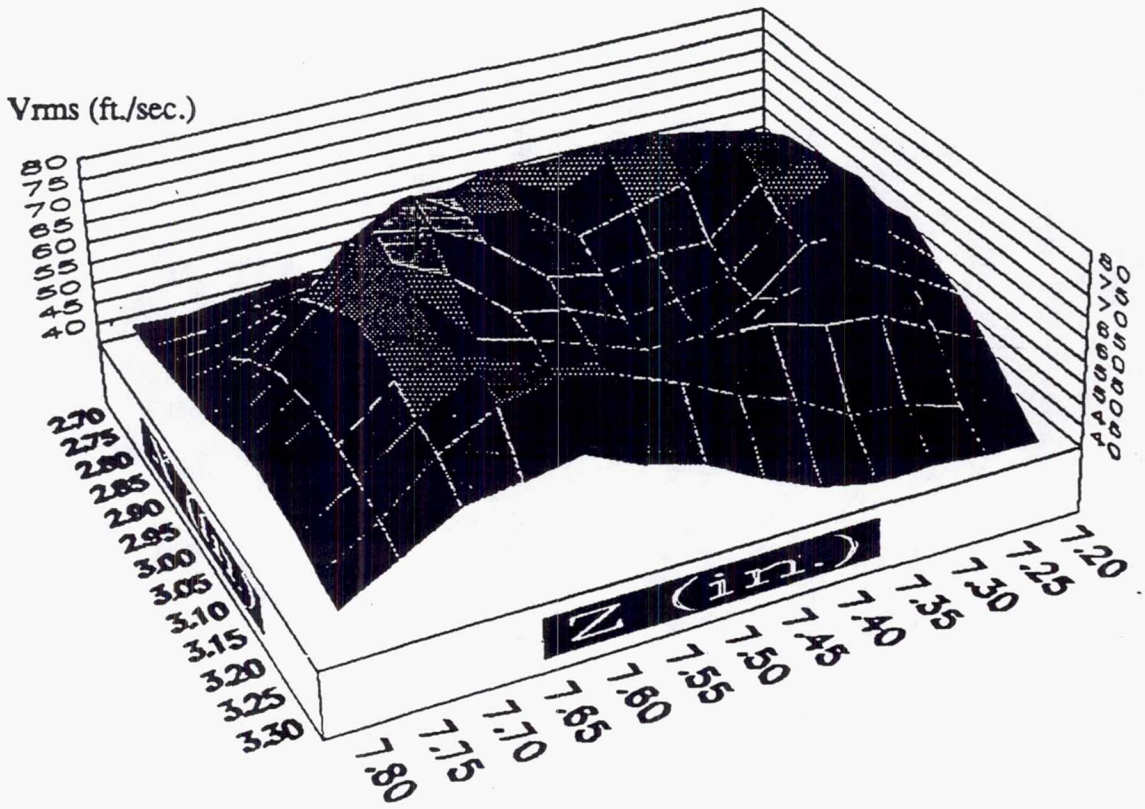

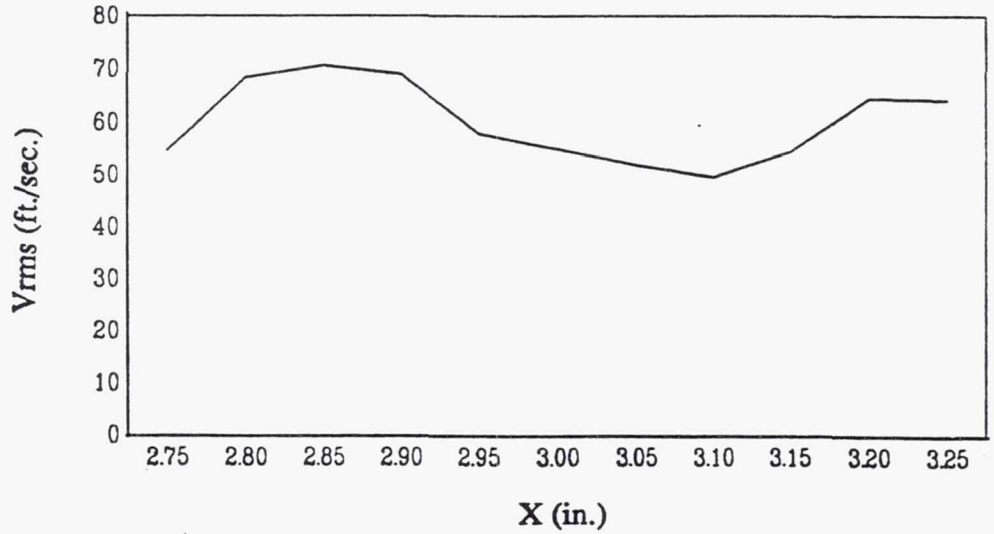

Figure 3.94 Contour and Line Plots of Vrms for Primary Cross Jet at Y=0.75 in.

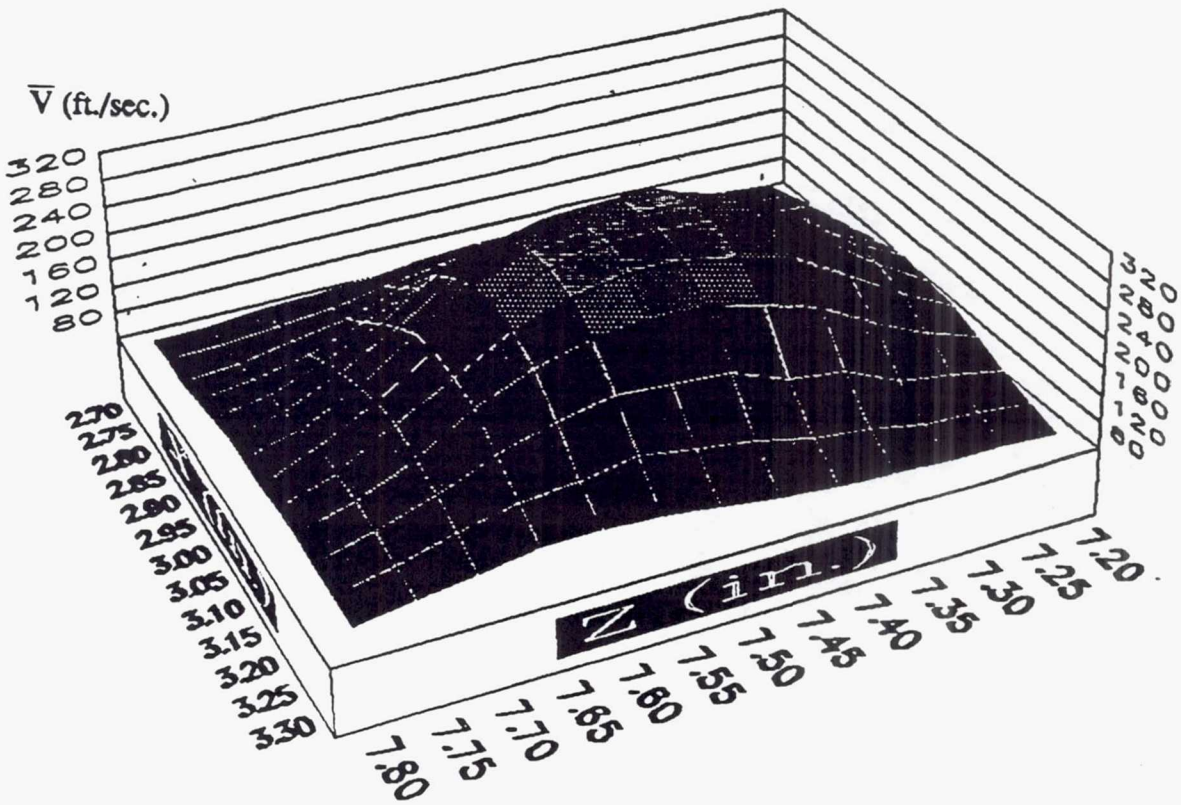

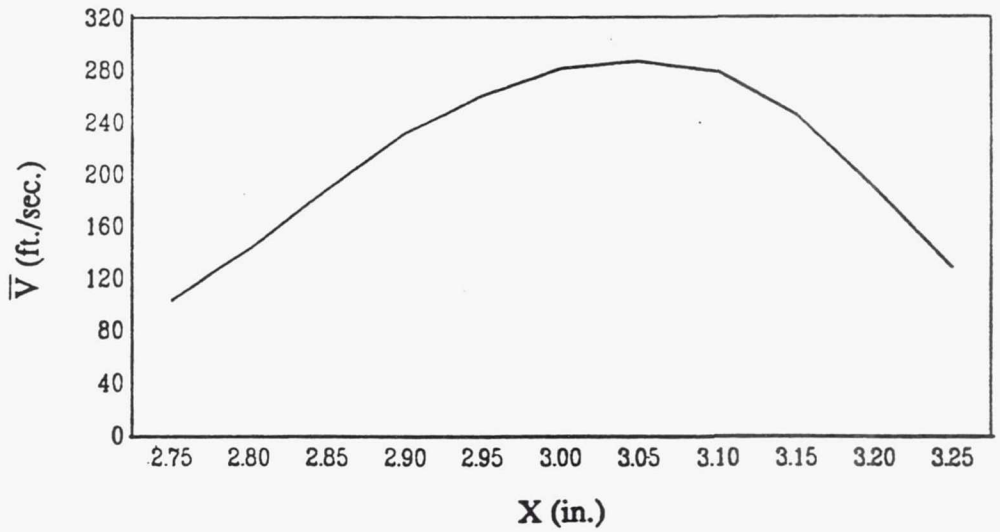

Figure 3.95 Contour and Line Plots of $\overline{V}$ for Primary Cross Jet at Y=1.00 in.

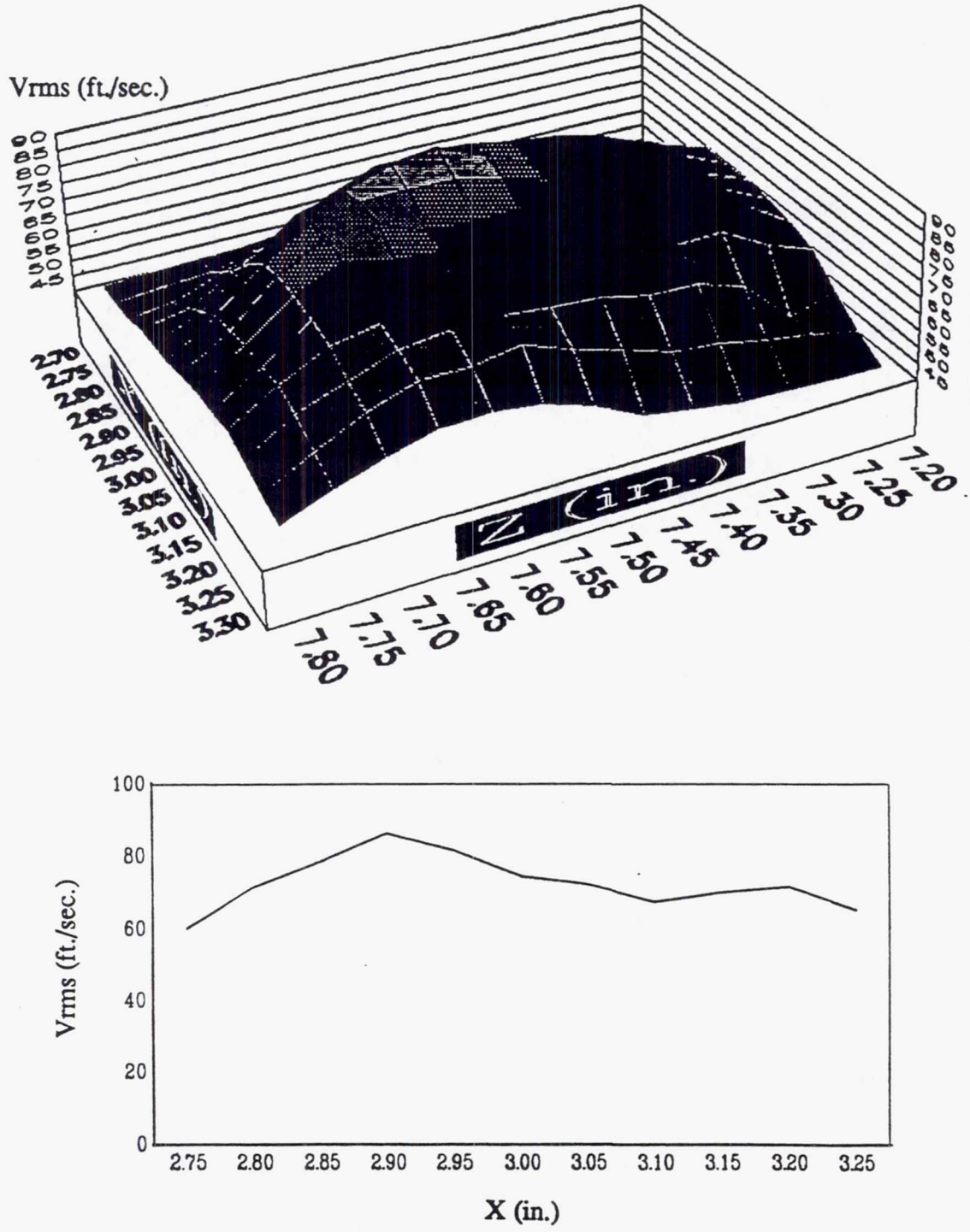

Figure 3.96 Contour and Line Plots of Vrms for Primary Cross Jet at Y=1.00 in.

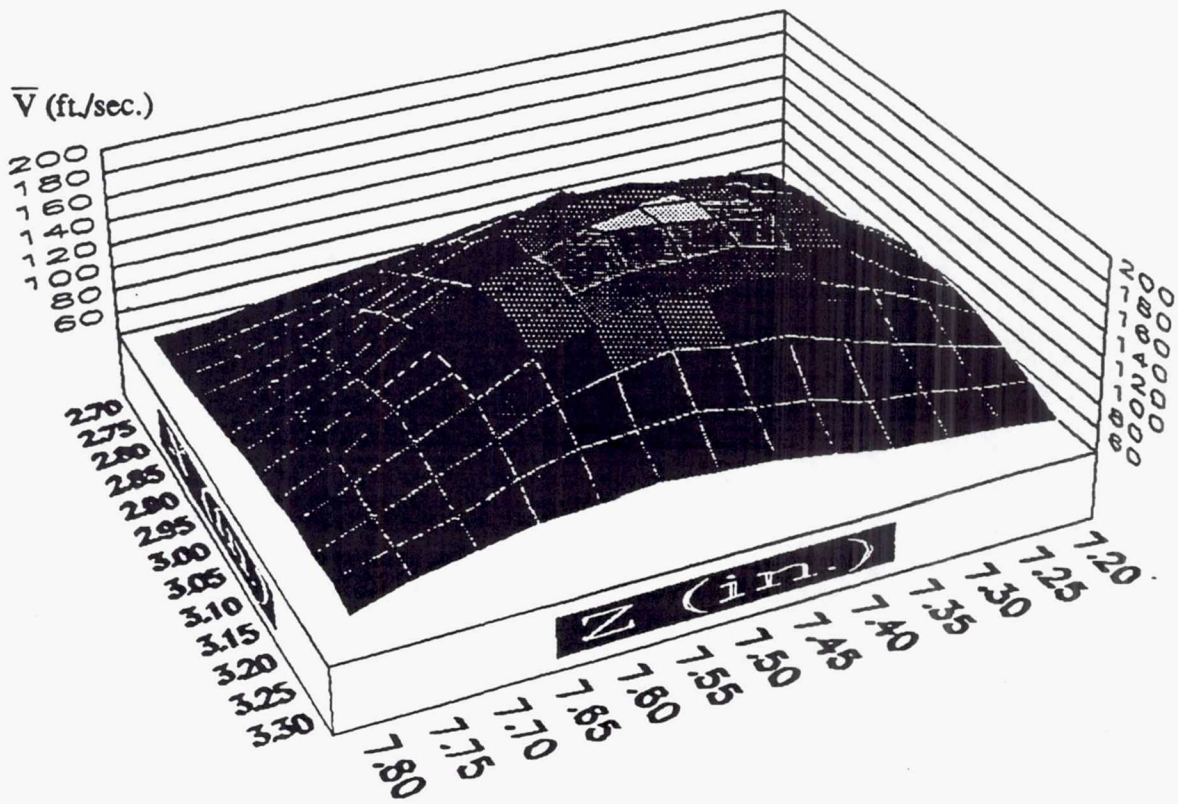

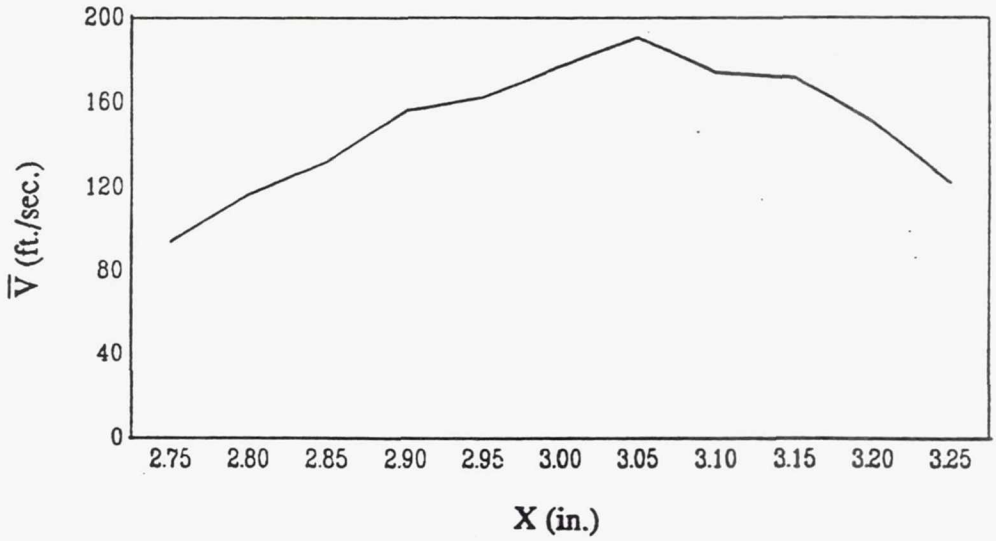

Figure 3.97 Contour and Line Plots of $\overline{V}$ for Primary Cross Jet at Y=1.25 in.

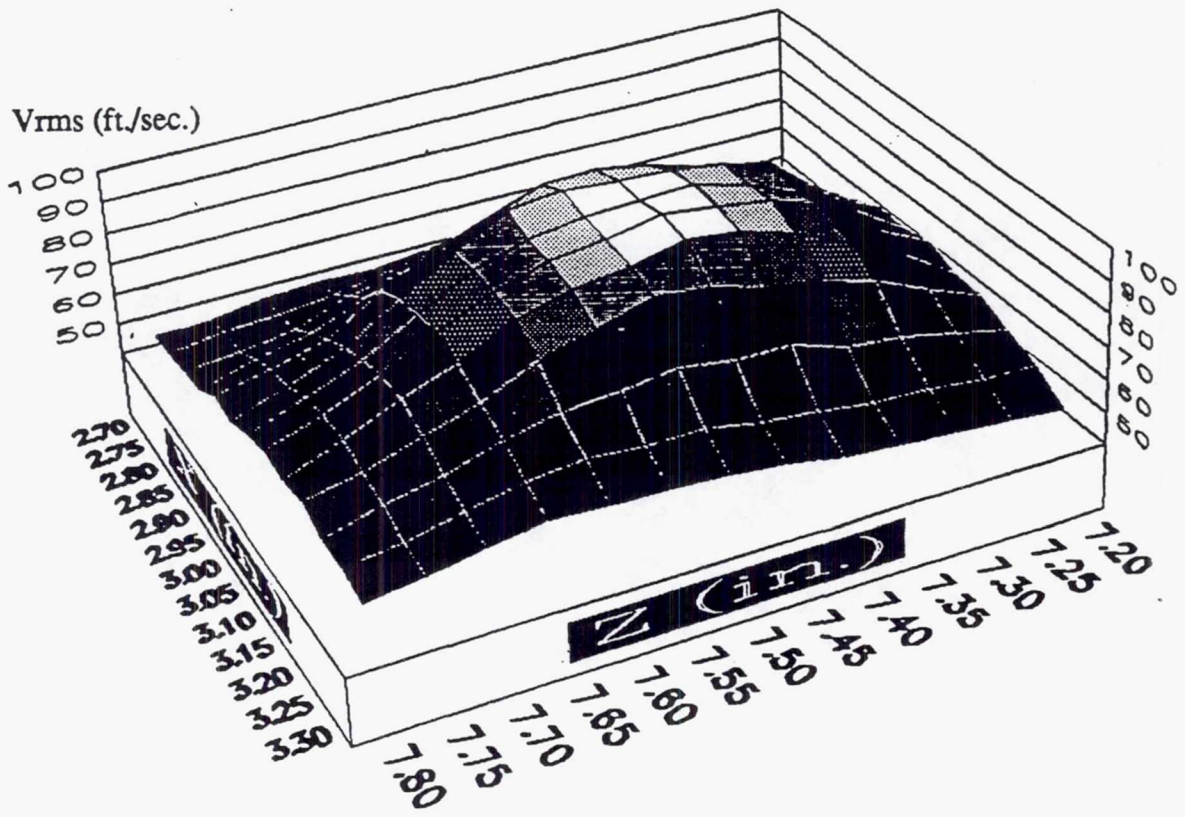

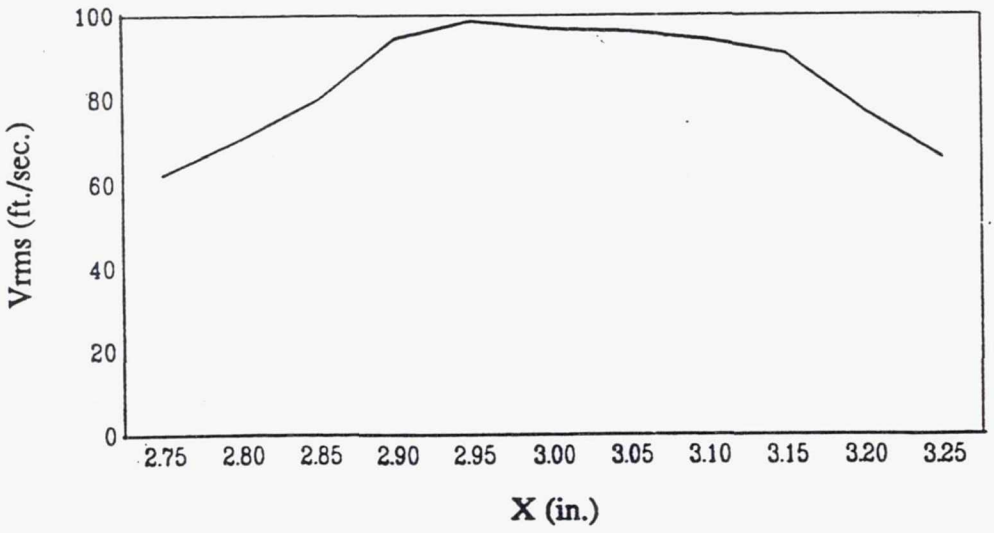

Figure 3.98 Contour and Line Plots of Vrms for Primary Cross Jet at Y=1.25 in.

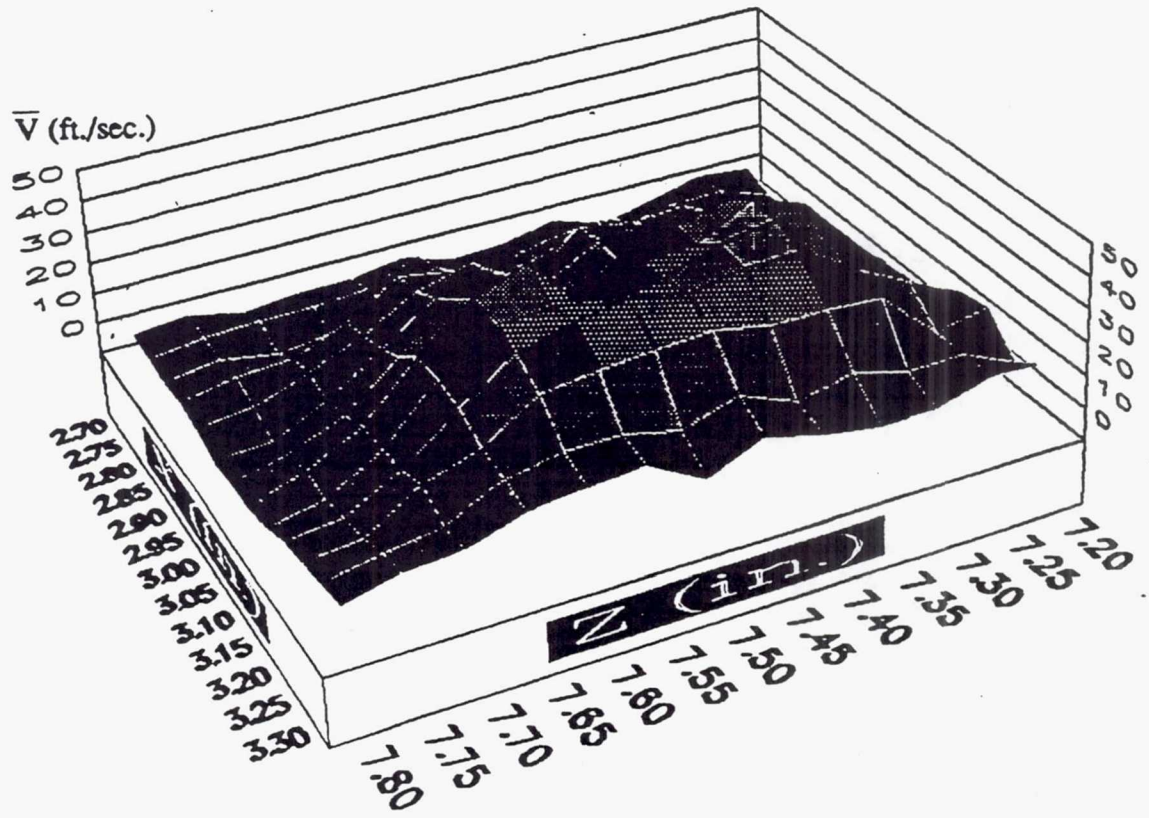

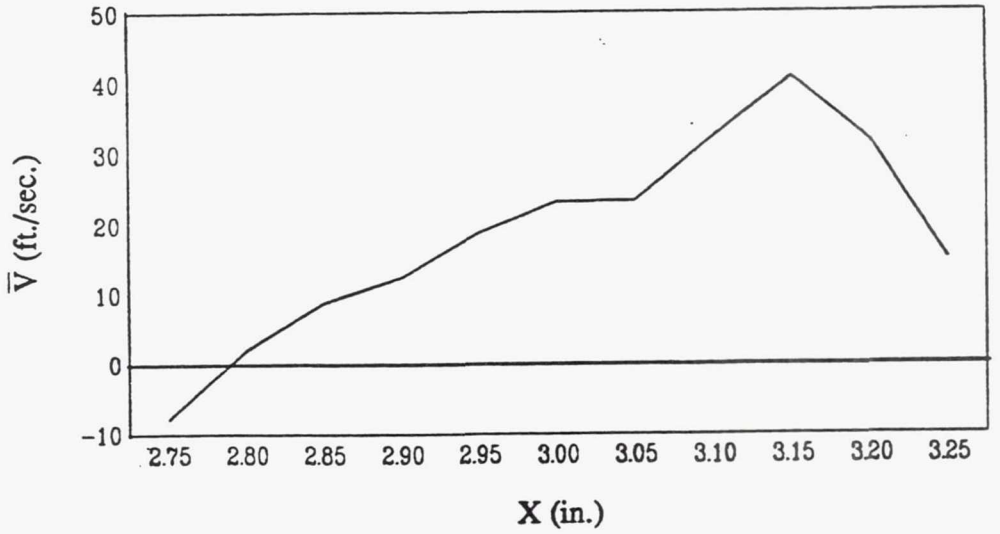

Figure 3.99 Contour and Line Plots of $\overline{V}$ for Primary Cross Jet at Y=1.50 in.

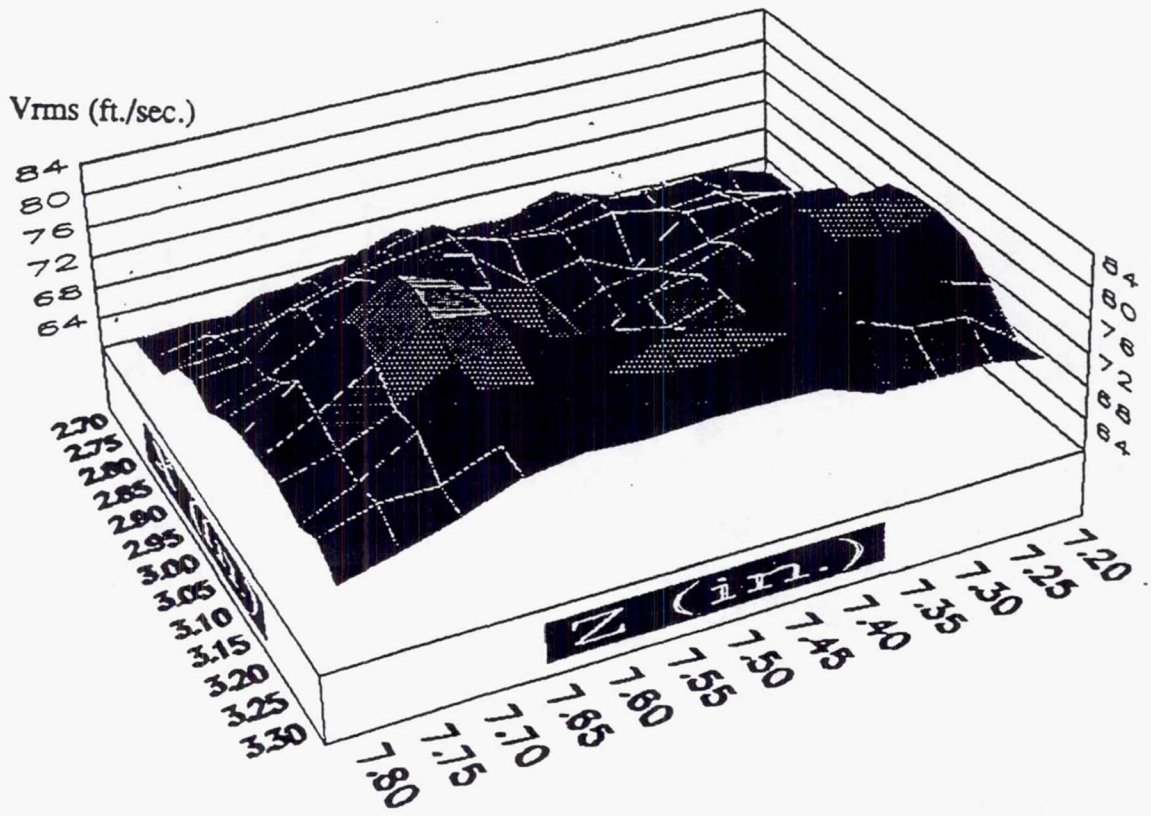

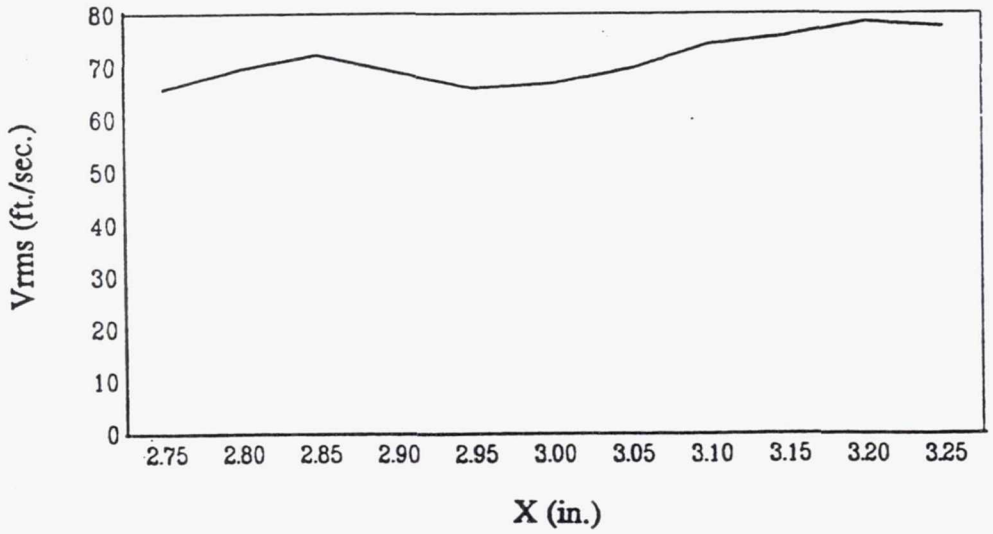

Figure 3.100 Contour and Line Plots of Vrms for Primary Cross Jet at Y=1.50 in.

CHAPTER 4: SUMMARY AND CONCLUSIONS

This thesis presents two experimental studies to further the understanding of flow phenomena and characteristics in gas turbine combustors. The first of these studies, an investigation of two-dimensional concentration fields of a free, swirling, turbulent jet, illustrated the changes in the jet flowfield structure, including the formation of the recirculation zone as well as other associated characteristics, over a wide range of swirl. The second study, an investigation of the three-dimensional flowfield structure in a simulated annular combustor flowfield under cold flow conditions, gave insight into the various flowfield phenomena occurring in typical annular combustors. These studies further the general understanding of swirling flows and their application to gas turbine combustors.

In the swirling jet study the two-dimensional concentration fields were measured by the method of marker nephelometry, a light scattering technique. Color enhanced video images of the concentration fields corresponding to single frames and 127 averaged frames were given for swirl ratios of 0.00, 0.33, 0.66, 1.00, 1.33, 1.66 an 2.00.

These concentration fields illustrated several important flowfield characteristics.

In the single frame images for any of the swirl ratios considered large scale fluctuations were seen to be prevalent. A comparison between the single frame images and averaged images indicated that the instantaneous concentration profiles did not resemble the mean profiles. This behavior suggests that large scale structures dominate the mixing and entrainment in this type of flowfield.

As was seen in figure (2.11) the change in the spread angle of the swirling jet flow with increasing swirl appears to follow a definite pattern, as the data represents a smooth and well-defined curve. This data was curve fit to give the relation

$$\theta = 12.49e^{1.41N} \qquad (2.3)$$

Since the results from previous works have indicated a strong dependence of the measured results on test section geometry, this relation may only apply to swirling flows driven by solid body rotation. For the N=2.00 case the flow was observed to flow around the lip of the jet and move in the upstream direction; the angle of spread had increased beyond 180 degrees.

The main characteristic of interest in swirling flows is the formation and existence of the recirculation zone.

The critical swirl ratio, the swirl ratio at which the first signs of recirculation are evident, was found to be near N=1.00. Single frame images indicated backflowing fluid, although no visible recirculation zone was seen in the mean. For swirl ratios above the critical swirl ratio the recirculation zone displays a generally well-defined form. The size of the recirculation zone increases with increasing swirl; for swirl ratios greater than N=2.00 the recirculation zone was larger than the physical area which was imaged. At swirl ratios above the critical well-defined forward stagnation points were evident; the downstream stagnation points were not evident in the images.

The concentration field images from this swirling jet study possess a large amount of information of the flowfield structure. These results allow the furthering of the knowledge base of swirling flows, jets in particular, and the associated characteristics such as the recirculation zone, with direct applications to the flowfields of current gas turbine combustors. Results such as these can also be of importance to the general study of turbulence, especially flow modelling, in that these images allow the study of mixing, entrainment, dissipation and large scale structures.

For the study of the three-dimensional flowfield structure in the annular combustor model of typical

annular combustor geometry, mean (time-averaged) and turbulence quantities were measured by Laser Doppler Velocimetry. The particular LDV system employed was equipped with a Bragg cell unit, a device which removes the directional ambiguity in the velocity measurement. The characteristics determined from measured quantities included the mean and root-mean-square velocities in the three coordinate directions, the turbulence kinetic energy and one of the Reynold's shear stress terms. For the mean flowfield structure certain characteristics were dominant: the formation of a toroidal recirculation zone and the effects of the primary cross jets on the local flowfield.

From additional flow visualization studies performed by this author on the single swirler apparatus of Barron [2] and the combustor model described in this thesis, the combustor model test section inlet flow profile was found to be of the wall jet type, similar to that found by Barron. This type of flow pattern is highly undesirable in gas turbine combustors due to heat transfer and material erosion problems.

The recirculation zone, resulting from the application of strong swirl to the test section inlet flow, the primary cross jets and the large step change in area, formed in the first duct height of the combustor model appeared to be asymmetric in the various downstream cell cross-sections, with the backflow region extending

into the upper left and upper right corners and strong positive axial flux existing in the lower left and lower right corners. The strongest measured recirculation was seen at the first downstream measurement plane where the central portion of the recirculation zone showed a relatively flat, high speed profile.

The primary cross jets, and the associated stagnation point region, had a strong effect on all the measured characteristics in the flowfield local to the cross jet injection location. One of the main objectives of the use of cross jets in gas turbine combustors is the shortening of the recirculation region; this objective was fulfilled as no backflow existed past the injection plane. The flow pattern resulting from the cross jet stagnation point region, in the form of a radial jet in the XZ-plane, was seen to drive the 4 cells of vortex-type motion seen in the cell cross-sections near the injection plane. The radial jet pattern also helps drive the recirculation bubble as a portion of the radial jet is injected into the center of the backflowing fluid. At the far downstream stations, nearly all mean gradients had decayed.

From the measured turbulence characteristics the main point of interest is, as before, the effect of the cross jet interaction on the local main flowfield. The cross jets were seen to cause very high levels of turbulence kinetic energy and shear in the immediate vicinity of the

stagnation point region with the highest measured levels occurring at the jet injection plane. The location of the stagnation point was seen from flow visualization to fluctuate in a random fashion, illustrating the unsteady nature of the flowfield. The effect of the cross jets was found to extend both downstream and upstream of the jet injection plane as the turbulence characteristics displayed patterns of peaking near the center of the cell cross-section.

The cross jets also affected the swirl in the combustor model. Acting as a flow straightener the radial jet, formed at the cross jet stagnation point, inhibited the swirl velocities, reducing the overall swirl to very low levels. The attached flow pattern and large step change in area were also seen to prevent the formation of an overall swirling motion in the model combustor.

Similar to the mean flowfield characteristics, the turbulence characteristics, K and $\overline{U'V'}$, displayed a central region of flat profile at the X=1.00 in. location corresponding to the recirculation zone. At the far downstream locations, X=6.00 in. and X=9.00 in., the high level of decay is illustrated in the turbulence characteristics as the magnitudes were reduced to very low levels compared to the levels at the upstream stations. The levels of the rms velocities, K and $\overline{U'V'}$ at the X=6.00 in. and X=9.00 in. stations, though, are still very high

when compared to typical fluid motions such as channel or pipe flow. Isotropy and homogeneity were seen to be valid assumptions at these locations due to the flat contours and low magnitudes of the turbulence characteristics compared to those at the upstream stations. The near zero magnitude of the turbulence shear term at the X=9.00 in. plane displayed the absence of gradients in the XY-plane.

Measurements of the characteristics of one of the primary cross jets injecting into the main flow were performed at various heights across the duct. Profiles of the jet exit flow (Y=0.06 in.) showed similarities to classical pipe flow data indicating the existence of fully developed flow upon entry into the test section. The profile of the turbulence intensity, in particular, displayed the effect of the main flow on the jet as the measured values were of the same profile shape but twice the magnitude of the classical data. The cross jet profiles illustrated a slight translation of the jet centerline due to the main flow. The very high levels of the RMS velocity measured in the region between the cross jets illustrates the highly turbulent and unsteady nature of the cross jet stagnation point interaction.

Since the geometry of the model combustor was typical of current annular gas turbine combustors a better understanding of the flow conditions inside an actual combustor is realized. Although combustion has a

significant effect on the flowfield characteristics the general flow features are illustrated by this study. The objective for this model combustor study was to obtain a quality database for purposes of computational model development. The experimental results can be used as control values in the assessment and analysis of the computational models, aiding in the development of prediction methods for future combustor design and analysis.

LIST OF REFERENCES

LIST OF REFERENCES

1. Adrian, R.J., Yao, Y.S., "Power Spectra of Fluid Velocities Measured by Laser Doppler Velocimetry", Experiments in Fluids, Vol. 5, 1987, pp. 17-28.

2. Barron, D.A., "LDV Measurements in an Annular Combustor Model", MS Thesis, Purdue University, August, 1986.

3. Becker, H.A., "Mixing, Concentration Fluctuations, and Marker Nephelometry", Studies in Convection, Vol. 2, Edited by B.E. Launder, Academic Press, New York, 1977, pp. 45-139.

4. Becker, H.A., Hottel, H.C., Williams, G.C., "On the Light Scattering Technique for the Study of Turbulence and Mixing", Journal of Fluid Mechanics, Vol. 30, 1967, pp. 259-284.

5. Beer, J.M., Chigier, N.A., "Combustion Aerodynamics", Robert E. Krieger Publishing, 1983.

6. Borleteau, J-P., "Concentration Measurement with Digital Image Processing", ICIASF '83 Record, pp. 37-42.

7. Borrego, C., Olivari, D., " A Method for the Measurements of Mixing Properties in a Flow", AGARD CP-281.

8. Brondum, D.C., Bennett, J.C., "Numerical and Experimental Investigation of Nonswirling and Swirling Confined Jets", AIAA Paper No. 86-0040, Presented at AIAA 24th Aerospace Sciences Meeting, Reno, Nevada, January, 1986.

9. Brum, R.D., Samuelson, G.S., "Two-component Laser Anemometry Measurements of Non-reacting and Reacting Complex Flows in a Swirl-stabilized Model Combustor", Experiments in Fluids, Vol. 5, 1987, pp. 95-102.

10. Buchhave, P., "The Measurement of Turbulence With the Burst-Type Laser Doppler Anemometer- Errors and Correction Methods", PhD Thesis, State University of New York at Bufflalo, September, 1979.

11. Buchhave, P., George, W.K., Jr., Lumley, J.L., "The Measurement of Turbulence With the Laser Doppler Velocimeter", Annual Review of Fluid Mechanics, Vol. 11, 1979, pp. 443-504.

12. Chigier, N.A., Chervinsky, A, "Experimental Investigation of Swirling Vortex Motion in Jets", Transactions of the ASME, Journal of Applied Mechanics, June, 1967, pp 443-450.

13. Crow, S.C., Champagne, F.H., "Orderly Structure in Jet Turbulence", Journal of Fluid Mechanics, Vol. 48, 1071, pp. 547-591.

14. Dahm, W.J.A., Dimotakis, P.E., "Measurements of Entrainment and Mixing in Turbulent Jets", AIAA Paper No. 85-0056.

15. Dimotakis, P.E., "Single Scattering Particle Laser Doppler Measurements of Turbulence", Appl. of Non-Intrusive Instrumentation in Fluid Flow Measurement, AGARD CP-193.

16. Durst, F., Melling, A., Whitelaw, J.H., "Principles and Practice of Laser-Doppler Anemometry", Second Edition, Academic Press, 1981.

17. Edwards, R.V.,(Ed.), "Report of the Special Panel On Statistical Particle Bias Problems in Laser Velocimetry", ASME Journal of Fluids Engineering, Vol. 109, June, 1987, pp. 89-93.

18. Edwards, R.V., Jenson, A.S., "Particle Sampling Statistics in Laser Anemometers: Sample-and-Hold Systems and Saturable Systems", J. Fluid Mech., Vol.133, pp. 397-411.

19. Erdmann, J.C., Tropea, C., "Turbulence Induced Statistical Bias in Laser Anemometry", Proceedings of the Seventh Symposium on Turbulence, Univ. of Missouri-Rolla, Septmeber, 1981.

20. Escudier, M.P., Keller, J.J., "Recirculation in Swirling Flow: A manifestation of Vortex Breakdown", AIAA Journal, Vol. 23, January, 1985, pp. 111-116.

21. Ferrell, G.B., Aoki, K., Lilley, D.G., "Flow Visualization of Lateral Jet Injection into Swirling Crossflow", AIAA 85-0059, Reno, Nevada, January 14-17, 1985.

22. Ferrell, G.B., Abujelala, M.T., Busnaina, A.A., Lilley, D.G., "Lateral Jet Injection into Typical Combustor Flowfields", AIAA Paper No. 84-0374, Presented at the AIAA 22nd Aerospace Sciences Meeting, Reno, Nevada, January, 1984.

23. Ferrell, G.B., Lilley, D.G., "Turbulence Measurements of Lateral Jet Injection into Confined Tubular Crossflow", AIAA 85-1102, Monterey, California, July 8-10, 1985.

24. Goldstein, R.J., "Fluid Mechanics Measurements", Hemisphere Publishing, 1983.

25. Gore, R.W., Ranz, W.E., "Backflows in Rotating Fluids Moving Axially through Expanding Cross Sections", A.I.Ch.E. Journal. Vol. 10, January, 1964, pp. 83-88.

26. Gould, R.D., Stevenson, W.H., Thompson, H.D., "A Parametric Study of Statistical Velocity Bias", Fifth Intl. Congress on Appl. of Lasers and Electro-Optics, Arlington, VA, November 10-13, 1986.

27. Gupta, A.K., Lilley, D.G., Syred, N., "Swirl Flows", Abacus Press, 1984.

28. Hinze, H.O., "Turbulence", McGraw-Hill, 1975.

29. Johnson, B.V., Bennett, J.C., "Statistical Characteristics of Velocity, Concentration, Mass Transport, and Momentum Transport for Coaxial Jet Mixing in a Confined Duct", ASME Journal of Engineering for Gas Turbines and Power, Vol. 106, January, 1984, pp. 121-127.

30. Kerr, N.M., Fraser, D., " Swirl. Part I: Effect on Axisymmetric Turbulent Jets", Journal of the Institute of Fuel, Vol. 38, No. 99, 1965, pp. 519-526.

31. Komori, S., Ueda, H., "Turbulent Flow Structure in the Near Field of a Swirling Round Free Jet", Physics of Fluids, Vol. 28, July, 1985, pp. 2075-2082.

32. Laufer, J., "The Structure of Turbulence in Fully Developed Pipe Flow", NACA Report 1174, 1954.

33. Lehmann, B., "A Spatially Working Model to Correct the Statistical Biasing Error of More Directional One Component LDA-Measurements", Int. Symp. on Appl. LDA to Fluid Mechanics, Lisbon, Portugal, July 5-7,1982.

34. Lilley, D.G., "Swirl Flows in Combustion: A Review", AIAA Journal, Vol. 15, August, 1977, pp. 1063-1078.

35. Long, M.B., Chu, B.J., Chang, R.K., "Instantaneous Two-Dimensional Gas Concentration Measurements by Light Scattering",AIAA Journal, Vol. 19, September, 1981, pp. 1151-1157.

36. Long, M.B., Webber, B.F., Chang, R.K., "Instantaneous Two-Dimensional Concentration Measurements in Jet Flow by Mie Scattering", Applied Physics Letters, Vol. 34, January, 1979, pp. 22-24.

37. McLaughlin, D.K., Tiederman, W.G., "Biasing Correction for Individual Realization of Laser Velocimeter Measurements in Turbulent Flows", Physics of Fluids, Vol.16, No. 12, December, 1973, pp. 2082-2088.

38. McMurry, C.B., Lilley, D.G., "Experiments on Two Opposed Lateral Jets Injected into Swirling Crossflow", NASA CR-175041.

39. Ong, L.H., Lilley, D.G., "Measurements of a Single Lateral Jet Injected into Swirling Crossflow", NASA CR-175040, January, 1986.

40. Pratte, B.D., Keffer, J.F., "The Swirling Turbulent Jet", ASME Journal of Basic Engineering, December, 1972, pp. 739-748.

41. Quigley, M.S., Tiederman, W.G., "Experimental Evaluation of Sampling Bias in Individual Realization Laser Anemometry", AIAA Journal, Vol. 15, February, 1977, pp. 266-268.

42. Ramos, J.I., "Turbulent Non-reacting Swirling Flows", AIAA Journal, Vol. 22, November, 1984, pp. 846-847.

43. Ramos, J.I., Somer, H.T., "Swirling Flow in a Research Combustor", AIAA Journal, Vol. 23, February, 1985, pp. 241-248.

44. Rhode, D.L., Lilley, D.G., McLaughlin, D.K., "Mean Flowfields in Axisymmetric Combustor Geometries with Swirl", AIAA Journal, Vol. 21, April, 1983, pp. 593-600.

45. Rose, W.G., "A Swirling Round Turbulent Jet", ASME Journal of Applied Mehanics, December, 1962, pp. 615-625.

46. Rosenweig, R.N., 1966 Sc.D. dissertation, Massachusetts Institute of Technology.

47. Rosenweig, R.E., Hottel, H.C., Williams, G.C., "Smoke Scattered Light Measurements of Turbulent Concentration Fluctuations",, Chemical Engineering Science, Vol. 15, July, 1961, pp. 111-129.

48. Schaughnessy, E.J., Morton, J.B., "Light Scattering Measurements of Particle Concentration in a Turbulent Jet", Journal of Fluid Mechanics, Vol. 80, Part 1 (1977), pp. 129-148.

49. Schlichting, H., "Boundary Layer Theory", McGraw-Hill, 1979.

50. Smith, G.D., Giel, T.V., Catalano, C.G., "Measurements of Reactive Recirculating Jet Mixing in a Combustor", AIAA Journal, Vol. 21, February, 1983, pp. 270-276.

51. TSI Model 1990 Instruction Manual, TSI Incorporated.

52. Tennekes, H., Lumley, J.L., "A First Course in Turbulence", MIT Press, 1973.

53. Vu, B.T., Gouldin, F.C., "Flow Measurement in a Model Swirl Combustor", AIAA Journal, Vol. 20, May, 1982, pp. 642-651.

54. Vranos, A., Liscinsky, D.S., "A Study of Turbulent Jet Mixing Through Planar Imaging and Gas Sampling", AIAA Paper No. 85-1444.

55. Yoon, H.K., Lilley, D.G., "Further Time-Mean Measurements in Confined Swirling Flows", AIAA Journal, Vol. , April, 1984, pp. 514-515.

APPENDICES

APPENDIX A. Details on Velocity Measurements

In order to acquire the three-dimensional flowfield mean and turbulence characteristics found in the annular combustor model, including Reynold's shear stresses, one cannot simply make measurements in the three coordinate directions. The measurement of, or more precisely the calculation of, the Reynold's shear stresses requires that measurements be made at +/- 45 degrees to the coordinate axes in the plane of each component. This requirement can be seen in the following relations (with the aid of figure (A.1).

By a simple transformation of coordinates, assuming 45 degree angles between the coordinate directions, one can find

$$U_1 = \frac{(U_{+45} + U_{-45})}{\sqrt{2}} \qquad (A.1)$$

$$U_2 = \frac{(U_{+45} - U_{-45})}{\sqrt{2}} \qquad (A.2)$$

Manipulation of equations (A.1) and (A.2) result in

$$U_{+45} = (U_1 + U_2)\sqrt{2} \qquad (A.3)$$

$$U_{-45} = (U_1 - U_2)\sqrt{2} \qquad (A.4)$$

Since the instantaneous velocity, U, is made up of a mean (time averaged) term, $\overline{U}$, and a fluctuating term, U', the time average of the square of equation (A.3) can be

written as

$$\overline{(U_{+45} + U_{-45})^2} = 2\overline{(\bar{U}_1 + U'_1 + \bar{U}_2 + U'_2)^2} \qquad (A.5)$$

If the right side of this relation is then expanded, the result is

$$\bar{U}_{+45}^2 + \overline{U'^2_{+45}} = 2(\bar{U}_1^2 + 2\bar{U}_1\bar{U}_2 + \overline{U'^2_1} + 2\overline{U'_1U'_2} + \bar{U}_2^2 + \overline{U'^2_2}) \qquad (A.6)$$

and if the mean of equation (A.3) is then squared,

$$\bar{U}_{+45}^2 = 2(\bar{U}_1^2 + 2\bar{U}_1\bar{U}_2 + \bar{U}_2^2) \qquad (A.7)$$

Subtraction of equation (A.7) from equation (A.6) results in

$$\overline{U'^2_{+45}} = 2(\overline{U'^2_1} + 2\overline{U'_1U'_2} + \overline{U'^2_2}) \qquad (A.8)$$

The same method can be applied to the -45 degree component to give

$$\overline{U'^2_{-45}} = 2(\overline{U'^2_1} - 2\overline{U'_1U'_2} + \overline{U'^2_2}) \qquad (A.9)$$

Now, if equation (A.9) is subtracted from equation (A.8) a relation for the Reynold's shear stress can be found, with the result being

$$\overline{U'_1U'_2} = \overline{U'^2_{+45}} + \overline{U'^2_{-45}} \qquad (A.10)$$

This relation shows the reason for the necessity of the +/-45 degree measurements in order to calculate the Reynold's stress components. If equations (A.8) and (A.9) are added together

$$\overline{U'^2_1} + \overline{U'^2_2} = \overline{U'^2_{+45}} + \overline{U'^2_{-45}} \qquad (A.11)$$

In order to have both mean and rms velocity information in the two coordinate directions 1 and 2 additional measurements must be made in either of the two

coordinate directions. If, say, U_z is measured,

$$\overline{U'_1{}^2} = \overline{U'_{+45}{}^2} + \overline{U'_{-45}{}^2} - \overline{U'_2{}^2} \qquad (A.12)$$

This general approach is applied to all the coordinate planes if all the Reynold's shear stress components are desired.

Main Flow

In the annular combustor model the only Reynold's shear stress component to be measured was the XY-plane term, $\overline{U'V'}$. Thus, the method described above was only applied to the XY-plane, requiring measurements along the +/- 45 and 0 degrees directions relative to the downstream (X) direction. Equations (A.10) and (A.12) take the forms

$$\overline{U'V'} = \overline{U'_{+45}{}^2} + \overline{U'_{-45}{}^2} \qquad (A.13)$$

$$\overline{V'^2} = \overline{U'_{+45}{}^2} + \overline{U'_{-45}{}^2} - \overline{U'^2} \qquad (A.14)$$

Equation (A.2) also takes the form

$$\overline{V} = \frac{\overline{U}_{+45} - \overline{U}_{-45}}{\sqrt{2}} \qquad (A.15)$$

The combustor model apparatus orientation for the U and V measurements can be seen in figure (A.2). In order to allow the measurements at +/- 45 degrees to be made, the transmitting optics unit consisting of the beam splitter, Bragg cell, and beam translator was rotated about the optical axis.

Although complete scans, from the lower wall (Y=0.00 in.) to the upper wall (Y=3.00 in.), were originally

desired interference of the incident laser beams imposed limits on the vertical travel of the probe volume. This interference occurred for the +/- 45 degree measurements due to the incident beams striking the edges of the side plates, as in figure (A.3), which resulted in reflections and no beam crossover.

One solution could have been to orient one of the beams parallel to one of the walls to allow measurements very close to that wall and then rotate the transmitting optics to measure near the other wall. This approach was deemed not feasible due to the amount of time that would have been required to perform the measurements. Thus, due to these geometric restrictions, the vertical travel of the probe volume was limited to 0.40 in.<Y< 2.60 in..

The remaining flow measurements made were those of the Z component of velocity, W. Since the Reynold's stress component, $\overline{U'W'}$, was not to be measured the only necessary measurement in the XZ-plane was along the Z coordinate direction. In order to facilitate this measurement the test section was rotated about the X direction, as in figure (A.4).

One problem encountered in these measurements resulted from geometric restrictions due to the cross jet throttle hardware. At the X=2.50, 3.00, and 3.50 in. locations the cross jet throttles prevented adequate movement of either the field lens or the receiving optics.

In order to allow measurements at the X=2.50 in. and X=3.50 in. stations the throttles and their mounting plate were removed; this alteration of the hardware also removed the ability to control the mass flow through the cross jets. The ability to measure the W characteristics at the X=3.00 in. station required the removal of the cross jet structural support; since this was not possible, these measurements could not be made.

After measuring the pressure drops across all of the jets the two with pressure drops closest to the operating condition pressure drop of 0.25 psi were mounted in the center cell. The pressure drops of these two jets were 0.245 psi and 0.240 psi, corresponding to velocities of 240.4 ft./sec. and 237.9 ft./sec., with the other jets having pressure drops in the range from 0.237 psi to 0.286 psi (243.4 ft./sec. to 267.4 ft./sec.). Velocities in this range should not have drastically affected the flowfield but several axial measurements were made to ensure this. The resulting flow profiles agreed with all previous data, supporting this assumption. After the measurements of the Z components, $\overline{W}$ and Wrms, the turbulence kinetic energy, K, could be calculated from the relation

$$K = U_{rms}^2 + V_{rms}^2 + W_{rms}^2 \qquad (A.16)$$

Cross Jet Flow

The measurement of the cross jet profiles necessitated very close proximity to the jet exit as conditions at the jet exit were desired, as well as conditions very small distances from the exit. This required the orientation of one of the incident beams parallel to one of the walls with the second beam intersecting the first one at an increased angle, as in figure (A.5). Since the beam angle was 5 degrees, roughly, the actual velocity component measured was not exactly aligned with the jet axis but at a slight angle of 2.5 degrees with the centerline of the jet (this is also illustrated in figure (A.5)). The cosine of 2.5 degrees is 0.999 indicating that negligible errors occur for this Y component measurement.

Statistics

For all the velocity components actually measured the characteristic mean and rms terms result from the reduction of instantaneous data samples, with at least 4000 of these samples taken at each data point. The mean velocity was calculated by a simple arithmetic average

$$\bar{U} = \frac{\sum_{i=1}^{N} U_i}{N} \qquad \text{(A.16)}$$

where N is the number of samples and U_i are the

instantaneous samples. The rms velocity was calculated from the relation

$$U_{RMS} = \left[\frac{\sum_{i=1}^{N} U_i^2 - \frac{\sum_{i=1}^{N} U_i \sum_{i=1}^{N} U_i}{N}}{N - 1} \right]^{\frac{1}{2}} \qquad \text{(A.17)}$$

All velocity component characteristics were formed in this manner, allowing substitution into equations (A.1-A.12) to derive the desired characteristics.

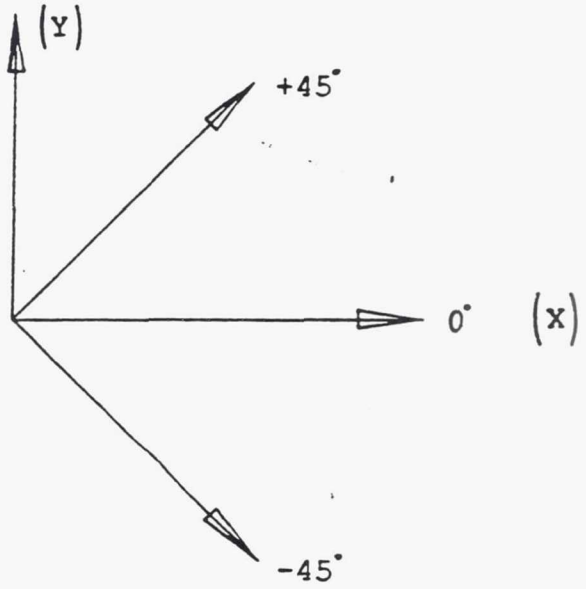

Figure A.1 Measured Velocity Component Orientations

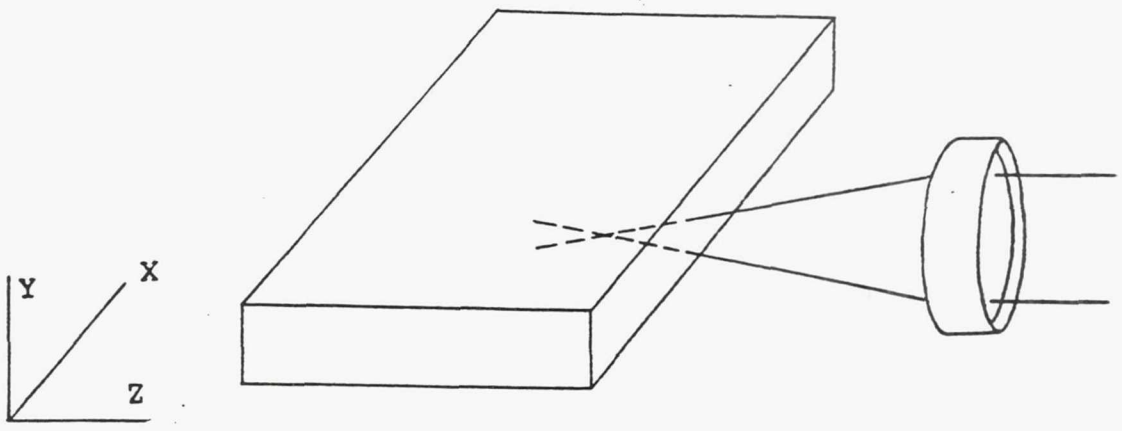

Figure A.2 Combustor Model Orientation for U and V Measurements

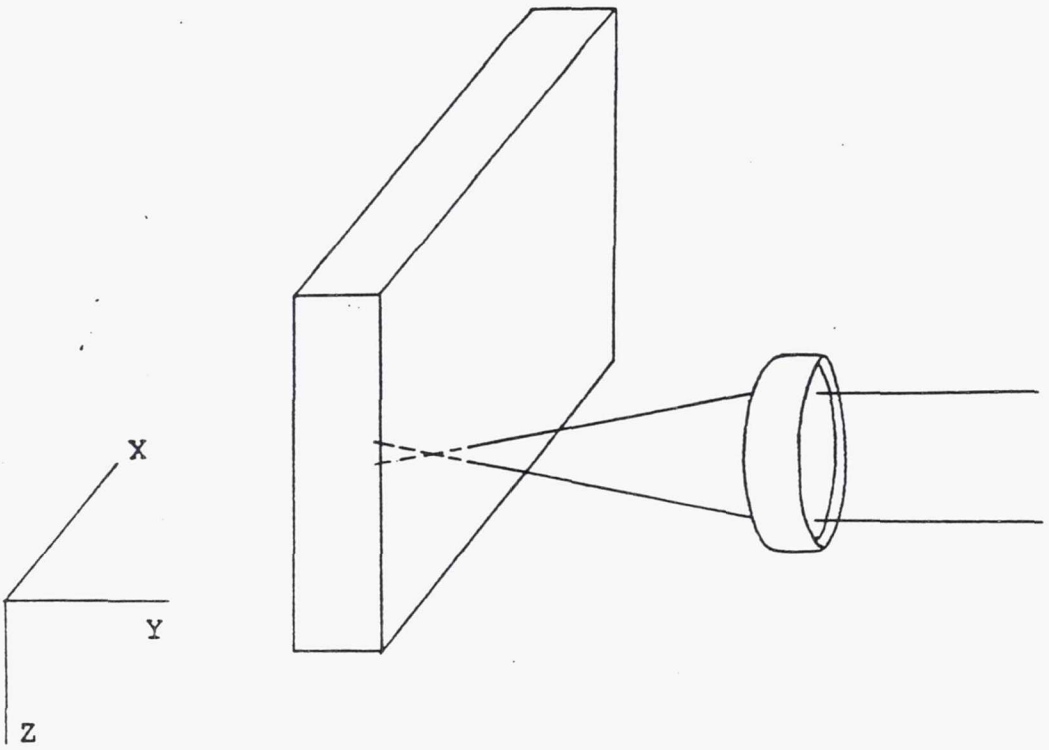

Figure A.3 Combustor Model Orientation for W Measurements

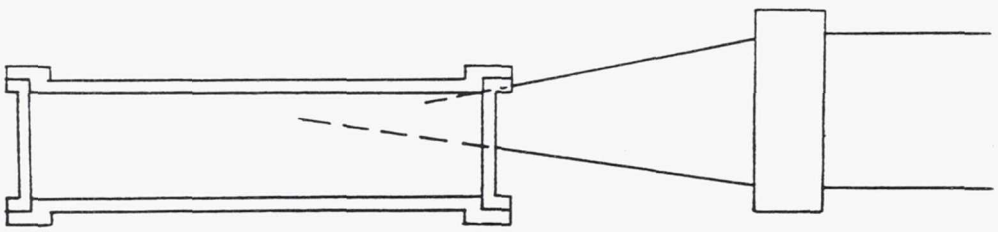

Figure A.4 Incident Laser Beam Geometric Interference

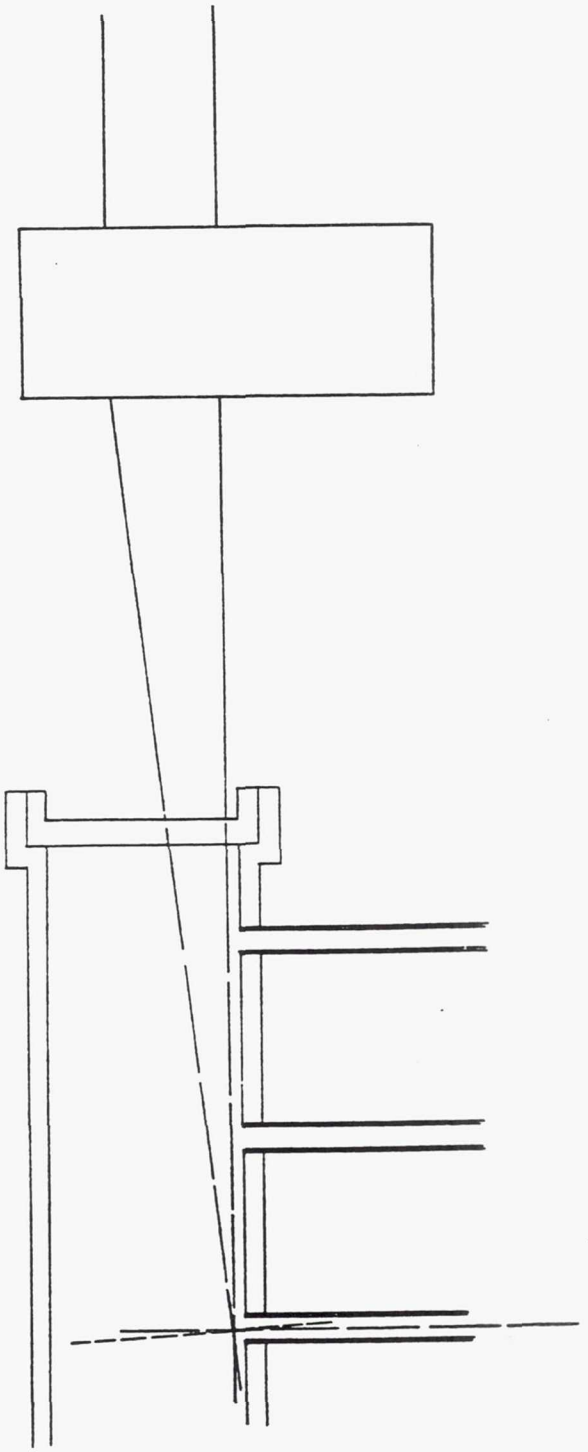

Figure A.5 Laser Beam Orientations for Primary Jet Measurements

APPENDIX B. Uncertainty Analysis

In order to determine the errors and uncertainty involved with the flow characteristics one must consider several sources. Errors and uncertainties are introduced during the actual measurement of the individual data samples, the determination of the measured velocity components from these individual samples and the calculation of the unmeasured characteristics from the measured quantities.

The main sources of error and uncertainty from the measurement of the individual samples are LDV biases, uncertainty in the incident beam intersection angle and the finite resolution of the frequency measurement. When a limited number of individual measurements are used to obtain statistics for a velocity component a certain amount of uncertainty, sampling error, is inherent in the results. From Appendix A the determination of unmeasured characteristics such as $\overline{V}$, Vrms, $\overline{U'V'}$ and K from the mean and rms velocities which were assumed to be measured in the +/- 45 and 0 degree orientations was described (see figure (A.1)). Uncertainties were involved in the measurement of these +/- 45 and zero degree angles, generating uncertainties in the calculated quantities. The

following includes a discussion of the various errors or uncertainties and their effects on the flow characteristics.

Although the Laser Doppler Velocimetry technique of velocity measurement has the advantage of being non-intrusive in nature, the method has disadvantages in that many types of statistical biases may alter the results if care is not taken in the setup of the experimental apparatus and optical and data acquisition systems. These types of biases include velocity, filter, angle and gradient bias. Many techniques and processors have been developed in an attempt to alleviate or reduce these bias errors, but most are applicable only to certain sets of conditions and thus are not universal.

Velocity bias occurs, in the individual realization, or burst, mode, of LDV operation, due to the fact that the velocity measurements are made when single particles pass through the measurement volume. The arrival rate of these particles is not independent of, but proportional to, the flow velocity for the case of well mixed marker particles. The result is that as the flow velocity increases the number of marker particles traversing the measurement volume also increases. This effect biases the mean velocity to a higher value since more samples will be taken at the higher flow velocities, resulting in an average that is biased towards the higher velocities. The

effect on the measured rms velocity is opposite to the effect on the measured mean: the measured rms velocity is biased towards the lower values of velocity. Thus for both the mean and the rms velocities the bias effect is one-sided. Velocity bias is especially problematic in highly turbulent flowfields where large fluctuations are the rule, not the exception.

Several methods of velocity bias correction have been developed: controlled processor [17], saturable detector [18], sample and hold [1], Mclaughlin and Tiederman Correction [37], residence time weighting [10], and rate measurement [17]. The most widely used method of these is the residence time weighting, a technique based on the time during which a particle resides in the measurement volume. This method requires the knowledge of the residence time in the measurement volume for every particle, but does provide the correct statistics for a uniformly seeded flow. The processing electronics used in this experiment did not allow for the measurement of the residence times which precluded the use of the residence time method. Due to the general restriction of high data density (and the inability for this to occur in large portions of the flow) the controlled processor, saturable detector, sample and hold and rate measurement methods were impractical to implement. Various experimental sampling techniques have been proposed that can remove all

traces of velocity biasing but these also require very high data rates for successful use, something that cannot always be generated in all flows.

The local turbulence intensities in the model combustor range from zero to infinity (local mean goes to zero). Most experimental studies have investigated flows with maximum turbulence intensities less than 100% ([10],[26]), making the estimates of possible bias errors for higher turbulence intensities difficult. Typical errors in the mean velocity when using free running processors (individual realization mode) for turbulence intensities of 15%, 30%, 75% and 100% are 3%, 10%, 25% and 30%.

Lehmann [33] performed a theoretical study similar to that of Mclaughlin and Tiederman [37] on velocity biasing using an extension of the McLaughlin-Tiederman Correction. Lehmann included results for very high levels of turbulence intensities, up to 1000%; in the lower range of turbulence intensities his results agreed with other literature ([10],[26]). Typical results for the possible mean velocity bias errors are 40% and 50% for local turbulence intensities of 175% and 300%, while for the turbulence intensity itself, the error is constant at -15% for turbulence intensities above 100%.

An important fact to remember is that these errors are possible errors; in the previous studies the flows

were either uniformly seeded or assumed to be (in theoretical models). The actual uncertainties could be either larger or smaller than the values given here; these values are to be used as a guideline. In order to illustrate the possible effects of velocity bias on the measured characteristics two sets of results are shown in figures (B.1) and (B.2) which include both the original measured values and the "corrected" values (using the percent errors given above).

The mean and rms velocities shown were measured at the downstream location X=1.00 in. and cross stream location Z=7.60 in. As can be seen from the data the bias error in the rms measurement is generally small whereas the potential mean error is considerably larger at nearly 20% across the channel.

Filter bias occurs due to the processor's operational efficiency being a function of the particle velocity, or the measured frequency. The signal from a particle that generates a frequency which is far outside the optimum frequency response range of the processing electronics may not possess sufficient strength to exceed the threshold value and thus will not be processed. Most processors on the market today have a wide enough frequency response range to allow measurements in most flows.

Another filter bias problem involves the settings of the high- and low-pass filters on the processors. If all

the frequencies from the particles traversing the measurement volume do not fall in the preset filter range serious alteration of velocity statistics will occur.

Angle bias, also known as fringe bias, occurs since LDV systems cannot make measurements for all particle trajectories. Since a certain preset number of interference fringes must be traversed in order for a signal to be processed particles moving near the perimeter of the measurement volume will not be included in the resulting statistics. The use of a Bragg cell reduces this effect since the fringes move at a rather high speed relative to the measurement volume. From [17], the fringe velocity (Bragg cell frequency shift) should be at least twice the highest velocity (maximum Doppler frequency shift) to be found in the flowfield.

In this experiment, the maximum absolute flow velocity was found at the exit of the primary jets. This velocity was on the order of 334 ft./sec., which corresponds to a Doppler frequency of roughly 18 MHz, less than one-half the Bragg shift of 40 MHz. One can conclude from this that angle bias was not a contributing factor to statistical bias in this experiment.

Gradient bias occurs when a mean velocity gradient exists across the measurement volume. Since the measurement volume is finite in size a range of velocities exists at any one time in this volume and the resulting

statistics are made over this range. Due to the very small size of the probe volume gradient bias was assumed to be negligible, especially compared to other forms of bias.

For the calculation of the individual velocities from the measured frequencies (time intervals) two sources of uncertainty exist: incident beam angle measurement uncertainty and uncertainty in the frequency measurement due to the resolution of the processing electronics. Since the incident beam angle measurement was performed by hand using basic trigonometric relations uncertainties appear due to the ability of the experimenter to precisely locate the center of the beam cross sections and the probe volume for the required distance measurements. From a study of the actual method used for the beam angle calculation a possible angular uncertainty, $\Delta\theta$, of +/- 0.1 degree (0.00174 radian) was concluded. The uncertainty in frequency, Δf_D , resulting from the resolution of the processing electronics is generated by the least significant bit, which in the case of this experiment was 1 bit out of 4096.

The uncertainty for each of the individual measurements due to uncertainties from both the incident beam angle measurement and the limited frequency measurement resolution can be found from an expansion of the relation

$$U = \frac{\lambda}{2\sin(\frac{\theta}{2})} f_D \tag{3.9}$$

When expanded to give the relation for the uncertainties in the velocity calculation in terms of the beam angle and the frequency the following equations result,

$$\Delta U_\theta = \frac{\partial U}{\partial \theta} \Delta\theta \tag{B.1}$$

$$\Delta U_{f_D} = \frac{\partial U}{\partial f_D} \Delta f_D \tag{B.2}$$

The partial derivatives in equations (B.1) and (B.2) are found from differentiation of equation (3.9):

$$\frac{\partial U}{\partial \theta} = \frac{-\lambda f}{4} \frac{\cos(\frac{\theta}{2})}{(\sin(\frac{\theta}{2}))^2} \tag{B.3}$$

$$\frac{\partial U}{\partial f_D} = \frac{\lambda}{2\sin(\frac{\theta}{2})} \tag{B.4}$$

The uncertainty of the velocity in terms of the beam angle can then be represented as (for a half-angle of 2.5 degrees and an angle uncertainty of +/- 0.1 degree)

$$\Delta U_\theta = 3.66 \times 10^{-7} f_D \tag{B.5}$$

The uncertainty from the beam angle is a bias which is present in all the data samples measured for that particular beam angle. When the velocity statistics are are to be calculated from the individual samples one can easily account for this bias. The bias averages through in

the calculation for the mean velocity while for the rms calculation the bias is averaged out (both the mean and individual samples consist of the same bias). Figure (B.3) illustrates the uncertainty interval in the measured mean axial velocity at the X=1.00 in. and Z=7.60 in. location due to the uncertainty in the incident beam angle measurement.

The output of the processor, in decimal digits, is related to the number of fringes, N, and the doppler frequency of the particles in the probe volume by the following relation (from the TSI counter processor instruction manual [51]),

$$D_m = \frac{Nx10^9}{2f_D} \tag{B.6}$$

If an expansion of Δf_D is made in terms of the processor output using only the first term of a Taylor's series expansion one finds,

$$\Delta f = \frac{\partial f}{\partial D_m}\Delta D_m \tag{B.7}$$

where

ΔD_m = uncertainty in decimal digits.

Taking the partial derivative of equation (B.4) when it is switched to give f as a function of Dm gives

$$\frac{\partial f}{\partial D_m} = \frac{-4x10^9}{D_m^2} \tag{B.8}$$

Substituting the equation (B.4) into equation (B.6)

followed by substitution into equation (B.5) results in

$$\Delta f = \frac{-f^2}{4x10^9}\Delta D_m \qquad (B.9)$$

This relation shows that the uncertainty in frequency is proportional to the square of the Doppler frequency from the probe volume.

Substitution of the above relations into equation (B.3) and using an average value of 2.5 degrees for the beam half angle results in

$$\Delta U_{f_D} = 2.294x10^{-15} f_D^2 \qquad (B.10)$$

One important characteristic of the above relation concerns the use of a variable frequency shift. Since the input signal to the counter processor consists of both the Doppler frequency as well as the variable frequency shift the uncertainty in the calculated velocity from the limited frequency measurement resolution is dependent on the variable frequency shift being employed. In general this error is very small. For this experiment the variable frequency shift was chosen to give an input signal to the counter processor of around 10 MHz; for this frequency and an incident beam half angle of 2.5 degrees the uncertainty in the individual velocity measurements is

$$\Delta U_{f_D} = 0.2 \text{ ft./sec.} \qquad (B.11)$$

which is a negligible amount compared to that due to the

beam angle measurement uncertainty; thus the uncertainty due to the limited frequency measurement resolution can be neglected.

Sampling error is due to the finite number of independent data samples measured to determine the velocity statistics. For this experiment a minimum of 4000 samples were taken at each data point location. For the actual measured components the 95% confidence interval for the mean velocity is

$$\overline{U} - 1.96\frac{U_{rms}}{\sqrt{N}} < \overline{U}_t < \overline{U} + 1.96\frac{U_{rms}}{\sqrt{N}} \qquad (B.12)$$

where

U_{rms} = root-mean-square velocity,

$\overline{U}$ = mean of velocity measurements,

N= number of data samples.

As an example, for the axial velocity the maximum rms velocity was found to be 70 ft./sec. For 4000 data samples the 95% confidence interval for the mean velocity becomes

$$\overline{U} - 2.17 \text{ ft./sec.} < \overline{U}_t < \overline{U} + 2.17 \text{ ft./sec.} \qquad (B.13)$$

For the root-mean-square velocity the 95% confidence interval is

$$\frac{U_{rms}}{1 + \frac{1.96}{\sqrt{2(N-1)}}} < U_{rms_t} < \frac{U_{rms}}{1 + \frac{1.96}{\sqrt{2(N-1)}}} \qquad (B.14)$$

where

U_{rms_t}= true root-mean-square velocity.

For a maximum rms velocity of 70 ft./sec. and 4000 data samples the confidence interval for the rms velocity becomes

$$68.499 \text{ ft./sec.} < U_{rms_t} < 71.568 \text{ ft./sec.} \quad \text{(B.15)}$$

The confidence intervals for a chosen set of data can be seen in figures (B.4) and (B.5). This data is, as before, the measured axial component from the X=1.00 in. and Z=7.60 in. locations. In the calculation of the total uncertainty of the velocities the limits of the confidence intervals are used as the uncertainty values.

For the total uncertainty in the statistics of the measured velocities the uncertainty components due to the beam angle measurement and the sampling error are combined in a sum of squares method such as

$$\Delta U = \sqrt{\Delta U_\theta^2 + \Delta U_{samp}^2} \quad \text{(B.16)}$$

The uncertainty due to the LDV velocity biasing is then added to this uncertainty. Since the LDV velocity biasing uncertainty is one-sided (the true mean is in some velocity magnitude range below the measured, biased mean velocity magnitude; the true rms is in some velocity magnitude range above the measured, biased rms velocity magnitude) the velocity bias cannot be added in the sum of squares technique. The calculated total uncertainty

intervals in the measured velocity components (mean and rms) can be found in figures (B.6) and (B.7)

As shown in Appendix A in equations (A.13), (A.14) and (A.15) algebraic relations involving measured quantities were used to evaluate V, Vrms, U'V' and K. These quantities were the mean and the rms velocities which were assumed to be measured along the +/- 45 and 0 degree directions (the 0 degree orientation corresponded to the measurement in the positive X direction). Due to uncertainty in the angular measurements of the +/- 45 degree directions uncertainties resulted in the calculated quantities. The 0 degree component (U) was able to be measured much more accurately than the +/- 45 degree cases and as such was assumed to cause a negligible amount of uncertainty.

From Durst, Melling and Whitelaw [16] relations between the measured components and the values along the three coordinate directions are given:

$$\overline{U}_i = \overline{U}\cos(a_x) + \overline{V}\cos(a_y) + \overline{W}\cos(a_z) \tag{B.17}$$

$$\begin{aligned}\overline{U'^2}_i = {} & \overline{U'^2}(\cos(a_x))^2 + \overline{V'^2}(\cos(a_y))^2 + \overline{W'^2}(\cos(a_z))^2 \\ & + 2(\overline{U'V'}\cos(a_x)\cos(a_y) + \overline{U'W'}\cos(a_x)\cos(a_z) \\ & + \overline{V'W'}\cos(a_y)\cos(a_z))\end{aligned} \tag{B.18}$$

In order to determine the uncertainties in the calculated quantities one must develop these relations. For the V term equation (B.17) must be used for the +/- 45 degree cases, while for the Vrms and $\overline{U'V'}$ terms equation (B.18)

cases, while for the Vrms and $\overline{U'V'}$ terms equation (B.18) must be implemented for the +/-45 and 0 degree cases.

Assuming the 0 degree angle measurement to be correct and all the velocity measurements made in a plane orthagonal to the Z direction (due to more accurate measurement), the resulting sets of relations, in matrix form, are

$$\begin{bmatrix} \overline{U}_{+45} \\ \overline{U}_{-45} \end{bmatrix} = \begin{bmatrix} \cos a_{3x} & \cos a_{3y} \\ \cos a_{4x} & \cos a_{4y} \end{bmatrix} \begin{bmatrix} \overline{U} \\ \overline{V} \end{bmatrix} \tag{B.19}$$

$$\begin{bmatrix} \overline{U'_0{}^2} \\ \overline{U'_{+45}{}^2} \\ \overline{U'_{-45}{}^2} \end{bmatrix} \quad \begin{bmatrix} (\cos a_{2x})^2 & (\sin a_{2x})^2 & \cos a_{2x} \sin a_{2x} \\ (\cos a_{3x})^2 & (\sin a_{3x})^2 & \cos a_{3x} \sin a_{3x} \\ (\cos a_{4x})^2 & (\sin a_{4x})^2 & \cos a_{4x} \sin a_{4x} \end{bmatrix} \begin{bmatrix} \overline{U'^2} \\ \overline{V'^2} \\ \overline{U'V'} \end{bmatrix} \tag{B.20}$$

To determine the uncertainties angles of +/- 45 +/- 0.5 degrees for a_{3x} and a_{4x} were substituted into the above matrices. The coefficient matrices were then inverted to give relations for V, Vrms and $\overline{U'V'}$ in terms of the measured quantities. In general form these relations are

$$\overline{V} = C_1\overline{U}_{+45} + C_2\overline{U}_{-45} \tag{B.21}$$

$$\overline{V'^2} = C_3\overline{U'_0{}^2} + C_4\overline{U'_{+45}{}^2} + C_5\overline{U'_{-45}{}^2} \tag{B.22}$$

$$\overline{U'V'} = C_6\overline{U'_0{}^2} + C_7\overline{U'_{+45}{}^2} + C_8\overline{U'_{-45}{}^2} \tag{B.23}$$

For the determination of the uncertainty in the calculation of the V, Vrms and $\overline{U'V'}$ terms these relations were then subtracted from the equations (A.13), (A.14) and (A.15), which were assumed to give the correct values and were used in the data reduction process.

If one considers the uncertainty in the calculated values solely due to the +/- 0.5 degree uncertainties in the measured component orientations one finds an uncertainty of less than +/- 0.5% for the V term. The uncertainties in the Vrms and $\overline{U'V'}$ terms were determined to be less than +/- 5% and +/- 10%.

When the total amount of uncertainty in the calculated terms is estimated, including all sources, one must consider all the possible combinations of the measured flow quantities. From equations (B.21), (B.22) and (B.23) two terms are involved in the relation for V whereas three are involved for the Vrms and $\overline{U'V'}$ terms. The relative strengths of these terms determine the value of the uncertainties.

After careful analysis of the possible combinations the total uncertainty associated with V was found to be less than +/- 3%. The analysis for the Vrms and $\overline{U'V'}$ terms was much more rigorous due to the existence of the third term in equations (B.22) and (B.23). From this analysis the total uncertainty for the Vrms term was found to be less than +/- 30%, while that associated with the $\overline{U'V'}$

term is less than +/- 35%. For the U term, from before, the uncertainty is in the range from -25% to 5%, while the uncertainty associated with Urms is -2% to 20%. The uncertainty in the calculated value of K was found to be +/- 50%.

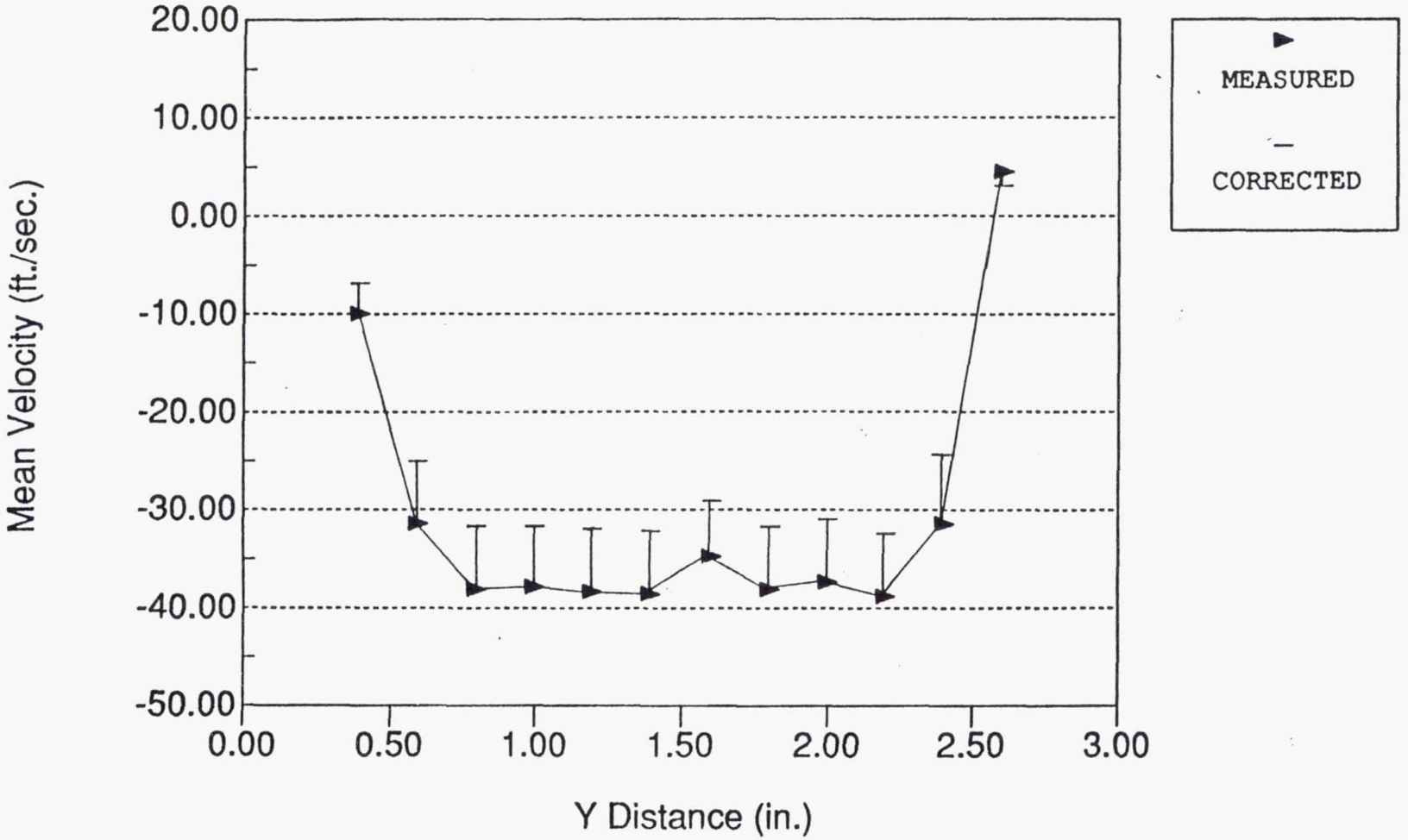

Figure B.1 Mean Velocity Bias Error at X=1.00 in. and Z=7.60 in.

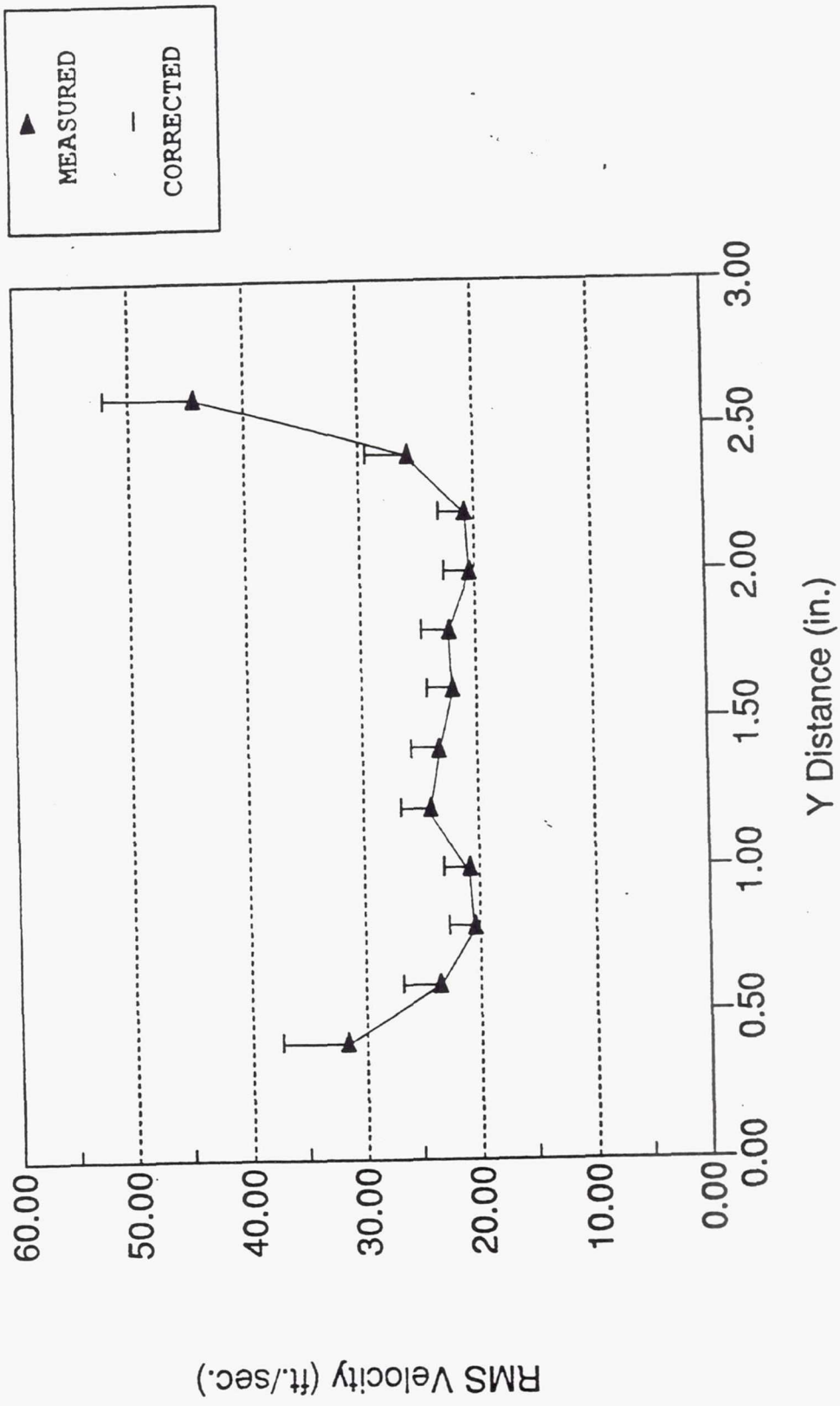

Figure B.2 RMS Velocity Bias Error at X=1.00 in. and Z=7.60 in.

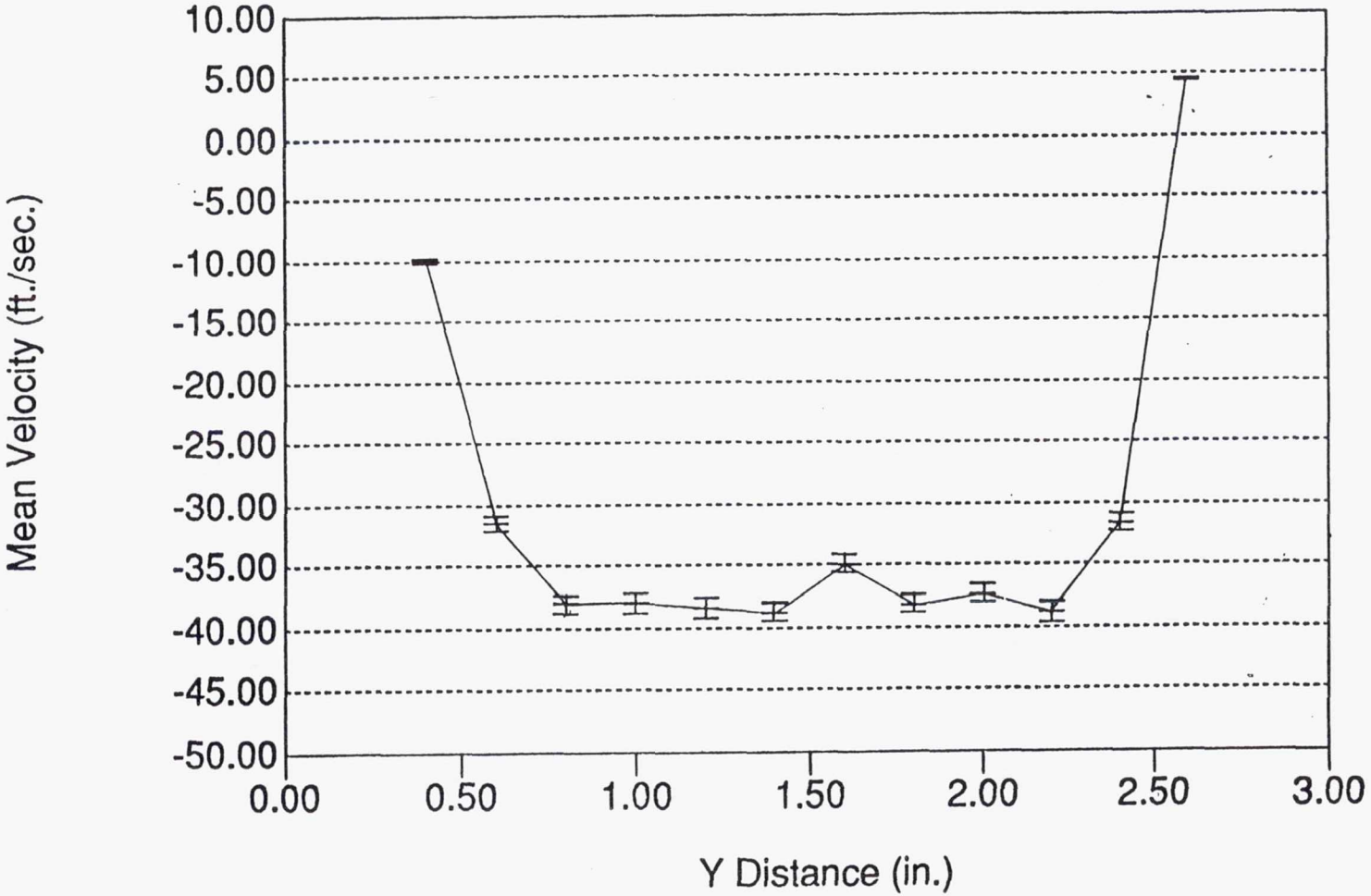

Figure B.3 Mean Velocity Uncertainty Due to Uncertainty in Incident Beam Angle Measurement at X=1.00in. and Z=7.60 in.

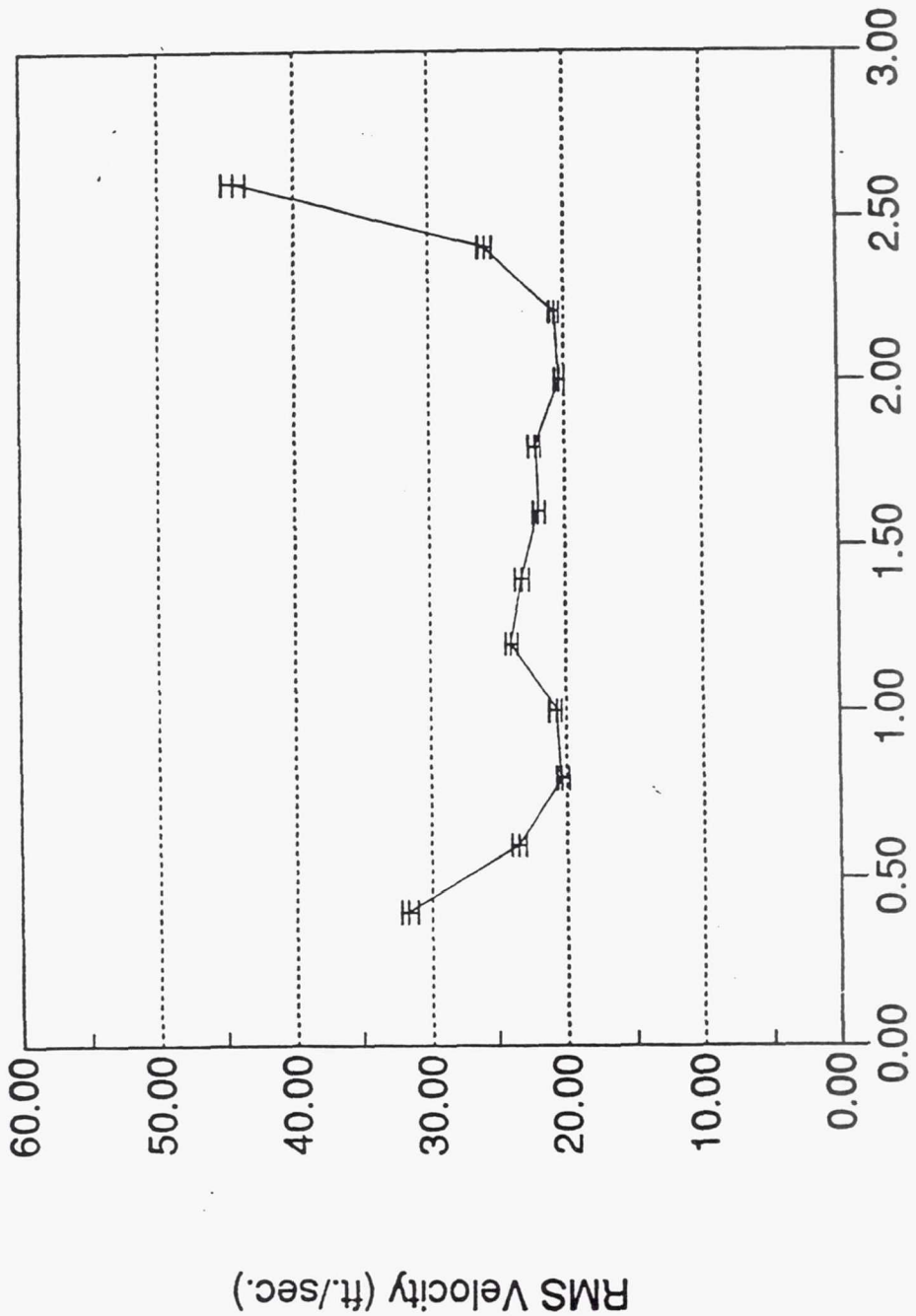

Figure B.5 RMS Velocity 95% Confidence Interval Due to Sampling Uncertainty at X=1.00 in. and Z=7.60 in.

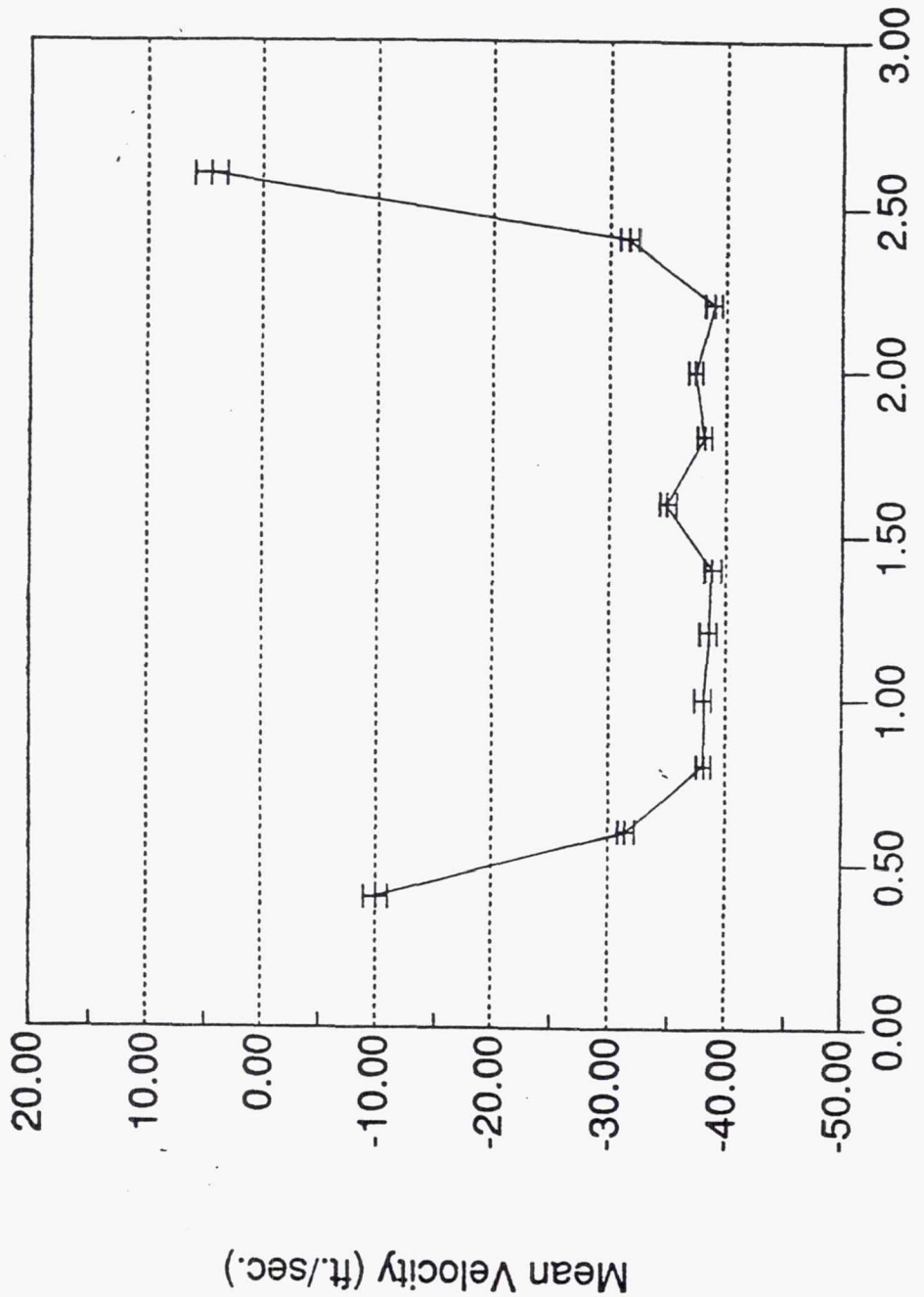

Figure B.4 Mean Velocity 95% Confidence Interval Due to Sampling Uncertainty at X=1.00 in. and Z=7.60 in.

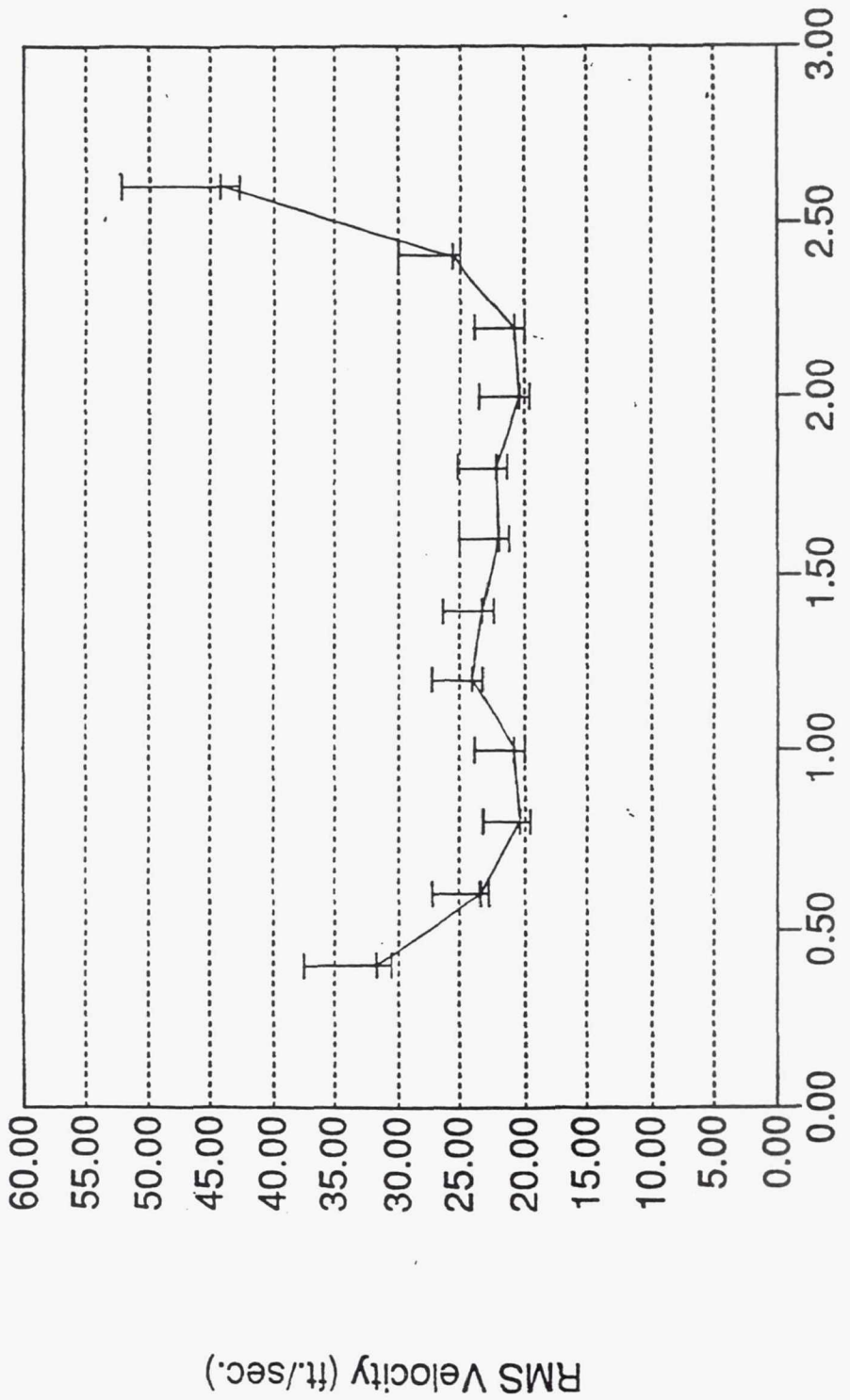

Figure B.7 Total Uncertainty Intervals for Measured RMS Velocity at X=1.00 in. and Z=7.60 in.

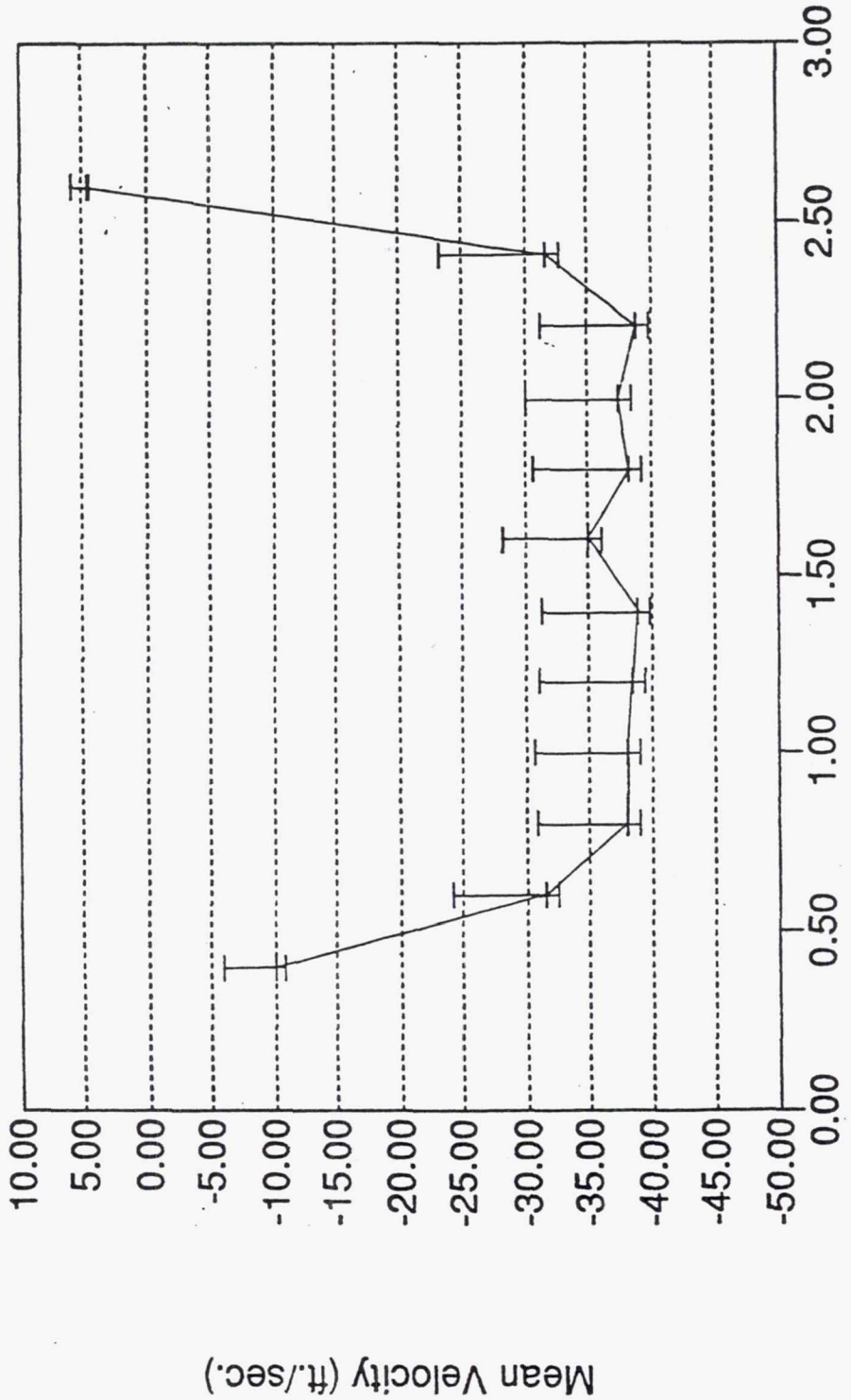

Figure B.6 Total Uncertainty Intervals for Measured Mean Velocity at X=1.00 in. and Z=7.60 in.

APPENDIX C. Additional Line Plots

This Appendix presents additional line plots of the mean velocities in the three coordinate directions, $\overline{U}$, $\overline{V}$ and $\overline{W}$. This data was not included in Chapter 3 due to the use of the vector plots.

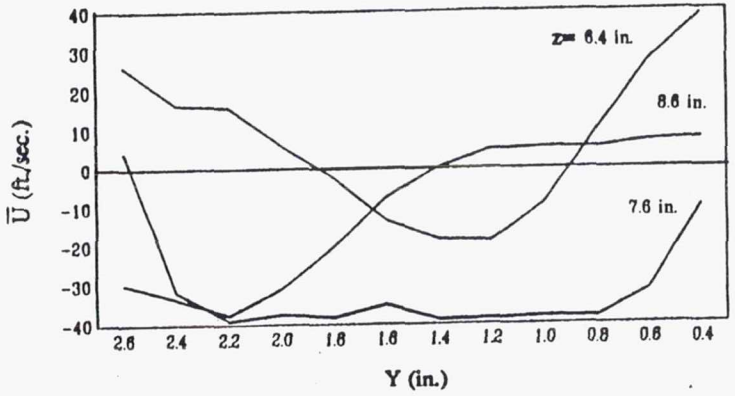

(a)

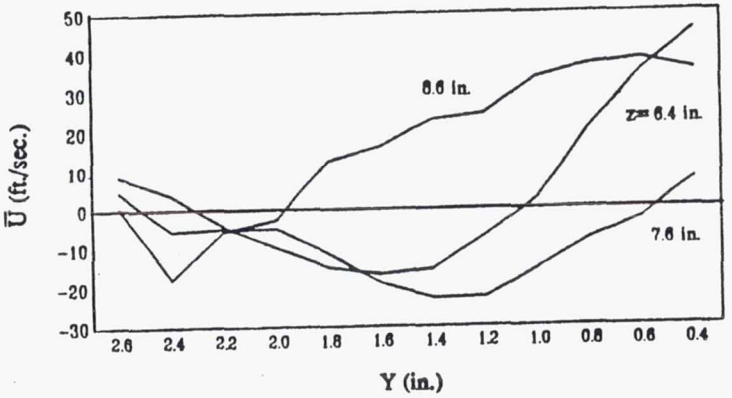

(c)

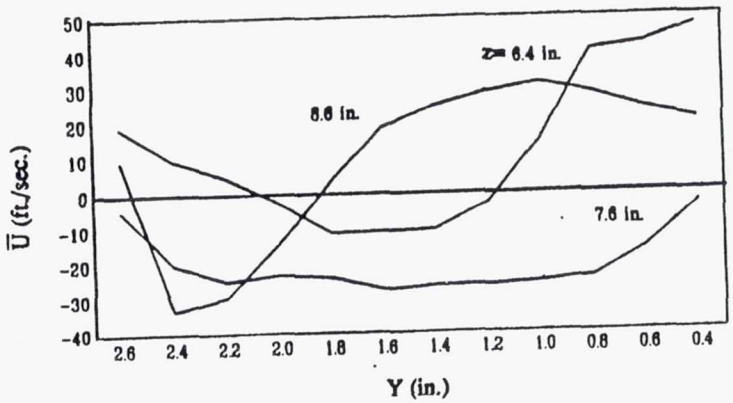

(b)

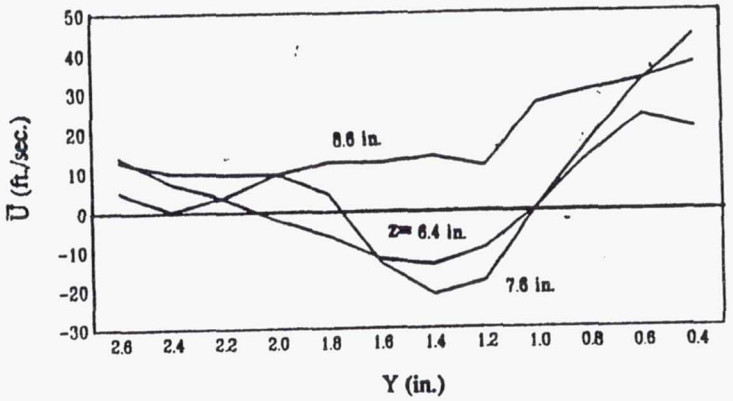

(d)

Figure C.1 Line Plots of $\bar{U}$ at X=1.00, 1.50, 2.00 and 2.50 in.

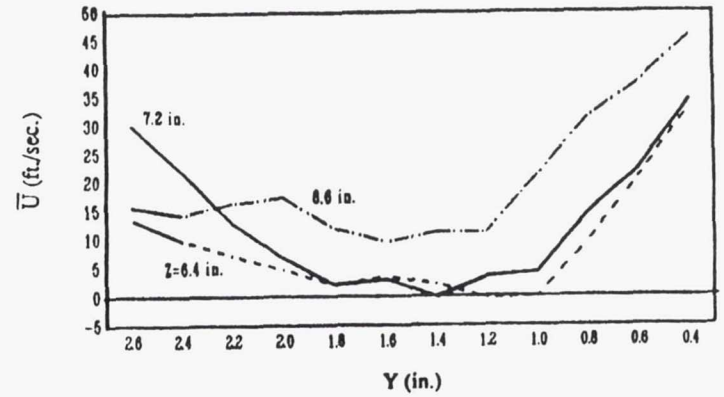

(a)

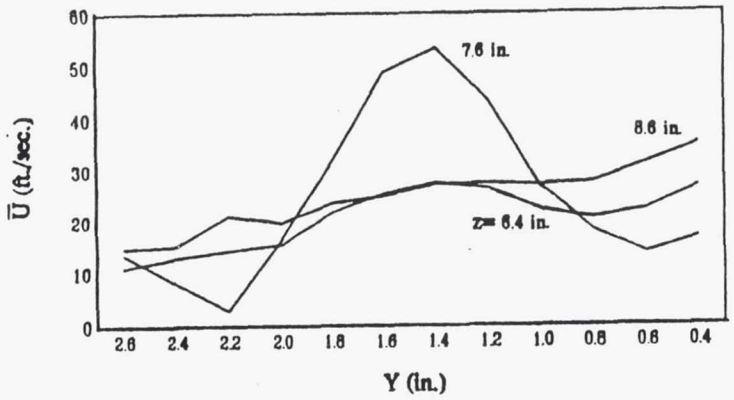

(c)

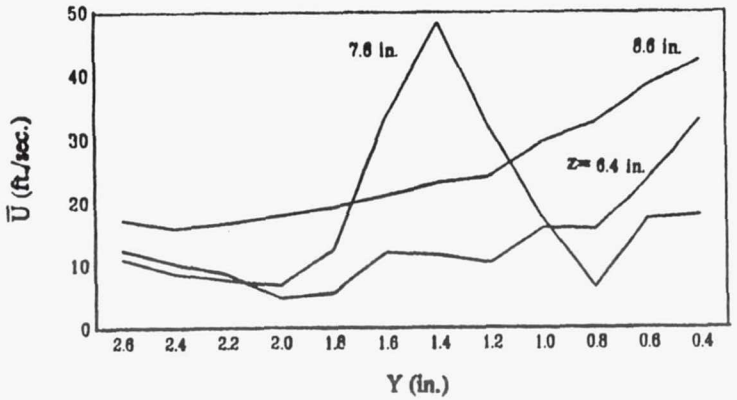

(b)

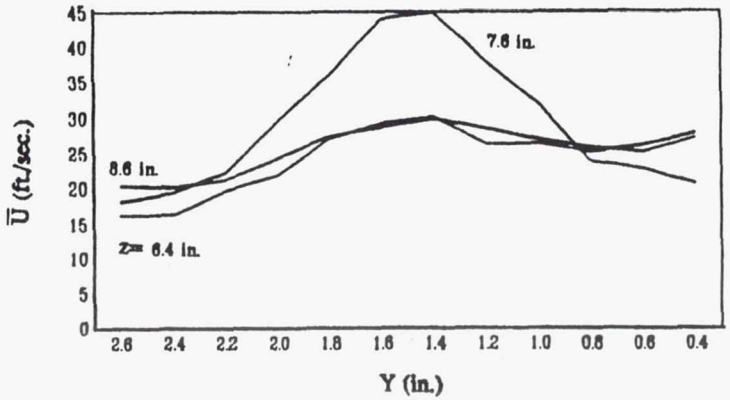

(d)

Figure C.2 Line Plots of $\bar{U}$ at X=3.00, 3.50, 4.00 and 4.50 in.

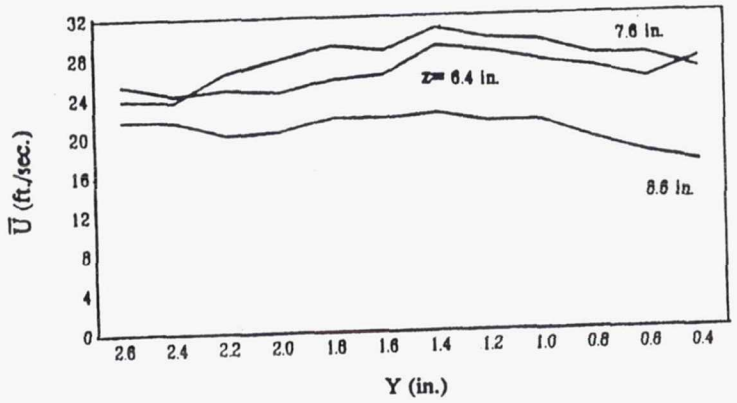

(a)

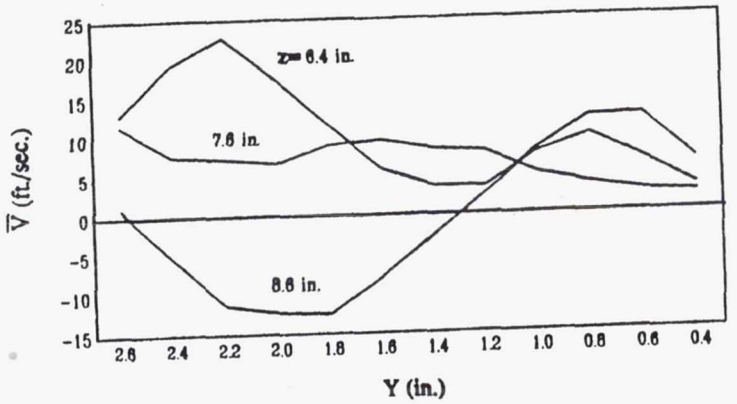

(c)

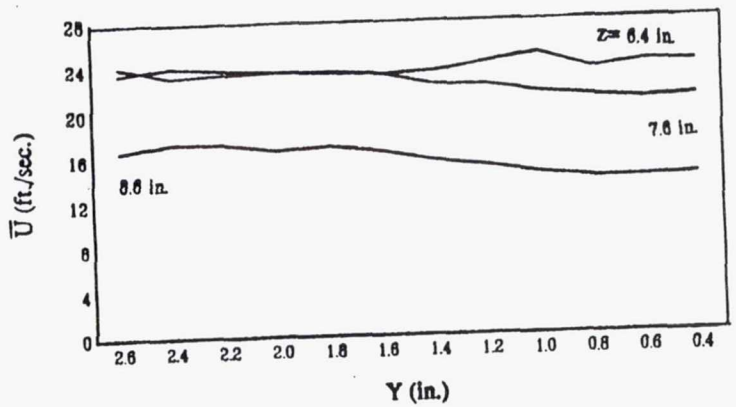

(b)

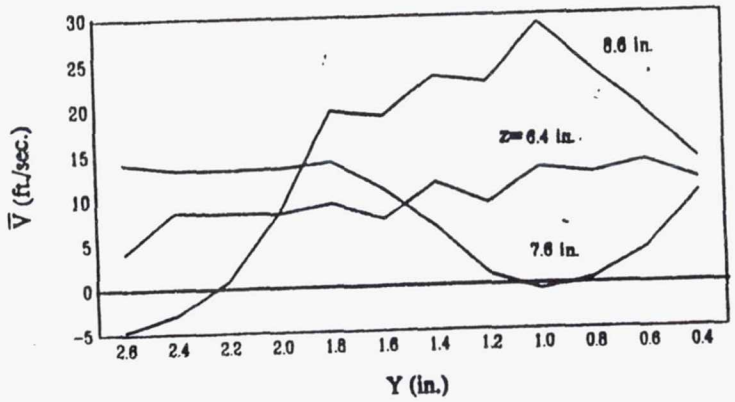

(d)

Figure C.3 Line Plots of $\overline{U}$ at X=6.00 in. and 9.00 in. and of $\overline{V}$ at X=1.00 in. and 1.50 in.

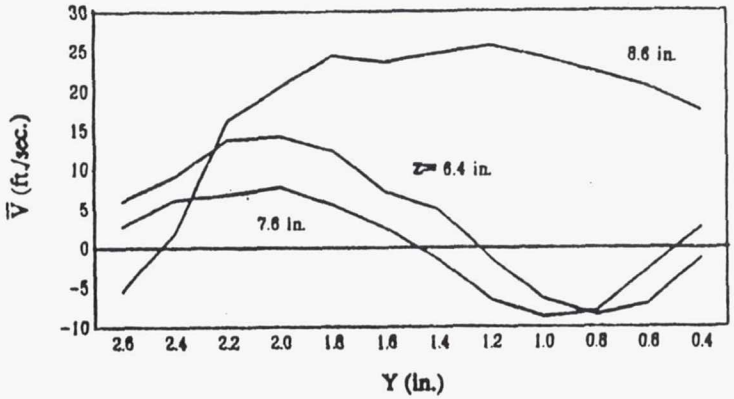

(a)

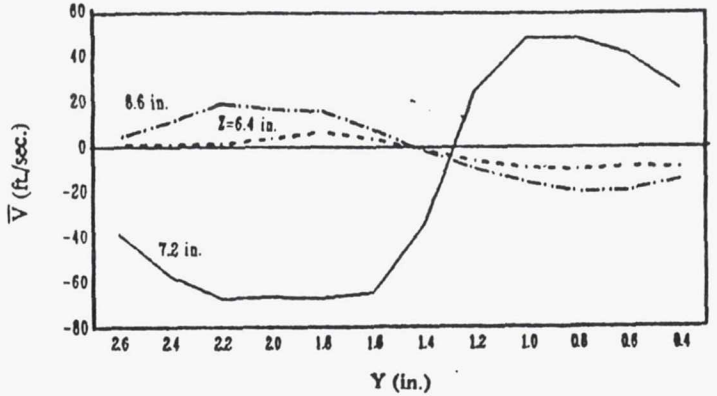

(c)

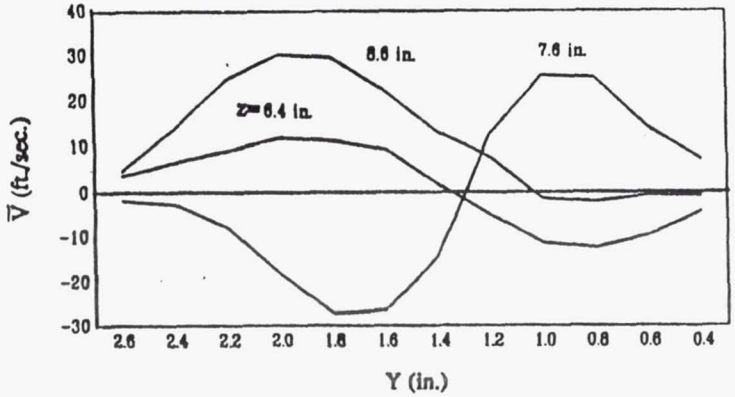

(b)

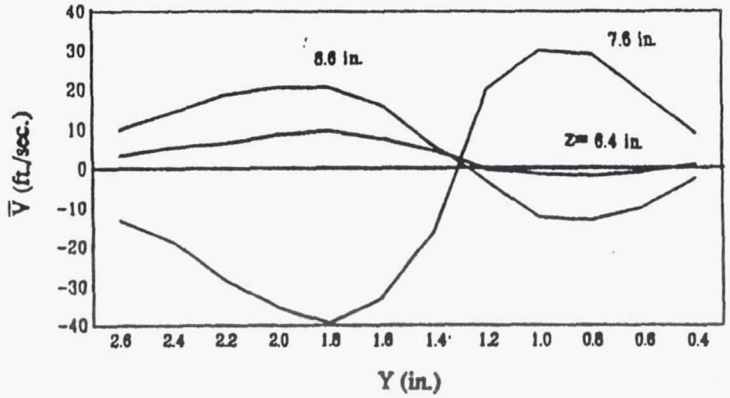

(d)

Figure C.4 Line Plots of $\overline{V}$ at X=2.00, 2.50, 3.00 and 3.50 in.

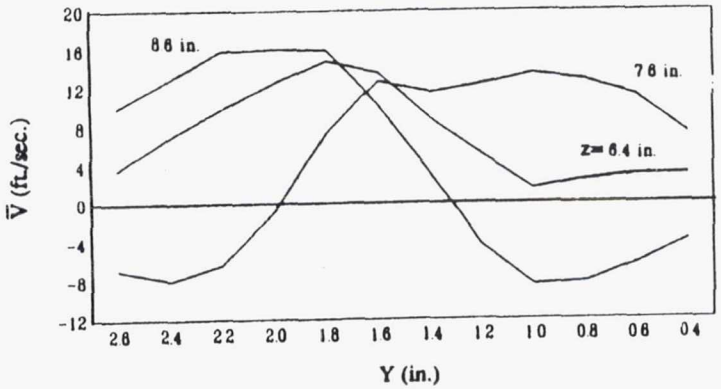

(a)

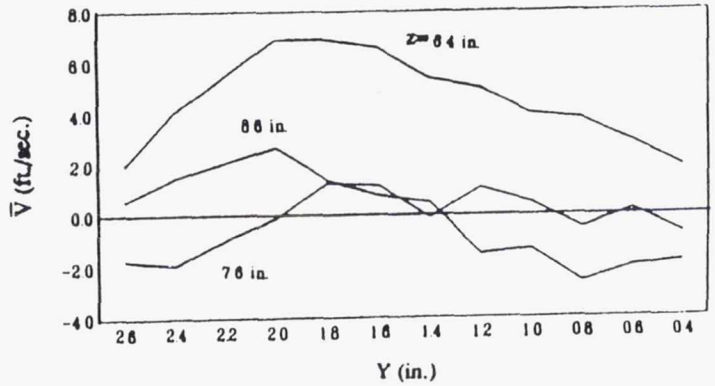

(c)

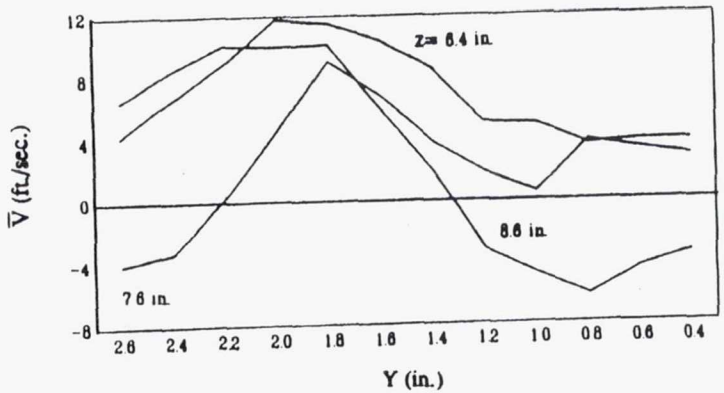

(b)

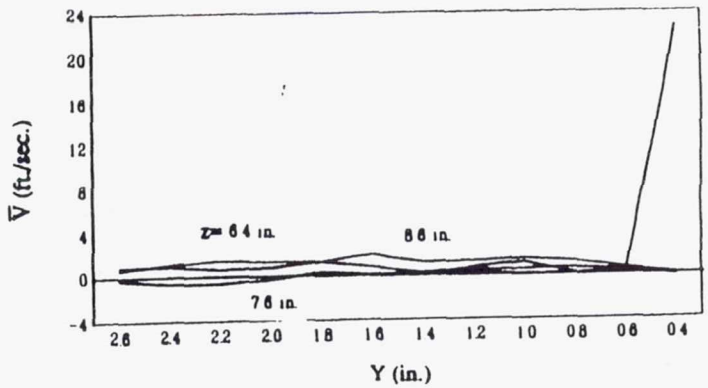

(d)

Figure C.5 Line Plots of $\overline{V}$ at X=4.00, 4.50, 6.00 and 9.00 in.

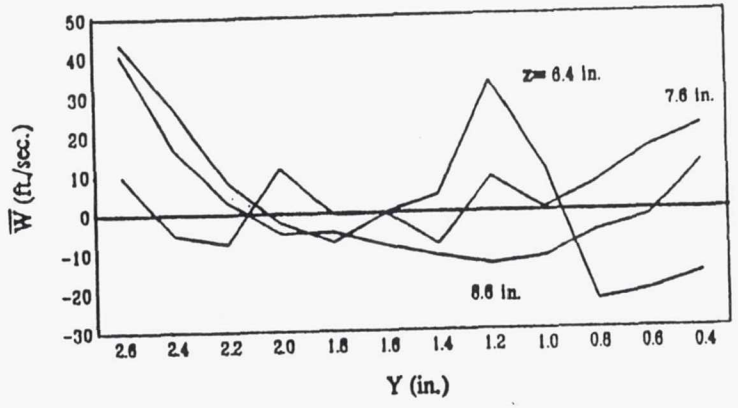

(a)

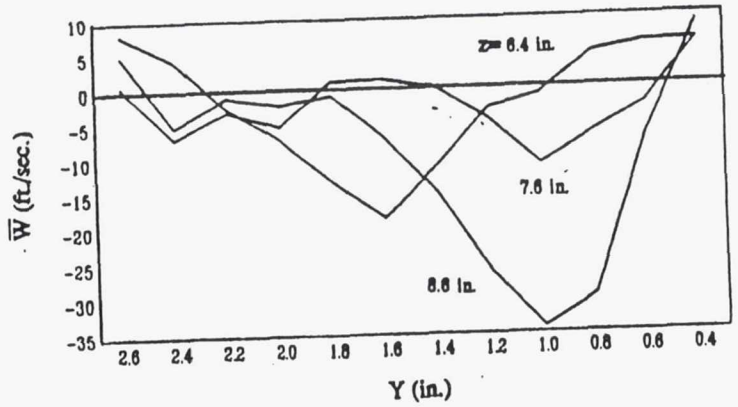

(c)

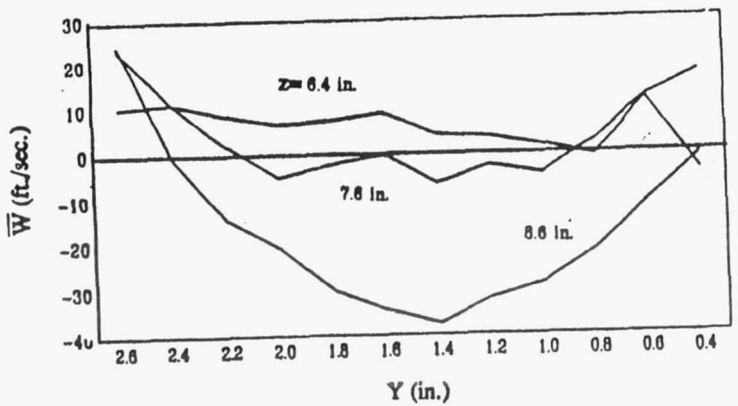

(b)

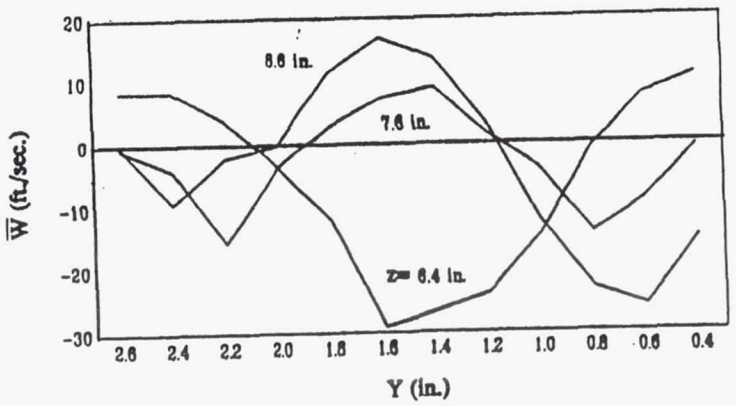

(d)

Figure C.6 Line Plots of $\overline{W}$ at X=1.00, 1.50, 2.00 and 2.50 in.

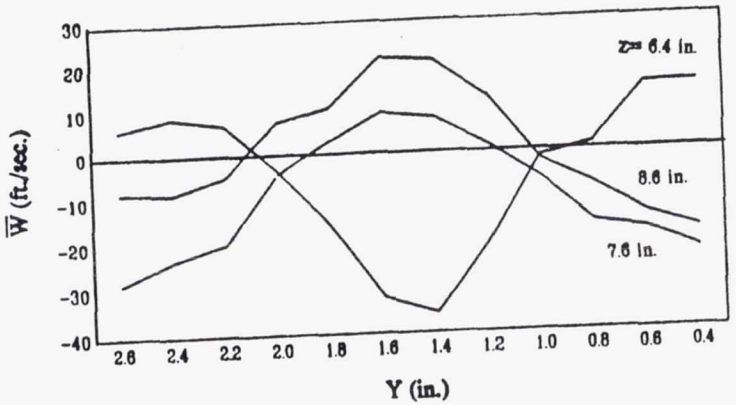

(a)

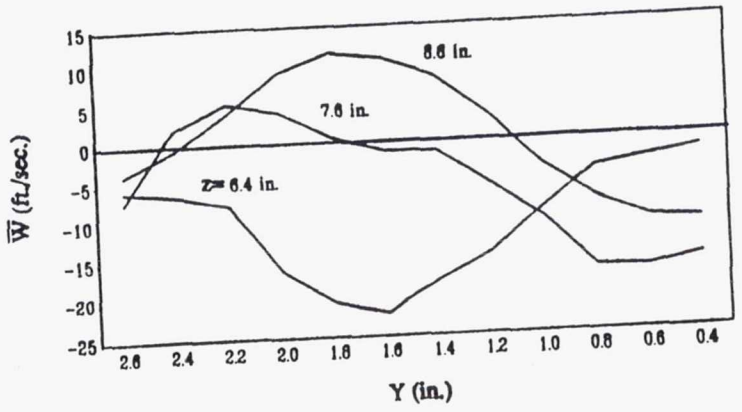

(c)

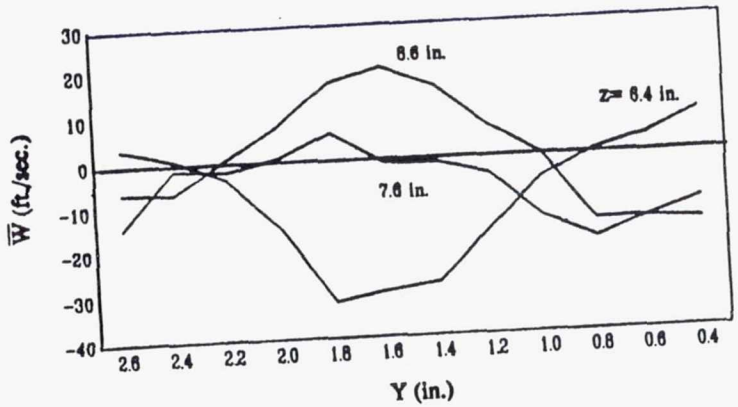

(b)

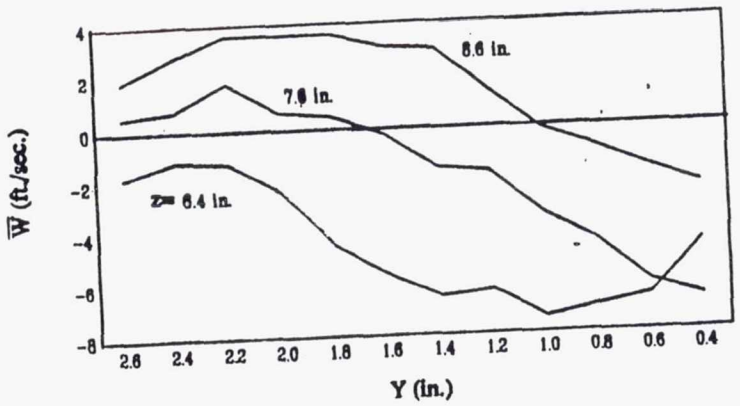

(d)

Figure C.7 Line Plots of $\overline{W}$ at X=3.50, 4.00, 4.50 and 6.00 in.

REPORT DOCUMENTATION PAGE

Form Approved
OMB No. 0704-0188

1. AGENCY USE ONLY (*Leave blank*)	2. REPORT DATE	3. REPORT TYPE AND DATES COVERED
	April 1997	Final Contractor Report

4. TITLE AND SUBTITLE

An Experimental Study of Swirling Flows as Applied to Annular Combustors

5. FUNDING NUMBERS

WU–505–62–52
C–NAS3–24350

6. AUTHOR(S)

Michael Damian Seal II

7. PERFORMING ORGANIZATION NAME(S) AND ADDRESS(ES)

Purdue University
West Lafayette, Indiana 47907

8. PERFORMING ORGANIZATION REPORT NUMBER

E–9867

9. SPONSORING/MONITORING AGENCY NAME(S) AND ADDRESS(ES)

National Aeronautics and Space Administration
Lewis Research Center
Cleveland, Ohio 44135–3191

10. SPONSORING/MONITORING AGENCY REPORT NUMBER

NASA CR–182271

11. SUPPLEMENTARY NOTES

This report was submitted as a thesis in partial fulfillment of the requirements for the degree Master of Science in Aeronautics and Astronautics to Purdue University, West Lafayette, Indiana 47907. Project Manager, J.D. Holdemen, Internal Fluid Mechanics Division, NASA Lewis Research Center, organization code 2650, (216) 433–5846.

12a. DISTRIBUTION/AVAILABILITY STATEMENT

Unclassified - Unlimited
Subject Category 07

This publication is available from the NASA Center for Aerospace Information, (301) 621–0390.

12b. DISTRIBUTION CODE

13. ABSTRACT ***(Maximum 200 words)***

This thesis presents an experimental study of swirling flows with direct applications to gas turbine combustors. Two separate flowfields were investigated: a round, swirling jet and a non-combusting annular combustor model. These studies were intended to allow both a further understanding of the behavior of general swirling flow characteristics, such as the recirculation zone, as well as to provide a base for the development of computational models. In order to determine the characteristics of swirling flows the concentration fields of a round, swirling jet were analyzed for varying amounts of swirl. The experimental method used was a light scattering concentration measurement technique known as marker nephelometry. Results indicated the formation of a zone of recirculating fluid for swirl ratios (rotational speed x jet radius over mass average axial velocity) above a certain critical value. The size of this recirculation zone, as well as the spread angle of the jet, was found to increase with increase in the amount of applied swirl. The annular combustor model flowfield simulated the cold-flow characteristics of typical current annular combustors: swirl, recirculation, primary air cross jets and high levels of turbulence. The measurements in the combustor model, made by the Laser Droppler Velocimetry technique, allowed the evaluation of the mean and rms velocities in the three coordinate directions, one Reynold's shear stress component and the turbulence kinetic energy: The primary cross jets were found to have a very strong effect on both the mean and turbulence flowfields. These cross jets, along with a large step change in area and wall jet inlet flow pattern, reduced the overall swirl in the test section to negligible levels. The formation of the strong recirculation zone is due mainly to the cross jets and the large step change in area. The cross jets were also found to drive a fourcelled vortex-type motion (parallel to the combustor longitudinal axis) near the cross jet injection plane.

14. SUBJECT TERMS

Turbulent viscous flow; Laser diagnostics; LDV; Velocity measurements; Annular combustor; Swirler

15. NUMBER OF PAGES

274

16. PRICE CODE

A12

17. SECURITY CLASSIFICATION OF REPORT	18. SECURITY CLASSIFICATION OF THIS PAGE	19. SECURITY CLASSIFICATION OF ABSTRACT	20. LIMITATION OF ABSTRACT
Unclassified	Unclassified	Unclassified	

National Aeronautics and
Space Administration

Lewis Research Center
21000 Brookpark Rd.
Cleveland, OH 44135-3191